Title

Seismic Response of Eighteen-story Core Wall Building with Force-limiting Connections and Low-damage Coupling Beams

Author

Lee, Kyoungyeon

Publication Date

2022

Peer reviewed|Thesis/dissertation

UNIVERSITY OF CALIFORNIA SAN DIEGO

Seismic Response of Eighteen-story Core Wall Building with Force-limiting Connections and Low-damage Coupling Beams

A thesis submitted in partial satisfaction of the
requirement for the degree Master of Science

in

Structural Engineering

by

Kyoungyeon Lee

Committee in charge:

Professor Georgios Tsampras, Chair
Professor Joel P. Conte
Professor Jose I. Restrepo

2022

The thesis of Kyoungyeon Lee is approved, and it is acceptable in quality and form for publication on microfilm and electronically.

University of California San Diego

2022

TABLE OF CONTENTS

THESIS APPROVAL PAGE iii

TABLE OF CONTENTS iv

LIST OF FIGURES ix

LIST OF TABLES xv

ACKNOWLEDGEMENTS xix

ABSTRACT OF THE THESIS xx

1 Introduction 1

1.1 Literature review 1

1.1.1 Structural walls 1

1.1.2 Interacting cantilever walls 2

1.1.3 Coupled walls and core walls 2

1.1.4 Coupling beam damage 8

1.1.5 Alternative designs for diagonally reinforced concrete coupling beams 10

1.1.6 Higher-mode effects 15

1.1.7 Past research toward high-performance earthquake-resistant buildings 17

1.1.8 Force-limiting connections 18

1.2 Motivation 20

1.2.1 Force-limiting connections on core wall system 20

1.2.2 Low-damage coupling beam 22

1.3 Goal and objectives 23

1.4 Tasks 24

1.5 Organization of document 24

2 Eighteen-story building model 26

2.1 Overview 26

2.2 Building model geometry 26

2.3 Description of the building model 29

2.4 Core wall piers 31

2.4.1 Elements 31

2.4.2 Concrete 33

2.4.3 Steel 44

2.5 Lean-on columns 54

2.5.1 Lean-on column sizes 54

2.5.2 Lean-on column elements 55

2.6 Reinforced coupling beams 57

2.7 Seismic mass 63

2.8 Diaphragm 64

2.9 Modal Analysis 66

2.10 Damping 70

2.10.1 Critical damping 71

2.10.2 Two circular frequencies, $\omega 1$ and $\omega 2$ 71

2.10.3 Damping coefficients, α and β 71

2.10.4 Damping ratio 72

2.11 Force-limiting connections 73

2.11.1 Calculation of FLx 73

2.11.2 Force-limiting connection types 76

2.12 Low-damage coupling beam 81

2.12.1 Design limiting moment of rotational friction connections 81

2.12.2 Design of the steel coupling beam 87

2.12.3 Summary of low-damage coupling beam design 91

2.12.4 Low-damage coupling beam element 91

3 Ground motions 93

3.1 Overview 93

3.2 Considered ground motions 93

3.3 RotD50 response spectrum 95

3.4 Scaling of the ground motions 98

4 Earthquake numerical simulation results 102

4.1 Analysis cases 102

4.2 Effects of the Modified FD force-limiting connections 103

4.2.1 Analysis cases to assess the effects of the Modified FD force-limiting connections 103

4.2.2 Structural level responses 104

4.2.3 Force-limiting connection deformation 109

4.2.4 Strain at the wall base 110

4.3 Effect of low-damage coupling beams 113

4.3.1 Analysis cases to assess the effects of the low-damage coupling beams 113

4.3.2 Difference between the low-damage coupling beam and the reinforced concrete coupling beam in the modeling approach 114

4.3.3 Structural level responses 118

4.3.4 Force-limiting connection deformation 122

4.3.5 Strain at the wall base 123

5 Conclusions 126

5.1 Effect of using the Modified FD force-limiting connections 126

5.2 Effect of using the low-damage coupling beams 127

6 [Appendix] Seismic response plots 129

6.1 Force-limiting connections with RDC = 1.5 and $KRB = 22.5 kip/in$ 129

6.2 Force-limiting connections with RDC = 1.0 131

6.3 Force-limiting connections with RDC = 1.5 134

6.4 Force-limiting connections with RDC = 2.0 137

6.5 Force-limiting connections with RDC = 2.5 140

6.6 Low-damage coupling beam 143

7 [Appendix] Statistics of the earthquake numerical simulation results 145

7.1 Comparison between the force-limiting connections 145

7.1.1 Structural level responses 145

7.1.2 Force-limiting connection deformation 160

7.2 Comparison between the low-damage coupling beams 163

7.2.1 Structural level responses 163

7.2.2 Force-limiting connection deformation 178

REFERENCES 181

LIST OF FIGURES

Figure 1-1: Lateral force resisting mechanisms of (a) interacting cantilever walls and (b) coupled walls (image reference: [1] [4] [7]) 3

Figure 1-2: Examples of floor plans with core walls (image reference: [1]) 4

Figure 1-3: (a) Free body diagram of the coupled walls and (b) free body diagram of the trailing wall and coupling beam at floor x 6

Figure 1-4: Relationship between the degree of coupling and the point of inflection 8

Figure 1-5: Examples of coupling beam damage [11] 8

Figure 1-6: Damaged coupling beams with full section confinement in accordance with ACI 318-08 subjected to (a) 6% and (b) 10% rotation [12] 9

Figure 1-7: Damaged coupling beams with diagonal confinement in accordance with ACI 318-08 subjected to (a) 6% and (b) 10% rotation [12] 9

Figure 1-8: Configuration of the RFD proposed by Dingbin Li and Yun Zhou (2022) [33] 15

Figure 1-9: Concrete cracking at the base and other stories [37] 16

Figure 1-10: Sketch of separated GLRS and SFRS [38] 17

Figure 1-11: Schematic example of a building with planar walls and force-limiting connections (Adopted from: [53]) 20

Figure 1-12: In contrast with the planar wall system, the relative movement between the floors and the core wall system is constrained by the rubber bearings. The planar wall system is shown in (a), and the core wall system is shown in (b). 22

Figure 2-1: (a) Typical floor plan and (b) section A of the eighteen-story building (all dimensions are in millimeters) 27

Figure 2-2: (a) 3D Schematic and (b) Opensees model of the eighteen-story core wall building 29

Figure 2-3: Opensees model of the eighteen-story building and the elements of a typical floor . 31

Figure 2-4: (a) Four core wall pier elements at a typical floor, and (b) one core wall pier element with fiber sections at 5 integration points 32

Figure 2-5: Wall fiber section on all floor levels 33

Figure 2-6: Unconfined concrete material constitutive model and governing parameters 34

Figure 2-7: Confined concrete material constitutive model and governing parameters 36

Figure 2-8: Effectively confined core for rectangular hoop reinforcement [60] 38

Figure 2-9: (a) RC beam-column modeled with strain-softening section response and, (b) moment and curvature profiles for elastic-perfectly plastic cantilever modeled with single force-based element [59] 41

Figure 2-10: Concrete stress-strain relationship and compression fracture energy by Kent-Park (1971) [59] 41

Figure 2-11: Stress-strain curve with constant fracture energy 42

Figure 2-12: Steel material constitutive model and governing parameters [64] 45

Figure 2-13: Geometry of TUA and TUB [65] 46

Figure 2-14: Geometry and Section detail of TUA and TUB [65] 47

Figure 2-15: (a) Displacement-controlled loading history, and the imposed displacement on (b) TUA and (c) TUB for the text and the model [65] 48

Figure 2-16: Confined strength determination from lateral confining stresses for rectangular sections [60] 51

Figure 2-17: Hysteretic response of TUA in (a) EW direction and (b) NS direction 54

Figure 2-18: Hysteretic response of TUB in (a) EW direction and (b) NS direction 54

Figure 2-19: Typical modeling approach for coupling beams 57

Figure 2-20: (a) Coupling beam modeling approach validation done by the reference report [54], and (b) Force-deformation response of the Pinching4 used on the first floor of the eighteen-story core wall building model. 58

Figure 2-21: Calculation of FY 60

Figure 2-22: Force-limiting connections connecting the SFRS and GLRS diaphragms 65

Figure 2-23: Difference between a GLRS diaphragm and SFRS diaphragm 66

Figure 2-24: Mode shapes of the eighteen-story core wall building model 67

Figure 2-25: Damping ratio model 73

Figure 2-26: (a) Acceleration coefficient CLx; (b) force-limiting connection design forces FLx; and (c) SFRS free-body diagram subjected to connection design force FLx. (image reference: [53]) 74

Figure 2-27: Limiting force at a given floor, FLx, with five different RDC values 76

Figure 2-28: Force-displacement relationship of the four different connection types between the GLRS and the SFRS 77

Figure 2-29: Assembled and exploded view of the prototype of the Modified FD connection [70] 79

Figure 2-30: Opensees Modeling approach of Modified FD 80

Figure 2-31: Nonlinear section analysis model of (a) the trailing wall and (b) the leading wall . 83

Figure 2-32: Relationship of degree of coupling with Pu,T, Pu,L, Mu,T, Mu,L, and ML 86

Figure 2-33: Moment-curvature of the wall section at the base from the last iteration 87

Figure 2-34: Conceptual drawing of the steel coupling beam with rotational friction connection 90

Figure 2-35: Opensees model of the low-damage coupling beam..... 92

Figure 3-1: Unscaled ground acceleration of the two orthogonal horizontal components of the twenty-two earthquake ground motions 96

Figure 3-2: Pseudo acceleration response spectrum of twenty-two earthquakes 97

Figure 3-3: (a) Scaled pseudo-acceleration response spectra, and (b) Ratio of mean scaled RotD50 to target design response spectrum 99

Figure 3-4: Scaled ground acceleration of the two orthogonal horizontal components of the eleven earthquake ground motions 100

Figure 3-5: Pseudo acceleration response spectra of scaled ground motions and design spectrum with a 5% damping ratio..... 101

Figure 4-1: Calculation of SFRS story torsional moment 107

Figure 4-2: Maximum responses of the building models 108

Figure 4-3: Peak connection deformation of the force-limiting connections 109

Figure 4-4: Fiber section strain distribution at the wall base with EQ15 from (a) the RE analysis case, (b) the FD analysis case ($RDC = 1.5$), (c) the FD+RB analysis case ($RDC = 1.5, KRB = 22.5\ kip/in$), and (d) the Modified FD analysis case 111

Figure 4-5: Maximum and minimum strain response at the wall base..... 112

Figure 4-6: Difference between the reinforced concrete coupling beam and the low-damage coupling beam..... 115

Figure 4-7: Maximum responses of the building models 121

Figure 4-8: Peak response of connection deformation 122

Figure 4-9: Fiber section strain distribution at the wall base with EQ15 from (a) the RE analysis case, (b) the Modified FD analysis case, and the Modified FD + LDCB analysis case with (c) *DoC*=0.3, (d) *DoC*=0.4, and (e) *DoC*=0.5 124

Figure 4-10: Maximum and minimum strain response at the wall base 125

Figure 6-1: Peak axial force of the four wall piers 129

Figure 6-2: Peak moment of the four wall piers about Global X-dir. 130

Figure 6-3: Peak moment of the four wall piers about Global Y-dir. 130

Figure 6-4: Maximum responses of the building models 131

Figure 6-5: Maximum and minimum strain response at the wall base 132

Figure 6-6: Peak connection deformation of the force-limiting connections 132

Figure 6-7: Peak axial force of the four wall piers 132

Figure 6-8: Peak moment of the four wall piers about Global X-dir. 133

Figure 6-9: Peak moment of the four wall piers about Global Y-dir. 133

Figure 6-10: Maximum responses of the building models 134

Figure 6-11: Maximum and minimum strain response at the wall base 135

Figure 6-12: Peak connection deformation of the force-limiting connections 135

Figure 6-13: Peak axial force of the four wall piers 135

Figure 6-14: Peak moment of the four wall piers about Global X-dir. 136

Figure 6-15: Peak moment of the four wall piers about Global Y-dir. 136

Figure 6-16: Maximum responses of the building models 137

Figure 6-17: Maximum and minimum strain response at the wall base 138

Figure 6-18: Peak connection deformation of the force-limiting connections 138

Figure 6-19: Peak axial force of the four wall piers 138

Figure 6-20: Peak moment of the four wall piers about Global X-dir. 139

Figure 6-21: Peak moment of the four wall piers about Global Y-dir. 139

Figure 6-22: Maximum responses of the building models 140

Figure 6-23: Maximum and minimum strain response at the wall base 141

Figure 6-24: Maximum responses of the building models 141

Figure 6-25: Peak axial force of the four wall piers 141

Figure 6-26: Peak moment of the four wall piers about Global X-dir. 142

Figure 6-27: Peak moment of the four wall piers about Global Y-dir. 142

Figure 6-28: Peak axial force of the four wall piers 143

Figure 6-29: Peak moment of the four wall piers about Global X-dir. 143

Figure 6-30: Peak moment of the four wall piers about Global Y-dir. 144

LIST OF TABLES

Table 2-1: Eighteen-story core wall building design summary [55] 28

Table 2-2: Unconfined concrete material properties 35

Table 2-3: Confined concrete material properties 36

Table 2-4: Calculated confined concrete properties for the three regions 40

Table 2-5: Tributary length of Gauss-Lobatto Integration points 43

Table 2-6: comparison of εcu and εccu to $\varepsilon 20$ 43

Table 2-7: Calibrated steel material parameters 45

Table 2-8: Yield displacements, yield drifts, maximum displacements, and maximum drifts of TUA and TUB subjected to different directions of loading [66] 49

Table 2-9: Coordinates of the imposed displacement on the Opensees model 49

Table 2-10: Material properties of unconfined concrete 50

Table 2-11: Material properties of confined concrete 50

Table 2-12: Material properties of steel 52

Table 2-13: Parameters used for calibration 52

Table 2-14: Proposed Multivariate Normal distribution (Grade A706) [65] 52

Table 2-15: Parameters for steel material properties 53

Table 2-16: Lean-on column sizes 55

Table 2-17: Pinching4 material parameters [55] 59

Table 2-18: Calculation of FY 61

Table 2-19: Four points of the Pinching4 material model used in the eighteen-story building model 62

Table 2-20: Dead load and live load applied to the building model 63

Table 2-21: Modal analysis results – Eigenvalue analysis 69

Table 2-22: Modal analysis results – Modal participation mass ratios (%) and cumulative modal participation mass ratios (%) 70

Table 2-23: Design limiting force at a given floor *x*, FLx 75

Table 2-24: Calculation of the limiting moment with $DoC = 0.3$ 84

Table 2-25: Calculation of the limiting moment with $DoC = 0.4$ 85

Table 2-26: Calculation of the limiting moment with $DoC = 0.5$ 85

Table 3-1: Twenty-two far-filed ground motions from FEMA P-695 [69] 94

Table 3-2: Earthquake ground motion scale factors 99

Table 4-1: Statistics of maximum and minimum strain response at the wall base 113

Table 4-2: Capacity of reinforced concrete coupling beam and low-damage coupling beam 116

Table 4-3: Comparison of *DoC* with different types of coupling beams 117

Table 4-4: Statistics of maximum and minimum strain response at the wall base 125

Table 7-1: Peak floor total acceleration, mean [g] 145

Table 7-2: Peak floor total acceleration, STD [g] 146

Table 7-3: Peak floor total acceleration, c.o.v [%] 147

Table 7-4: Peak GLRS story drift ratio, mean [%] 148

Table 7-5: Peak GLRS story drift ratio, STD [%] 149

Table 7-6: Peak GLRS story drift ratio, c.o.v [%] 150

Table 7-7: Peak SFRS story drift ratio, mean [%] 151

Table 7-8: Peak SFRS story drift ratio, STD [%] 152

Table 7-9: Peak SFRS story drift ratio, c.o.v [%] 153

Table 7-10: Peak SFRS story shear, mean [kN] 154

Table 7-11: Peak SFRS story shear, STD [kN] 155

Table 7-12: Peak SFRS story shear, c.o.v [%] 156

Table 7-13: Peak SFRS story torsional moment, mean [kN-m] 157

Table 7-14: Peak SFRS story torsional moment, STD [kN-m] 158

Table 7-15: Peak SFRS story torsional moment, c.o.v [%] 159

Table 7-16: Connection deformation, mean [mm] 160

Table 7-17: Connection deformation, STD [mm] 161

Table 7-18: Connection deformation, c.o.v [%] 162

Table 7-19: Peak Floor total acceleration, mean [g] 163

Table 7-20: Peak Floor total acceleration, STD [g] 164

Table 7-21: Peak Floor total acceleration, c.o.v [%] 165

Table 7-22: Peak GLRS story drift ratio, mean [%] 166

Table 7-23: Peak GLRS story drift ratio, STD [%] 167

Table 7-24: Peak GLRS story drift ratio, c.o.v [%] 168

Table 7-25: Peak SFRS story drift ratio, mean [%] 169

Table 7-26: Peak SFRS story drift ratio, STD [%] 170

Table 7-27: Peak SFRS story drift ratio, c.o.v [%] 171

Table 7-28: Peak SFRS story shear, mean [kN] 172

Table 7-29: Peak SFRS story shear, STD [kN] 173

Table 7-30: Peak SFRS story shear, c.o.v [%] 174

Table 7-31: Peak SFRS story torsional moment, mean [kN-m] 175

Table 7-32: Peak SFRS story torsional moment, STD [kN-m] 176

Table 7-33: Peak SFRS story torsional moment, c.o.v [%] 177

Table 7-34: Connection deformation, mean [mm] 178

Table 7-35: Connection deformation, STD [mm] 179

Table 7-36: Connection deformation, c.o.v [mm] 180

ACKNOWLEDGEMENTS

I would like to express my deepest appreciation to my advisor Professor Georgios Tsampras for his kind support and guidance throughout my master's program, which made this thesis possible.

My sincere gratitude extends to my committee members, Professor Jose I. Restrepo and Professor Joel P. Conte, for their insightful comments and suggestions.

I could not have undertaken this journey without my colleagues, Kaixin Chen and C. Franco Mayorga. I truly appreciate all their help, and I always enjoy our lively discussions.

My appreciation also goes out to my husband, Sungmoon Wea, and my family and friends for their continuous encouragement and support.

ABSTRACT OF THE THESIS

Seismic Response of Eighteen-story Core Wall Building with Force-limiting Connections and Low-damage Coupling Beams

by

Kyoungyeon Lee

Master of Science in Structural Engineering

University of California San Diego, 2022

Professor Georgios Tsampras, Chair

This thesis studies the seismic response of an eighteen-story core wall building with force-limiting connections and low-damage coupling beams. Force-limiting connections allow the movement of the gravity load resisting system (GLRS) relative to the seismic force-resisting system (SFRS) and control the seismic-induced horizontal forces transferred between the two systems. Past research developed force-limiting connections that consist of a friction device or a

buckling-restrained brace along with low-damping rubber bearings for buildings with planar SFRS with flexural inelastic base mechanism or rocking base mechanism. This thesis considers a force-limiting connection modified to accommodate the three-dimensional kinematic requirements between the GLRS and the SFRS in a reinforced concrete core wall building. The discrete variable limiting force is a novel characteristic in the force-displacement response of the modified force-limiting connection. Low-damage coupling beams, which consist of steel coupling beams with rotational friction connection ends, provide controlled moments with nonlinear responses concentrated on the rotational friction connections. Three-dimensional earthquake numerical simulations of an eighteen-story core wall building with modified force-limiting connections and low-damage coupling beams are performed. The use of modified force-limiting connections reduces the magnitude and the variability of the seismic-induced shear force, torsional moment, and acceleration responses of the building compared to the conventional core wall building with monolithic connections between the GLRS and the SFRS of the building while maintaining a reasonable connection deformation. The use of low-damage coupling beams instead of reinforced coupling beams could potentially reduce the coupling beam damage to accelerate the post-earthquake functional recovery of the building.

1 Introduction

1.1 Literature review

1.1.1 Structural walls

Building structures consist of a gravity load resisting system (GLRS) and a lateral load resisting system. The gravity load resisting system supports the self-weight of the structure itself (i.e., dead load) and unfixed sources of weight that are mounted on the structure (i.e., live load). The lateral load resisting system resists wind loads and earthquake ground motions. In the context of earthquake engineering, the lateral force-resisting system is also called the seismic force-resisting system (SFRS). The term SFRS will be used in the thesis. During an earthquake, most of the seismic-induced inertial forces are developed in the GLRS, where most of the mass of the building is located. The seismic-induced horizontal inertial forces are resisted by the SFRS. Examples of the SFRS are moment-resisting frames, braced frames, and structural walls.

Structural walls are invariably stiffer than moment-resisting frames, reducing the possibility of having significant deformations under small earthquakes [1]. With properly detailed wall reinforcement, structural damage can be avoided under moderate earthquakes [1]. And with special wall details, the walls can achieve ductile response under major earthquakes [1]. The two typical structural wall systems are the interacting cantilever walls connected by slabs and the coupled walls connected by coupling beams [1].

1.1.2 Interacting cantilever walls

Interacting cantilever walls are cantilever walls that are connected by slabs, as illustrated in Figure 1-1. The floor slabs stabilize the wall against lateral buckling in the out-of-plane direction, allowing the walls to have relatively thin sections. The slabs are commonly assumed to be rigid in the axial motion and the in-plane motion, and they are assumed to be flexible in the out-of-plane motion. In this case, the walls move with the same displacement at each floor level due to the diaphragm action of the slab. The stiffness of a planar wall about its weak axis is generally ignored because it is small compared to the stiffness of the planar wall about its strong axis. Cantilever structural walls dissipate energy at the base as the reinforcing steel yields and behave inelastically. [1]

1.1.3 Coupled walls and core walls

Coupled walls are structural walls that are connected by beams distributed along the height of the structure, as shown in Figure 1-1(b). Coupled walls are created by one or more consecutive openings in vertical rows separating the structural wall. The walls separated by the openings are connected by beams with large depths compared to their clear span. The walls connected by the beams are called wall piers, and the beams are called coupling beams. [2, 3] Coupled walls are designed in a way that the nonlinear inelastic mechanism takes place at the coupling beams and at the base of the walls, with the rest of the structure designed to remain linear elastic [4]. The coupled wall system is beneficial compared to uncoupled cantilever walls because of its additional energy dissipation capacity from the coupling beams [5, 6] and its large lateral stiffness due to the coupling action [4, 5], which also results in the reduction of lateral story drift [6].

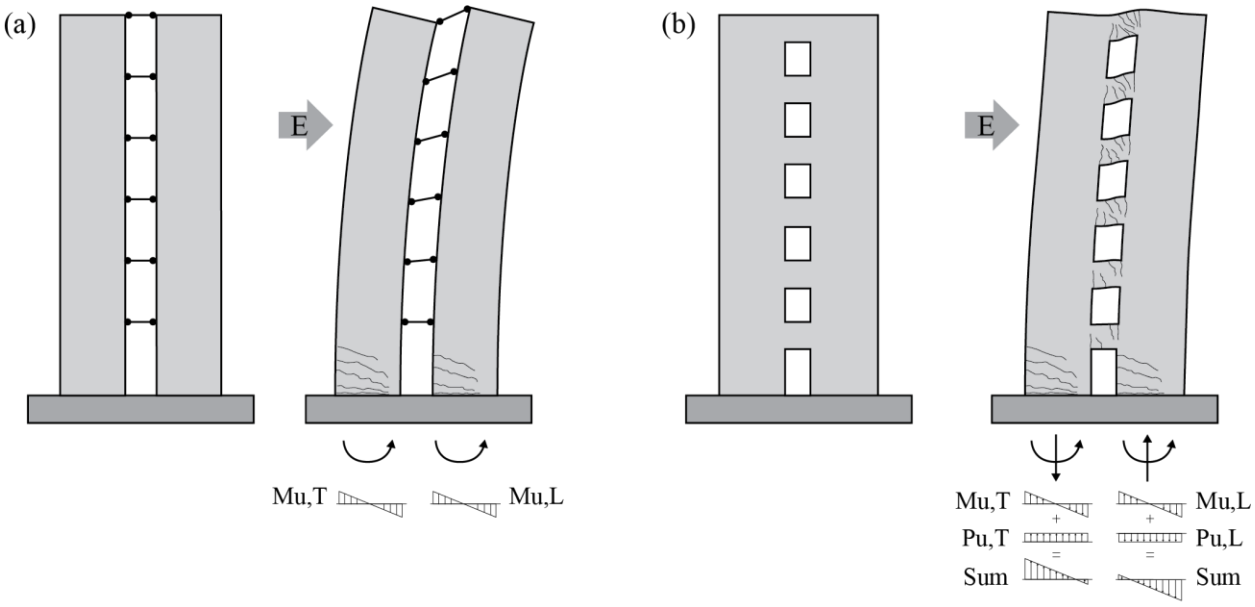

Figure 1-1: Lateral force resisting mechanisms of (a) interacting cantilever walls and (b) coupled walls (image reference: [1] [4] [7])

Core wall systems consist of walls that typically are oriented in two orthogonal directions in the floor plan of a building, as shown in Figure 1-2. The walls are coupled using coupling beams either in one direction or in both directions. Core walls typically enclose elevators and stairways with wall components connected by coupling beams over doorways. Like coupled walls, core walls have larger energy dissipation capacity and smaller inter-story drift compared to cantilever walls. Core walls are also laterally stable in both horizontal translation directions without external supporting mechanisms. As a result, the core wall SFRS is a popular system for mid-rise and tall buildings. The centroid of the core wall is commonly located at the center of a building plan. This helps with the architectural layout of the building floor plan. Aligning the center of stiffness aligns with the center of mass also reduces the effect of torsion [7].

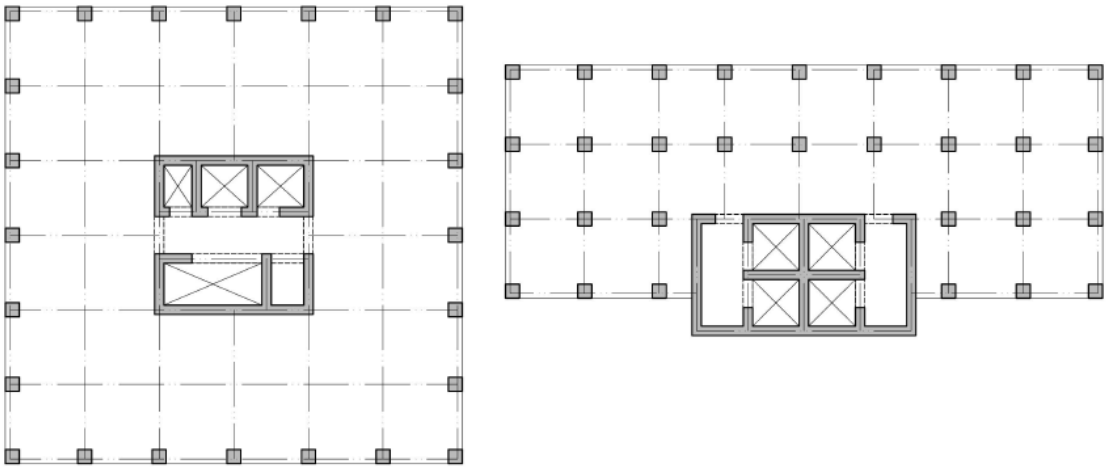

Figure 1-2: Examples of floor plans with core walls (image reference: [1])

Coupling beams. The wall piers impose rotation on coupling beams because the walls deform predominantly as cantilevers. And the coupling beams, which are designed to deform plastically, can dissipate energy over the height of the building while providing stiffness to the coupled walls [1] [3]. The span-to-depth ratio l_{CB}/h indicates if the coupling beams are expected to behave in a flexural dominant response or shear dominant response, where l_{CB} is the length of the coupling beam and h is the height of the coupling beam as defined in the American Concrete Institute Building Code Requirements for Structural Concrete (i.e., ACI 318) [2]. Coupling beams with an aspect ratio of $l_{CB}/h > 4$ are flexural controlled, and they are allowed to be detailed similarly to columns. Coupling beams with an aspect ratio of $l_{CB}/h < 4$ are shear controlled, and they are allowed to be detailed using diagonal reinforcements. Diagonal reinforcement provides adequate resistance in deep coupling beams, and it is only effective when the diagonal bars are placed with a large inclination [3]. The inelastic deformation at the ends of coupling beams, in addition to the inelastic deformation at the wall base, results in more energy

dissipated compared to the cantilever walls, where the nonlinear response only takes place at the wall base [6].

Coupling action. Coupling action between the wall piers and the coupling beams results in resisting moments in addition to the resisting moment at the base of each wall pier. Figure 1-1 compares how the uncoupled cantilever walls and coupled walls resist the total structural overturning moment generated by external lateral forces. The cantilever wall system resists the structural overturning moment (M_{OTM}) with the two moments at the wall bases ($M_{u,L} + M_{u,T}$). On the other hand, the coupled wall system resists the structural overturning moment (M_{OTM}) with the sum of the bending moment ($M_{u,L} + M_{u,T}$) from the flexural deformation of the walls and the couple moment created by the axial forces ($P_{u,L}$ and $P_{u,T}$) in the wall piers originating from the coupling beam shear forces. As a result, coupled walls have larger lateral stiffness compared to uncoupled cantilever walls [4, 7].

Figure 1-3(a) shows the free body diagram of the coupled walls, and Figure 1-3(b) shows the free body diagram of the trailing wall and coupling beam at floor x. The calculation of the total structural overturning moment of coupled walls is shown in Equations 1-1, 1-2, and 1-3. The summation of moments is computed about point A in Figure 1-3(a). Figure 1-3(b) shows the free body diagram of the trailing wall and the free body diagram of the coupling beam at floor x. The lateral force applied to the core wall system could be the lateral seismic force at floor x (F_x) from the floor diaphragm for conventional core wall buildings with a monolithic connection between GLRS and SFRS, or it can also be the design limiting force at floor x (F_{Lx}) transmitted through the force-limiting connections from GLRS to SFRS. The design limiting force at floor x (F_{Lx}) will be defined in section 2.11.1. $P_{u,L}$ and $P_{u,T}$ are the base axial forces of the leading and trailing walls, respectively. $M_{u,L}$ and $M_{u,T}$ are the base moments in the leading and trailing walls,

respectively. W_x is the seismic weight for one wall at each floor x. h_x is the height at floor x. $V_{CB,x}$ is the magnitude of the coupling beam shear force at floor x. $l_{w,L}$ and $l_{w,T}$ are the length of the leading and trailing walls, respectively. l_{CB} is the length of the coupling beam. n is the number of stories. [7]

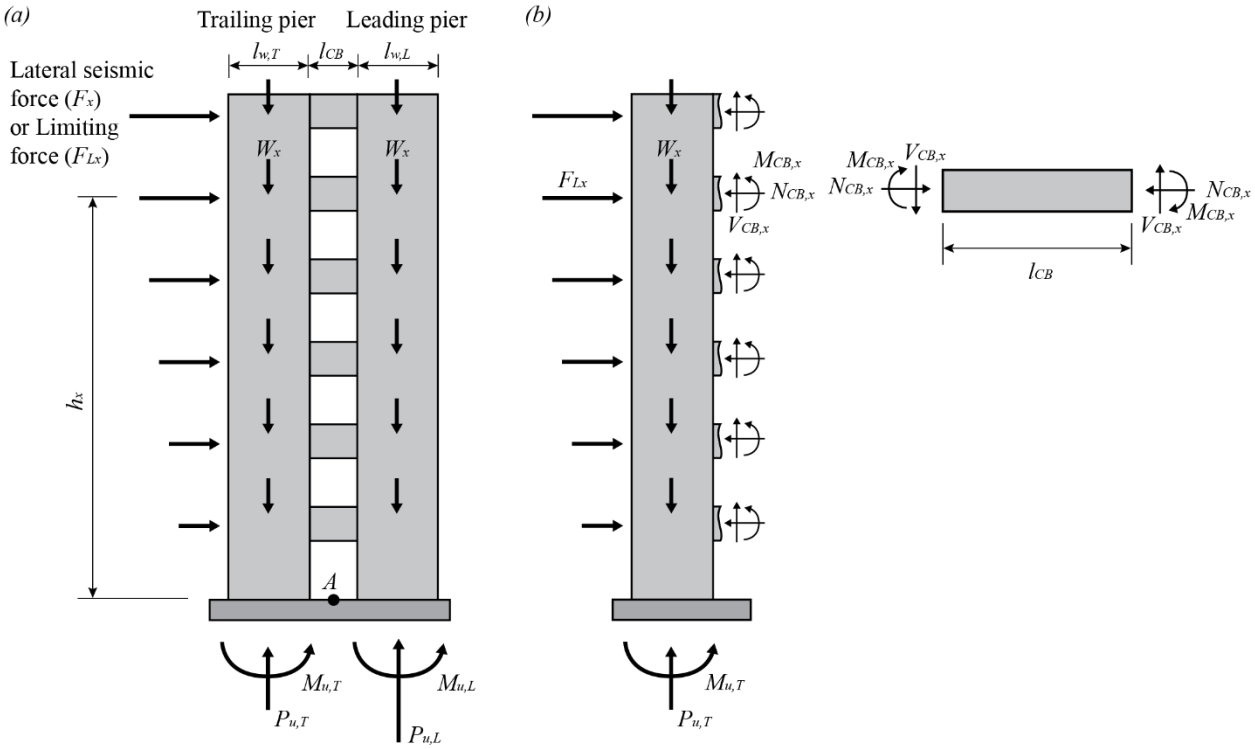

Figure 1-3: (a) Free body diagram of the coupled walls and (b) free body diagram of the trailing wall and coupling beam at floor x

$$M_{OTM} = \sum_{x=1}^{n} F_x h_x = M_{u,L} + M_{u,T} + M_C \quad \text{1-1}$$

$$M_C = P_{u,L}\left(\frac{l_{w,L}}{2} + \frac{l_{CB}}{2}\right) - P_{u,T}\left(\frac{l_{w,T}}{2} + \frac{l_{CB}}{2}\right) \quad \text{1-2}$$

$$P_{u,L} = \sum_{x=1}^{n} W_x + \sum_{x=1}^{n} V_{CB,x} \quad , \; P_{u,T} = \sum_{x=1}^{n} W_x - \sum_{x=1}^{n} V_{CB,x} \quad \text{1-3}$$

Degree of coupling (DoC) is the ratio of the overturning moment due to axial force couple at the wall base (M_C) over the total overturning moment at the wall base (M_{OTM}) as shown in Equation 1-4 [1, 6, 7].

$$\text{Degree of coupling (DoC)} = \frac{\text{Overturning moment due to axial force couple at wall base}}{\text{Total overturning moment at wall base}}$$

$$\begin{aligned} \text{DoC} = \frac{M_C}{M_{OTM}} &= \frac{M_C}{M_{u,L} + M_{u,T} + M_C} \\ &= \frac{P_{u,L}\left(l_{w,L} + l_{CB}\right) - P_{u,T}\left(l_{w,T} + l_{CB}\right)}{P_{u,L}\left(l_{w,L} + l_{CB}\right) - P_{u,T}\left(l_{w,T} + l_{CB}\right) + 2\left(M_{u,L} + M_{u,T}\right)} \end{aligned} \quad \text{1-4}$$

The axial force in each wall is the sum of the self-weight of each wall and the shear forces of all the coupling beams connected to the wall. Therefore, the magnitude of the axial force depends on the stiffness and strength of the coupling beams. It means that coupled walls with stiffer coupling beams will have a larger DoC, and this also results in lowering the point of inflection, as shown in Figure 1-4. Having the point of inflection at a lower position of the building leads to a reduction of lateral deflection and inter-story drift, especially in the upper levels of tall buildings. DoC is zero for cantilever walls without coupling beams because there are no axial forces in the wall piers created from the coupling beam shear forces, and the point of inflection is located at the very top. DoC is one when the lateral force is solely resisted by the wall axial forces, but there is no such case except when there is an engineering pin connection at the wall base to create zero moments. Buildings with coupled walls are typically designed assuming a DoC within the range of 0.25 to 0.75. [1, 6, 7]

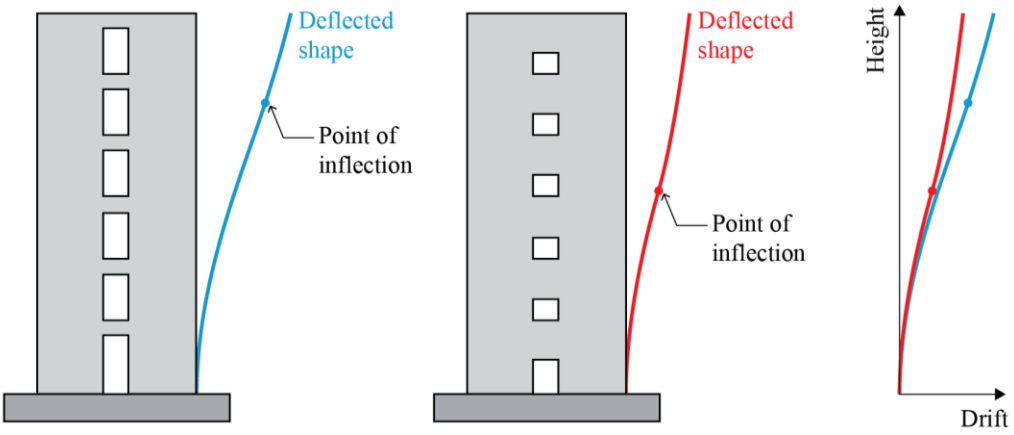

Figure 1-4: Relationship between the degree of coupling and the point of inflection

1.1.4 Coupling beam damage

As mentioned in section 1.1.3, coupling beams in conventional core wall buildings play an essential role by creating coupling action and dissipating energy. However, repairing the damaged coupling beams after earthquakes may be expensive and time-consuming [8–10]. Figure 1-5 shows an example of significant coupling beam damage from the 2011 Christchurch earthquake of a nine-story reinforced concrete coupled wall structure designed and built in the 1960s. The coupling beams had diagonal and horizontal deformed reinforcement but did not have vertical confinements, which led to substantial concrete spalling after shear failure [11].

Figure 1-5: Examples of coupling beam damage [11]

Figure 1-6(a) and Figure 1-6(b) show damaged coupling beams with full section confinement in accordance with ACI 318-08 subjected to 6% and 10% rotation, respectively [12]. Figure 1-7(a) and Figure 1-7(b) show damaged coupling beams with diagonal confinement in accordance with ACI 318-05 subjected to 6% and 10 % rotation [12].

In addition, the construction of coupling beams is difficult due to reinforcement congestion, especially for the diagonally reinforced coupling beams [9]. Several past studies have suggested alternative designs for diagonally reinforced concrete coupling beams, which are presented in the next section.

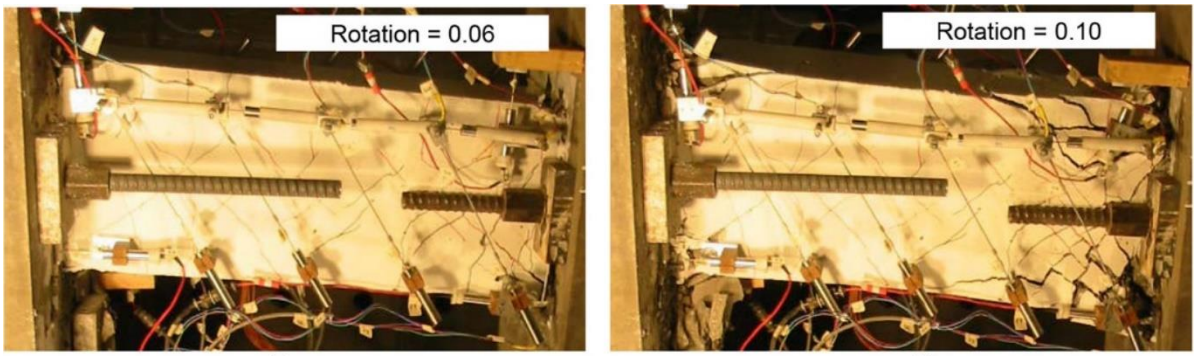

Figure 1-6: Damaged coupling beams with full section confinement in accordance with ACI 318-08 subjected to (a) 6% and (b) 10% rotation [12]

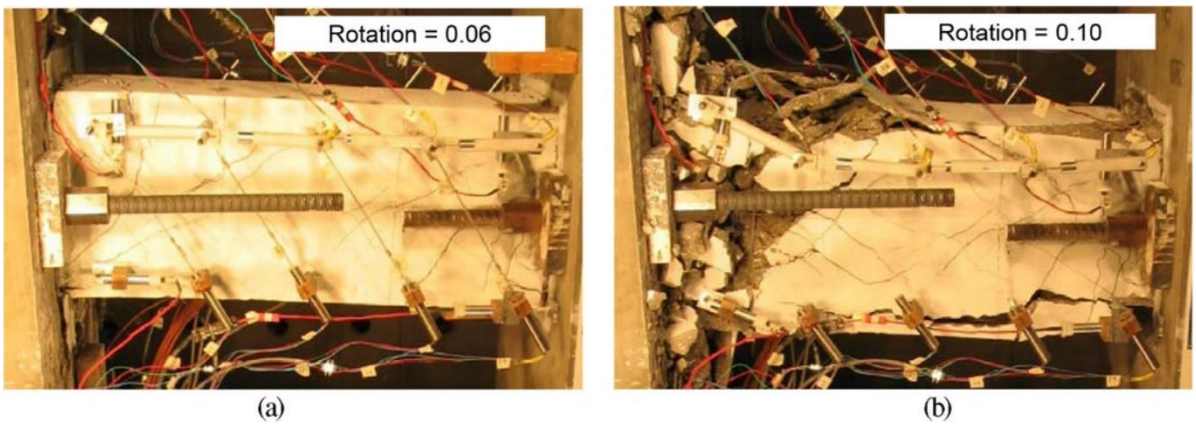

Figure 1-7: Damaged coupling beams with diagonal confinement in accordance with ACI 318-08 subjected to (a) 6% and (b) 10% rotation [12]

1.1.5 Alternative designs for diagonally reinforced concrete coupling beams

Fiber-reinforced concrete

Canbolat et al. (2005) [13] presented high-performance fiber-reinforced cementitious composites in coupling beams with simplified reinforcement detailing. The high-performance fiber-reinforced cementitious composites showed higher damage tolerance compared with regular concrete. Coupling beams with high-performance fiber-reinforced cementitious composites and no transverse reinforcement around the diagonal bars showed higher shear strength and stiffness retention compared to coupling beams with regular concrete and transverse reinforcement around the diagonal bars.

Steel coupling beams

Harries et al. (1997) [14] proposed a steel coupling beam where it is embedded into the wall piers at each end. Shear critical steel beams were proposed as an alternative to diagonally reinforced concrete coupling beams, and flexural critical steel beams were proposed as an alternative to diagonally reinforced concrete coupling beams. The results showed that the shear critical steel beams exhibited greater energy dissipation capacity and ductility than their diagonally reinforced concrete counterpart. The flexure critical steel beams have greater energy dissipation capacity than diagonally reinforced concrete coupling beams.

Replaceable steel coupling beams

One alternative design for coupling beams is a replaceable steel coupling beam that can be replaced after it is damaged. The damage can be localized on the part of the coupling beam

providing the nonlinearity that the conventional coupling beam used to provide. The damaged part can easily be detached and replaced.

Fortney et al. (2007) [15] first proposed a fuse steel coupling beam, a steel coupling beam embedded into the wall piers on each side, with a replaceable fuse located in the middle of the coupling beam. The test results showed that most of the damage was concentrated in the fuse, with little damage at the coupling beam-wall pier interfaces. Ji et al. (2017) [16] presented and tested four types of replaceable steel coupling beams, and Ji et al. (2017) [17] introduced and tested four types of reinforced concrete slabs with replaceable steel coupling beams to minimize slab damage from the deformation of the replaceable steel coupling beams.

Farsi et al. (2016) [18] presented a replaceable steel coupling beam with an end-plate connection. Embedded plates are cast with the wall piers, and coupling beams can be replaced after damage. From an experimental study, the replaceable steel coupling beam exhibited excellent energy-dissipation capacity but showed concrete crushing and spalling in the coupling beam-to-wall-pier connection region. Lu et al. (2016) [8] proposed a replaceable coupling beam, which has the middle part of the coupling beam replaced by a steel beam, with the rest of the coupling beam as reinforced concrete connected to the wall piers. The steel beam is bolted to the coupling beam by embedded plates that are embedded into coupling beams and the wall piers. During strong earthquakes, damages are concentrated in the replaceable steel beam part, whiles the other parts of the structure remain intact. Ji and Hutt (2020) [9] RC wall piers connected with replaceable steel coupling beams. The steel coupling beams have a central fuse shear link connected to steel beam segments at both ends. The fuse shear links yield and dissipate energy, and they can be replaced after being damaged.

Li et al. (2018) [5] proposed a two-level yielding steel coupling beam composed of a shear-yielding beam and a bend-yielding beam. The shear-yielding beam is designed to yield first under minor earthquakes, and the bend-yielding beam is designed to yield under major earthquakes. The bend-yield beam can therefore guarantee the stiffness of coupling beams under minor earthquakes after the yielding of the shear-yielding beams. Li et al. (2019) [10] proposed a coupling beam with a replaceable combined damper installed in the middle of the coupling beam. The replaceable combined damper is composed of one metallic damper made of steel and two viscoelastic dampers in parallel. During minor earthquakes, the viscoelastic damper dissipates energy, and the metallic damper remains elastic, providing stiffness and strength. The metallic damper yields and dissipates a large portion of energy during moderate or major earthquakes.

Steel coupling beams with dampers

Christopoulos and Montgomery (2013) [19] proposed and tested viscoelastic coupling dampers to enhance the wind and seismic performance of high-rise buildings. The result shows that the viscoelastic material dissipates energy and reduces the lateral accelerations and torsional velocities. Also, a replaceable fuse element in the viscoelastic coupling damper is activated if predesigned force limits are reached to limit the force transferred to the structural system and to prevent tearing of the viscoelastic material. Chung et al. (2009) [20] proposed a coupling beam with friction dampers using the flexural behavior of shear walls. Qu et al. (2020) [21] studied specimens of steel coupling beams with mid-span friction dampers and investigated the performance of the friction damper. Also, specimens, including a cast-in-site reinforced concrete slab, were tested to investigate the influence of the slab on the coupling beams. Cui et al. (2022) [22] [23] proposed frictional steel truss coupling beams, which concentrate inelastic deformation

in friction dampers while keeping the rest of the members elastic. Separate designs, shear-critical and bending-critical frictional steel truss coupling beams, are proposed to accommodate different span-to-height ratios.

Rotational friction dampers

Mualla and Belev (2002) [24] developed a friction damper device that was evaluated experimentally and numerically. The numerical analysis of the single-story steel frame model with the friction damper device showed that the response displacement and base shear were reduced. Several research extended the studies with this rotational friction damper. Kim et al. (2011) [25] presents a combined system of rotational friction dampers connected to high-strength tendons to enhance both seismic behaviors of existing structures. Mirzabagheri et al. (2015) [26] experimentally evaluated the performance of rotational friction dampers with two and three units, and it was compared to the original one-unit damper. Jarrahi et al. (2020) [27] proposed an optimal design of the rotational friction dampers to enhance the seismic performance of an inelastic single-story steel moment-resisting frame. Naeem and Kim (2020) [28] presented the seismic performance of a rotational friction damper with restoring force using torsional springs. Veismoradi et al. (2021) [29] developed a self-centering rotational friction damper. The self-centering rotational friction damper was analytically and numerically developed and experimentally tested.

Yang et al. (2022) [30] proposed dry-connected rotational friction dissipative beam-to-column joints (DRFDBJ). The seismic performance of a properly designed precast concrete frame with DRFDBJ is better than that of the counterpart monolithic reinforced concrete frame. For study cases with 3, 6, and 9 stories, the maximum inter-story drift ratios of the optimal PC

frame with DRFDBJs study cases are 9.5%, 17.1%, and 24.5% lower than those of the counterpart monolithic reinforced concrete frame, respectively.

Lee et al. (2022) [31] developed a rotational friction damper for electrical facilities vulnerable to overturning. A cyclic loading experimental test was performed to investigate the hysteresis responses. Numerical dynamic analyses were performed based on the experimental test results. The numerical analysis results showed that using the rotational friction dampers reduced the displacement response and overturning moment.

Coupling beams with rotational friction dampers

Choi and Kim (2014) [32] performed a numerical nonlinear dynamic analysis of a 30-story core wall building with frictional hysteretic energy dissipating devices at both ends of the coupling beams. Due to the increased seismic energy dissipation capacity of the frictional hysteretic energy dissipating devices, the core wall system with frictional hysteretic energy dissipating devices has better seismic performance than the core wall systems with diagonally reinforced concrete coupling beams.

Dingbin Li and Yun Zhou (2022) [33] proposed a force-resisting rotary friction damper (RFD) which can be applied where there is a large rotational deformation such as beam-column connections, coupling beams, panel zones, column bases, and braces. A prototype of the proposed RFD was manufactured and tested. The configuration of the RFD is shown in Figure 1-8. The test results showed that the moment–angle hysteretic curve of the proposed RFD was an ideal rectangle, indicating a reasonable mechanism.

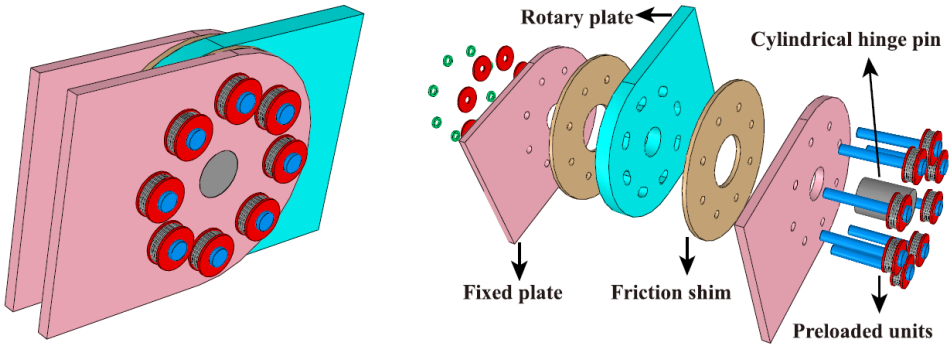

Figure 1-8: Configuration of the RFD proposed by Dingbin Li and Yun Zhou (2022) [33]

1.1.6 Higher-mode effects

The total dynamic linear-elastic response of a building is a result of the superposition of the individual modal responses of the building. The dynamic response of each mode depends on the modal participation of each mode and also the frequency and amplitude characteristics of the ground motion spectrum to which the building is subjected. In general, the modal participation of the first mode is large for short and stiff buildings compared to tall and slender buildings, and as the building becomes taller and slenderer, the modal participation of the higher mode increases. The contribution of the second and higher mode dynamic responses to the total dynamic response of the building is termed higher-mode effects.

The current reinforced concrete core wall structure design assumes the inelastic deformation is restricted at the wall base and coupling beams while the rest of the structure remains elastic. This inelastic response at the wall base dissipates energy and reduces the acceleration and the force response due to the flexural dominant first mode response. However, the inelastic response at the wall base does not reduce the shear dominant second or higher mode response [34]. As a result, this remaining large participation of higher mode response in the total dynamic response can lead to seismic amplification of story shear forces and floor accelerations.

As shown in Figure 1-9, damage spread over multiple stories above the intended ductile region at the base [35]. The actual seismic demands in these systems were larger than expected even after the formation of the base hinge mechanism, and the dynamic response of higher modes that are not controlled by the base plastic hinging mechanism amplified story shear forces and floor accelerations [35].

The increase of seismic demand is especially true after the flexural yielding at the wall base that elongates the fundamental mode period and further increases the contribution of higher vibration modes [35]. Also, although the yielding of coupling beams changes the dynamic behavior of coupled walls compared to cantilever walls, coupled wall structures are still prone to higher mode effects once the plastic hinging mechanisms at their base are activated, often exceeding the expected designed values calculated based on the intended ductility of the coupled wall structures [36]. Figure 1-9 shows an example case of structural damage due to the higher mode effect, where the damage is observed not only at the base of the walls but also at locations on other stories.

Figure 1-9: Concrete cracking at the base and other stories [37]

1.1.7 Past research toward high-performance earthquake-resistant buildings

Skinner et al. (1974) [38] introduced the concept of separating the GLRS and the SFRS and connecting them with hysteretic dampers, allowing relative movement between the GLRS and the SFRS and restricting the inelastic deformation to the dampers.

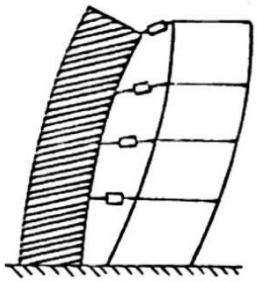

Figure 1-10: Sketch of separated GLRS and SFRS [38]

Key (1984) [39] conducted numerical earthquake simulations of a 10-story building with an energy-dissipative hysteretic damper between the stiff shear wall core part of the building and the flexible column/beam/slab part of the building. The results showed significant reductions in structural response. Luco and De Barros (1998) [40] performed a numerical analysis of tall buildings having a structural system of a stiff and lightly damped structure and a flexible and moderately damped structure connected by stiff or flexible links. Mar and Tipping (2000) [41] presented a system consisting of the gravity frame, which is laterally isolated from the base, and the reaction frames, which resist the lateral load. The gravity frame and the reaction frames are connected by springs and dampers at each level. As a result, the base shear and roof acceleration demands are reduced. Johnston et al. (2014) [42] presented a system for a concrete frame building. The system includes dissipative connections between beams and columns and between the floor and the beams. The use of these connections reduced the acceleration responses in the floors. Crane (2004) [43] performed a shake-table test of small-scale 6-story buildings with and

without triangular-plate energy dissipative connections between the GLRS and the SFRS. The results showed that the use of the energy dissipative connections reduced the overturning moment demand on the lateral resistance system, the lateral displacements and drifts demand at all floor levels, and floor acceleration demand at all floor levels.

1.1.8 Force-limiting connections

Zhang et al. (2014) [44] and Fleischman et al. (2015) [45] introduced the use of force-limiting connections to limit the seismic-induced demand for earthquake-resistant buildings. Force-limiting connections allow the movement of the gravity load resisting system (GLRS) relative to the seismic force-resisting system (SFRS) and control the seismic-induced horizontal forces transferred between the two systems.

The development of force-limiting connections is presented in Tsampras et al. (2016) [46]. Parametric numerical studies have been performed with a 12-story building model with force-limiting connections to define a feasible design space and configuration. The force-limiting connection developed for planar SFRS consists of a friction device or a buckling-restrained brace and low-damping rubber bearings. A friction device or a bucking restrained brace has limited-strength hysteretic properties. Low-damping rubber bearings provide post-elastic stiffness to the force-limiting connections to prevent excessive connection deformation, which is equivalent to the relative displacement between the GLRS and the SFRS. Low-damping rubber bearings also stabilize the out-of-plane motion of planar walls.

Tsampras and Sause (2014a, 2014b) [47, 47] and Tsampras et al. (2017, 2018) [48, 49] conducted experimental studies of full-scale force-limiting connections at the Natural Hazards Engineering Research Infrastructure (NHERI) experimental facility at Lehigh University [50].

Fleischman et al. (2014) [47] and Zhang et al. (2018) [51] presented the shake table test of a half-scale 4-story reinforced concrete flat-plate shear wall building with force-limiting connections simulated with 22 ground motions at the NHERI experimental facility at the University of California, San Diego [52].

Tsampras et al. (2016) [46] presented numerical earthquake simulations of a 12-story reinforced concrete shear wall building model with and without force-limiting connections. The 12-story planar wall building with the force-limiting connections is shown in Figure 1-11. The element model for the force-limiting connection was calibrated with experimental results. The use of force-limiting connections reduces the magnitude and the variability of the seismic-induced force and acceleration responses of the building compared to the seismic-induced force and acceleration responses of the conventional core wall building with monolithic connections between the GLRS and the SFRS. Force-limiting connections mitigate the higher mode effect due to the nonlinearity provided by the force-limiting connections, which modify the stiffness of the structure, elongating higher mode periods during an earthquake.

Tsampras and Sause (2022) [53] present a force-based design method to determine the limiting force of the force-limiting connections along the height of the structure. Numerical simulations were performed with 12-, 8-, and 4-story reinforced concrete planar wall building models with force-limiting connections.

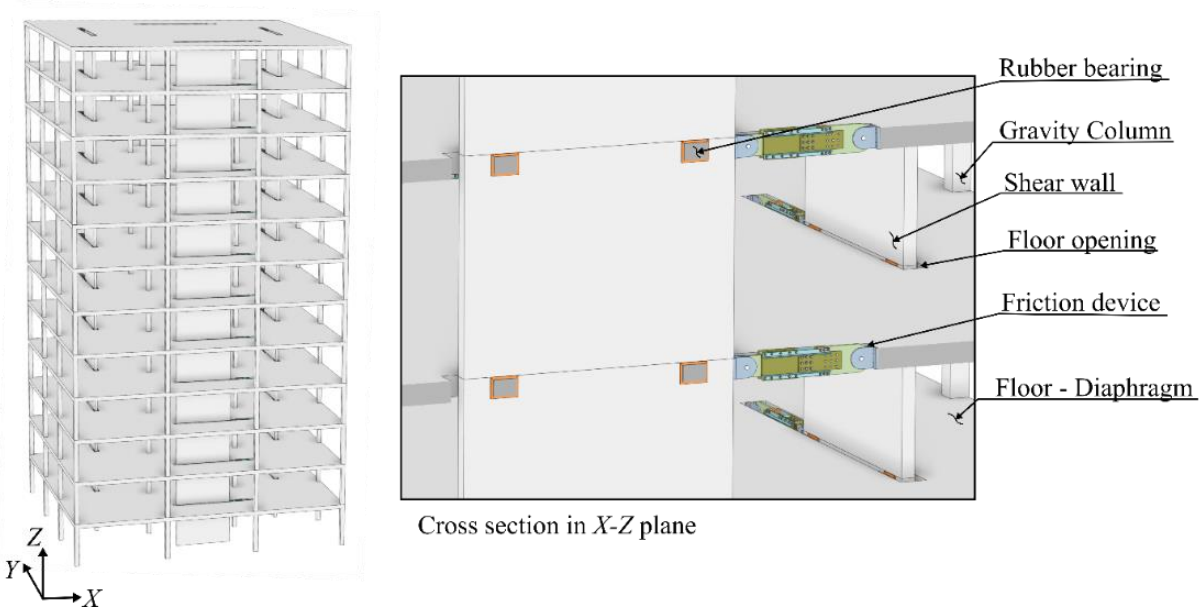

Figure 1-11: Schematic example of a building with planar walls and force-limiting connections (Adopted from: [53])

1.2 Motivation

1.2.1 Force-limiting connections on core wall system

The literature review shows that higher mode effects may be significant in buildings with a core wall. The use of force-limiting connections on buildings with planar walls can mitigate the higher mode effects and reduce the seismic-induced force and acceleration responses. Therefore, to improve the seismic performance of core wall buildings, this thesis will study the effect of force-limiting connections on the seismic response of a core wall system.

However, the force-limiting connections developed for planar buildings need to be modified to be used on core wall buildings because the three-dimensional kinematic requirements in force-limiting connections between the floors and the core wall differ from those in force-limiting connections between floors and planar walls. The high stiffness of the rubber bearings under compression constrains the relative movement between the floors and the core

wall, making the force-limiting connection ineffective, as shown in Figure 1-12. Therefore, the rubber bearings should be removed from the force-limiting connections on core wall buildings. As mentioned, the rubber bearings in the force-limiting connection for a planar wall system serve two purposes: to stabilize the out-of-plane motion of the planar walls and to provide the post-elastic stiffness to the force-limiting connections. Core walls are laterally stable, which eliminates the need for low-damping rubber bearings in the force-limiting connections. However, the post-elastic stiffness of the force-limiting connections is essential to prevent excessive deformation of the force-limiting connection. Thus, the force-limiting connection for the core wall system should be modified to eliminate the use of low-damping rubber bearings while having sufficient post-elastic stiffness to prevent excessive post-elastic displacement demand in the floors relative to the core wall.

In this study, a friction-based force-limiting connection is considered with a novel force-displacement response that results in an effective post-elastic stiffness through a discrete variable friction force instead of a constant friction force. The term Modified Friction Device connection (Modified FD connection) is used in this document to refer to the above-mentioned force-limiting connection. The numerical model of the Modified FD connection will be presented in section 2.11, and the earthquake numerical simulation results of the eighteen-story core wall building model with the Modified FD connection will be discussed in section 4. The development of the physical embodiment of the Modified FD connection is presented in Chen et al. (2022) [54].

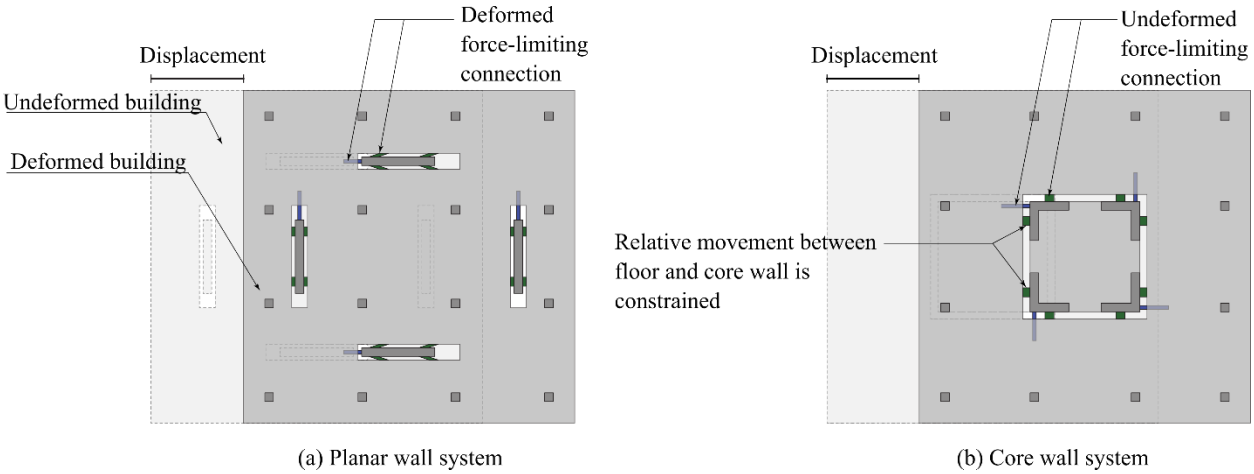

Figure 1-12: In contrast with the planar wall system, the relative movement between the floors and the core wall system is constrained by the rubber bearings. The planar wall system is shown in (a), and the core wall system is shown in (b).

1.2.2 Low-damage coupling beam

The literature review showed alternative design methods to reduce the damage expected in the coupling beams. This thesis will study the use of an alternative coupling beam design used together with force-limiting connections. The alternative coupling beam design is termed as the low-damage coupling beam that could potentially minimize coupling beam damage. This thesis will assess if the use of low-damage coupling beams will result in a similar seismic response of the buildings as the reinforced concrete coupling beams. If so, the low-damage coupling beam will be a good alternative for reinforced concrete coupling beams while serving its purpose of minimizing the coupling beam damage.

A low-damage coupling beam consists of a steel coupling beam and rotational friction connections at each end. The rotational friction connections connect the steel coupling beam to the wall piers on each side. The nonlinear response provided by the rotational friction connection

limits the amount of force and moment transferred from one wall pier to another through coupling beams.

The amount of force and moment to be limited is a design value termed the design limiting moment (M_L). The design limiting moment is the target moment value when the rotational friction connection response transitions from linear-elastic to post-elastic. The design limiting moment (M_L) of the low-damage coupling beam will determine the degree of coupling (DoC) of the core wall system. Limiting the moment transferred to the steel coupling beam results in limited shear force in the steel coupling beam, which contributes to the limited axial force developed in the wall piers. This means the controlled nonlinear response of the low-damage coupling beam leads to the controlled nonlinear response at the core wall base.

The design processes of the low-damage coupling beam are presented in section 2.12. With a specified degree of coupling (DoC), a design limiting moment (M_L) can be calculated. In this thesis, three limiting moments of the low-damage coupling beams are calculated from three different values of degrees of coupling. After the calculation of the design limiting moment (M_L), the design limiting moment (M_L) is used to capacity design the steel coupling beams to remain elastic (i.e., damage free).

1.3 Goal and objectives

This thesis aims to improve the seismic performance of core wall buildings. The objectives of the thesis are, firstly, to examine the seismic performance of an eighteen-story core wall building with force-limiting connections, and secondly, to examine the seismic performance of an eighteen-story core wall building with force-limiting connections and low-damage coupling beams via earthquake numerical simulations.

1.4 Tasks

- Develop a three-dimensional building model of an example eighteen-story core wall building. The building model will explicitly simulate the core wall piers, the gravity columns, the coupling beams, and the force-limiting connections between the GLRS and the core wall piers. The building model must accurately simulate the expected inelastic seismic response of the building. Thus, the inelastic response of the core wall piers and the coupling beams will be simulated using experimentally validated models.
- Select and scale the recorded ground motion acceleration time histories. Eleven ground motions will be scaled so that the mean of the scaled response spectra best matches the target design response spectrum within the selected range of period.
- Conduct numerical earthquake simulations of the building model. There will be five types of analysis cases, each analysis case having different types of force-limiting connection force-displacement responses and different types of coupling beam model approaches.
- Assess the effect of Modified FD connections and low-damage coupling beams in the seismic response of the building model by comparing the numerical analysis results from appropriate analysis cases.

1.5 Organization of document

Chapter 2 explains a numerical model of an eighteen-story building used for this study in detail. The modeling of the Modified FD connection, which is a feasible design for a core wall system, is presented. Also, the design process and the modeling approach of the low-damage coupling beam are discussed.

Chapter 3 explains the selection and scaling of the ground motion used in the time-history analysis.

Chapter 4 presents the results from the earthquake numerical simulation results and discusses the seismic response of the eighteen-story building model with the force-limiting connections and the low-damage coupling beam connections.

Chapter 5 presents the conclusion of this study with a summary of the effects of using the force-limiting connections and the low-damage coupling beam.

2 Eighteen-story building model

2.1 Overview

To perform a numerical simulation of the core wall building with force-limiting connections, a three-dimensional eighteen-story core-wall building is adopted from a reference report by Tauberg et al. [55], and a numerical model of this building is generated in Opensees. The Opensees model consists of elements that simulate the core wall piers, the gravity columns, the coupling beams, and the connections between the core wall piers and the floors. The inelastic response of core wall piers, coupling beams, and force-limiting connections is simulated using nonlinear finite elements. The gravity columns are assumed to remain linear elastic, and linear elastic finite elements are used.

2.2 Building model geometry

An example eighteen-story core wall building designed by Tauberg et al. [55] is adopted in this study. The building model is used to perform earthquake numerical simulations. Figure 2-1 shows the typical floor plan, an elevation, and a schematic of the eighteen-story building. The building includes a core wall in the center of the floor plan and lean-on columns located around the edge of the slab. The core wall consists of four L-shaped wall piers connected by diagonally reinforced coupling beams. Twelve lean-on columns are placed 30 feet apart from each other. The typical story height is 3048mm (10ft), and the wall length (l_w) is 2743mm (9ft). The aspect ratio of the coupling beams (l_n/h) is 3.0 with a length (l_n) of 2286mm (7.5ft) and height (h) of 762mm (30in). The slabs are post-tensioned slabs with a thickness of 203mm (8in) with an 1829mm (6ft) cantilever slab overhang.

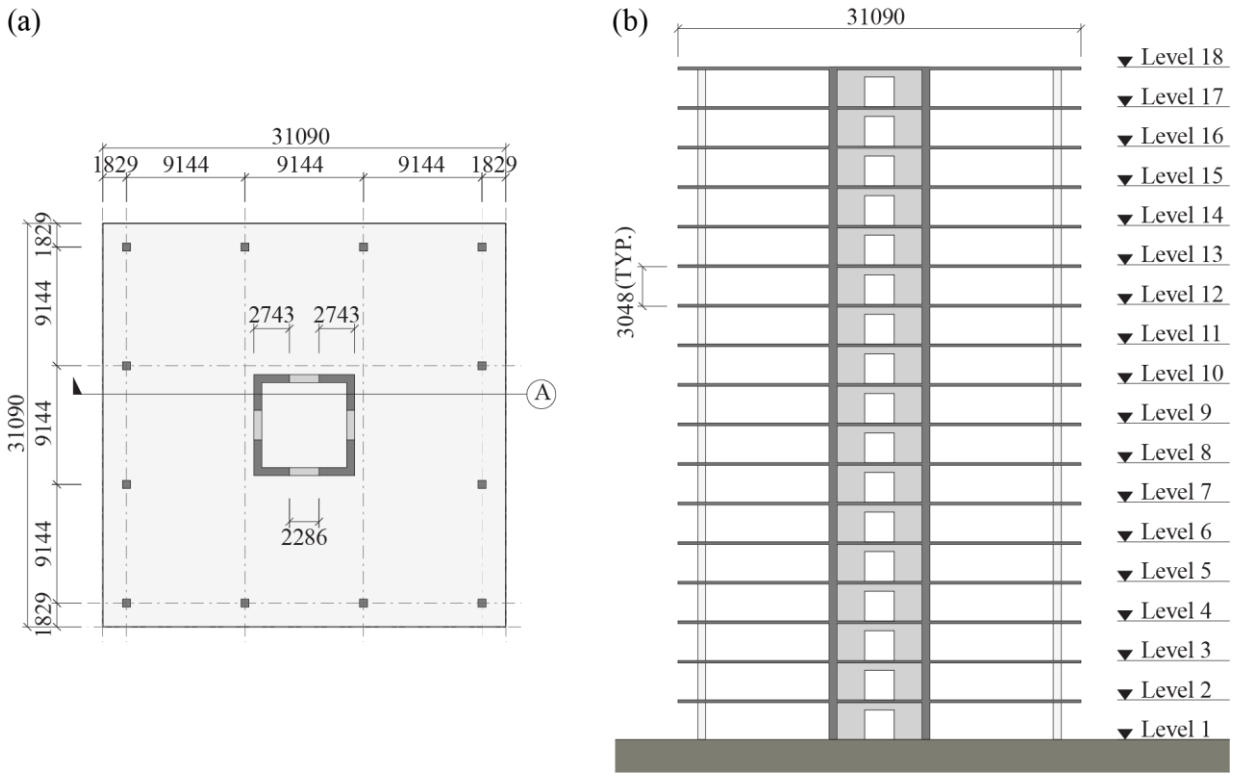

Figure 2-1: (a) Typical floor plan and (b) section A of the eighteen-story building (all dimensions are in millimeters)

This building falls into the definition of a tall building. A building is defined as 'tall' if the height exceeds 160 feet [56]. Tall buildings have characteristics of having the fundamental translational period of vibration significantly exceeding 1 second [57], high mass participation and lateral response in higher modes of vibration [57], and a seismic-force resisting system with a slender aspect ratio such that substantial portions of the lateral drift result from axial deformation of the walls and/or columns as compared to shearing deformation of the frames or walls [57].

The eighteen-story core wall building is a "ductile coupled wall" system with design parameters of $R = 8$, $C_d = 8$, and $\Omega_0 = 2.5$, where each represents the response modification coefficient (R), overstrength factor (Ω_0), and deflection amplification factor (C_d). The building is

designed according to ASCE 7-16, ACI 318-14, and the design parameters for the "ductile coupled wall" system in ACI 318-19. The archetype is designed for Seismic Design Category (SDC) D_{max}, which uses S_{DS} = 1.0g and S_{D1} = 0.6g as defined in FEMA P695. S_{DS} and S_{D1} represents the design, 5% damped, spectral response acceleration parameter at short periods and at a period of 1 second, respectively. T_s, which is a period defined by ratio S_{D1}/S_{DS}, is calculated as 0.6 sec. The long-period transition period, T_L, was not defined in the report and assumed to be 8 sec of Los Angeles. Also, the importance factor, I_e, of 1.0 was used. Table 2-1 shows the designed thickness of the wall, the longitudinal reinforcements of the wall, and the diagonal reinforcement of the coupling beams of the eighteen-story core wall building.

Table 2-1: Eighteen-story core wall building design summary [55]

Floor	Wall Thickness [in]		Wall Longitudinal Bars		Coupling Beam Diagonal Bars
	[in]	[mm]	[in]	[mm]	
18	16	406	2#5 @ 12"	2#5 @ 305	6#8
17	16	406	2#5 @ 12"	2#5 @ 305	6#8
16	16	406	2#5 @ 9"	2#5 @ 229	6#9
15	16	406	2#5 @ 9"	2#5 @ 229	6#9
14	16	406	2#6 @ 6"	2#6 @ 152	6#10
13	16	406	2#6 @ 6"	2#6 @ 152	6#10
12	16	406	2#6 @ 6"	2#6 @ 152	6#10
11	16	406	2#7 @ 6"	2#7 @ 152	6#10
10	16	406	2#7 @ 6"	2#7 @ 152	6#10
9	16	406	2#7 @ 6"	2#7 @ 152	6#10
8	20	508	3#7 @ 6"	3#7 @ 152	6#11
7	20	508	3#7 @ 6"	3#7 @ 152	6#11
6	20	508	3#7 @ 6"	3#7 @ 152	6#11
5	24	610	3#9 @ 6"	3#9 @ 152	8#10
4	24	610	3#9 @ 6"	3#9 @ 152	8#10
3	24	610	3#9 @ 6"	3#9 @ 152	8#10
2	24	610	3#10 @ 6"	3#10 @ 152	8#10
1	24	610	3#10 @ 6"	3#10 @ 152	8#10

2.3 Description of the building model

A numerical model of the eighteen-story core wall building is developed in Opensees. Figure 2-2(a) shows the 3D schematic of the eighteen-story building, and Figure 2-2(b) shows the numerical model of the building developed in Opensees. This section explains the elements used in the numerical model to simulate the eighteen-story building. The foundation is not modeled, and the wall pier elements and the lean-on column elements are assumed to have fixed base boundary conditions. A rigid diaphragm is assumed at each floor level. P-Delta geometric nonlinearity is assumed for all elements.

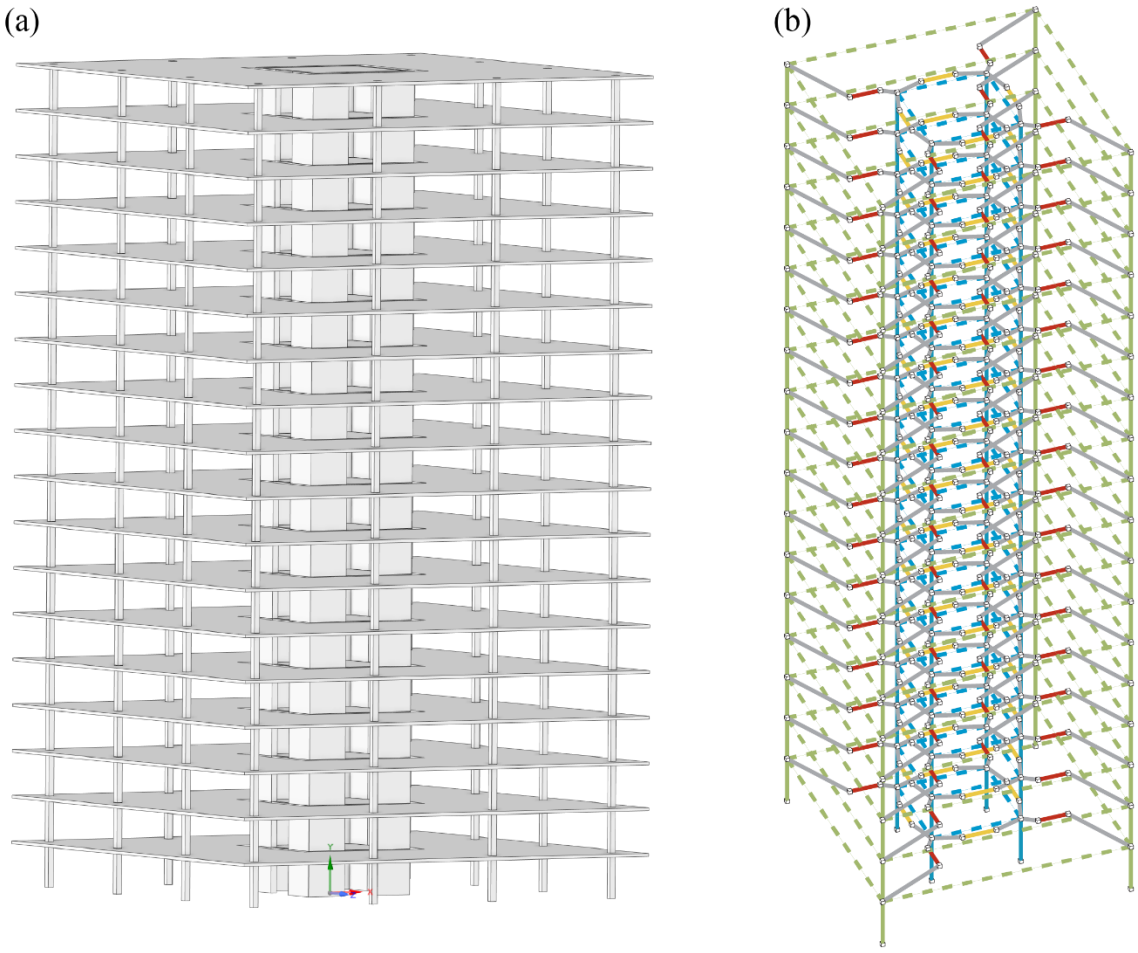

Figure 2-2: (a) 3D Schematic and (b) Opensees model of the eighteen-story core wall building

Figure 2-3 shows the Opensees model of the eighteen-story building and the elements of a typical floor. One core wall pier finite element represents one actual L-shaped core wall pier on one story, having four core wall pier finite elements on each floor level. The shear deformation of the core wall piers is ignored, assuming their seismic response is governed by flexure dominant behavior. Bond slip and bar buckling of the wall piers are not modeled. One lean-on column finite element represents three actual gravity columns. The wall pier finite elements are connected by either a series of finite elements that simulate the inelastic response of reinforced concrete coupling beams or finite elements that simulates the low-damage coupling beams. The reinforced concrete coupling beam element is assumed to be located at the top of the coupling beam at the same as the top nodes of the core wall pier element and the lean-on column elements.

The slab inside the core is simulated using the SFRS diaphragm, and the slab outside the core is simulated using the GLRS diaphragm. The floor diaphragm inside the core is connected to the floor diaphragm outside the core with corotational truss elements that simulate either monolithic connections or force-limiting connections. Rigid links connect the geometric centroids of the elements enforcing the two nodes at their ends to move as a rigid body. The rigid link is simulated using an elastic beam-column element with a very large value for the area, the moment of inertial, and the torsion constant compared to the section properties of the elements of the model that are deformable.

Section 2.4 to section 2.8 provide modeling details of the core wall piers, the lean-on columns, the reinforced coupling beams, the seismic mass, and the diaphragms, respectively. Section 2.9 shows modal analysis results of the eighteen-story core wall building model with monolithic connections between the SFRS and the GLRS and with reinforced coupling beams. Section 2.10 explains the modeling of damping using the modal analysis results. Section 2.11

and section 2.12 describes the modeling of the force-limiting connections and the low-damage coupling beams, respectively.

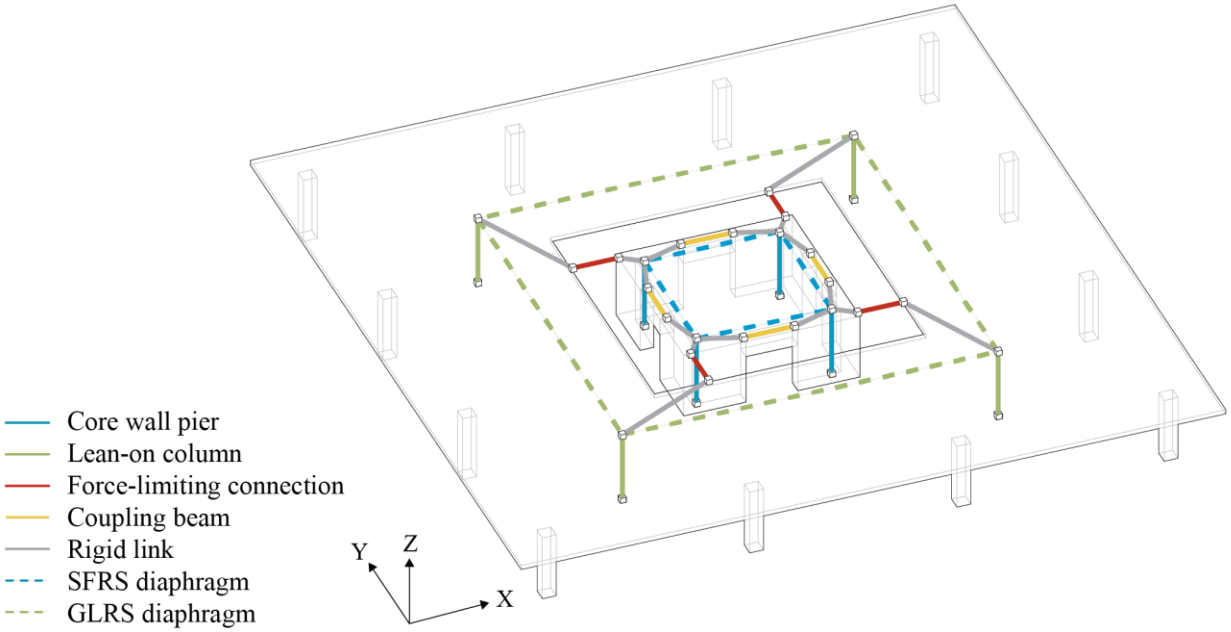

Figure 2-3: Opensees model of the eighteen-story building and the elements of a typical floor

2.4 Core wall piers

2.4.1 Elements

The core wall piers are modeled using force-based nonlinear elements with fiber sections. Figure 2-4(a) shows the four core wall pier elements in a typical story. One L-shaped wall section represents one-quarter of the whole core wall, and the four L-shaped walls have the same reinforcement details. The element is located at the geometric center, which is marked as the local y-axis and the local z-axis origin, with the local x-axis directing out-of-the-page, parallel to the element length. Figure 2-4(b) shows one core wall pier element with fiber sections at five integration points. The wall fiber sections consist of fibers that simulate the stress-strain response

of concrete and steel materials. Concrete is distinguished to unconfined concrete and confined concrete based on the structural details. Material properties of confined concrete depend on the reinforcement of each confined region.

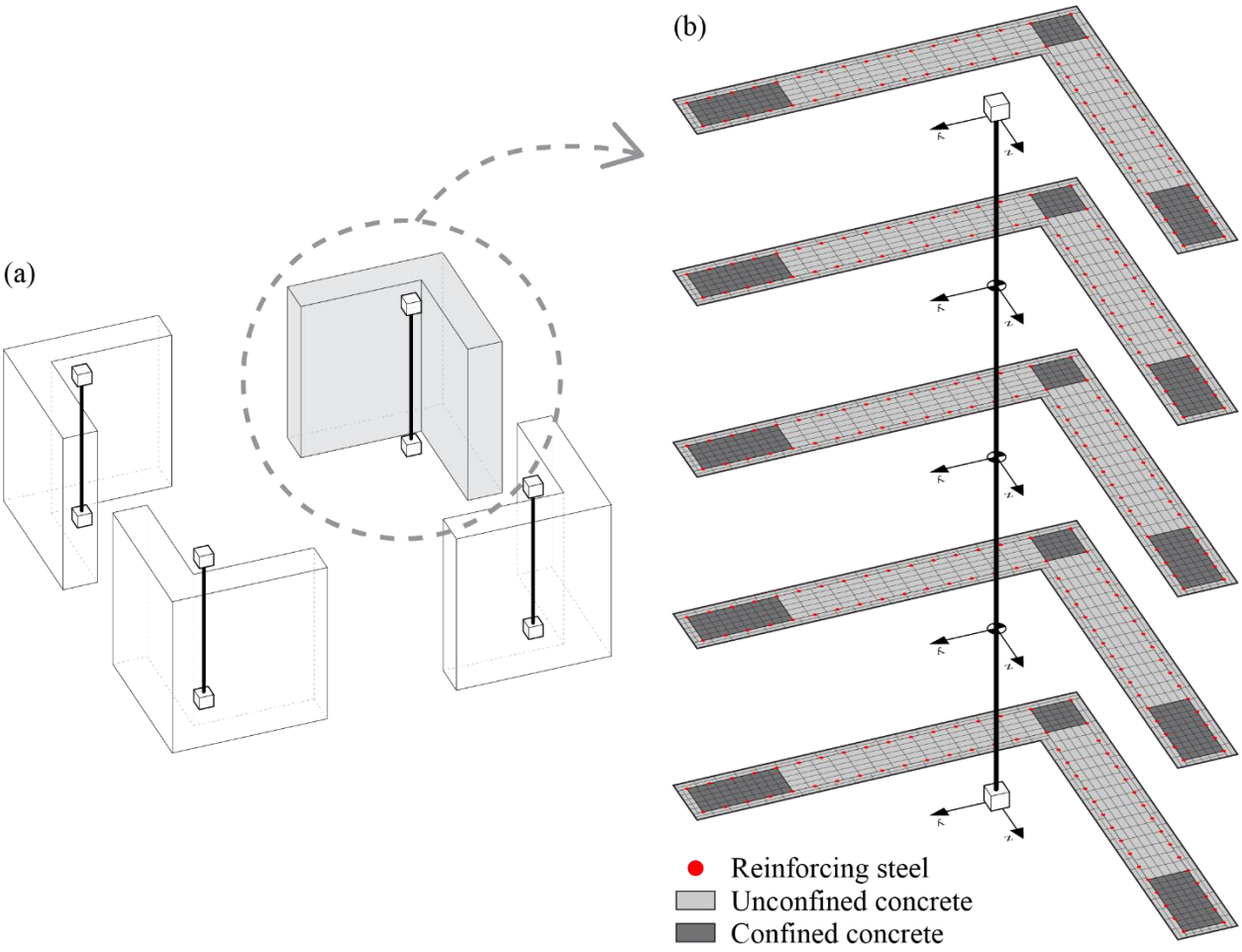

Figure 2-4: (a) Four core wall pier elements at a typical floor, and (b) one core wall pier element with fiber sections at 5 integration points

Figure 2-5 shows the fiber section of the L-shaped wall pier with unconfined concrete fibers, confined concrete fibers, and steel fibers on all floor levels. It indicates the location of three different confinement regions: Region 1 (R1), region 2 (R2), and region 3 (R3). Regions 2 and 3 have the same confined concrete properties due to symmetry. The lower floors (from the

1st floor to the 8th floor) have larger confined areas compared to the upper floors (from the 9th floor to the 18th floor).

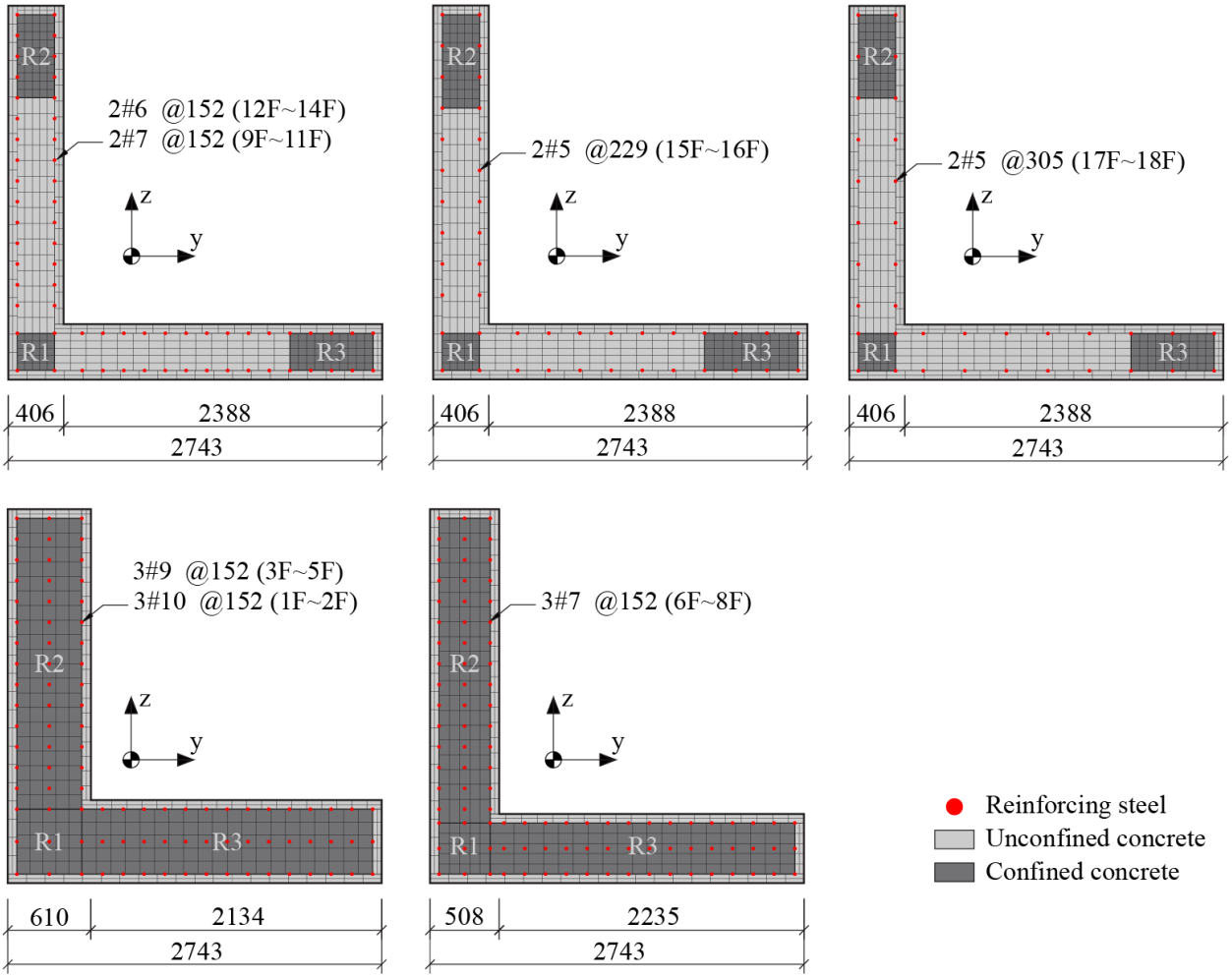

Figure 2-5: Wall fiber section on all floor levels

2.4.2 Concrete

The stress-strain response of concrete in the core wall is simulated using the Concrete02 material model in Opensees. The concrete model parameters are quantified based on the selected nominal material properties and references. Material parameters for the material model of the unconfined and confined concrete are presented in section 2.4.2.1 and section 2.4.2.2,

respectively. Localization phenomenon related to reinforced concrete nonlinear force-base element was considered for the core wall pier elements and is presented in section 2.4.2.3.

2.4.2.1 Unconfined concrete

In this section, the material model used to simulate the stress-strain relationship of the unconfined concrete is presented. Figure 2-6 shows the stress-strain relationship of the material model used for the unconfined concrete, along with the parameters that define the stress-strain relationship of the model.

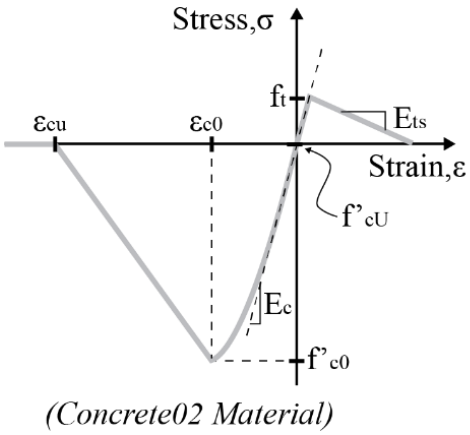

Figure 2-6: Unconfined concrete material constitutive model and governing parameters

The material parameters of the unconfined concrete model are shown in Table 2-2. Numerical convergence issues may occur if a non-zero value is used for the tensile strength f_t in Concrete02. A sensitivity study was conducted to assess the effect of the value f_t in the numerical simulation results. The effect of the f_t value in the numerical simulation results is small. Therefore, the value of f_t was set to zero to prevent numerical convergence issues during the earthquake simulations of the seismic response of the eighteen-story building model. As a comparison, the concrete tensile strength used in the reference report [55] is $f_t = 3.7\sqrt{f'_{cc0}(psi)}$,

the concrete tensile strength formula from the split cylinder test is $f_t = 7.5\sqrt{f'_{c0}(psi)}$ (i.e., modulus of rupture, f_r, in ACI318-19 [3]), and the concrete tensile strength formula from concrete panel subjected to in-plane normal and shear stresses is $f_t = 3.75\sqrt{f'_{cc0}(psi)}$ [58].

Table 2-2: Unconfined concrete material properties

Parameters	Notation	Units	Values	Reference
Concrete compressive strength	f'_{c0}	$[MPa]$	-55	Reference report [55]
		$[ksi]$	-8.0	
Concrete strain at maximum (peak) compressive strength	ε_{c0}	[-]	-0.002	Kent and Park (1971) [59]
Concrete crushing strength	f'_{cu}	$[MPa]$ or $[ksi]$	0	Reference report [55]
Concrete strain at crushing strength	ε_{cu}	[-]	-0.0040	Kent and Park (1971) [59]
Concrete strain when the stress reaches 20% of f'_{c0} at the end of a linear post-peak softening branch	ε_{20}	[-]	-0.0046	Eq. 2-6 from Coleman and Spacone (2001) [60]
Ratio between unloading slope at ε_{cu} and initial slope	λ	[-]	0.25	Assumed value
Concrete tensile strength	f_t	$[MPa]$ or $[ksi]$	0	-
Tension softening stiffness	E_t	$[MPa]$ or $[ksi]$	0.1 E_c	Assumed value

2.4.2.2 Confined concrete

This section presents the material model used to simulate the stress-strain relationship of the confined concrete. Figure 2-6 shows the stress-strain relationship of the material model of the confined concrete and the parameters that define the stress-strain relationship of the models. The material parameters of the confined concrete are shown in Table 2-3. The value of f_t was set to zero for the same reason as the unconfined concrete material model.

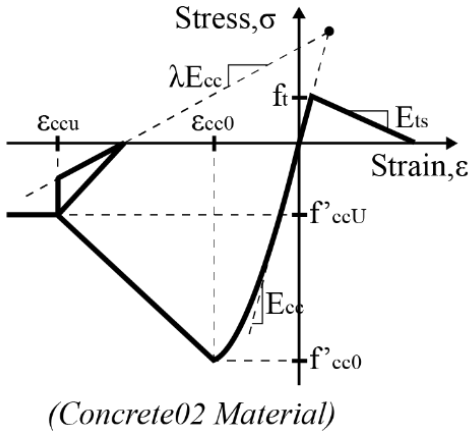

Figure 2-7: Confined concrete material constitutive model and governing parameters

Table 2-3: Confined concrete material properties

Parameters	Notation	Units	R1		R2 & R3		Reference
			1F~8F	9F~18F	1F~8F	9F~18F	
Confined concrete compressive strength	f'_{cc0}	$[MPa]$	69.64	73.98	72.60	75.08	Eq. 2-1 from Mander et al (1988) [61]
		$[ksi]$	-10.10	-10.73	-10.51	-10.89	
Confined concrete strain at maximum (peak) compressive stress	ε_{cc0}	[-]	-0.0046	-0.0054	-0.0051	-0.0056	Eq. 2-4 from Mander et al (1988) [61]
Ultimate confined compressive strength	f'_{ccu}	$[MPa]$ or $[ksi]$	0.2 f'_{cc0}				Kent and Park (1971) [59]
Ultimate compressive strain	ε_{ccu}	[-]	-0.0200	-0.0248	-0.0216	-0.0218	Eq. 2-5 from Moehle (2015) [58]
Concrete strain when the stress reaches 20% of f'_{cc0} at the end of a linear post-peak softening branch	ε_{20}	[-]	-0.0253	-0.0313	-0.0272	-0.0273	Eq. 2-6 from Coleman and Spacone (2001) [60]
Ratio between unloading slope at ε_{ccu} and initial slope	λ	[-]	0.25				Assumed value
Concrete tensile strength	f_t	$[MPa]$ or $[ksi]$	0				-
Tension softening stiffness	E_t	$[MPa]$ or $[ksi]$	0.1 E_{cc}				Assumed value

2.4.2.2.1 Confined concrete compressive strength, f'_{cc0}

Confined compressive strength (f'_{cc0}) is calculated according to Mander et al. (1988) [61] by adding the confinement effect ($K_c * K_e * f_l$) to the unconfined concrete compressive strength (f'_{c0}), as shown in Equation 2-1. K_c is the confinement coefficient, and K_e is the confinement effective coefficient. f'_l is the effective lateral confining pressure. f_l is the lateral confining stress. f'_{lx} and f'_{ly} are the effective lateral confining stress in x and y direction. f_{lx} and f_{ly} are the lateral confining stress in x and y direction.

$$f'_{cc0} = f'_{c0} + K_c * f'_l = f'_{c0} + K_c * K_e * f_l \quad \text{2-1}$$

$$f'_l = \sqrt{f'_{lx} * f'_{ly}} \quad , \quad f_l = \sqrt{f_{lx} * f_{ly}}$$

The confinement coefficient (K_c) used is equal to 4.1, as proposed by Richart et al. (1928) based on a low-strength cylinder test [62]. Rechart et al. (1929) confirmed that K_c = 4.1 works well for low-strength concrete (2~4 ksi) confined with 20~36 ksi steel hoops [63]. Later, large-scale testing by Richart et al (1934) at Lehigh University confirmed that K_c = 4.1 could be used for large columns [64]. For high-strength concrete (HSC) and ultra-high-strength concrete (UHSC), K_c = 4.1 is conservative to use, where HSC is concrete with a compressive strength greater than 55 MPa, according to the ACI 318 [3].

The confinement effective coefficient (K_e) is calculated according to Mander et al. (1988) [61] as the ratio of the effectively confined concrete area (A_e) to the confined area enclosed by the hoops (A_{cc}), as shown in Equation 2-2 and Figure 2-8. A_e is the area of the effectively confined concrete core, which accounts for the arched shape of the concrete body after the cover concrete falls off. A_{cc} is the area of the core section enclosed by the center lines of the perimeter spiral or hoop. s' is the clear vertical spacing between spiral or hoop bars, h_x and h_y are the core

dimensions to centerlines of the perimeter hoop in x and y directions, respectively. w_i is the i-th clear distance between adjacent longitudinal bars. N is the number of longitudinal bars.

$$K_e = A_e / A_{cc} \tag{2-2}$$

$$A_e = \left(A_{cc} - \sum_{i=1}^{N} \frac{(w_i)^2}{6}\right)\left(1 - \frac{s'}{2 * h_x}\right)\left(1 - \frac{s'}{2 * h_y}\right)$$

$$A_{cc} = h_x * h_y$$

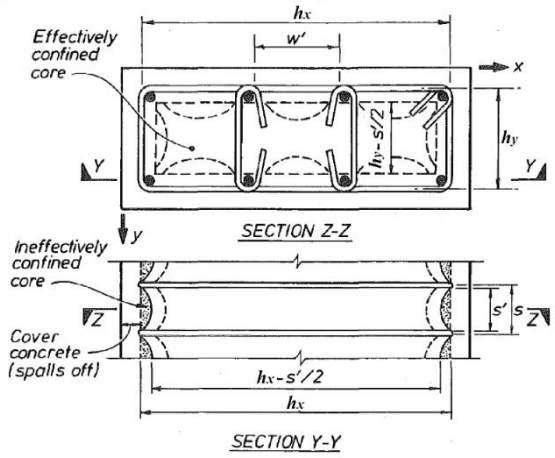

Figure 2-8: Effectively confined core for rectangular hoop reinforcement [61]

The lateral confining stress (f_{lx} and f_{ly}) is calculated according to Mander et al. (1988) [61] from the force equilibrium of the confining reinforcement and the confined concrete as the total transverse bar force divided by the vertical area of confined concrete, as shown in Equation 2-3. A_{sx} and A_{sy} are the total area of transverse bars running in the x and y direction, respectively. ρ_{sx} and ρ_{sy} are the ratio of the volume of transverse confining steel to the volume of confined concrete core in the x and y direction, respectively.

$$f_{lx} = \frac{A_{sx}}{s*h_y} * f_{yh} = \rho_{sx} * f_{yh} \qquad f_{ly} = \frac{A_{sy}}{s*h_x} * f_{yh} = \rho_{sy} * f_{yh} \qquad 2\text{-}3$$

$$\rho_{sx} = \frac{A_{sx}}{s*h_y} \qquad \rho_{sy} = \frac{A_{sy}}{s*h_x}$$

2.4.2.2.2 Confined concrete strain at maximum compressive stress, ϵ_{cc0}

Confined concrete strain at maximum compressive stress (ε_{cc0}) is calculated according to Mander et al. (1988) [61], as shown in Equation 2-4.

$$\varepsilon_{cc0} = \varepsilon_{c0}\left(1 + 5\left(\frac{f'_{cc0}}{f'_{c0}} - 1\right)\right) \qquad 2\text{-}4$$

2.4.2.2.3 Ultimate compressive strain, ϵ_{ccu}

Ultimate compressive strain **(**ε_{ccu}) is calculated according to Moehle (2015) [58], as shown in Equation 2-5. $f_{e,min}$ is the smaller of the effective confinement stresses f'_{lx} and f'_{ly}.

$$\varepsilon_{ccu} = 0.004 + \frac{f_{e,min}}{4 * f'_{c0}} \qquad 2\text{-}5$$

$$f_{e,min} = \min(f_{lx}, f_{ly}) * K_e = \min(f'_{lx}, f'_{ly})$$

2.4.2.2.4 Calculated confined concrete properties

Calculated confined concrete properties for the three regions are shown in Table 2-4. For simplicity of the building model, the 1st floor to 8th floor used the values from the 1st floor, and the 9th floor to 18th floor used values from the 9th floor, as shown in Table 2-3 with other summarized material properties of confined concrete.

Table 2-4: Calculated confined concrete properties for the three regions

Floor Level	f'_{cc0}				ε_{cc0} [-]		ε_{ccu} [-]	
	SI Unit [MPa]		Imperial Unit [ksi]					
	R1	R2 & R3	R1	R2 & R3	R1	R2 & R3	R1	R2 & R3
1 ~ 5	69.64	72.60	10.10	10.51	0.0046	0.0051	0.0200	0.0216
6 ~ 8	72.60	73.29	10.53	10.63	0.0052	0.0053	0.0233	0.0231
9 ~ 14	73.98	75.08	10.73	10.89	0.0054	0.0056	0.0248	0.0218
15 ~ 16	73.98	75.36	10.73	10.93	0.0054	0.0057	0.0248	0.0221
17 ~ 18	73.98	75.08	10.73	10.89	0.0054	0.0056	0.0248	0.0218

2.4.2.3 Localization phenomenon

In nonlinear force-based elements, strains are localized at the integration points [60]. For example, Figure 2-9 (a) shows a column model with a single nonlinear force-based element subjected to an axial load and a horizontal displacement at the top. As the applied displacement at the top increases, the curvature at the base integration point increases. When the moment demand is larger than the plastic moment of the base section, the curvature demand increases with a constant moment (assuming elastic-plastic moment-curvature response). Since the moment at the base of the element is limited to the maximum moment, the curvature or moment on the rest of the integration points does not change as the curvature at the base increases. As a result, the inelastic strains are localized at the base of the beam-column element and do not propagate over the height of the expected plastic hinge. In addition, Figure 2-9 (b) shows that the curvature demand at the base is larger when the plastic hinge length is shorter since the plastic hinge length is a function of the number of integration points.

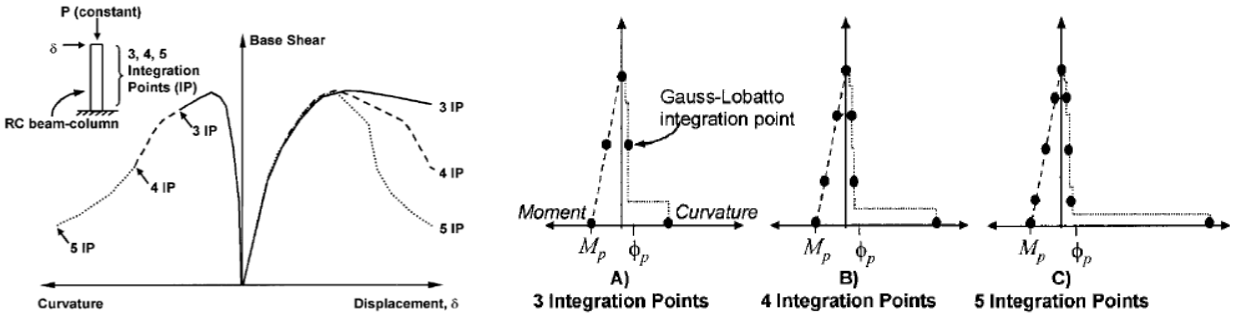

Figure 2-9: (a) RC beam-column modeled with strain-softening section response and, (b) moment and curvature profiles for elastic-perfectly plastic cantilever modeled with single force-based element [60]

To solve this issue of localization of inelastic strains, the process of regularization is done using the fracture energy in compression (G_f^c),

$$G_f^c = \int \sigma \, du_i = h \int \sigma \, d\varepsilon_i$$

where, σ is the concrete stress, and u_i is the inelastic displacement, and ε_i is the inelastic strain. h is the length of the softening integration point L_{IP} for force-based frame elements. The integral represents the area under the post-peak portion of the compressive stress-strain curve shown in Figure 2-10.

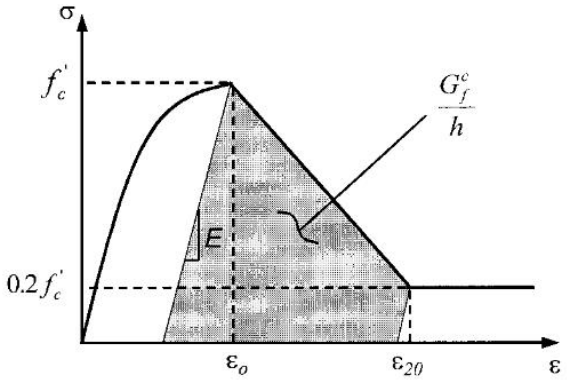

Figure 2-10: Concrete stress-strain relationship and compression fracture energy by Kent-Park (1971) [60]

The fracture energy in compression (G_f^c) is constant regardless of the number of integration points and the length of the softening integration point (L_{IP}). So, the ultimate compressive strain (ε_{cu}) is calibrated to maintain a constant energy release considering the length of the softening integration point (L_{IP}), as shown in Figure 2-11. The calibrated ultimate compressive strain is termed ε_{20}, which is the concrete strain when the stress reaches 20% of f'_{cc0} at the end of a linear post-peak softening branch.

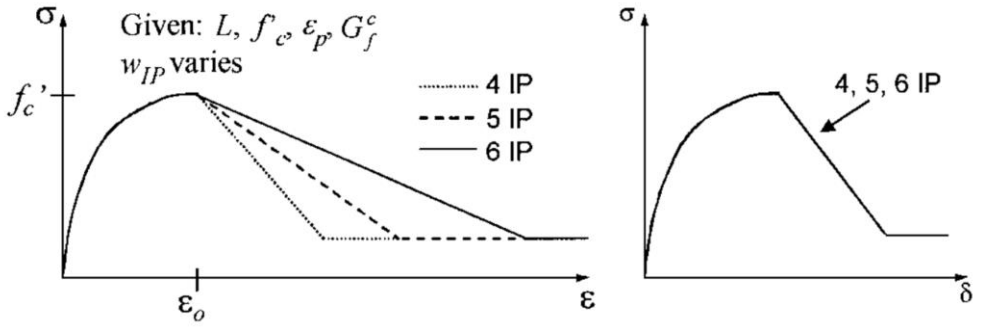

Figure 2-11: Stress-strain curve with constant fracture energy

The expression for ε_{20} is shown in Equation 2-6, where E is Young's modulus and ε_{c0} is the strain corresponding to maximum compressive strength. The fracture energy in compression (G_f^c) is calculated using the material properties of the cylinder test of the individual experiment. For the eighteen-story building model, h is assumed to be the general height of the cylinder test. The properties of concrete material used for the calculation of the fracture energy in compression (G_f^c) are assumed to be equal to the properties used in the eighteen-story building model.

$$\varepsilon_{20} = \frac{G_f^c}{0.6 f'_{c0} L_{IP}} - \frac{0.8 f'_{c0}}{E} + \varepsilon_{c0} \qquad 2\text{-}6$$

$$\frac{G_f^c}{h} = \frac{f'_{c0} + f'_{cu}}{2}\left(\frac{f'_{c0} - f'_{cu}}{E_c} + \varepsilon_{cu} - \varepsilon_{c0}\right)$$

$$G_f^c = h\left(\frac{f'_{c0} + f'_{cu}}{2}\right)\left(\frac{f'_{c0} - f'_{cu}}{E_c} + \varepsilon_{cu} - \varepsilon_{c0}\right)$$

L_{IP} is found in Table 2-5. Table 2-5 shows the tributary length of the Gauss-Lobatto Integration points (L_h) with five integration points. The length of the element (L) is the element length of one wall element in the eighteen-story building model. For the base integration point, the integration point location (ξ_h) is 1.0, the integration point weight (w_h) is 1/10, and the length of the softening integration point (L_{IP}) is L/20.

Table 2-5: Tributary length of Gauss-Lobatto Integration points

Number of integration points	Integration point location ξ_h	Integration point weight w_h	Tributary length $L_h = L * \frac{w_h}{2}$
5	-1.0	1/10	L/20
	-0.65	49/90	L*49/180
	0.0	32/45	L*32/90
	0.65	49/90	L*49/180
	1.0	1/10	L/20

Using Equation 2-6, ε_{20} values for unconfined and confined concrete are calculated and listed in Table 2-6 with ε_{cu} and ε_{ccu} values. It is observed that the absolute value of the ultimate strain has increased when the localization phenomenon is considered.

Table 2-6: comparison of ε_{cu} and ε_{ccu} to ε_{20}

	Region	Floor Level	ε_{cu} [mm/mm]	ε_{20} [mm/mm]
Unconfined Concrete	N/A	All	-0.0040	-0.0046
Confined Concrete	Region 1	1~8	-0.0200	-0.0253
		9~18	-0.0248	-0.0313
	Regions 2 & 3	1~8	-0.0216	-0.0272
		9~18	-0.0218	-0.0273

2.4.3 Steel

2.4.3.1 Steel material parameters

The stress-strain relationship of the steel in the core wall piers is simulated using the Steel MPF material model in Opensees. The stress-strain relationship of the Steel MPF material model is governed by 10 parameters: yield strength (f_y), initial Young's modulus (E_s), strain hardening ratio (b), initial value of the curvature parameter R (R_0), curvature degradation parameters (cR_1 and cR_2), isotropic hardening components (a_1, a_2 , a_3, and a_4). These parameters are related to elastic behavior (f_y, E_s), Bauschinger effect (R_0, cR_1, cR_2), kinematic hardening (b), and isotropic hardening (a_1, a_2 , a_3, a_4) of steel, as shown in Figure 2-12. b governs the slope of the post-yield branch. a_1 shifts the post-yield slope in compression with fixed a_2, and a_3 shifts the post-yield slope in tension with fixed a_4. Parameter R governs the curvature of the transition between elastic and hardening slopes. A larger value of R creates a sharper transition between elastic and hardening slopes. R is a function of parameters R_0, cR_1, and cR_2. The relationship between R_0, cR_1, and cR_2 is shown in the equation below, where ξ is the plastic range of deformation normalized by the initial yield point $\epsilon_y = F_y/E$. ϵ_p is the maximum strain recorded in the loading direction after the reversal point ϵ_r. ϵ_0 is the strain of the updated yield point. [65]

$$R = R_0 * \left(1 - \frac{cR_1 * \xi}{cR_2 + \xi}\right), \quad R(\xi) > 0$$

$$\xi = \left|\frac{\epsilon_p - \epsilon_0}{\epsilon_y}\right|$$

The elastic parameters (f_y and E_s) of the Steel MPF are quantified based on the selected nominal material. However, the post-yield parameters (b, R_0, cR_1, cR_2, a_1, a_2 , a_3, and a_4) need

to be quantified using calibration at the element level because they are not nominal values, and there are no empirical equations given in the literatures to estimate these values. The calibrated steel material parameters are shown in Table 2-7, and the calibration process is presented in section 2.4.3.2. [65]

Table 2-7: Calibrated steel material parameters

Parameter	f_y	E_s	b	R_0	cR_1	cR2	a_1	a_2	a_3	a_4
Units	$[MPa]$ ($[ksi]$)	$[MPa]$ ($[ksi]$)	[-]	[-]	[-]	[-]	[-]	[-]	[-]	[-]
Values	414 (60)	206629 (29969.0)	0.02921	20.0	0.96	0.07	0.05075	1.0	0.022	1.0

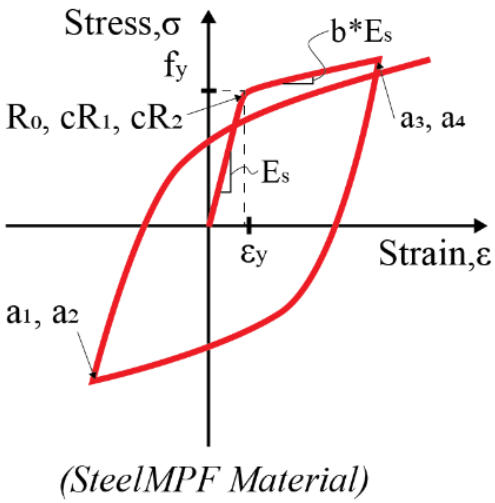

Figure 2-12: Steel material constitutive model and governing parameters [65]

2.4.3.2 Steel material calibration

In this section, the steel material model parameters are calibrated using experimental results at the component level. It is done by comparing the results from the experimental results with the results from a numerical model that simulates that experiment. The element level force-

displacement response will be calibrated by adjusting the parameters of the stress-strain model of the steel material.

The experimental test results at the component level for this calibration are provided by Beyer et al. (2008) [66], where quasi-static cyclic loading was applied to two types of U-shaped reinforced concrete wall specimens with different wall thicknesses. The two specimens are termed TUA and TUB.

2.4.3.2.1 Geometry

Numerical models of the two specimens, TUA and TUB, are generated in Opensees. The geometry and the wall section fibers are modeled with the information provided in the paper by Beyer et al. [66]. Figure 2-13 shows the geometry of the TUA and TUB specimens, and Figure 2-14 shows the fiber section detail of the TUA and TUB specimens.

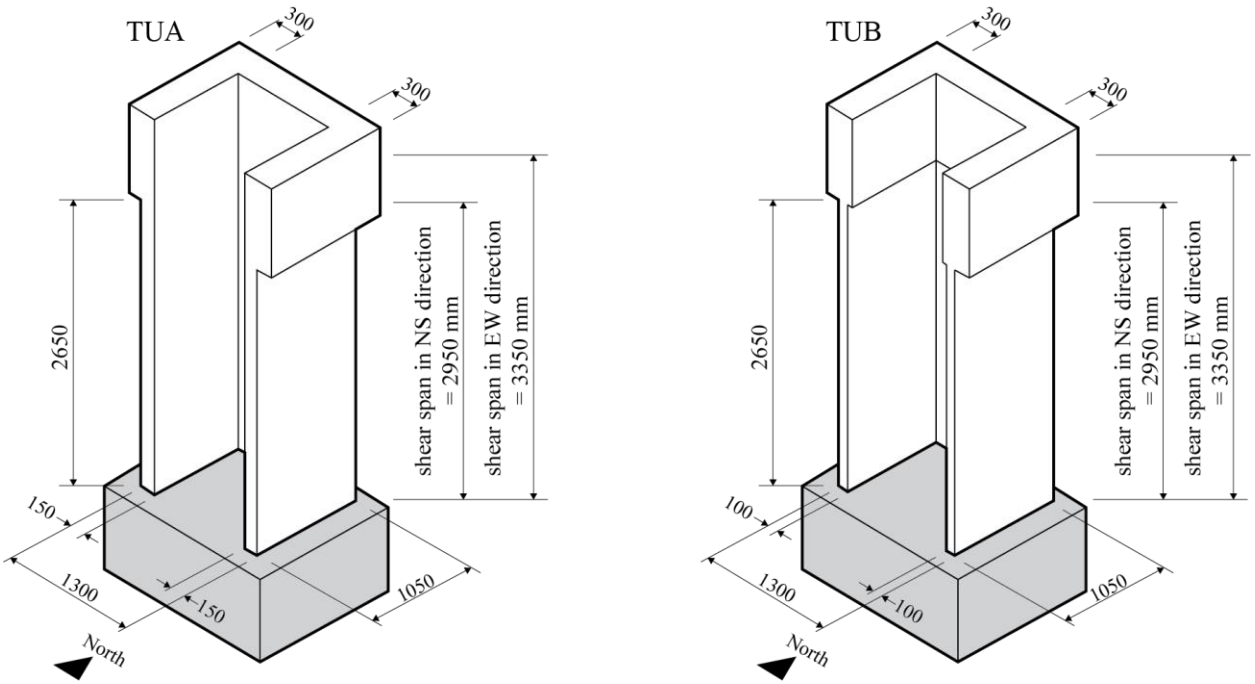

Figure 2-13: Geometry of TUA and TUB [66]

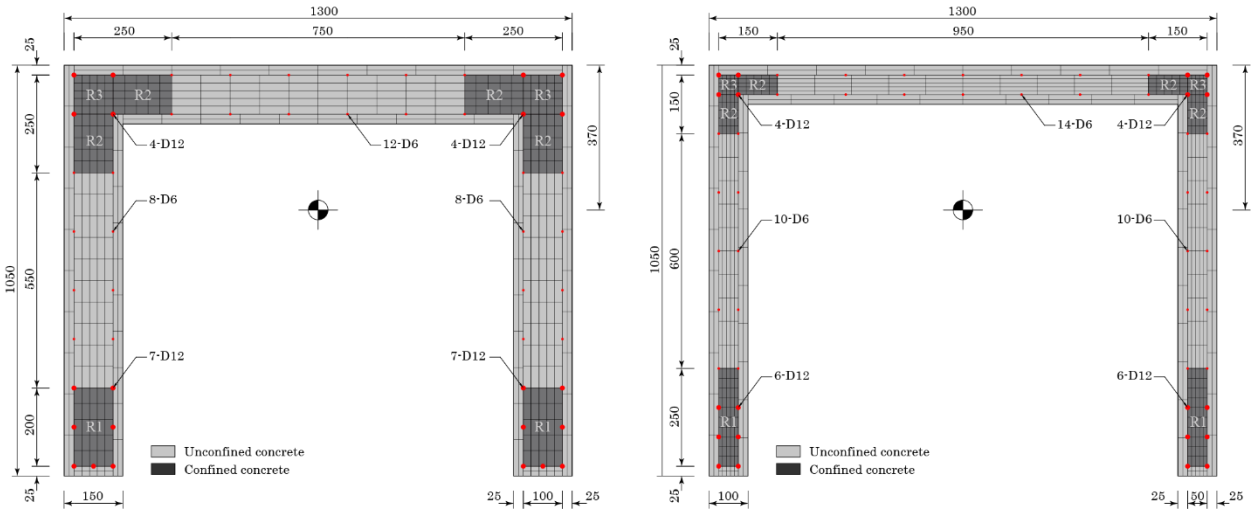

Figure 2-14: Geometry and Section detail of TUA and TUB [66]

2.4.3.2.2 Axial load

During the experiment, a constant axial load accounting for the typical tributary area of a core wall of a 6-story building was applied to the specimens by post-tensioning. The axial load at the wall base was 780 kN, which included the self-weight of the test unit and the weight of any installations mounted on the wall. Therefore, the numerical model of the specimens was loaded with the same amount of axial load (780 kN).

2.4.3.2.3 Lateral load

During the experiment, the specimens are applied with four displacement-controlled loading patterns: EW, NS, diagonal, and “sweep”. Figure 2-15(a) shows the displacement-controlled loading history. The EW cycle is a full cycle parallel to the web (O → A → B → O), the NS cycle is a full cycle parallel to the flanges (O → C → D → O), the diagonal cycle is a full cycle in a diagonal direction (O → E → F → O), and the ‘‘sweep’’ cycle is a cycle includes two-

directional movement (O → A → G → D → C → H → B → O). During these cycles, the twist of the wall head was restrained.

The cycles started with a small amplitude of the four types of loadings in series. Then, the amplitude level was increased after completing the four types of cycles. The first four loadings were force-controlled with 0.25, 0.50, 0.75, and 1.0 of the predicted lateral forces at the first yield of the specimens. During this time, the sweep cycle was replaced by (O → H → G → O) cycles. After the four force-controlled loadings, the specimens were applied to a displacement-controlled loading with displacement ductility levels of 1, 2, 3, 4, 6, and 8 until failure.

Figure 2-15(b) and (c) show the actual imposed displacement pattern of the specimen TUA and TUB from the data obtained from the experimental testing. The displacement was controlled at 2.95 m in height when loading in the NS or the diagonal direction, and the displacement was controlled at 3.35 m in height when loading in the EW direction.

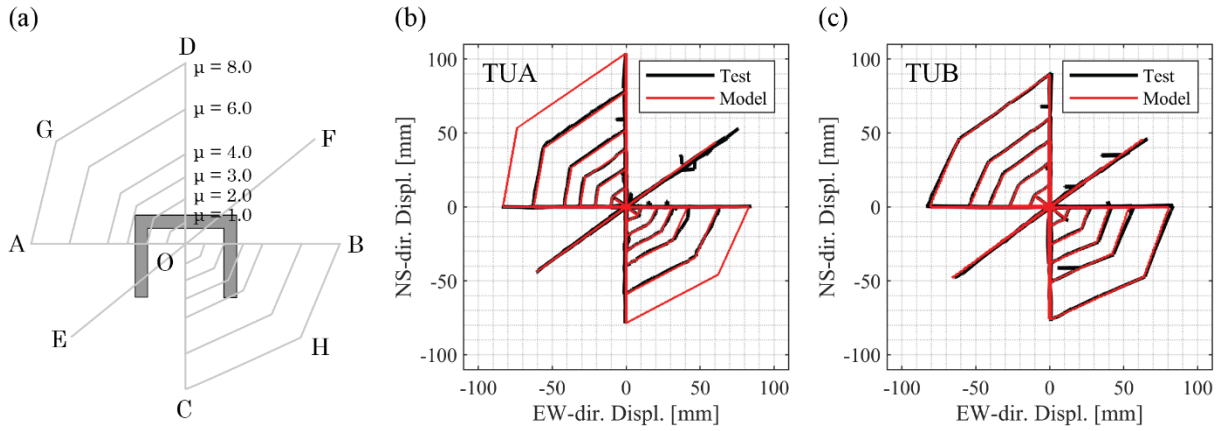

Figure 2-15: (a) Displacement-controlled loading history, and the imposed displacement on (b) TUA and (c) TUB for the text and the model [66]

Table 2-8 shows the yield displacements, yield drifts, maximum displacements, and maximum drifts of TUA and TUB subjected to different directions of loading during the

experimental test done by Beyer et al. [66]. Δ_y is the yield displacement, δ_y is the yield drift, Δ_{max} is the maximum displacement, and δ_{max} is the maximum drift from the experiment.

Table 2-8: Yield displacements, yield drifts, maximum displacements, and maximum drifts of TUA and TUB subjected to different directions of loading [66]

Positions	Displacement controlled level	TUA				TUB			
		Δ_y	δ_y	Δ_{max}	δ_{max}	Δ_y	δ_y	Δ_{max}	δ_{max}
		[mm]	[%]	[mm]	[%]	[mm]	[%]	[mm]	[%]
Pos. A, B	3.35 m	10.4	0.31	83.2	2.48	13.5	0.40	81.0	2.42
Pos. C	2.95 m	9.8	0.33	78.4	2.66	12.7	0.43	76.2	2.58
Pos. D	2.95 m	13.0	0.44	104.0	3.53	15.0	0.51	90.0	3.05
Pos. E, H	2.95 m	8.8	0.30	70.4	2.39	12.7	0.43	67.2	2.58
Pos. F, G	2.95 m	10.5	0.36	84.0	2.85	12.1	0.41	72.6	2.46

Using the values from Table 2-8, the coordinates of displacement-controlled loading for each ductility level for the numerical models of TUA and TUB were computed, and they are shown in Table 2-9.

Table 2-9: Coordinates of the imposed displacement on the Opensees model

Posi-tion	Displ. Controll-ed level	μ = 1		μ = 2		μ = 3		μ = 4		μ = 6	
		EW-dir	NS-dir	EW-dir	NS-dir	EW-dir	NS-dir	EW-dir	NS-dir	EW-dir	NS-dir
		[mm]	[mm]	[mm]	[mm]	[mm]	[mm]	[mm]	[mm]	[mm]	[mm]
A	3.35 m	-13.87	0.05	-27.31	-0.46	-41.01	-0.09	-54.59	-0.02	-82.61	0.36
B	3.35 m	13.57	0.17	27.81	0.01	42.28	-0.30	56.82	-0.24	83.15	0.00
C	2.95 m	0.45	-12.69	0.23	-25.69	0.02	-38.01	0.14	-50.28	0.68	-76.82
D	2.95 m	0.35	14.69	-0.03	14.69	0.19	44.71	0.24	60.05	0.33	90.07
E	2.95 m	-12.54	-8.98	-10.34	-8.33	-21.50	-16.24	-33.20	-23.86	-64.33	-47.69
F	2.95 m	9.11	6.75	10.95	8.26	21.94	15.55	32.67	23.07	66.23	46.00
G	2.95 m	-10.63	7.16	-20.80	15.18	-31.46	22.83	-41.15	30.92	-60.89	46.60
H	2.95 m	10.67	-8.15	21.41	-14.74	32.97	-23.39	43.27	-32.29	64.38	-47.26

2.4.3.2.4 Concrete

Unconfined concrete material properties of TUA and TUB are summarized in Table 2-10. The three different regions for confinements, Region 1 (R1), region 2 (R2), and region 3 (R3) are shown in Figure 2-14. Confined concrete material properties are shown in Table 2-11 according to equations in chapter 2.4.2, except the compressive strength of confined concrete (f'_{cc0}). The compressive strength of confined concrete (f'_{cc0}) is computed using Figure 2-16 from Mander et al. (1988) [61]. The confined strength ratio (f'_{cc0}/f'_{c0}) can be identified using the smallest confining stress ratio (f'_{lx}/f'_{c0}) and the largest confining stress ratio (f'_{ly}/f'_{c0}).

Table 2-10: Material properties of unconfined concrete

	f'_{c0} $[MPa]$	ε_{c0} [-]	ε_{cu} [-]	ε_{20} [-]
TUA	77.9	0.0020	0.0040	0.0043
TUB	54.7	0.0020	0.0040	0.0043

Table 2-11: Material properties of confined concrete

	f'_{c0}		f'_{lx}	f'_{ly}	f'_{lx}/f'_{c0}	f'_{ly}/f'_{c0}	f'_{cc0}/f'_{c0}	f'_{cc0}	ε_{cc0}	ε_{ccu}	ε_{20}
Unit	$[MPa]$		$[MPa]$	$[MPa]$	[-]	[-]	[-]	$[MPa]$	[-]	[-]	[-]
TUA	77.9	R1	1.87	2.49	0.024	0.032	1.19	92.70	0.0039	0.0100	0.0115
		R2	1.45	2.18	0.019	0.028	1.14	88.81	0.0034	0.0087	0.0100
		R3	2.64	2.64	0.034	0.034	1.22	95.04	0.0042	0.0125	0.0144
TUB	54.7	R1	1.31	3.28	0.024	0.06	1.3	71.11	0.005	0.0100	0.0112
		R2	1.15	2.29	0.021	0.042	1.2	65.64	0.004	0.0092	0.0105
		R3	2.97	2.27	0.054	0.054	1.35	73.85	0.0055	0.0176	0.0202

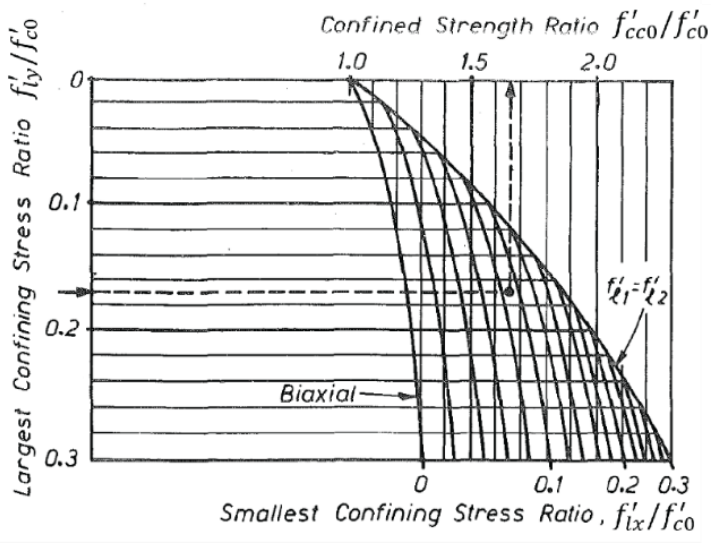

Figure 2-16: Confined strength determination from lateral confining stresses for rectangular sections [61]

2.4.3.2.5 Calibration

Steel material properties used in the experiment are shown in Table 2-12. Steel material parameters are calibrated with baseline values adopted from Mayorga et al. [67]. The baseline values are listed in the second column of Table 2-13. The range of values that were considered for the calibration of the parameters was selected based on the standard deviation (STD) of the parameters from Birrell et al. [65], shown in Table 2-14. The mean yield stress (f_y) value of Grade A706, which is 467 MPa, is similar to the yield stress (f_y) of steel used in the specimens TUA and TUB, which are 488 MPa and 471 MPa, respectively. Using the standard deviation (STD) of each parameter in Table 2-14, the values considered for calibration for each parameter are selected as 0.5 or 1.0 times the standard deviation (STD) larger or smaller than the baseline values, as shown in Table 2-13.

Table 2-12: Material properties of steel

	f_y (*D12*) [Mpa]	f_y (*D06*) [Mpa]
TUA	488	518
TUB	471	518

Table 2-13: Parameters used for calibration

Parameter	E_s [ksi]	b	R_0	cR_1	cR_2	a_1	a_3
Units	[MPa]	[-]	[-]	[-]	[-]	[-]	[-]
Baseline values*	29969	0.02921	20	0.9466	0.09300	0.05075	0.02200
STD	-	0.00324	-	0.01778	0.02565	0.01092	0.00812
Baseline values* - 1.0 STD	same	0.02597	same	0.92882	0.06735	0.03983	0.01388
Baseline values* - 0.5 STD	same	0.02759	same	0.93771	0.080175	0.04529	0.01794
Baseline values* + 0.5 STD	same	0.03083	same	0.95549	0.105825	0.05621	0.02606
Baseline values* + 1.0 STD	same	0.03245	same	0.96438	0.11865	0.06167	0.03012

Baseline values* = Values adopted from Mayorga et al. [67]

Table 2-14: Proposed Multivariate Normal distribution (Grade A706) [65]

Parameter	f_y	E_s	b	cR_1	cR2	a_1	a_3
Units	[MPa]	[MPa]	[-]	[-]	[-]	[-]	[-]
Mean	467	206	0.018	0.889	0.095	0.039	0.029
Standard Deviation (STD)	46.7	8.24	0.00324	0.01778	0.02565	0.01092	0.00812

2.4.3.2.6 Results

A parametric study was performed by quasi-static numerical analysis of the model of TUA and TUB in Opensees with steel parameters listed in Table 2-13. As a result, one value for

each parameter was chosen by comparing the stiffness of loading and unloading branches and the maximum force levels of the numerical model results with that of the experimental test data. The results are listed in Table 2-15. TUB, which has a thinner wall thickness than TUA, is expected to have more flexural dominant behavior than TUA. Also, since the numerical models of TUA and TUB assume negligible shear deformation, the analysis result of TUB is more appropriate to compare with the experimental results than the analysis results of TUA.

Table 2-15: Parameters for steel material properties

Parameter	f_y	E_s	b	R_0	cR_1	cR2	a_1	a_2	a_3	a_4
Units	$[MPa]$ ($[ksi]$)	$[MPa]$ ($[ksi]$)	[-]	[-]	[-]	[-]	[-]	[-]	[-]	[-]
Baseline Values*	488.0 (70.8)	206629 (29969.0)	0.02921	20.0	0.9466	0.093	0.05075	1.0	0.022	1.0
Values Selected after Calibration	Same	Same	Same	Same	0.9600	0.070	Same	Same	Same	Same

Baseline values* = Values adopted from Mayorga et al. [67]

Figure 2-17 shows the hysteretic response of TUA in EW and NS direction with the calibrated steel material parameters. Figure 2-18 shows the hysteretic response of TUB in EW and NS direction with the calibrated steel material parameters. The responses of TUA and TUB from the numerical model well match the responses of TUA and TUB from the experimental test.

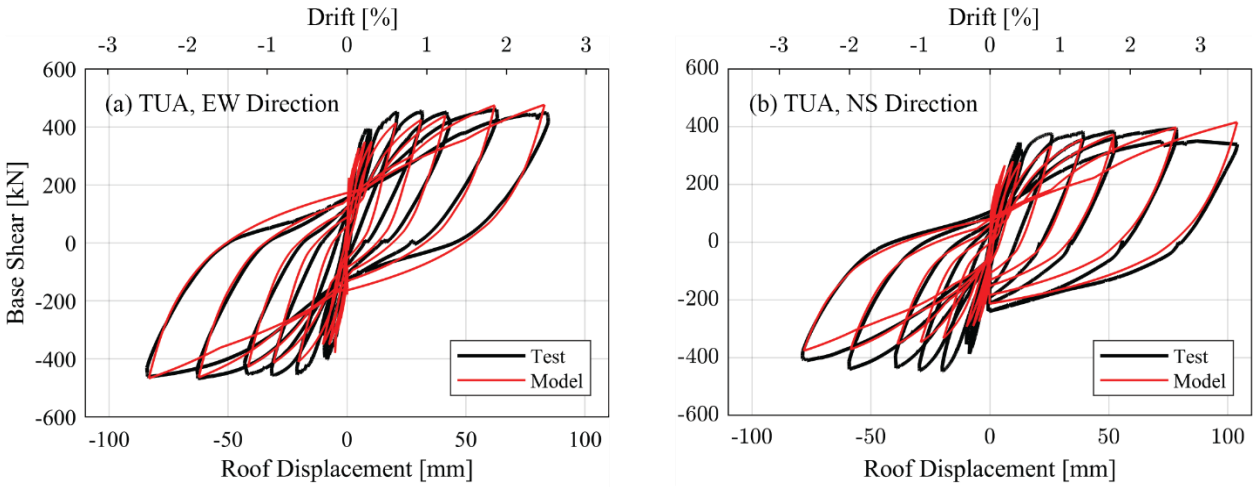

Figure 2-17: Hysteretic response of TUA in (a) EW direction and (b) NS direction

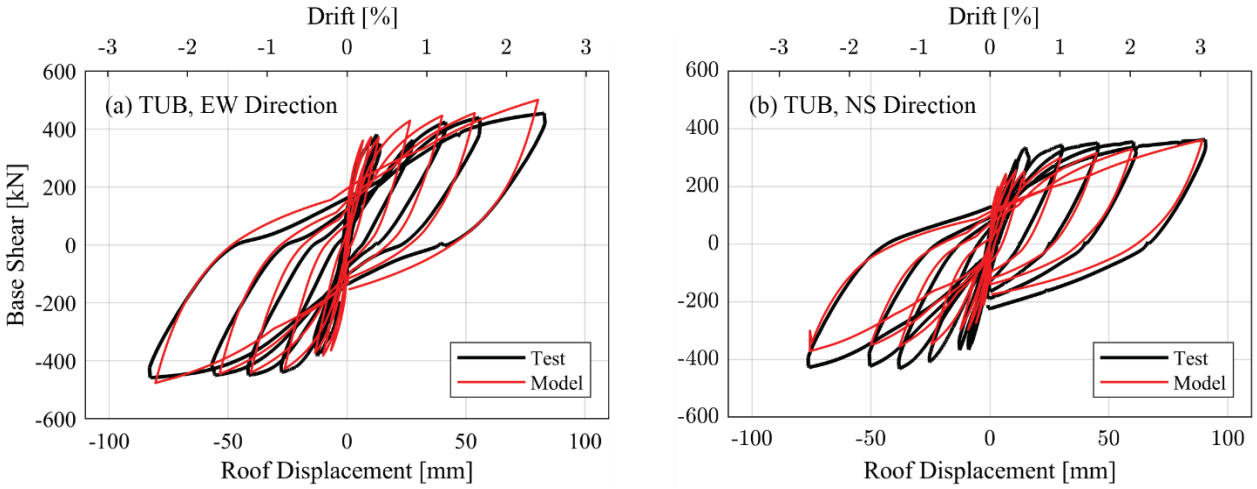

Figure 2-18: Hysteretic response of TUB in (a) EW direction and (b) NS direction

2.5 Lean-on columns

2.5.1 Lean-on column sizes

The reference report [55] does not provide information on the design of the gravity columns. In this section, the design of the lean-on columns is presented.

$$\phi P_n \geq P_u$$

$$\phi P_{n,max} \geq 1.2D + 1.6L$$

where, $\phi = 0.65$ (Compression controlled, ACI Table 21.2.2, Fig R21.2.2b)

$P_{n,max} = 0.80\ P_o$ (ACI Table 5.3.1)

$P_o = 0.85 f_c'(A_g - A_{st}) + f_y * A_{st}$ (ACI Eq.22.4.2.2)

The section of the column is assumed to have equal width and depth. In the beginning of the design, the size started at 610 mm by 610 mm. Then the column size is increased accordingly to satisfy the demand. Table 2-16 lists the selected column sizes, which are increased to 813 mm by 813 mm from floor 1 to floor 5 and increased to 711 mm by 711 mm from floor 6 to floor 8.

Table 2-16: Lean-on column sizes

Floor Level	Column Size	
	[in x in]	[mm x mm]
1 ~ 5	32 x 32	813 x 813
6 ~ 8	28 x 28	711 x 711
9 ~ 18	24 x 24	610 x 610

2.5.2 Lean-on column elements

In the building model, one elastic beam-column elements represent three gravity columns in one story. Therefore, the section properties of the lean-on column element are calculated based on the sectional properties of the gravity columns.

The area of one lean-on column element in the model (A_{col}) is calculated as the sum of the area of three gravity columns, as shown in Equation 2-7.

$$A_{col} = A_{column1} + A_{column2} + A_{column3} \quad \text{2-7}$$

The moment of inertia of one lean-on column element in the model (I_{col}) is calculated as the sum of the moment of inertia of three gravity columns, as shown in Equation 2-8. The lean-on column element uses the moment of inertia of a cracked section, $I_e = 0.7I_g$, according to ACI 318-19, assuming cracked ends. I_g is the moment of inertia of the gross concrete cross-section about the centroidal axis, and I_e is the effective moment of inertia. The reason why the moment of inertia of the lean-on column element is the sum of that of the gravity columns is that the diaphragm which connects the columns is assumed to have negligible out-of-plane flexural stiffness. Therefore, the $A_i d_i^2$ term in the general moment of inertia formula, $I_y = \sum(I_{yi} + A_i d_i^2)$, is neglected. The term $A_i d_i^2$ would be added if the slab (i.e., diaphragm) is assumed to be rigid in out-of-plane flexure.

$$I_{col} = 0.7I_{g\_column1} + 0.7I_{g\_column2} + 0.7I_{g\_column3} \quad \text{2-8}$$

The torsional constant of the lean-on column element (J_{col}) is calculated as in Equation 2-9. In the equation, *a* and *b* are half the width or half the height of a rectangular bar where a is equal to or smaller than b. The value k_1 is equal to 0.1406 when the ratio of b/a is equal to 1.0.

$$T = k_2(2a)^2(2b)\tau_{max}$$

$$\tau_{max} = G\gamma_{max}$$

$$\gamma_{max} = k2a\frac{d\theta}{dx}, \qquad k_1 = k * k_2$$

$$T = k_1(2a)^3(2b)G\frac{d\theta}{dx}$$

$$J_{col} = k_1(2a)^3(2b) \quad \text{2-9}$$

2.6 Reinforced coupling beams

A reinforced coupling beam element in Opensees consists of two parts: the elastic part and the shear hinge part located at the center of the coupling beam, as shown in Figure 2-19. The elastic part captures the deformation of the coupling beam using an elastic beam-column element with effective flexural stiffness of $0.07(l_n/h)I_g = 0.07 * 3.0 * I_g = 0.21I_g$, per LATBSDC (2017) [68]. The shear hinge accounts for the nonlinear hysteretic behavior of the coupling beam using the zero-length element, which connects two nodes at the same location at the center of the coupling beam only in the global Z-direction translational degree of freedom. Other degrees of freedom of the two nodes are set as equal using the equal DOF command. The inelastic response of the reinforced concrete coupling beams was simulated using the material model Pinching4 that is available in Opensees, as shown on the right in Figure 2-19. The Pinching4 model consists of four points in the shear force-deformation response. Point 1 defines the yield point, Point 2 defines the ultimate shear, Point 3 defines the onset of shear degradation, and Point 4 defines the ultimate deformation at which the model reaches the residual shear force.

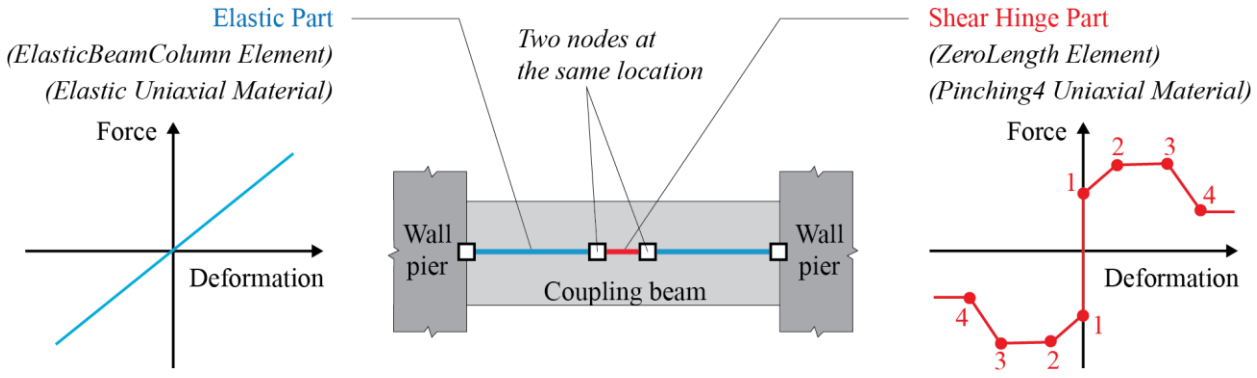

Figure 2-19: Typical modeling approach for coupling beams

The coupling beam hysteretic behavior is calibrated in the reference report [55]. The reference report used experimental results from of coupling beam specimen tested by Naish et al. (2013). The specimen used post-tensioned slabs and reinforced concrete coupling beams. The calibration result from the reference report is shown in Figure 2-20(a), which shows the match between the analytical and experimental force-displacement response that is acceptable to the purpose of this study.

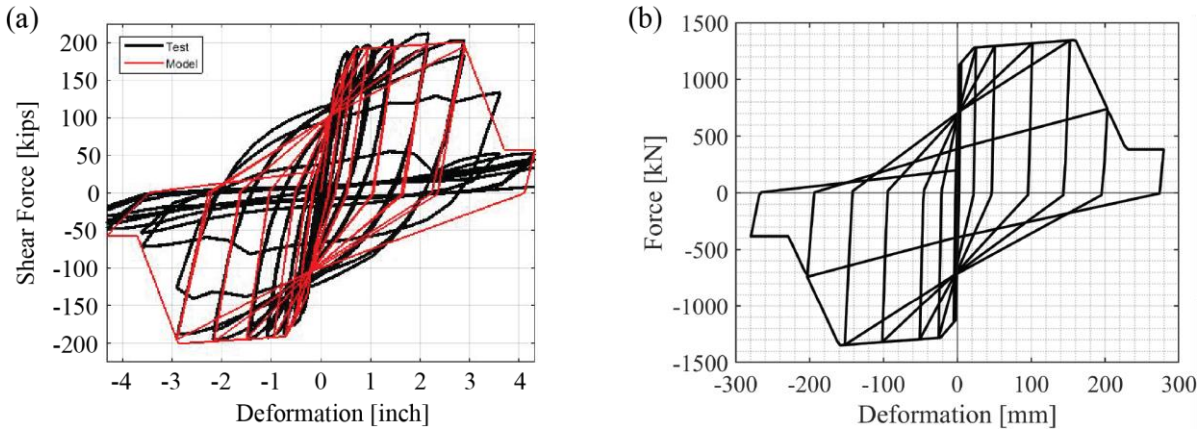

Figure 2-20: (a) Coupling beam modeling approach validation done by the reference report [55], and (b) Force-deformation response of the Pinching4 used on the first floor of the eighteen-story core wall building model.

Table 2-17 lists the calibrated parameters of the Pinching4 material model from the reference report [55]. The four deformations are functions of the length of the coupling beam ($L = l_n$). The four force values are functions of the beam shear strength (FY). FU is computed as $FU = 1.4FY$, where factor 1.4 accounts for the shear overstrength of the post-tensioned slab. For comparison, the overstrength factor is 1.1 for beams without a slab and 1.3 for a reinforced concrete slab.

Table 2-17: Pinching4 material parameters [55]

k	FU	Point 1	Point 2	Point 3	Point 4	rForceP
0.15	1.4*FY	(0.001*L, FY)	(0.01*L, FU)	(0.07*L, 1.05*FU)	(0.1*L, 0.3*FU)	0.55
rDisP	uForceP	gammaK 1	gammaK 2	gammaK 3	gammaK 4	gammaK Limit
0.05	0.01	0.5	0.45	0.4	0.35	1.0

FY is calculated as $2A_{vd} * f_y * sin\alpha$ according to the reference report [55], which is also denoted as the coupling beam shear strength ($V_n = 2A_{vd}f_y \sin\alpha$) in ACI 318-19, § 18.10.7.4 [3], where A_{vd} is the area of all steel rebars in one diagonal reinforcement and α is the angle defining the orientation of reinforcement.

$d_{tr} = 0.625\ in = 15.9\ mm$, $d_{spacing} = 8\ in = 203.2\ mm$, $d_{cover} = 1.5\ in = 38.1\ mm$

$$approx.\alpha\ =\ atan\left(\frac{h}{l_n}\right) =\ atan\left(\frac{30\text{ inch}}{90\text{ inch}}\right) =\ 0.3218 = 18.4\ degree$$

$$h_{end} = \left(\frac{d_{spacing} - d_b}{2\cos\left(approx.a\right)}\right) + \frac{d_b}{\cos(approx.\alpha)} + d_{tr} + d_{cover}$$

$$h_{cen} = h - 2\ h_{end}$$

$$\alpha = \text{atan}(h_{cen}/l_n)$$

$$FY = 2A_{vd}\ f_y \sin(\alpha)$$

$$MY = 2A_{vd}\ f_y \cos(\alpha)\ h_{cen} \quad \text{or} \quad MY = FY\ (l_n/2)$$

Figure 2-21 shows the calculation of the beam shear strength (FY). In the figure, $approx.\alpha$ is the approximation of the angle α, $d_b = 1.128\ in$ is the diameter of the diagonal bars, $d_{tr} = 0.625\ in$ is the diameter of the transverse reinforcement in the diagonal coupling beam, $d_{cover} = 1.5\ in$ is the thickness of the cover concrete, and $d_{spacing} = 8\ in$ is the spacing of the row 1 and the row 2 within the diagonal reinforcement.

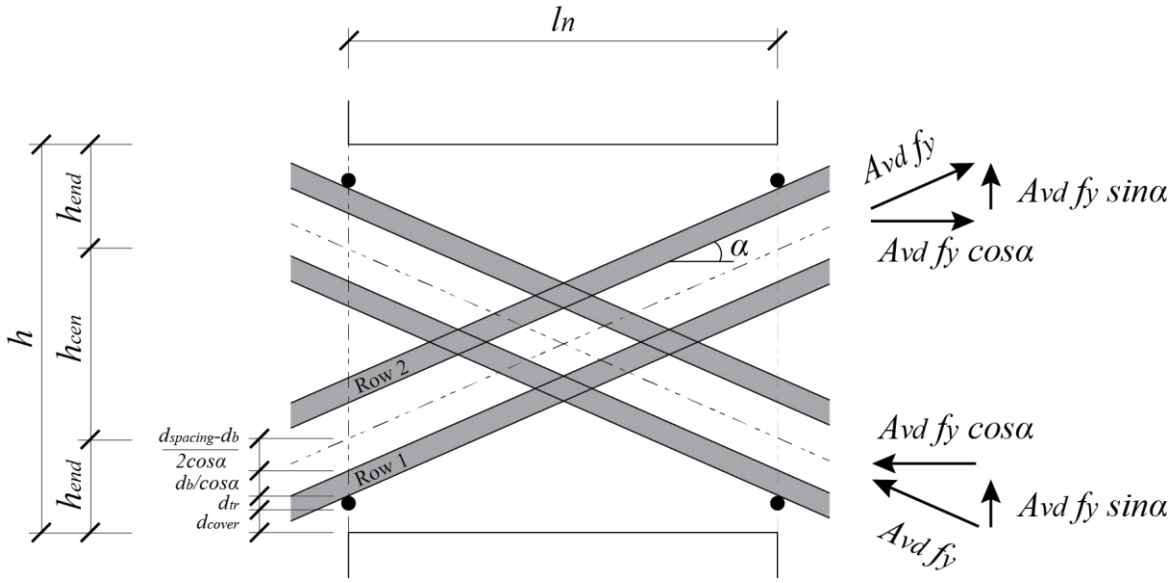

Figure 2-21: Calculation of *FY*

Table 2-18 lists the beam shear strength (*FY*) and the values of the parameters used in calculating the *FY*. Table 2-19 lists the force and displacement values used for the four points in the Pinching4 material at all floor levels. Figure 2-20(b) shows the force-deformation hysteretic response of Pinching4 on the first floor of the eighteen-story building model.

Table 2-18: Calculation of FY

Floor Number	Diagonal Bars	A_{vd}	$approx.\alpha$	α	FY		MY	
-	-	$[inch^2]$	[rad]	[rad]	[kips]	[kN]	[kip-in]	[kN-m]
18	6#8	4.74	0.32	0.21	121	539	5,458	617
17	6#8	4.74	0.32	0.21	121	539	5,458	617
16	6#9	6.00	0.32	0.21	152	674	6,818	770
15	6#9	6.00	0.32	0.21	152	674	6,818	770
14	6#10	7.62	0.32	0.21	190	843	8,531	964
13	6#10	7.62	0.32	0.21	190	843	8,531	964
12	6#10	7.62	0.32	0.21	190	843	8,531	964
11	6#10	7.62	0.32	0.21	190	843	8,531	964
10	6#10	7.62	0.32	0.21	190	843	8,531	964
9	6#10	7.62	0.32	0.21	190	843	8,531	964
8	6#11	9.36	0.32	0.21	229	1,020	10,323	1,166
7	6#11	9.36	0.32	0.21	229	1,020	10,323	1,166
6	6#11	9.36	0.32	0.21	229	1,020	10,323	1,166
5	8#10	10.16	0.32	0.21	253	1,124	11,374	1,285
4	8#10	10.16	0.32	0.21	253	1,124	11,374	1,285
3	8#10	10.16	0.32	0.21	253	1,124	11,374	1,285
2	8#10	10.16	0.32	0.21	253	1,124	11,374	1,285
1	8#10	10.16	0.32	0.21	253	1,124	11,374	1,285

Table 2-19: Four points of the Pinching4 material model used in the eighteen-story building model

Floor	*FY*	*FU*	Point 1		Point 2		Point 3		Point 4	
			Def.	Force	Def.	Force	Def.	Force	Def.	Force
			0.001*L	FY	0.010*L	FU	0.070*L	1.05*FU	0.100*L	0.3*FU
[-]	[kN] ([kip])	[kN] ([kip])	[mm] ([in])	[kN] ([kip])	[mm] ([in])	[kN] ([kip])	[mm] ([in])	[kN] ([kip])	[mm] ([in])	[kN] ([kip])
18	539 (121)	615 (138)	2.3 (0.09)	539 (121)	22.9 (0.9)	615 (138)	160.0 (6.3)	646 (145)	228.6 (9)	185 (41)
17	539 (121)	615 (138)	2.3 (0.09)	539 (121)	22.9 (0.9)	615 (138)	160.0 (6.3)	646 (145)	228.6 (9)	185 (41)
16	674 (152)	768 (173)	2.3 (0.09)	674 (152)	22.9 (0.9)	768 (173)	160.0 (6.3)	807 (181)	228.6 (9)	230 (52)
15	674 (152)	768 (173)	2.3 (0.09)	674 (152)	22.9 (0.9)	768 (173)	160.0 (6.3)	807 (181)	228.6 (9)	230 (52)
14	843 (190)	961 (216)	2.3 (0.09)	843 (190)	22.9 (0.9)	961 (216)	160.0 (6.3)	1009 (227)	228.6 (9)	288 (65)
13	843 (190)	961 (216)	2.3 (0.09)	843 (190)	22.9 (0.9)	961 (216)	160.0 (6.3)	1009 (227)	228.6 (9)	288 (65)
12	843 (190)	961 (216)	2.3 (0.09)	843 (190)	22.9 (0.9)	961 (216)	160.0 (6.3)	1009 (227)	228.6 (9)	288 (65)
11	843 (190)	961 (216)	2.3 (0.09)	843 (190)	22.9 (0.9)	961 (216)	160.0 (6.3)	1009 (227)	228.6 (9)	288 (65)
10	843 (190)	961 (216)	2.3 (0.09)	843 (190)	22.9 (0.9)	961 (216)	160.0 (6.3)	1009 (227)	228.6 (9)	288 (65)
9	843 (190)	961 (216)	2.3 (0.09)	843 (190)	22.9 (0.9)	961 (216)	160.0 (6.3)	1009 (227)	228.6 (9)	288 (65)
8	1020 (229)	1163 (262)	2.3 (0.09)	1020 (229)	22.9 (0.9)	1163 (262)	160.0 (6.3)	1221 (275)	228.6 (9)	349 (78)
7	1020 (229)	1163 (262)	2.3 (0.09)	1020 (229)	22.9 (0.9)	1163 (262)	160.0 (6.3)	1221 (275)	228.6 (9)	349 (78)
6	1020(229)	1163 (262)	2.3 (0.09)	1020 (229)	22.9 (0.9)	1163 (262)	160.0 (6.3)	1221 (275)	228.6 (9)	349 (78)
5	1124 (253)	1282 (288)	2.3 (0.09)	1124 (253)	22.9 (0.9)	1282 (288)	160.0 (6.3)	1346 (303)	228.6 (9)	385 (86)
4	1124 (253)	1282 (288)	2.3 (0.09)	1124 (253)	22.9 (0.9)	1282 (288)	160.0 (6.3)	1346 (303)	228.6 (9)	385 (86)
3	1124 (253)	1282 (288)	2.3 (0.09)	1124 (253)	22.9 (0.9)	1282 (288)	160.0 (6.3)	1346 (303)	228.6 (9)	385 (86)
2	1124 (253)	1282 (288)	2.3 (0.09)	1124 (253)	22.9 (0.9)	1282 (288)	160.0 (6.3)	1346 (303)	228.6 (9)	385 (86)
1	1124 (253)	1282 (288)	2.3 (0.09)	1124 (253)	22.9 (0.9)	1282 (288)	160.0 (6.3)	1346 (303)	228.6 (9)	385 (86)

2.7 Seismic mass

Seismic mass is calculated as 1.05DL + 0.25LL according to FEMA P695 [69], where DL is the nominal dead load and LL is the nominal live load. The nominal dead loads and the nominal live loads of the eighteen-story building are calculated based on Table 2-20 from the reference report [55]. Also, the weight of the core wall piers and the lean-on columns are not included in Table 2-20.

Table 2-20: Dead load and live load applied to the building model

	Dead load		Live load	
Outside the core	slab self-weight	4.79 kN/m^2 (100 psf)	floor live load (Residential buildings, for CB ln/h <=3.0)	1.92 kN/m^2 (40 psf)
	superimposed dead load including perimeter and partition loading	1.20 kN/m^2 (25 psf)	floor live load (Roof per ASCE7-16 Table 4-1)	0.96 kN/m^2 (20 psf)
	total	5.99 kN/m^2 (125 psf)		
Inside the core	slab self-weight	4.79 kN/m^2 (100 psf)	floor live load	4.79 kN/m^2 (100 psf)

The seismic mass inside the core of each floor is equally divided and applied at the top node of the four wall elements on each floor. Similarly, the seismic mass outside the core of each floor is equally divided and applied at the top node of the four lean-on column elements on each floor.

2.8 Diaphragm

The eighteen-story building model has two diaphragms in this building model: the SFRS diaphragms representing the slabs inside the core and the GLRS diaphragms representing the slabs outside the core. Figure 2-22 shows the configuration of the SFRS diaphragm, the GLRS diaphragm, and the combined configuration of the two diaphragms on a typical floor. The two top configurations show the SFRS diaphragm and the GLRS diaphragm, which are two separate systems and have relative motions. The bottom configuration demonstrates how the two diaphragms are connected by either monolithic connections or force-limiting connections.

The SFRS diaphragm, which represents the slab inside the core, consists of four SFRS diaphragm beams that connect the four wall pier elements. On the top of each wall pier element is a lumped mass that accounts for one-quarter of the inside core mass on each floor. The wall pier elements are located at the geometric center of each L-shaped wall section.

The GLRS diaphragm, which represents the slab outside the core, consists of four GLRS diaphragm beams that connect the four lean-on column elements. On the top of each lean-on column element is a lumped mass that accounts for one-quarter of the outside slab on each floor. The lean-on column elements are located at the center of mass of the quarter of the outside slab instead of the geometric center of three actual lean-on columns. The reason for this location is that, since the GLRS diaphragm is flexible in out-of-plane, the moment of inertia of the lean-on column element equals three times that of the actual lean-on columns. It implies that the location of the lean-on column does not significantly impact the lateral stiffness of the lean-on column element. Also, the lean-on columns have relatively small lateral stiffness compared to the wall piers.

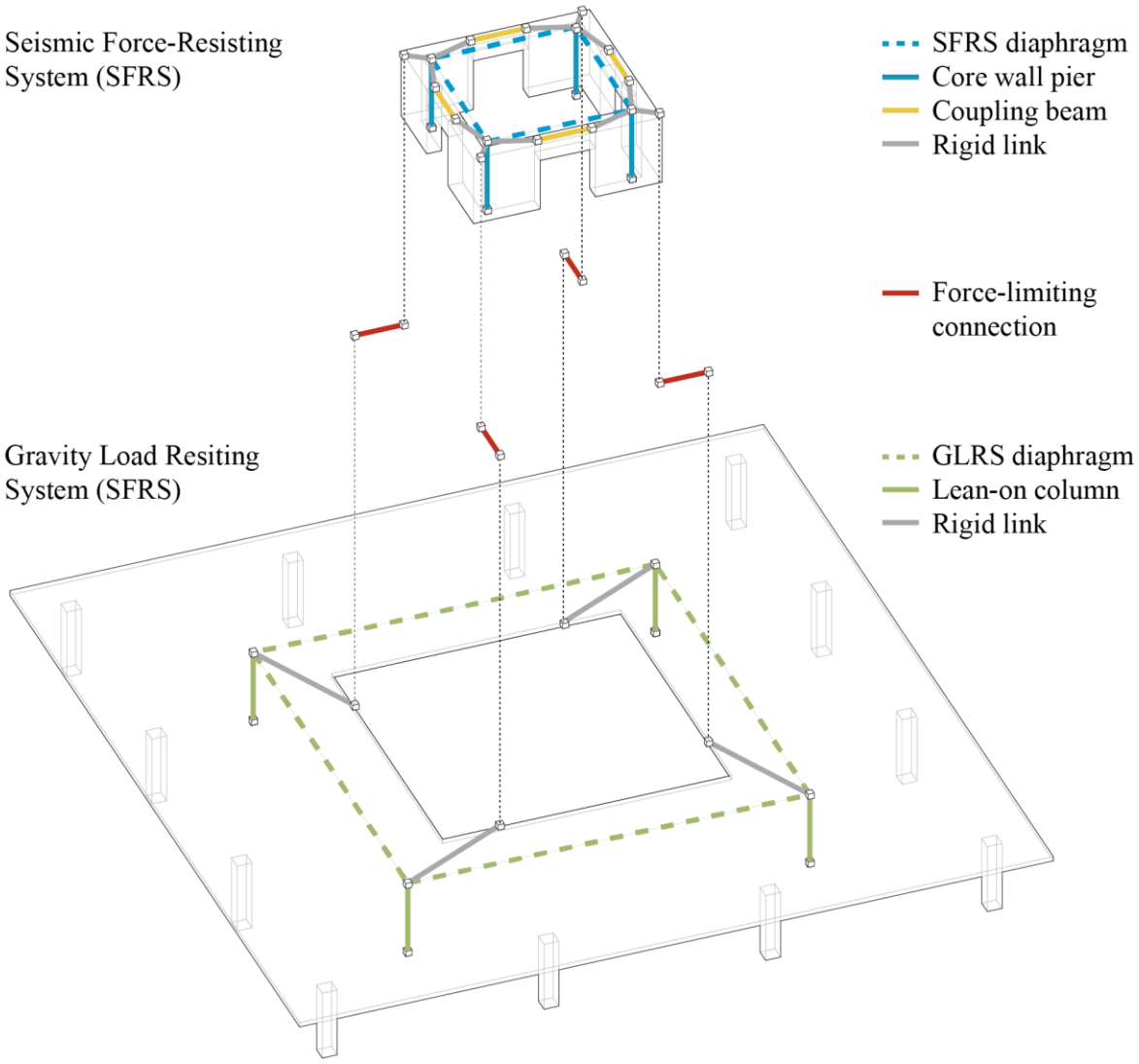

Figure 2-22: Force-limiting connections connecting the SFRS and GLRS diaphragms

The SFRS diaphragm and the GLRS diaphragm both have high in-plane flexural stiffness and low out-of-plane flexural stiffness to represent the slabs. The nodes connected by the beams move as a rigid body in in-plane motion, and they are free to deform in out-of-plane motion.

The difference between the SFRS diaphragm and GLRS diaphragm is that the SFRS diaphragm beams allow axial deformation between the walls, whereas the GLRS diaphragm beams do not, as shown in Figure 2-23. The GLRS diaphragm, having high axial stiffness, acts

the same as a rigid diaphragm and does not allow axial deformation between the columns. On the other hand, the SFRS diaphragm inside the core has low axial stiffness to represent the voids in the core and ensure the axial load transfer through the coupling beams. If the SFRS diaphragm beams are axially rigid as the GLRS diaphragm beams, the force from one wall pier to another will be transferred through the SFRS diaphragm beams and not through the coupling beams. In reality, the axial stiffness of the floor inside the core will be somewhere between the axial stiffness of the GLRS diaphragm beam and the SFRS diaphragm beams.

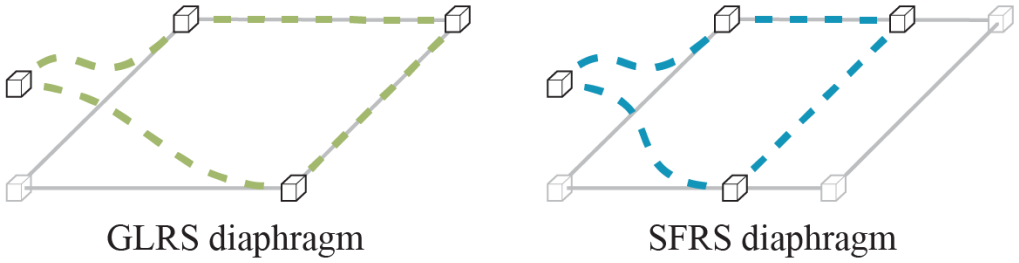

Figure 2-23: Difference between a GLRS diaphragm and SFRS diaphragm

2.9 Modal Analysis

Modal analysis is used to quantify the dynamic properties of the eighteen-story building model. The modal analysis results in this study are compared with the modal analysis results published in the reference report [55]. The modal analysis assumes the building model to be at its initial linearly elastic state. The modal analysis results will be used to compute the parameters required for the damping model discussed in section 2.10. The modal analysis was performed using core wall pier linear elastic beam-column elements with effective stiffness that accounts for the cracking of concrete.

Figure 2-24 shows the deflected shapes of the dynamic modes of vibration of the eighteen-story building model. The gray lines represent the undeformed shape, and the black lines represent the mode shapes. Mode 1 is the first rotational mode, mode 2 is the first translational mode with motion primarily in the global Y direction, and mode 3 is the first translational mode with motion primarily in the global X direction. Mode 4 is the second rotational mode, Mode 5 is the second translational mode with motion primarily in the global Y direction, and mode 6 is the second translational mode with motion primarily in the global X direction.

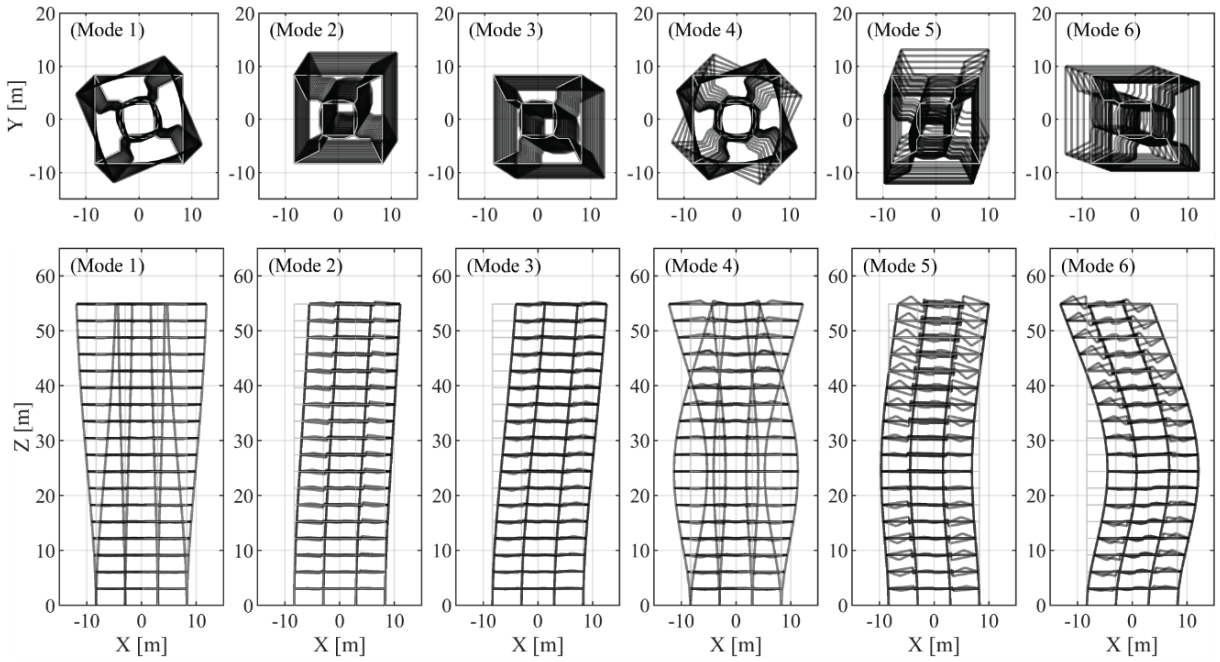

Figure 2-24: Mode shapes of the eighteen-story core wall building model

Table 2-21 shows the results from the eigenvalue analysis, including the natural periods of each mode. Eigenvalue analysis is finding solutions for the equation of motion, $[M]\{\ddot{u}\} + [K]\{u\} = \{0\}$, where $[M]$ is the mass matrix, $[K]$ is the stiffness matrix, $\{\ddot{u}\}$ is the acceleration vector, $\{u\}$ is the displacement vector, and $\{0\}$ is the zero vector. Having $\{u(t)\} = e^{i\omega_n t}\{\phi_n\}$ as

the solution, the equation of motion can be written as $e^{i\omega_n t}(-\omega_n^2[M]\{\phi_n\} + [K]\{\phi_n\}) = \{0\}$, where ω_n is the natural circular frequency, and ϕ_n is the mode shape. Then, because $e^{i\omega_n t} \neq 0$, the equation can be further simplified as $([K] - \omega_n^2[M])\{\phi_n\} = \{0\}$, which is an algebraic eigenvalue problem with eigenvalues being ω_n^2 and eigenvectors being ϕ_n as solutions.

Table 2-22 shows the modal participation mass ratios and the cumulative modal participation ratios. Mode 1 is considered as the fundamental mode with a period of 3.18 seconds which is a torsional mode because the rotational mode along the global Z axis has the largest modal participation mass ratio. Mode 2 and mode 3 are considered as the first translational modes in the global Y direction and X direction, respectively, with a period of 2.06 seconds. This is because mode 2 has the largest modal participation mass ratio in the translational global Y direction and mode 3 has the largest modal participation mass ratio in the translational global X direction. Larger modal participation mass ratio indicates a larger contribution of the motion in the corresponding direction to the total motion of the building model.

The fundamental mode being a rotational mode indicates that the structure is more likely to have a rotational response than a translational response. And the two first translational modes (i.e., mode 2 and mode 3) having the same modal participation mass ratios in orthogonal direction indicates that the structure is systematic in global X and global Y direction. Similar modal analysis results were presented in the reference report by Tauberg et al. [55].

Table 2-21: Modal analysis results – Eigenvalue analysis

Mode	Eigenvalue Analysis				Main Direction(s) of Modal Participation Mass Ratios
	Lambda ($\lambda = \omega_n^2$)	Natural circular frequency (ω_n) [$Hz = rad/sec$]	Natural frequency ($f_n = \omega_n/2\pi$) [$1/sec$]	Natural period ($T_n = 1/f_n$) [sec]	
1	3.91	1.98	0.31	3.18	RZ
2	9.29	3.05	0.49	2.06	Y + RX
3	9.29	3.05	0.49	2.06	X + RY
4	43.37	6.59	1.05	0.95	RZ
5	135.34	11.63	1.85	0.54	RX + Y
6	135.34	11.63	1.85	0.54	RY + X
7	183.58	13.55	2.16	0.46	RZ
8	546.84	23.38	3.72	0.27	RZ
9	675.79	26.00	4.14	0.24	RX + Y
10	675.79	26.00	4.14	0.24	RY + X
11	1264.05	35.55	5.66	0.18	RZ
12	2106.64	45.90	7.30	0.14	RX + Y
13	2106.64	45.90	7.30	0.14	RY + X
14	2402.84	49.02	7.80	0.13	RZ
15	3956.06	62.90	10.01	0.10	RZ

Table 2-22: Modal analysis results – Modal participation mass ratios (%) and cumulative modal participation mass ratios (%)

Mode	Modal Participation Mass Ratios (%)						Cumulative Modal Participation Mass Ratios (%)					
	X	Y	Z	RX	RY	RZ	X	Y	Z	RX	RY	RZ
1	0.00	0.00	0.00	0.00	0.00	**71.42**	0.00	0.00	0.00	0.00	0.00	71.42
2	19.97	**47.60**	0.00	**19.96**	8.37	0.00	19.97	**47.60**	0.00	19.96	8.37	71.42
3	**47.60**	19.97	0.00	8.37	**19.96**	0.00	**67.57**	67.57	0.00	28.33	28.33	71.42
4	0.00	0.00	0.00	0.00	0.00	**12.47**	67.57	67.57	0.00	28.33	28.33	83.89
5	1.78	**14.01**	0.00	**28.05**	3.57	0.00	69.36	**81.58**	0.00	56.38	31.90	83.89
6	**14.01**	1.78	0.00	3.57	**28.05**	0.00	**83.37**	83.37	0.00	59.95	59.95	83.89
7	0.00	0.00	0.00	0.00	0.00	**5.53**	83.37	83.37	0.00	59.95	59.95	89.43
8	0.00	0.00	0.00	0.00	0.00	**3.20**	83.37	83.37	0.00	59.95	59.95	92.63
9	1.80	**3.82**	0.00	**7.18**	3.39	0.00	85.17	**87.18**	0.00	67.13	63.34	92.63
10	**3.82**	1.80	0.00	3.39	**7.18**	0.00	**88.99**	88.99	0.00	70.51	70.51	92.63
11	0.00	0.00	0.00	0.00	0.00	2.11	88.99	88.99	0.00	70.51	70.51	94.74
12	1.23	**2.00**	0.00	**4.89**	3.01	0.00	90.22	**90.99**	0.00	75.40	73.52	94.74
13	**2.00**	1.23	0.00	3.01	**4.89**	0.00	**92.22**	92.22	0.00	78.41	78.41	94.74
14	0.00	0.00	0.00	0.00	0.00	**1.48**	92.22	92.22	0.00	78.41	78.41	96.22
15	0.00	0.00	0.00	0.00	0.00	**0.98**	92.22	92.22	0.00	78.41	78.41	97.20

2.10 Damping

The Rayleigh damping model is used for the time history analysis of the eighteen-story building model. The advantage of the Rayleigh damping model is the convenience of calculation since it is a linear combination of the stiffness and mass matrices which are usually banded.

2.10.1 Critical damping

Critical damping ($\zeta_{critical}$) is calculated as recommended in the LATBSDC 2020 [70], where H is the height of the roof in feet.

$$H = 10\,ft * 18\,stories = 180\,ft.$$

$$0.025 \leq \zeta_{critical} = 0.36/\sqrt{H} = 0.36/\sqrt{180} = 0.0268 \leq 0.05$$

$$\therefore \zeta_{critical} = 0.0268$$

2.10.2 Two circular frequencies, ω_1 and ω_2

Rayleigh damping specifies the critical damping ratio to the two periods that can represent the period of the structure. The two periods are $0.2T_1$ and $1.5T_1$(NEHRP 2010) [50], where T_1 is the fundamental period of the structure. $0.2T_1$ represents the period of the higher mode of the structure assumed to be linearly elastic. $1.5T_1$ represents the elongated period of the damaged structure with reduced stiffness. The fundamental period of the structure (T_1) in the calculation uses the first translational period as the reference report [55]. The periods (T) and circular frequencies $\left(\omega = \frac{2\pi}{T}\right)$ of the two modes are shown below.

$$T_1 = 2.06\ [sec]$$

$$T_m = 0.2T_1 = 0.4120\ [sec], \qquad T_n = 1.5T_1 = 3.0900\ [sec]$$

$$\therefore \omega_m = \frac{2\pi}{T_m} = 15.2504\ [rad], \qquad \omega_n = \frac{2\pi}{T_n} = 2.0334\ [rad]$$

2.10.3 Damping coefficients, α and β

The mass-proportional Rayleigh damping coefficient (α) and the stiffness-proportional Rayleigh damping coefficient (β) for the Rayleigh damping model are determined below.

$$\begin{bmatrix}\zeta_m\\ \zeta_n\end{bmatrix} = \frac{1}{2}\begin{bmatrix}\frac{1}{\omega_m} & \omega_m\\ \frac{1}{\omega_n} & \omega_n\end{bmatrix}\begin{bmatrix}\alpha\\ \beta\end{bmatrix}$$

$$\begin{bmatrix}\alpha\\ \beta\end{bmatrix} = 2\begin{bmatrix}\frac{1}{\omega_m} & \omega_m\\ \frac{1}{\omega_n} & \omega_n\end{bmatrix}^{-1}\begin{bmatrix}\zeta_m\\ \zeta_n\end{bmatrix}$$

$$\begin{bmatrix}\alpha\\ \beta\end{bmatrix} = 2\frac{\omega_m\omega_n}{(\omega_n^2-\omega_m^2)}\begin{bmatrix}\omega_n & -\omega_m\\ -\frac{1}{\omega_n} & \frac{1}{\omega_m}\end{bmatrix}\begin{bmatrix}\zeta_m\\ \zeta_n\end{bmatrix}$$

Because $\zeta_m = \zeta_n = \zeta_{critical}$,

$$\therefore \begin{bmatrix}\alpha\\ \beta\end{bmatrix} = 2\frac{\zeta_{critical}}{(\omega_m+\omega_n)}\begin{bmatrix}\omega_m\omega_n\\ 1\end{bmatrix} = \begin{bmatrix}0.0963\frac{1}{\text{sec}}\\ 0.0031\ \text{sec}\end{bmatrix} \quad \text{2-10}$$

In Opensees, the damping model is expressed using the following equation: $D = \alpha M + \beta_{current}K_{current} + \beta_{initial}K_{initial} + \beta_{commit}K_{commit}$, where $K_{current}$, $K_{initial}$, and K_{commit} are the current, initial, and committed stiffness matrix, respectively, and $\beta_{current}$, $\beta_{initial}$, and β_{commit} are the stiffness proportional Rayleigh damping coefficient for the current, initial, and committed stiffness matrix, respectively. The β calculated is set as $\beta_{current}$. The stiffness matrix of the structure (K) gets updated at every time step. But the Rayleigh damping coefficients α and β do not change over time step which means the fundamental period (T_1) does not get updated during the time-history analysis and remains constant from the beginning of the analysis.

2.10.4 Damping ratio

The damping ratio (ζ) is a function of frequencies (or period) of the structure, where $\left(\frac{\alpha}{2}\frac{1}{\omega}\right)$ is the mass-proportional damping and $\left(\frac{\beta}{2}\omega\right)$ is the stiffness-proportional damping. Figure 2-25 shows the damping ratio.

$$\zeta = \frac{\alpha}{2}\frac{1}{\omega} + \frac{\beta}{2}\omega = \frac{0.0963}{2\omega} + \frac{0.0031}{2}\omega \quad \text{2-11}$$

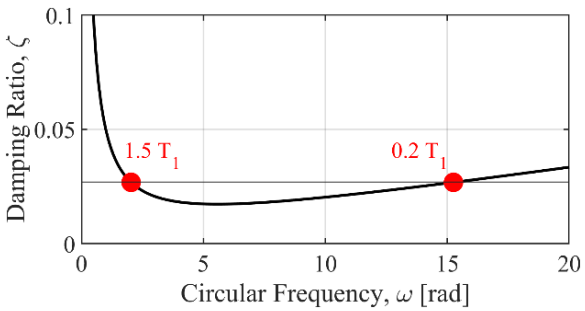

Figure 2-25: Damping ratio model

2.11 Force-limiting connections

2.11.1 Calculation of F_{Lx}

Tsampras and Sause [53] proposed a force-based method to design force-limiting connections. This section briefly describes this method. F_{Lx} is the design limiting force at a given floor *x*, which is the target force value at which the connection response transitions from linear-elastic to post-elastic. F_{Lx} for $n \geq 3$ are shown in Equation 2-12 and in Figure 2-26, where n is the total number of stories of a structure.

$$F_{Lx} = \frac{C_{Lx}}{R_{DC}}\frac{w_{px}}{n_{Lx}} \quad \text{2-12}$$

$$C_{Lo} = 0.4 S_{DS} I_e \quad \text{2-13}$$

$$C_{Ln} = \sqrt{(\Gamma_{m1} C_s)^2 + (\Gamma_{m2} C_{s2})^2} \quad \text{2-14}$$

C_{Lx} is the design acceleration coefficient at level x, C_{Ln} is the design acceleration coefficient at level n, and C_{Lo} is the design acceleration coefficient at the base of the building. R_{DC} is the force-limiting connection design force reduction factor that accounts for the

deformation capacity of the force-limiting connection, w_{px} is the seismic weight tributary to the diaphragm at level x, and n_{Lx} is the number of force-limiting connections at level x. S_{DS} is the design spectral acceleration at short periods, and I_e is the importance factor. Γ_{m1} is the first mode contribution factor, C_s is the seismic response coefficient, Γ_{m2} is the second mode contribution factor, and C_{s2} is the higher mode seismic response coefficient. $V_{bF_{Lx}}$ is the base shear in the SFRS, and $M_{bF_{Lx}}$ is the base moment in the SFRS.

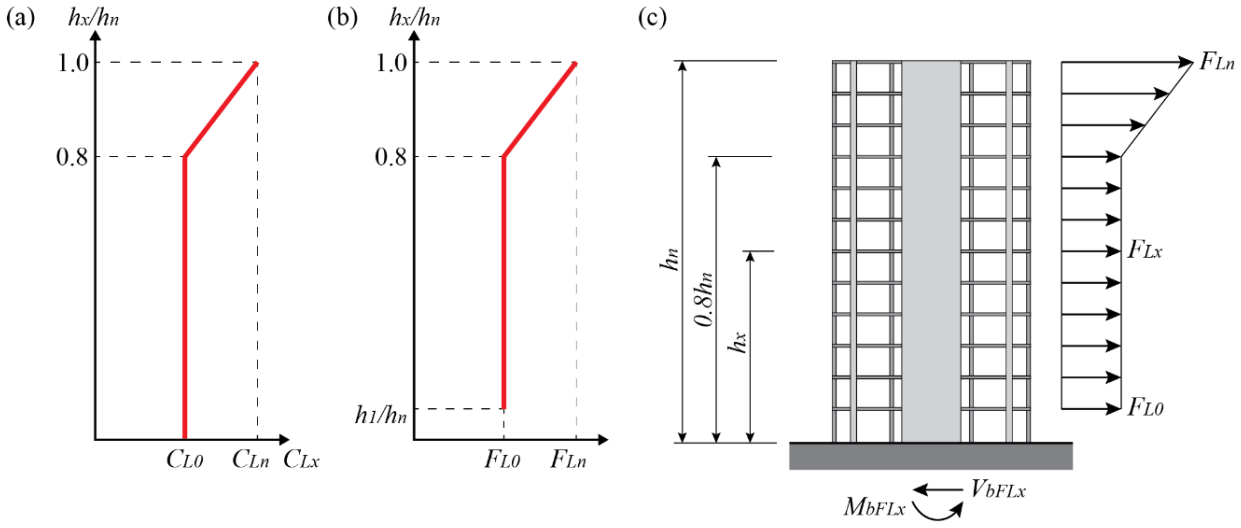

Figure 2-26: (a) Acceleration coefficient C_{Lx}; (b) force-limiting connection design forces F_{Lx}; and (c) SFRS free-body diagram subjected to connection design force F_{Lx}. (image reference: [53])

Table 2-23 shows the design limiting force at a given floor *x* (F_{Lx}) for one force-limiting connection at each floor calculated with five different R_{DC} values. Figure 2-27 shows the limiting forces along the height with five different R_{DC} values. It is observed that F_{Lx} is constant from the first floor to the 14th floor and increases from the 14th to the 18th floor. Also, it can be observed that a higher R_{DC} value results in smaller F_{Lx} values.

Table 2-23: Design limiting force at a given floor *x*, F_{Lx}

Floors	Design limiting force at a given floor *x* (F_{Lx})									
	R_{DC} = 1.0		R_{DC} = 1.5		R_{DC} = 2.0		R_{DC} = 2.5		R_{DC} = 3.0	
	$[kN]$	$[kips]$	$[kN]$	$[kips]$	$[kN]$	$[kips]$	$[kN]$	$[kips]$	$[kN]$	$[kips]$
18	1894	426	1263	284	947	213	757	170	693	156
17	1624	365	1081	243	812	183	649	146	586	132
16	1354	304	9.3	203	677	152	541	122	479	108
15	1084	244	721	162	542	122	434	97	372	84
14	922	207	614	138	461	104	369	83	307	69
13	922	207	614	138	461	104	369	83	307	69
12	922	207	614	138	461	104	369	83	307	69
11	922	207	614	138	461	104	369	83	307	69
10	922	207	614	138	461	104	369	83	307	69
9	922	207	614	138	461	104	369	83	307	69
8	922	207	614	138	461	104	369	83	307	69
7	922	207	614	138	461	104	369	83	307	69
6	922	207	614	138	461	104	369	83	307	69
5	922	207	614	138	461	104	369	83	307	69
4	922	207	614	138	461	104	369	83	307	69
3	922	207	614	138	461	104	369	83	307	69
2	922	207	614	138	461	104	369	83	307	69
1	922	207	614	138	461	104	369	83	307	69

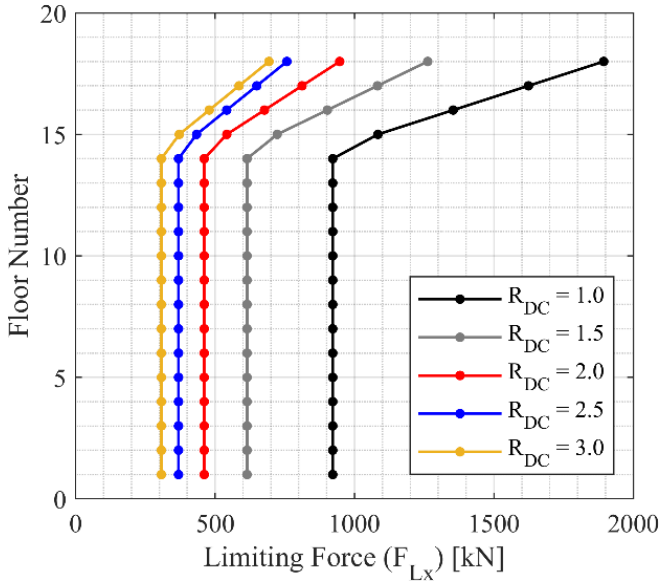

Figure 2-27: Limiting force at a given floor, F_{Lx}, with five different R_{DC} values

2.11.2 Force-limiting connection types

Four types of connection between the GLRS and the SFRS are considered in this study: 1) the RE connection, 2) the FD connection, 3) the FD+RB connection, and 4) the Modified FD connection. The RE connection represents the monolithic connection between the GLRS and the SFRS. The FD connection, the FD+RB connection, and the Modified FD connection are force-limiting connections with different force-displacement responses.

All four types of connections are modeled using the corotational truss element with different force-displacement responses in Opensees, as shown in Figure 2-28. The design limiting force at a given floor x (F_{Lx}) is the same for all three force-limiting connection types. The difference between the three types is how the post-elastic response is modeled.

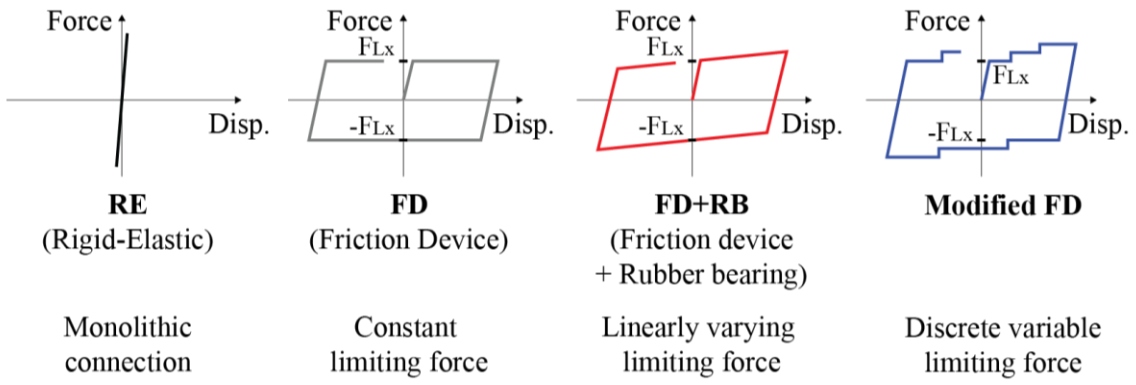

Figure 2-28: Force-displacement relationship of the four different connection types between the GLRS and the SFRS

The RE connection assumes rigid elastic connections to simulate the monolithic connections between the GLRS and the SFRS. RE is an acronym for Rigid-Elastic. The RE connection is modeled in Opensees as a corotational truss with an area of $A_{truss} = 10^{12}\ in^2 = 645.16 * 10^{12}\ mm$ and an elastic material with the modulus of elasticity $E = 1\ ksi = 6.89\ MPa$.

The FD connection has a constant limiting force with zero post-elastic stiffness after reaching the design limiting force at a given floor *x* (F_{Lx}). FD is an acronym for Friction Device. The FD connection is modeled in Opensees as a corotational truss with an area of $A_{one} = 1\ in^2 = 645\ mm$ and a Steel01 material with $F_y = F_{Lx}, E = K_{fr} * L_{truss}/A_{one},\ b = 0.000001$, representing the friction mechanism. E is a modulus of elasticity of a pseudo material, L_{truss} is the length of the force-limiting connection, and b is a parameter used to define the post-elastic stiffness, bE. The value 0.000001 for b is used as a very small value to simulate the zero post-elastic stiffness of the friction device. The stiffness of the friction device $K_{fr} = 8{,}000\ kip/in = 1{,}401{,}014\ kN/m$ is an approximate value of the calculated stiffness of springs in series, $K_{fr} = 1/K_{friction} + 1/K_{clevis1} + 1/K_{clevis2} = 8{,}169\ kip/in = 1{,}430{,}611\ kN/m$. A smaller value was chosen for the approximation to account for other unconsidered sources of flexibility. $K_{friction} =$

$9{,}500\ kip/in = 1{,}663{,}705\ kN/m$ is the stiffness of the friction from preliminary numerical simulation results. $K_{clevis1} = 130{,}500\ kip/in = 22{,}854{,}046\ kN/m$ and $K_{clevis2} = 105{,}455\ kip/in = 18{,}467{,}996\ kN/m$ are the elastic stiffness of clevises that connects the friction device to the wall at both ends.

The FD+RB connection has a linearly varying limiting force (i.e., constant positive post-elastic stiffness) after reaching the design limiting force at a given floor *x* (F_{Lx}). RB is an acronym for Rubber Bearing. The FD+RB connection simulates a force-limiting connection with a friction device in parallel with a linear-elastic component that provides positive post-elastic stiffness. This positive post-elastic stiffness can be achieved with the low-damping rubber bearings in a planar wall structure. The FD+RB connection is modeled in Opensees as a corotational truss with an area of $A_{one} = 1\ in^2 = 645\ mm^2$ and a material that is two materials in parallel. The first material is the same Steel01 material used in the FD connection. The second material is an Elastic material with $E = K_{RB} * L_{truss}/A_{one}$ to simulate the constant positive post-elastic stiffness. K_{RB} is the stiffness of the rubber bearing, which is a parameter in this study that uses values of $K_{RB} = 22.5\ \ kip/in = 3{,}940\ kN/m$, $K_{RB} = 45.0\ \ kip/in = 7{,}880\ kN/m$, K_{RB} =67.5 $kip/in = 11{,}820\ kN/m$, and $K_{RB} = 90.0\ kip/in = 15{,}760\ kN/m$. In section 4, the FD+RB connection uses $K_{RB} = 22.5\ kip/in = 3{,}940\ kN/m$. In section 6, the FD+RB1 connection, the FD+RB2 connection, and the FD+RB3 connection represent FD+RB connections with $K_{RB} = 22.5\ kip/in = 3{,}940\ kN/m$, $K_{RB} = 45.0\ kip/in = 7{,}880\ kN/m$, and $K_{RB} = 67.5\ kip/in = 11{,}820\ kN/m$, respectively.

The Modified FD connection has a discrete variable limiting force. This is the type of force-limiting connection that could potentially be used on core wall buildings, as discussed in section 1.2.1, with a series of additional friction forces activated at different displacement levels

in the post-elastic region. The force-displacement response of the Modified FD connection can potentially reduce the post-elastic deformation demand in the force-limiting connection without the need for low-damping rubber bearings. Currently, the physical embodiment of the Modified FD connection is under development to achieve this type of force-displacement response. A prototype of the Modified FD connection has been developed [54] and is shown in Figure 2-29. The prototype of the Modified FD connection will be used to experimentally characterize the force-displacement response of this new type of friction-based force-limiting connection.

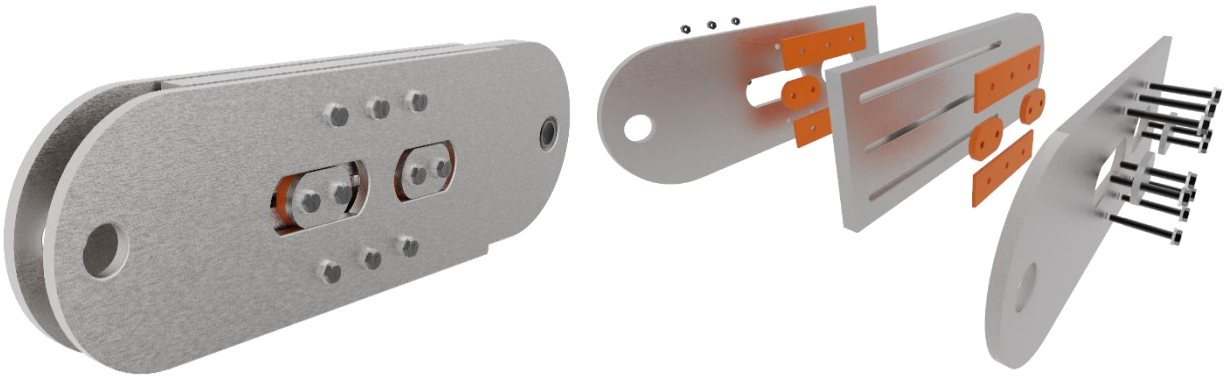

Figure 2-29: Assembled and exploded view of the prototype of the Modified FD connection [54]

The expected force-displacement response of the Modified FD connection is modeled in Opensees as a corotational truss with an area of $A_{one} = 1\ in^2 = 645\ mm^2$ and a material that is three materials in parallel, as shown in Figure 2-30. The first material is the same Steel01 material used in the FD connection. The second material is a Steel01 material with $F_y = F_1, E = K_{fr} * L_{truss}/A_{one},\ b = 0.000001$, representing the first additional friction force modeled to be activated at a deformation of D_1. To activate the force F_1 at displacements D_1, an Elastic Multilinear Uniaxial Material with a large stiffness relative to K_{fr} at displacement D_1/L_{truss} was added in series with the Steel01 Material. Similarly, the third material is a Steel01 material with

$F_y = F_2, E = K_{fr} * L_{truss}/A_{one}$, $b = 0.000001$, representing the second additional friction force modeled to be activated at a deformation of D_2. To activate the force F_2 at displacements D_2, an Elastic Multilinear Uniaxial Material with a large stiffness relative to K_{fr} at displacement D_2/L_{truss} was added in series with the Steel01 Material. The D_1 and D_2 values used in this thesis are 0.3 $inch$ and 2.5 $inch$, respectively.

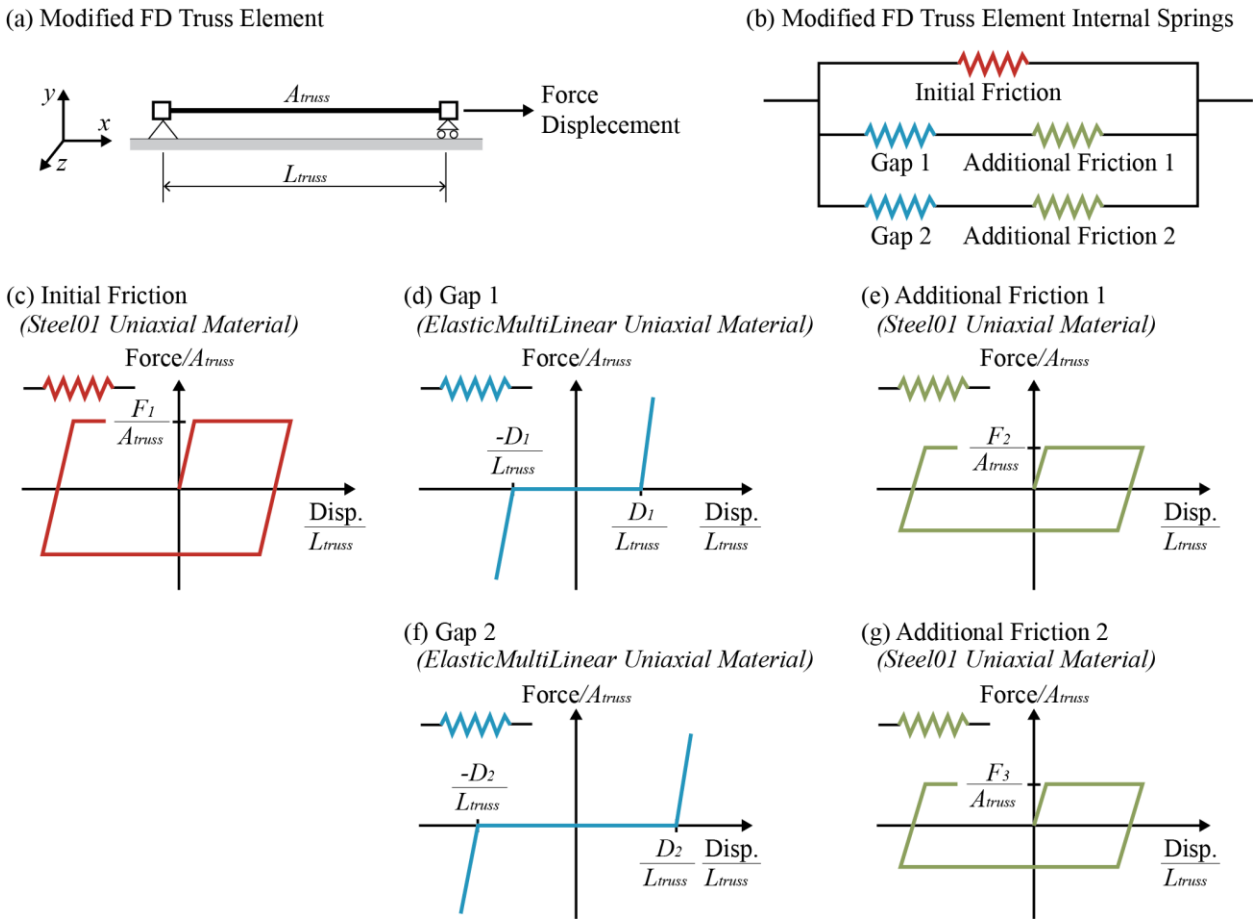

Figure 2-30: Opensees Modeling approach of Modified FD

2.12 Low-damage coupling beam

2.12.1 Design limiting moment of rotational friction connections

This section explains the calculation of the design limiting moment (M_L) of the rotational friction connections. The wall base is assumed to yield when the rotational friction moment of all low-damage coupling beams reaches the design limiting moment (M_L). Also, the design limiting moment (M_L) is assumed to be constant over the height of the building, meaning equal strength for all coupling beams at each floor level.

With equal strength assumed for all coupling beams at each floor level, the coupling beam shear force at floor x ($V_{CB,x}$) can be set as the coupling beam shear force at all floors (V_{CB}), and the coupling beam moment at floor x ($M_{CB,x}$) can be set as the coupling beam moment at all floors (M_{CB}). Then, the sum of the coupling beam shear force at all floors ($\sum_{x=1}^{n} V_{CB,x}$) can be set as nV_{CB}, where *n* is the number of stories.

Equation 2-17, simplified from Equation 2-15 (Repeated), shows the formula for the coupling beam shear force (V_{CB}). l_m is the sum of the length of the wall and the length of the coupling beam (i.e., $l_m = l_{w,L} + l_n = l_{w,T} + l_n$). With an equal length of the leading and trailing walls, l_m is also equal to the distance between the center of the two wall piers.

$$\text{Degree of coupling } (DoC) = \frac{\text{Overturning moment due to axial force couple at wall base}}{\text{Total overturning moment at wall base}}$$

$$DoC = \frac{M_C}{M_{OTM}} = \frac{M_C}{M_{u,L} + M_{u,T} + M_C}$$

$$= \frac{P_{u,L}(l_{w,L} + l_n) - P_{u,T}(l_{w,T} + l_n)}{P_{u,L}(l_{w,L} + l_{CB}) - P_{u,T}(l_{w,T} + l_{CB}) + 2(M_{u,L} + M_{u,T})} \quad \text{2-15 (Repeated)}$$

$$P_{u,L} = \sum_{x=1}^{n} W_x + \sum_{x=1}^{n} V_{CB,x} \ , \ P_{u,T} = \sum_{x=1}^{n} W_x - \sum_{x=1}^{n} V_{CB,x} \quad \text{2-16 (Repeated)}$$

$$V_{CB} = \frac{DoC * M_{OTM}}{n\, l_m} = \frac{DoC(M_{u,L} + M_{u,T})}{(1 - DoC)(n\, l_m)} \quad \text{2-17}$$

Based on statics, the shear force and the bending moment of the coupling beam have a relationship of $V_{CB,x} = 2M_{CB,x}/l_n$, and M_{CB} can be calculated from V_{CB}. Equation 2-18 shows the formula of the coupling beam moment at all stories (M_{CB}), which is equal to the design limiting moment (M_L). The base moment reaction of the leading and trailing wall ($M_{u,L}$ and $M_{u,T}$) is also equal to the moment capacity of each base wall section which is set as the nominal moment of the wall section ($M_{n,L}$ and $M_{n,T}$).

In this equation, the length of the coupling beam l_n, the lengths of the leading and trailing walls ($l_{w,L}$ and $l_{w,T}$), $l_m = l_{w,L} + l_n = l_{w,T} + l_n = (108 + 90)[in] = 5029[mm]$ and the number of stories n are known values. Therefore, with an assumed value of the degree of coupling (DoC), the nominal moments of the wall section ($M_{n,L}$ and $M_{n,T}$) are the only unknown values to calculate the design limiting moment (M_L).

$$M_L = M_{CB} = \frac{DoC\left(M_{u,L} + M_{u,T}\right)}{(1 - DoC)(n\, l_m)} * \frac{l_n}{2} = \frac{DoC\left(M_{n,L} + M_{n,,T}\right)}{(1 - DoC)(n\, l_m)} * \frac{l_n}{2} \qquad 2\text{-}18$$

The nominal moment of the wall section of the leading and trailing wall ($M_{n,L}$ and $M_{n,T}$) is computed. Nonlinear section analysis is performed in Opensees is performed to compute the relationship between the moment and the curvature for the cross-section of the wall piers at the base of the core wall. Figure 2-31 shows the model of (a) the trailing wall and (b) the leading wall. They are separate models, and each model consists of a zero-length element with a fiber section of the base wall section. For the trailing wall, as shown in Figure 2-31(a), the section of the L-shape wall is subjected to an increasing curvature along the local z-axis with an applied axial load, $P_{u,T}$, along the local-x direction. And the moment demand ($M_{u,T}$) of the section is computed as an output. Similarly, for the leading wall, as shown in Figure 2-31(b), the section of the L-shape wall is subjected to an increasing curvature along the local z-axis with an applied

axial load, $P_{u,L}$, along the local-x direction. And the moment demand ($M_{u,L}$) of the section is computed as an output. Then, a moment-curvature can be plotted using the curvature and the moment demand for each trailing wall and the leading wall, and the nominal moment of the wall section ($M_{n,L}$ and $M_{n,T}$) is identified.

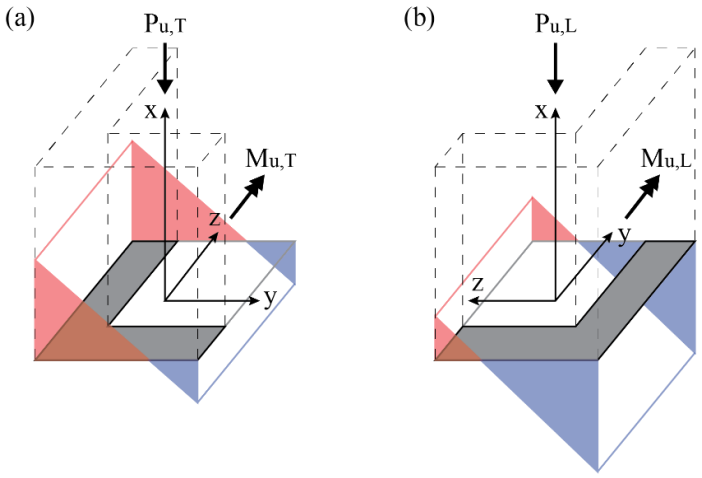

Figure 2-31: Nonlinear section analysis model of (a) the trailing wall and (b) the leading wall

However, $P_{u,L}$ and $P_{u,T}$ are unknown since they are functions of M_L, as shown in Equation 2-19 and Equation 2-20.

$$P_{u,L} = \sum_{x=1}^{n} W_x + \sum_{x=1}^{n} \frac{2M_L}{l_n} = \sum_{x=1}^{n} W_x + \mathrm{N} * \frac{2M_L}{l_n} \quad \text{2-19}$$

$$P_{u,T} = \sum_{x=1}^{n} W_x - \sum_{x=1}^{n} \frac{2M_L}{l_n} = \sum_{x=1}^{n} W_x - \mathrm{N} * \frac{2M_L}{l_n} \quad \text{2-20}$$

Therefore, the values of $M_{u,L}$ and $M_{u,T}$ need to be approximated through iterations, with first iteration assuming the zero M_L, as shown in Equation 2-21.

$$P_{u,L} = P_{u,T} = \sum_{x=1}^{n} W_x \quad \text{2-21}$$

With $M_{u,L}$ and $M_{u,T}$ from the first iteration, M_L for the first iteration is calculated. Then, with the M_L from the first iteration, $P_{u,L}$ and $P_{u,T}$ for the second iteration are calculated using Equation 2-19 and Equation 2-20.

For the second iteration, $M_{u,L}$ and $M_{u,T}$ are computed from pushover analysis with $P_{u,L}$ and $P_{u,T}$ applied to the wall. M_L is calculated with $M_{u,L}$ and $M_{u,T}$ using Equation 2-18. A few more iterations were repeated to compute the estimated value of M_L. The iteration continued until the value of M_L converged to the first digit in the $[kN * m]$ unit.

The applied axial forces on the leading wall and the trailing wall ($P_{u,L}$ and $P_{u,T}$), the base moment reaction of the leading and trailing wall ($M_{u,L}$ and $M_{u,T}$) from the pushover analysis, and the calculated design limiting moment (M_L) are listed in Table 2-24, Table 2-25, and Table 2-26, with the degree of coupling (DoC) assumed to be 0.3, 0.4 and 0.5, respectively. A negative value of $P_{u,T}$ implies that the wall is in tension.

As a result, the estimated values of design limiting moment (M_L) computed with the degree of coupling (DoC) of 0.3, 0.4, and 0.5 are equal to 7,210 *kip*in* (815 *kN*m*), 10,836 *kip*in* (1,224 *kN*m*), and 15,536 *kip*in* (1,755 *kN*m*), respectively. The M_L value from the last iteration is used to design the steel coupling beam.

Table 2-24: Calculation of the limiting moment with $DoC = 0.3$

Number of iterations	$P_{u,T}$		$P_{u,L}$		$M_{u,T}$		$M_{u,L}$		M_L	
	$[kip]$	$[kN]$	$[kip]$	$[kN]$	$[kip * in]$	$[kN * m]$	$[kip * in]$	$[kN * m]$	$[kip * in]$	$[kN * m]$
1	1,208	5,373	1,208	5,373	457,324	51,670	336,060	37,969	7,708	871
2	-1,875	-8,340	4,291	19,087	348,300	39,352	390,786	44,153	7,180	811
3	-1,664	-7,402	4,080	18,149	355,695	40,188	386,719	43,693	7,213	815
4	-1,677	-7,460	4,094	18,211	355,131	40,124	387,031	43,728	**7,210**	**815**

Table 2-25: Calculation of the limiting moment with $DoC = 0.4$

Number of iterations	$P_{u,T}$		$P_{u,L}$		$M_{u,T}$		$M_{u,L}$		M_L	
	$[kip]$	$[kN]$	$[kip]$	$[kN]$	$[kip * in]$	$[kN * m]$	$[kip * in]$	$[kN * m]$	$[kip * in]$	$[kN * m]$
1	1,208	5,373	1,208	5,373	457,324	51,670	336,060	37,969	11,990	1,355
2	-3,587	-15,956	6,004	26,707	286,273	32,344	420,858	47,550	10,686	1,207
3	-3,066	-13,638	5,482	24,385	305,316	34,496	411,703	46,516	10,836	1,224
4	-3,126	-13,905	5,543	24,656	302,521	34,180	412,920	46,653	10,812	1,222
5	-3,116	-13,861	5,533	24,612	302,969	34,231	412,726	46,632	**10,816**	**1,222**

Table 2-26: Calculation of the limiting moment with $DoC = 0.5$

Number of iterations	$P_{u,T}$		$P_{u,L}$		$M_{u,T}$		$M_{u,L}$		M_L	
	$[kip]$	$[kN]$	$[kip]$	$[kN]$	$[kip * in]$	$[kN * m]$	$[kip * in]$	$[kN * m]$	$[kip * in]$	$[kN * m]$
1	1,208	5,373	1,208	5,373	457,324	51,670	336,060	37,969	17,985	2,032
2	-5,986	-26,627	8,402	26,627	213,330	24,103	463,843	52,407	15,350	1,734
3	-4,931	-21,934	7,348	32,685	241,562	27,293	444,966	50,274	15,562	1,758
4	-5,016	-22,312	7,433	33,063	238,440	26,940	446,642	50,464	15,530	1,755
5	-5,004	-22,259	7,420	33,006	239,042	27,008	446,389	50,435	15,538	1,756
6	-5,007	-22,272	7,424	33,023	238,892	26,991	446,453	50,442	15,536	1,755
7	-5,006	-22,268	7,423	33,019	238,929	26,995	446,437	50,440	**15,536**	**1,755**

Figure 2-32 shows the relationship of the degree of coupling (DoC) with $P_{u,T}$, $P_{u,L}$, $M_{u,T}$, $M_{u,L}$, and M_L. It is observed that as the degree of coupling increases, the axial force and the moment demand increases in the leading wall and decreases in the trailing wall. As a result, the design limiting moment increases as the degree of coupling increases.

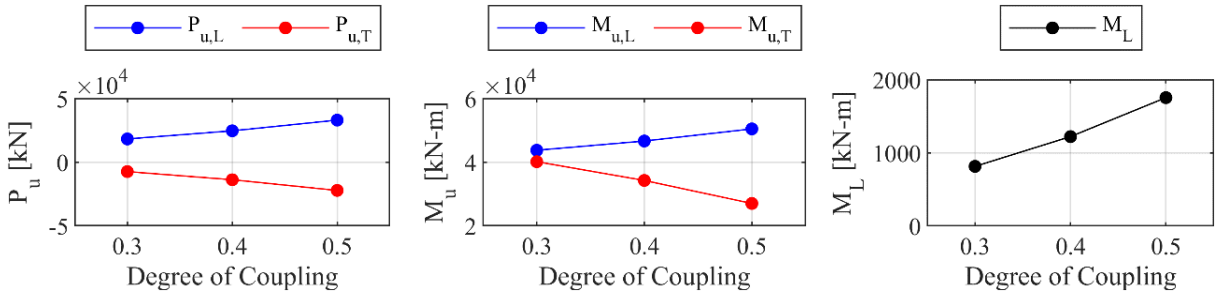

Figure 2-32: Relationship of degree of coupling with $P_{u,T}$, $P_{u,L}$, $M_{u,T}$, $M_{u,L}$, and M_L

Figure 2-33 shows the pushover curve of the last iteration of the leading and the trailing wall sections with the degree of coupling (DoC) values of 0.3, 0.4, and 0.5. In each figure, the first point with a diamond-shaped marker represents the first yield point where the extreme-most longitudinal bar in tension attains the yield strength (f_y), or the extreme fiber in compression attains the concrete strain at maximum compressive strength (ε_{c0}). The second point with the circular-shaped marker represents the crushing point where the extreme fiber in compression attains the concrete strain at a crushing strength of $\varepsilon_{cu} = -0.003\ [in/in]$. The third point with the star-shaped marker (i.e., *) represents the nominal moment (M_n) point where the extreme fiber in compression attains strain of $\varepsilon_s = -0.004\ [in/in]$. This nominal moment is used in the calculation of the design limiting moment (M_L). The ultimate point is either when the extreme-most layer of confined concrete core in compression attains the ultimate compressive strain, $\varepsilon_{ccu} = -0.02\ [in/in]$, or the extreme-most longitudinal bar in tension attains a tensile strain of $\varepsilon_s = -0.06\ [in/in]$. These strains are theoretical failure values that do not account for the effect of cyclic loading, such as longitudinal bar buckling.

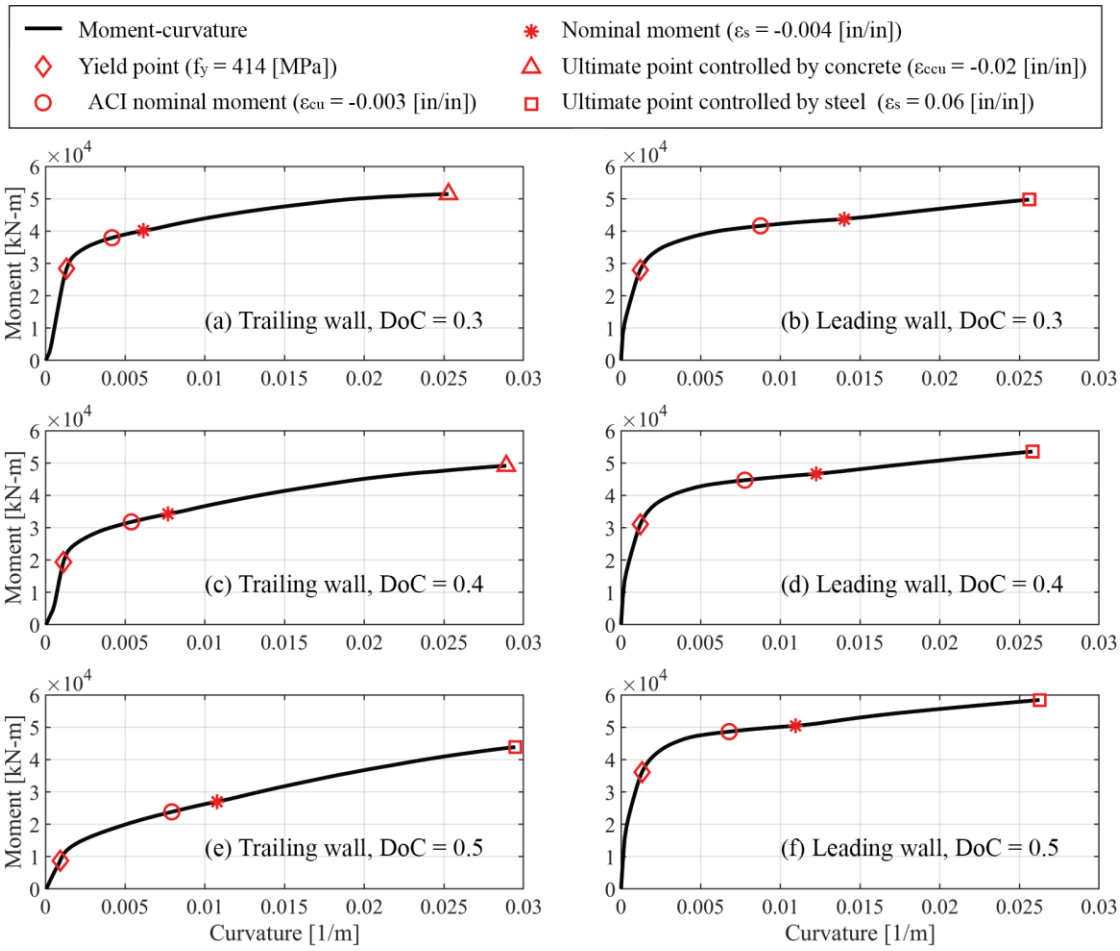

Figure 2-33: Moment-curvature of the wall section at the base from the last iteration

2.12.2 Design of the steel coupling beam

The steel coupling beams are capacity designed for an expected moment equal to 1.2 times M_L. The capacity design ensures that the nonlinear behavior is limited to the rotational friction connection while the steel coupling beams remain undamaged. The rotational friction mechanism at the ends of the steel coupling beams will provide the nonlinearity that the inelastic response of the reinforced concrete coupling beams used to provide in conventional core wall systems. The selection of the steel beam section is proceeded in accordance with AISC [71]. The

section is checked as a member subjected to combined axial force and flexure. The design procedure is as follows.

2.12.2.1 Calculate the capacity

M_L is constant over the height of the building. Thus, the same wide flange section is used for the steel coupling beam over the height of the building. The selected section for the steel coupling beams is W24X207, and the capacity of this section is computed as follows.

Material properties: Modulus of elasticity of steel, $E_s = 29000\ [ksi]$

Yield strength of steel, $F_y = 50\ [ksi]$

Element properties: Element length, $L = 7.5\ [ft]$

Effective length coefficient, $K_y = 1.0$

Effective length, $L_{c1} = K_y * L = 7.5\ [ft]$

Section properties: Selected section: W24X207

Gross area, $A_g = 60.7\ [in^2]$

Moment of inertia about the x-axis, $I_x = 6820\ [in^4]$

Moment of inertia about the y-axis, $I_y = 578\ [in^4]$

Torsional constant, $J = 38.3\ [in^4]$

Calculated capacity: Available compressive strength, $\phi_c P_n = 2565\ [kip]$

Available flexural strength, $\phi_b M_{nx} = 2270\ [kip]$

Available strength in shear, $\phi_v V_n = 671\ [kip]$

2.12.2.2 Calculate the demand

The force demand for the steel coupling beam design is shown below. The applied axial force (P) used in the design is $1894\ kN$ ($i.e., 426\ kip$), which is assumed as the maximum value of the limiting force (F_{Lx}) from all floor levels calculated from all considered DoC values.

Calculate P_r: Required axial force, $P_r = 1.2 * P = 1.2 * 426 = 511\ [kip]$

Calculate M_{rx} : Factored required moment, $M_x = 1.2M_L = 21233\ [kip * in]$

$M_{rx} = B_1 M_x = 8493\ [kip * in]$ (AISC, A-8-1)

Calculate M_{ry}: Factored required moment, $M_y = 0\ [kip * in]$

$M_{ry} = B_1 M_y = 0\ [kip * in]$ (AISC, A-8-1)

Calculate V_{uy}: Required shear, $V_{uy} = 2 * M_x / l_n = 472\ [kip]$

Calculate V_{ux}: Required shear, $V_{ux} = 2 * M_y / l_n = 0\ [kip]$

where,

$B_1 = \frac{C_m}{1 - P_r/P_{e1}} = 0.4 \geq 1$ (AISC, A-8-3)

$C_m = 0.6 - 0.4(M_1/M_2)$ (AISC, A-8-4)

$P_{e1} = \frac{\pi^2 EI}{(L_{c1})^2}$ (AISC, A-8-5)

B_1 is the multiplier to account for $P - \delta$ effects, and it shall be taken as 1.0 for members not subjected to compression. B_2 is the multiplier to account for $P - \Delta$ effects. C_m is an equivalent uniform moment factor, assuming no relative translation of the member ends. M_1/M_2 is positive when the member is bent in reverse curvature and negative when the member is bent in single curvature. C_m shall be determined either by analysis or conservatively taken as 1.0 for all cases. EI is the flexural rigidity required to be used in the analysis. L_{c1} is the effective length in the plane of bending.

2.12.2.3 Unity check

The section capacity is checked for combined axial force and flexure. For a case of $\frac{P_r}{\phi_c P_n} < 0.2$, the unity check follows the below equation.

$$\frac{P_r}{2P_c} + \left(\frac{M_{rx}}{M_{cx}} + \frac{M_{ry}}{M_{cy}}\right) = 0.412 \leq 1.0$$

Also, the section capacity is checked for shear force following the below equation.

$$\frac{V_u}{\phi_v V_n} = 0.703 \leq 1.0$$

2.12.2.4 Results

The selected section W24X207 leads to a demand-to-capacity ratio of less than one and will be used in the eighteen-story core wall building with the low-damage coupling beam. Figure 2-34 shows conceptual drawings of the steel coupling beam with rotational friction connection. A physical design of the steel coupling beam and rotational friction connection is to be developed.

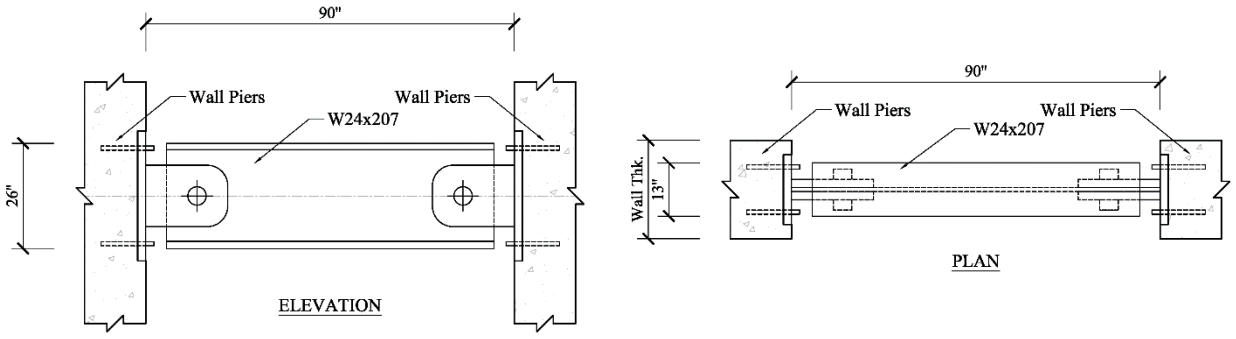

Figure 2-34: Conceptual drawing of the steel coupling beam with rotational friction connection

2.12.3 Summary of low-damage coupling beam design

The design limiting moment (M_L) of the rotational friction connections is calculated using the formula of the degree of coupling (DoC). The computed limiting moments (M_L) are 7,210 $kip * in$ (815 $kN * m$), 10,836 $kip * in$ (1,224 $kN * m$), and 15,536 $kip * in$ (1,755 $kN * m$) for the degree of coupling (DoC) of 0.3, 0.4, and 0.5, respectively. Then, the steel coupling beam is designed using the principle of capacity design in accordance with AISC assuming that the friction moment in the rotational friction connection is constant. The selected section for the steel coupling beam is W24X207.

2.12.4 Low-damage coupling beam element

A low-damage coupling beam element in Opensees consists of two parts: the elastic part in the middle and the inelastic part at each ends, as shown in Figure 2-35. The elastic part represents the steel coupling beam, and it is modeled using an elastic beam-column element. The inelastic parts represent the nonlinear rotational friction connections, and they are modeled as rotational springs using the Zero-length element with the Steel01 uniaxial material. The direction of the rotational spring is parallel to the width of the coupling beam. The Steel01 uniaxial material follows a moment-curvature response that has a transition from linear-elastic to post-elastic when the moment reaches the design limiting moment (M_L). The rotational stiffness of the initial linear-elastic region is $K_\theta = 2{,}000{,}000\ [kip * in]$. The rotational stiffness of the post-elastic region is 0.000001 of K_θ to simulate zero post-elastic stiffness. K_θ value will be a parameter along with M_L for future work because K_θ affects the global stiffness of the building.

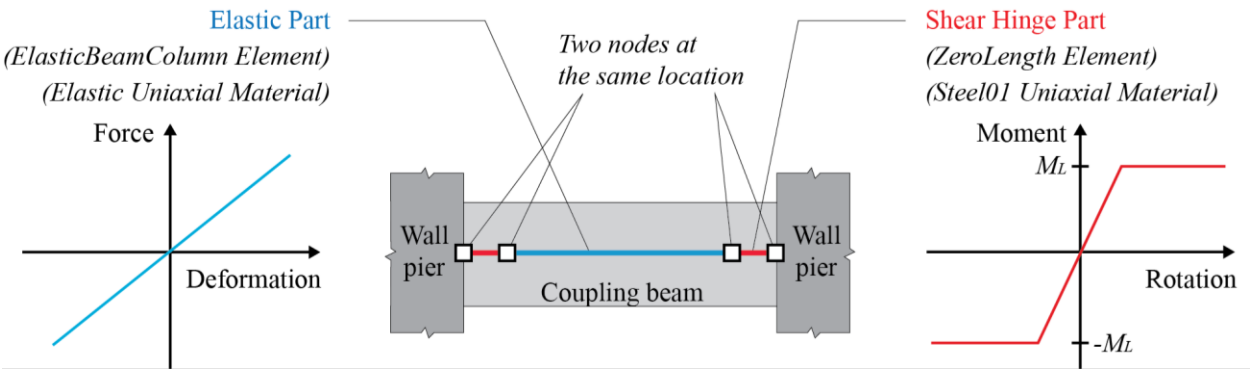

Figure 2-35: Opensees model of the low-damage coupling beam

3 Ground motions

3.1 Overview

The twenty-two far-field earthquake ground motions from FEMA P-695 are considered for this study. Utilizing the two orthogonal horizontal components of each recorded ground motion acceleration data, ground motion accelerations corresponding to an angle ranging from 0 degrees to 180 degrees were calculated. The response spectrum was computed from ground motions of each degree, and the median of those response spectra, which is called the RotD50 response spectrum, was calculated [72]. The RotD50 response spectrum is computed from each twenty-two ground motions. From twenty-two RotD50 response spectra, eleven RotD50 were selected which could best fit the design response spectrum by visual inspection. Then the selected eleven ground motions are scaled so that the mean of the scaled RotD50 response spectra best matches the target design response spectrum within the selected range of period.

3.2 Considered ground motions

The twenty-two far-field earthquake ground motions from FEMA P-695 [69] are considered for time-history analysis of the eighteen-story building model. Table 3-1 lists the information related to the ground motions. Each ground motion has two orthogonal horizontal components, termed H_1 and H_2. Figure 3-1 shows the unscaled ground acceleration of the two orthogonal horizontal components of the twenty-two earthquake ground motions.

Table 3-1: Twenty-two far-filed ground motions from FEMA P-695 [69]

EQ number used in this study	Earthquake Number used in FEMA P-695	Name of Earthquake Ground Motion	Length of Time Step [sec]
EQ1	68	LA - Hollywood Stor FF_24303	0.0100
EQ2	125	Tolmezzo_8012	0.0050
EQ3	169	Delta_6605	0.0100
EQ4	174	El Centro Array #11_5058	0.0050
EQ5	721	El Centro Imp. Co. Cent_1335	0.0050
EQ6	725	Poe Road (temp)_9400	0.0100
EQ7	752	Capitola_47125	0.0050
EQ8	767	Gilroy Array #3_47381	0.0050
EQ9	829	Rio Dell Overpass - FF_89324	0.0200
EQ10	848	Coolwater_23	0.0025
EQ11	900	Yermo Fire Station_22074	0.0200
EQ12	953	Beverly Hills - 14145 Mulhol_90013	0.0100
EQ13	960	Canyon Country - W Lost Cany_90057	0.0100
EQ14	1111	Nishi-Akashi_99999	0.0100
EQ15	1116	Shin-Osaka_99999	0.0100
EQ16	1148	Arcelik_99999	0.0050
EQ17	1158	Duzce_Duzce_99999	0.0050
EQ18	1244	CHY101_99999	0.0050
EQ19	1485	TCU045_99999	0.0050
EQ20	1602	Bolu_99999	0.0100
EQ21	1633	Abbar_99999	0.0200
EQ22	1787	Hector_99999	0.0100

3.3 RotD50 response spectrum

RotD50 response spectrum [72] is a response spectrum that considers various horizontal orientations of a ground motion recorded acceleration time history.

Using the time series of horizontal ground accelerations in two orthogonal directions, H_1 and H_2, a time series corresponding to a given rotation angle θ, $\alpha_{ROT}(t, \theta)$, is computed. The considered rotation angle had a range of 0° to $(180° - \Delta\theta)$, with an increment of rotation angle, $\Delta\theta$, equals to 5°. The equation for α_{ROT} is shown below, where t is time.

$$\alpha_{ROT}(t, \theta) = H_1(t)cos\theta + H_2(t)sin\theta$$

For each $\alpha_{ROT}(t, \theta)$, a pseudo-acceleration response spectrum is computed corresponding to each ground motion with the range of period from 0.05 seconds to 4.0 seconds with increments of 0.05 seconds. A 5% damping ratio was used, and Newmark's integration method was used with α = 0.5 and β = 0.25.

Then, the RotD50 response spectrum for each ground motion is computed as the median of the pseudo-acceleration response spectra of all rotational angles. Figure 3-2 shows the RotD50 response spectrum and the pseudo-acceleration response spectrum of all rotational angles from 0° to $(180° - \Delta\theta)$ of the twenty-two earthquakes considered.

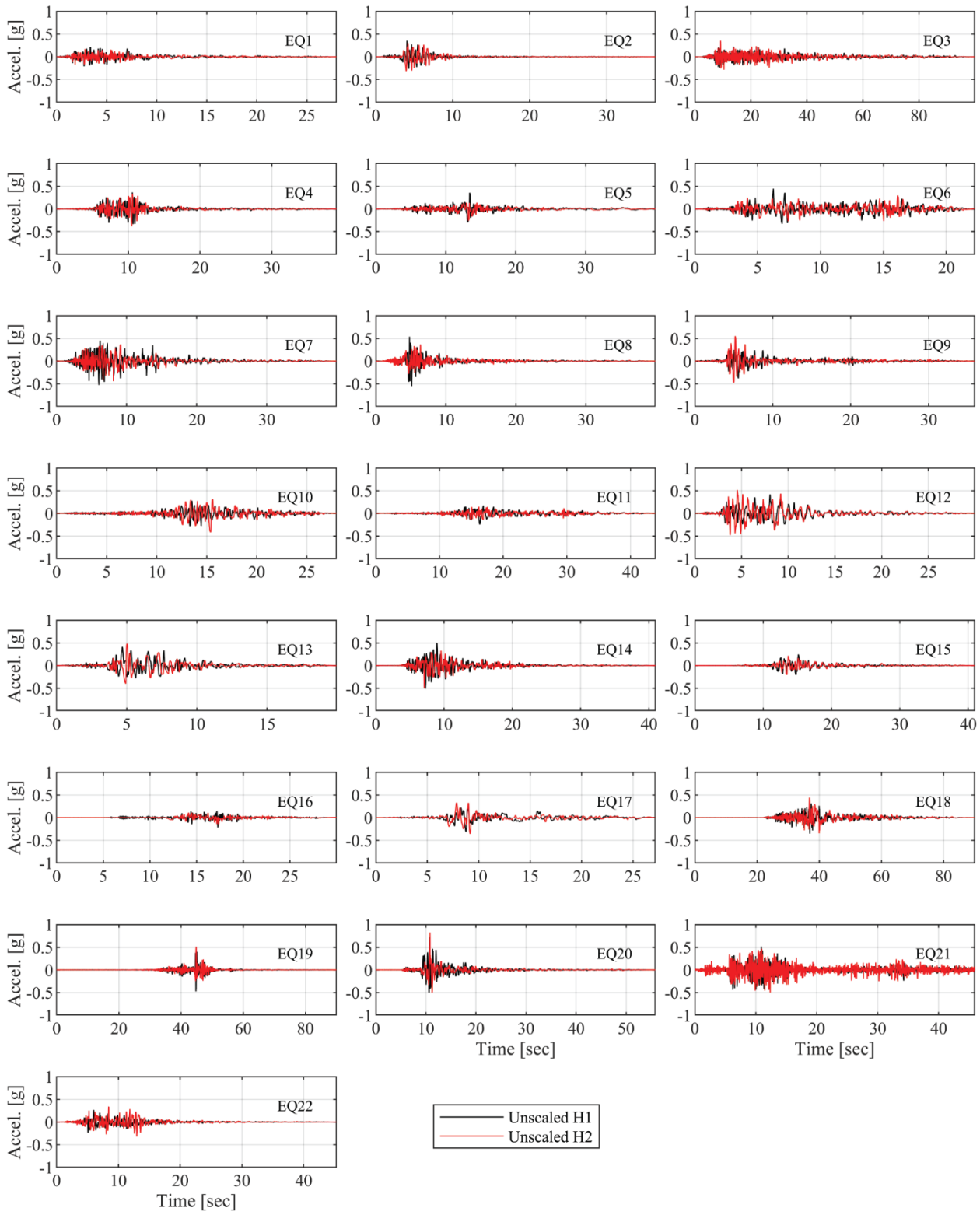

Figure 3-1: Unscaled ground acceleration of the two orthogonal horizontal components of the twenty-two earthquake ground motions

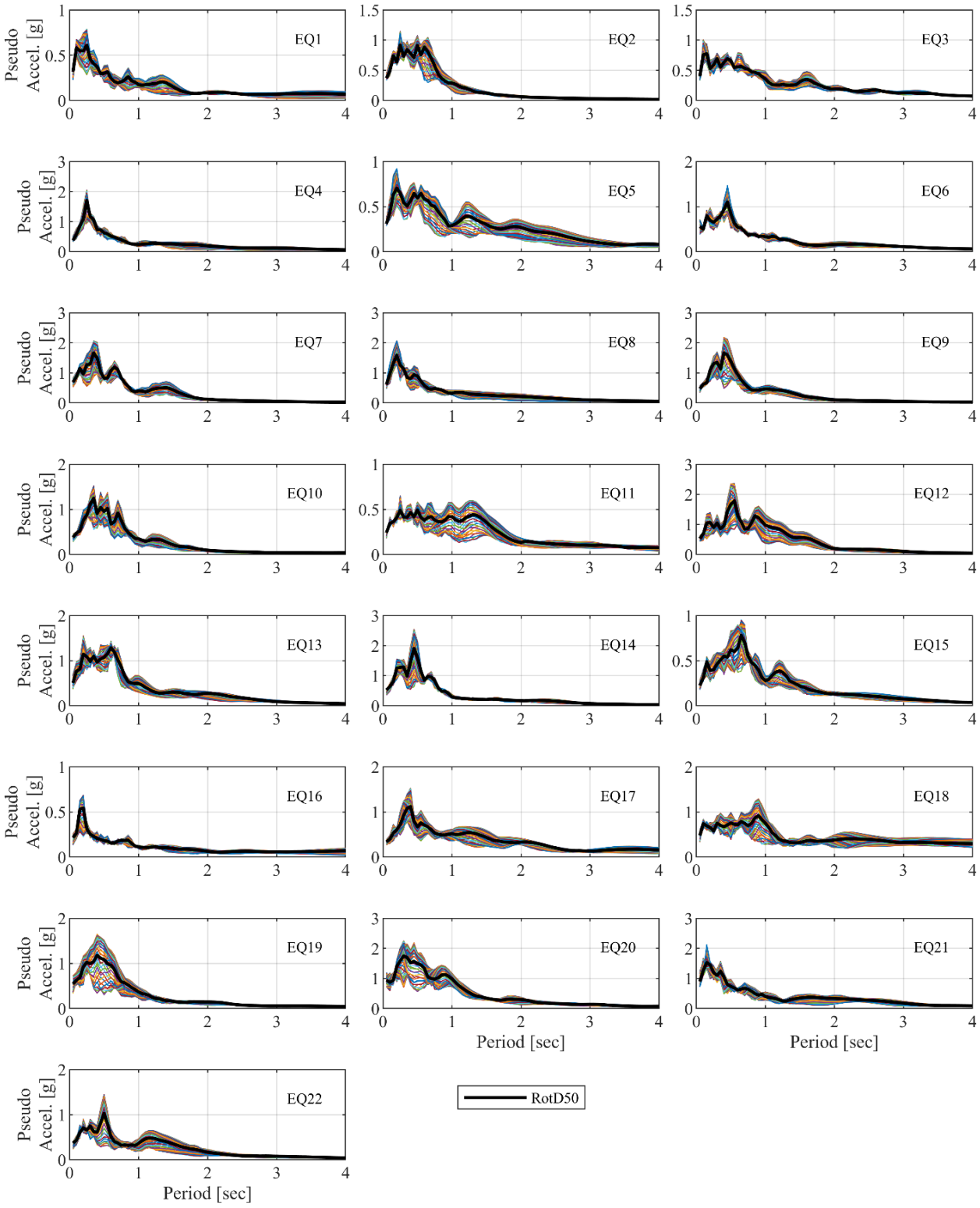

Figure 3-2: Pseudo acceleration response spectrum of twenty-two earthquakes

3.4 Scaling of the ground motions

The target response spectrum to scale the ground motions is set as the design response spectrum calculated according to ASCE7-16 [73]. The period range for scaling and matching is selected in accordance with ASCE7-16, section 16.2.3.1 [73]. The lower limit of the period range is the minimum of 0.2 times the period of the smallest first translational mode (T_2) and the period where 90% cumulative mass is achieved in both translational directions ($T_{90\%}$). The upper limit of the period range is calculated as twice the period of the largest first translational mode (T_1).

$$\text{Lower limit} = \min(0.2T_2, T_{90\%}) = 0.13 \text{ sec}, \text{ Upper limit} = 2\,T_1 = 3.80 \text{ sec}$$

where, T_1 is the largest first translational mode period, T_2 is the smallest first translational model period, and $T_{90\%}$ is the period where 90% cumulative mass is achieved in both translational directions.

The scale factors for the ground motions are selected so that the mean of the scaled RotD50 response spectra best matches the target design response spectrum within the selected period of range. From twenty-two RotD50 response spectra, eleven RotD50, which could best fit the design response spectrum, were selected by visual inspection. Then, the selected eleven ground motions are scaled to have the ratio of the mean of the scaled RotD50 response spectra to the target design spectrum larger than the target ratio of 0.9, as shown in Figure 3-3 (b). Figure 3-3 (a) shows the eleven scaled RotD50 response spectra with 5% damping in the gray lines, the mean of the eleven scaled RotD50 response spectra in the thick black line, and the target design response spectrum in the thick red line. The selected scale factors for each ground motion that will be used in the time history analysis of the eighteen-story core wall building model are shown in Table 3-2.

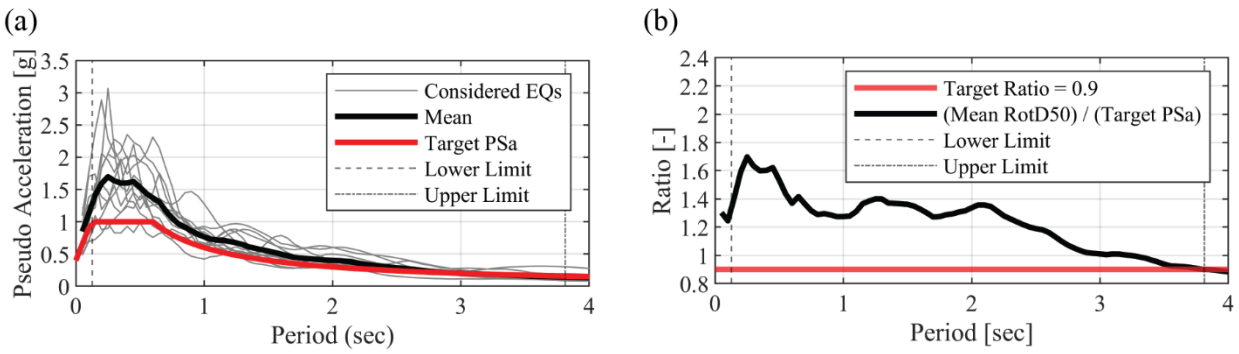

Figure 3-3: (a) Scaled pseudo-acceleration response spectra, and (b) Ratio of mean scaled RotD50 to target design response spectrum

Table 3-2: Earthquake ground motion scale factors

EQ number	EQ3	EQ4	EQ5	EQ6	EQ8	EQ11	EQ13	EQ15	EQ17	EQ19	EQ21
Scale factor	1.80	1.80	2.00	2.00	2.0	2.0	2.0	2.0	1.5	2.0	2.0

Scaled ground acceleration of the two orthogonal horizontal components of the scaled ground motion, scaled H_1 and scaled H_2, of the eleven earthquake ground motions are shown in Figure 3-4. The pseudo-acceleration response spectra of the eleven scaled ground motions and the design response spectrum are shown in Figure 3-5. For each ground motion, the response spectrum of the two orthogonal horizontal components of the scaled ground motion, scaled H_1 and scaled H_2, are shown in the black and grey lines, respectively, and the target design response spectrum is shown in the red line.

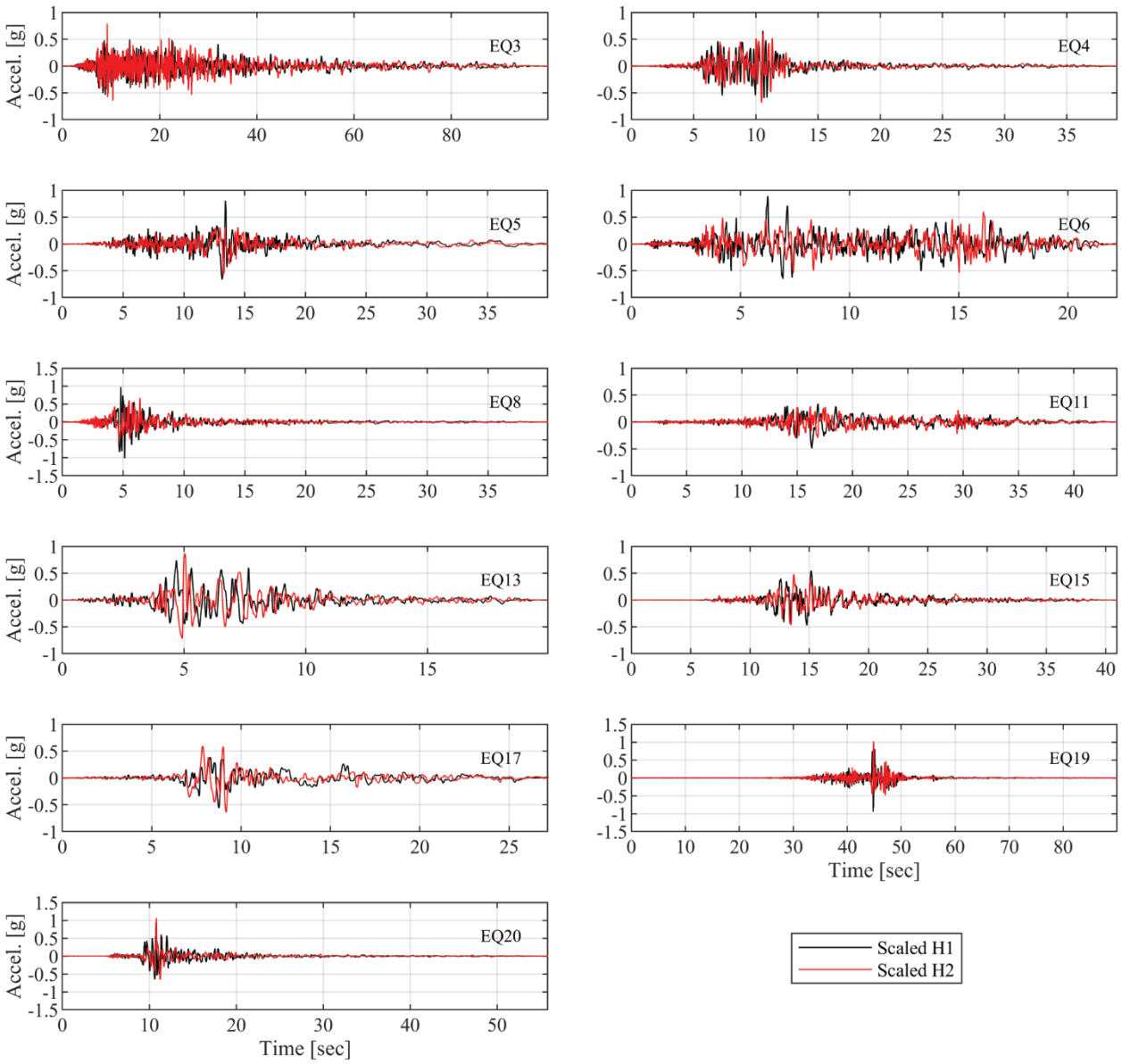

Figure 3-4: Scaled ground acceleration of the two orthogonal horizontal components of the eleven earthquake ground motions

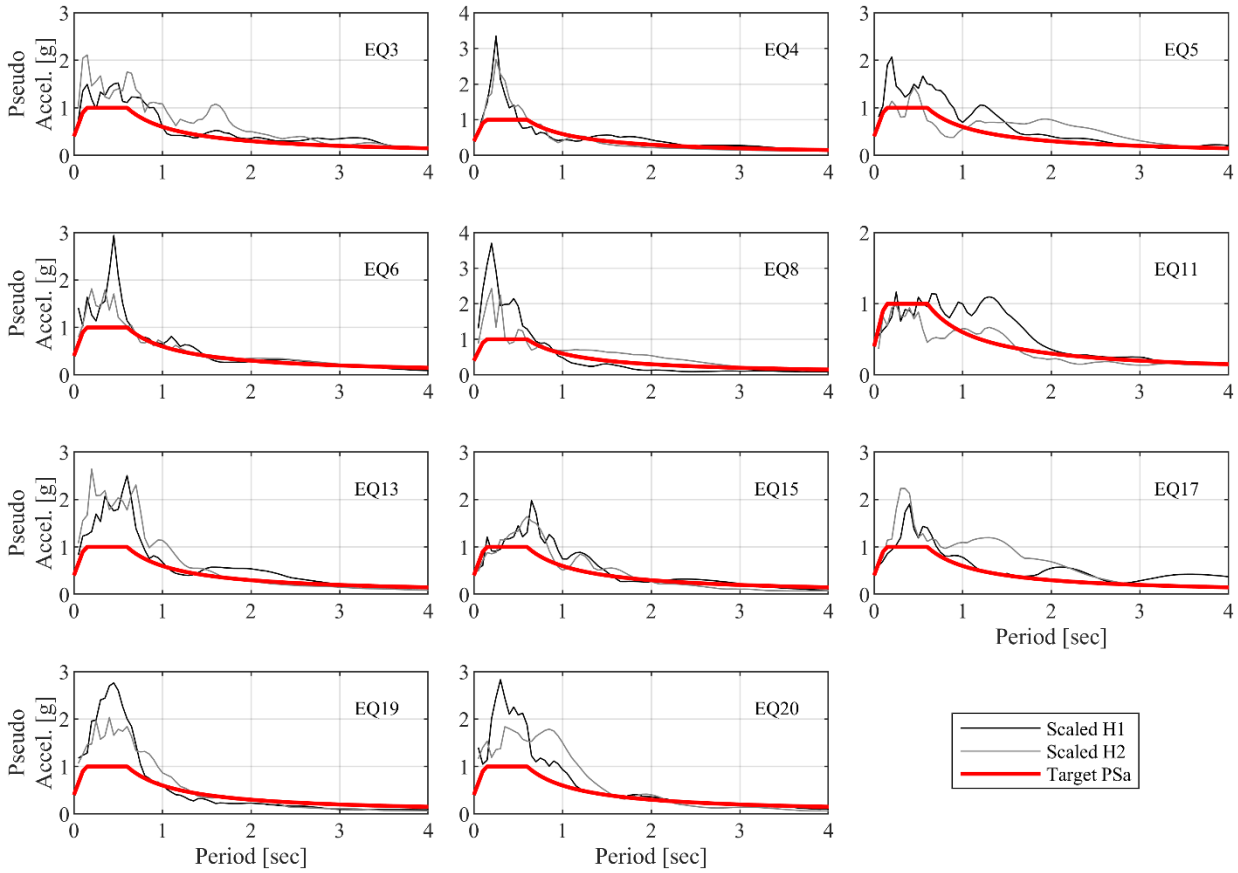

Figure 3-5: Pseudo acceleration response spectra of scaled ground motions and design spectrum with a 5% damping ratio

4 Earthquake numerical simulation results

4.1 Analysis cases

Time history analysis is performed with five different analysis cases. All analysis cases use the same eighteen-story building but have different force-limiting connections and different types of coupling beams. The four different force-limiting connections are the RE connections, the FD connections, the FD+RB connections, and the Modified FD connections, and they are explained in section 2.11. The two different coupling beams are the reinforced concrete coupling beams and the low-damage coupling beams, and they are described in section 2.6 and section 2.12, respectively.

The first analysis case, termed the "RE analysis case," assumes the RE connections between the GLRS and the SFRS and assumes reinforced concrete coupling beams. The second analysis case, termed the "FD analysis case," assumes the FD connections between the GLRS and the SFRS and assumes reinforced concrete coupling beams. The third analysis case, termed the "FD+RB analysis case," assumes the FD+RB connections between the GLRS and the SFRS and assumes reinforced concrete coupling beams. As mentioned in section 1.2.1, the FD+RB connection is not physically possible for the core wall system. But, the FD+RB analysis case is included in this analysis because the force-displacement response of the FD+RB connection has been verified to improve the seismic performance of the building with planar walls by past research. Therefore, the FD+RB analysis case will serve as a reference analysis case with which the seismic response of the core wall building model with Modified FD connections will be compared. The fourth analysis case, termed the "Modified FD analysis case," assumes the Modified FD connections between the GLRS and the SFRS and assumes reinforced concrete

coupling beams. The fifth analysis case, termed the "Modified FD + LDCB analysis case," assumes the Modified FD connections between the GLRS and the SFRS and assumes low-damage coupling beams. LDCB is an acronym for low-damage coupling beams. The Modified FD + LDCB analysis case has three main sources of nonlinearity which are the wall base, the force-limiting connections, and the low-damage coupling beams. The ratio of the nonlinearity taken care of by these sources can be controlled by changing the design limiting force (F_{Lx}) of the Modified FD connections and the design limiting moment (M_L) of the low-damage coupling beams.

4.2 Effects of the Modified FD force-limiting connections

4.2.1 Analysis cases to assess the effects of the Modified FD force-limiting connections

The RE analysis case, the FD analysis case, the FD+RB analysis case, and the Modified FD analysis case are compared to assess the effect of the Modified FD connections on the eighteen-story core wall building.

First, the Modified FD analysis case will be compared to the FD+RB analysis case. This comparison is made to observe if using the discrete variable limiting force (i.e., the Modified FD connections) can accomplish a similar seismic response of the core wall building as using the linearly varying limiting force (i.e., the FD+RB connection).

Second, the Modified FD analysis case will be compared to the RE analysis case. This comparison is made to assess the effect of having the Modified FD connections, potentially feasible force-limiting connection for core wall buildings, compared to having conventional monolithic connections between the GLRS and the SFRS (i.e., RE connections).

Third, the Modified FD analysis case will be compared to the FD analysis case. This comparison is made to identify the necessity of post-elastic stiffness in the force-limiting connection. The FD analysis case will demonstrate the seismic response of the building model with force-limiting connections without post-elastic stiffness (i.e., the FD connections).

4.2.2 Structural level responses

The seismic responses at a structural level of the four analysis cases of the eighteen-story building model are shown in Figure 4-2. The figure shows the total floor acceleration, the GLRS story drift ratio, the SFRS story drift ratio, and the SFRS story shear. The horizontal axis shows either the floor number or the story number, and each marker on the figure represents the peak (i.e., absolute maximum) value from the time history response. The color of the marker indicates different analysis cases. On each floor level or story level, for each analysis case (i.e., each marker color), there are eleven markers indicating the eleven ground motions considered in the analysis. The mean value of the results from the eleven ground motions is shown with a white marker face and black marker edge.

The statistics of the floor total acceleration, the GLRS drift ratio, the SFRS story drift ratio, and the SFRS story shear are listed in Table 7-1 to Table 7-18. The tables show the mean, standard deviation (STD), and coefficient of variation (c.o.v) of the peak responses from the eleven ground motions. The calculation of the mean and the c.o.v follows the equations below.

For a random variable X,

Mean or expended value of X: $\mu_x = E[X]$

Variance of X: $Var[X] = E[(X - \mu_x)^2] = E[X^2] - \mu_x^2$

Standard deviation (STD) of X: $\sigma_x = \sqrt{Var[X]}$

Coefficient of variation (c.o.v) of X: $\delta_x = \frac{\sigma_x}{|\mu_x|}$

Floor total acceleration. The use of force-limiting connections of any type (i.e., the FD connections, the FD+RB connections, and the Modified FD connections) overall reduces the magnitude and the variability in the peak values of the floor total acceleration compared to the magnitude and the variability in the peak values of the floor total acceleration for the building model with RE connections. Table 7-1, Table 7-2, and Table 7-3 list the mean, STD, and c.o.v of the peak floor total acceleration, respectively. The mean of the peak floor total acceleration at the top floor is 47%, 47%, and 39% less from the FD analysis case, the FD+RB analysis case, and the Modified FD analysis case, respectively, compared to the RE analysis case. The STD of the peak floor total acceleration at the top floor is 76%, 81%, and 67% less from the FD analysis case, the FD+RB analysis case, and the Modified FD analysis case, respectively, compared to the RE analysis case.

GLRS story drift ratio and SFRS story drift ratio. The peak GLRS story drift ratio and the peak SFRS story drift ratio from the FD analysis case, the FD+RB analysis case, and the Modified FD analysis case are similar to that from the RE analysis case. Table 7-4, Table 7-5, and Table 7-6 list the mean, STD, and c.o.v of the peak GLRS story drift ratio, respectively. Table 7-7**,** Table 7-8**,** Table 7-9 list the mean, STD, and c.o.v of the peak SFRS story drift ratio, respectively.

SFRS story shear. The use of force-limiting connections of any type (i.e., the FD connections, the FD+RB connections, and the Modified FD connections) overall reduces the magnitude and the variability in the peak values of the SFRS story shear in the first story (i.e., the base shear) compared to the magnitude and the variability in the peak values of the SFRS story shear in the first story (i.e., the base shear) for the building model with RE connections.

The peak SFRS story shears from the second story to the roof from the FD analysis case, the FD+RB analysis case, and the Modified FD analysis case are similar to that from the RE analysis case. Table 7-10, Table 7-11, and Table 7-12 list the mean, STD, and c.o.v of the peak SFRS story shear. The mean of the peak SFRS base shear is 43%, 41%, and 33% less from the FD analysis case, the FD+RB analysis case, and the Modified FD analysis case, respectively, compared to the RE analysis case. The STD of the peak SFRS base shear is 72%, 71%, and 72% less from the FD analysis case, the FD+RB analysis case, and the Modified FD analysis case, respectively, compared to the RE analysis case. Having less base shear demand can reduce the amount of reinforcement at the wall base, where typically has congested reinforcements.

SFRS Story Torsional moment. SFRS story torsional moment is calculated as the sum of the torsion in all wall pier and the sum of the moment created by the forces in all wall piers. The forces and moments developed in each wall piers are shown in Figure 4-1, where $C.G.$ is the center of gravity of the SFRS, and $Dist_{Wall}$ is the distance from $C.G.$ to the wall pier element. $Dist_{Wall}$ is constant over the height and is equal to 2,981 mm (i.e., 117.375 inches). $PX_{W1,x}$, $PX_{W2,x}$, $PX_{W3,x}$, and $PX_{W4,x}$ are the force in global *X*-direction at level *x* of the W1, W2, W3, and W4, respectively. $PY_{W1,x}$, $PY_{W2,x}$, $PY_{W3,x}$, and $PY_{W4,x}$ are the force in the global *Y*-direction at level *x* of the W1, W2, W3, and W4, respectively. $MZ_{W1,x}$, $MZ_{W2,x}$, $MZ_{W3,x}$, and $MZ_{W4,x}$ are the moment in global *Z*-direction at level *x* of the W1, W2, W3, and W4, respectively.

$$SFRS\ story\ torsion\ at\ story\ level\ x = MZ_{W1,x} + MX_{W2,x} + MZ_{W3,x} + MZ_{W4,x} + Dist_{Wall}\left(+PX_{W1,x} - PX_{W2,x} - PX_{W3,x} + PX_{W4,x}\right) + Dist_{Wall}\left(-PY_{W1,x} - PY_{W2,x} + PY_{W3,x} + PY_{W4,x}\right)$$

The use of force-limiting connections reduced the peak SFRS story torsional moment in all levels, both in magnitude and in variability from ground motions, compared to the peak SFRS

story torsional moment when monolithic connections are used between the GLRS and the SFRS. Table 7-13, Table 7-14, and Table 7-15 list the mean, STD, and c.o.v of the peak SFRS story torsional moment, respectively. The mean of the peak SFRS story torsional moment at the base is 51%, 50%, and 52% less from the FD analysis case, the FD+RB analysis case, and the Modified FD analysis case, respectively, compared to the RE analysis case. The STD of the peak SFRS story torsional moment at the base is 58%, 53%, and 59% less from the FD analysis case, the FD+RB analysis case, and the Modified FD analysis case, respectively, compared to the RE analysis case.

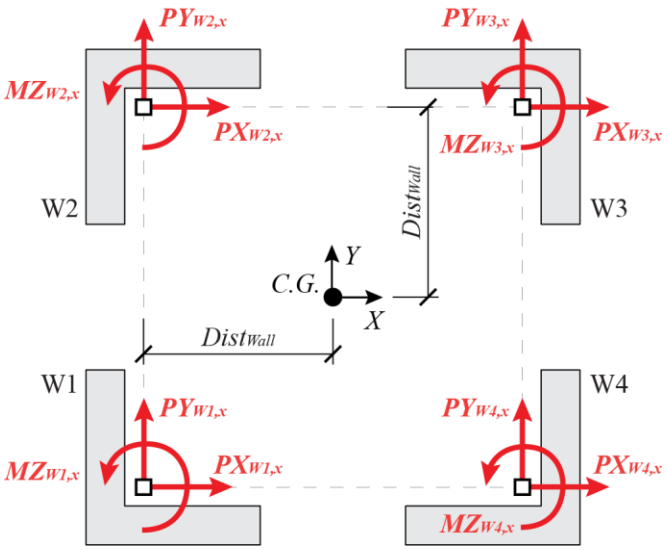

Figure 4-1: Calculation of SFRS story torsional moment

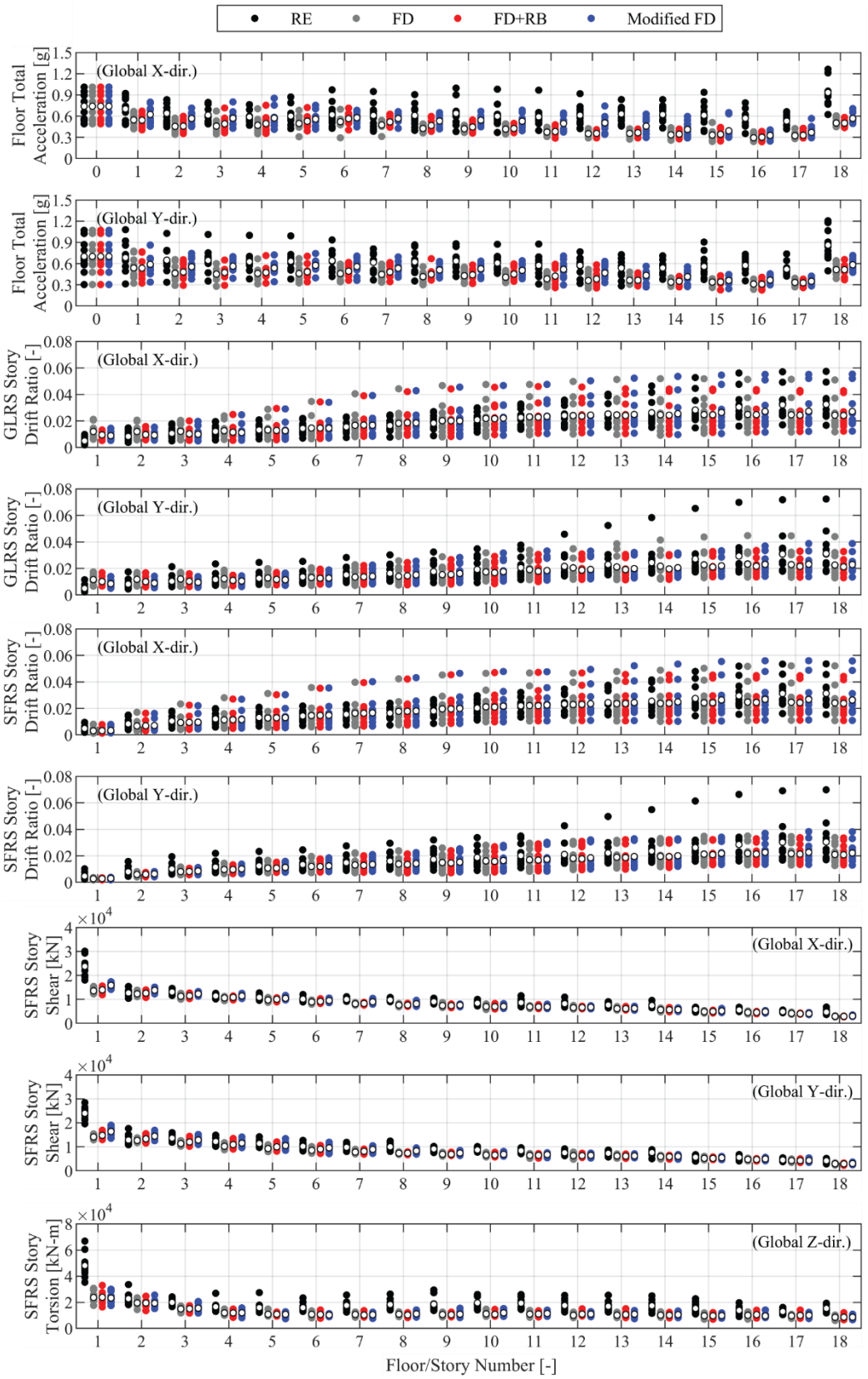

Figure 4-2: Maximum responses of the building models

4.2.3 Force-limiting connection deformation

The peak connection deformation of the force-limiting connection at each floor level in the global *X*-direction and the global *Y*-direction is shown in Figure 4-3. In each direction, there are two force-limiting connections on each floor level. The maximum connection deformation in each direction is calculated as the larger value of the maximum deformation of the two force-limiting connections. The figure shows results from the eleven ground motions with markers indicated in the legend. The mean value of the results from the eleven ground motions is shown with a white marker face and black marker edge.

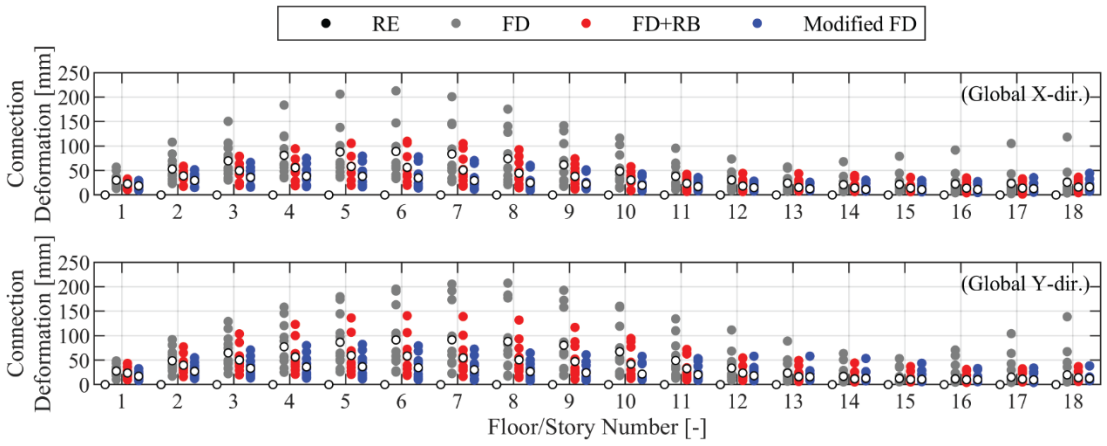

Figure 4-3: Peak connection deformation of the force-limiting connections

Table 7-16, Table 7-17, and Table 7-18 list the mean, STD, and c.o.v of the peak connection deformation of the force-limiting connections. The mean of the peak connection deformation of the RE analysis case is zero at all floor levels because the RE connection is intended to simulate the monolithic connection.

The mean of the peak connection deformation is the largest from the FD analysis case due to the zero post-elastic stiffness of the FD connection. The mean of the peak connection deformation from the Modified FD analysis case is smaller than or similar to the mean of the

peak connection deformation from the FD+RB analysis case. This indicates that the Modified FD connection had a reasonable connection deformation. The STD of the peak connection deformation is larger from the FD analysis case compared to the STD of the peak connection deformation from the FD+RB analysis case and the Modified FD analysis case. This indicates that the variability of the connection deformation reduced with the presence of post-elastic stiffness.

In addition, all three analysis cases with force-limiting connections (i.e., the FD analysis case, the FD+RB analysis case, and the Modified FD analysis case) have relatively large connection deformation around floors from 6 to 8 and at the roof, and they have relatively small connection deformation at the base and around floors from 13 to 15. The distribution of the connection deformation over the height of the building model follows the mode shape of the second mode of the building. This indicates that the building model has a large participation of higher mode responses in its total dynamic response. The deformation around floors 6 to 8 is large because forces below 80% of the story height over the total building height have been designed to have the same F_{Lx}, whereas responses around the roof have been limited with higher F_{Lx}. Therefore, the large response around floors 6 to 8 is not as limited as the floors near the roof. In future research, F_{Lx} can be adjusted to accommodate the higher mode effect in the floors from 6 to 8.

4.2.4 Strain at the wall base

Figure 4-4 shows the distribution of the strain demand at the base section of the core wall piers at the time when the moment reaction is equal to the absolute maximum value of the

moment reactions from the four core wall piers. It shows a result from the time history analysis of EQ15 out of eleven ground motions.

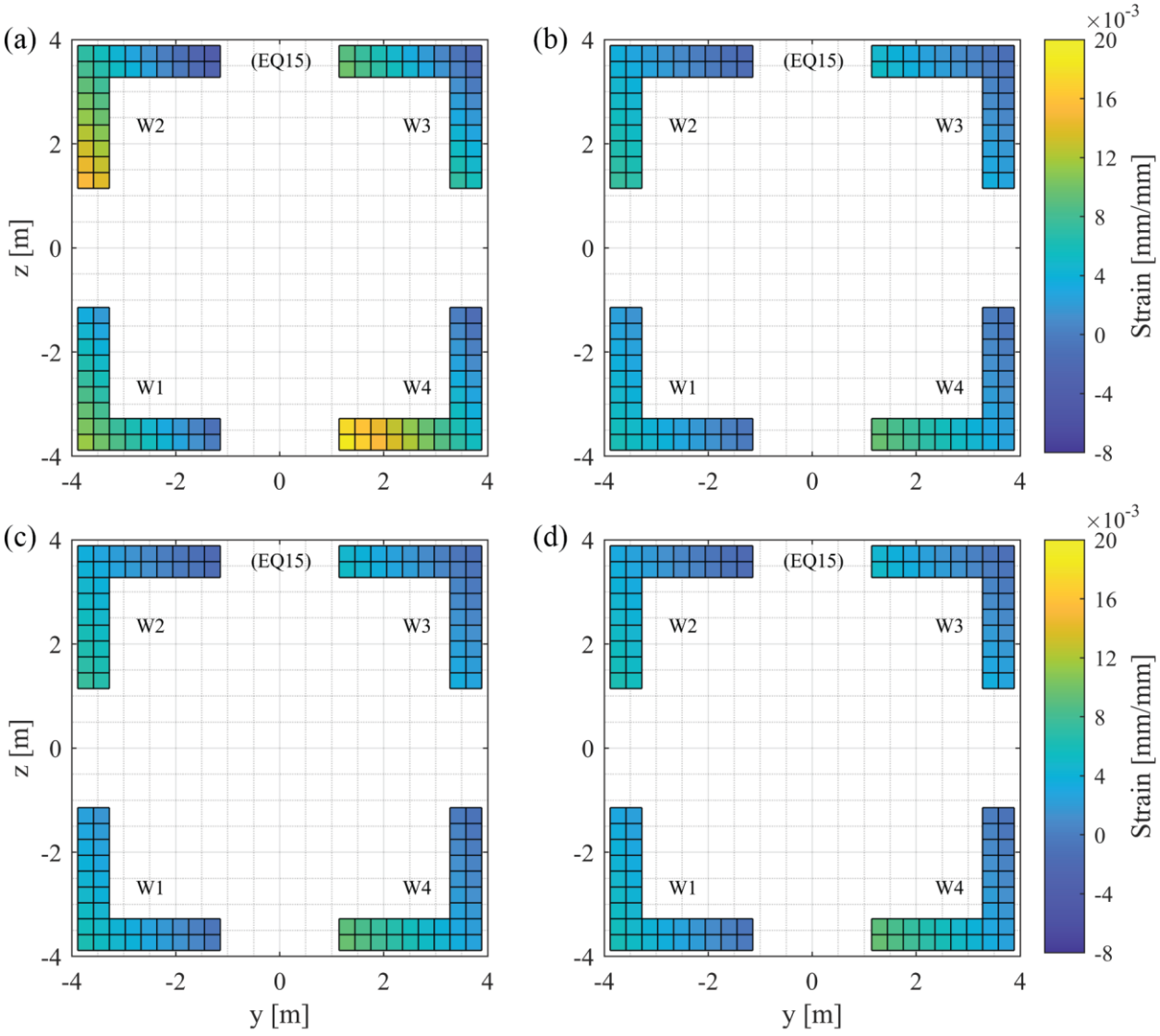

Figure 4-4: Fiber section strain distribution at the wall base with EQ15 from (a) the RE analysis case, (b) the FD analysis case ($R_{DC} = 1.5$), (c) the FD+RB analysis case ($R_{DC} = 1.5, K_{RB} = 22.5\ kip/in$), and (d) the Modified FD analysis case

The maximum and minimum strain response at the wall base from the four analysis cases are shown in Figure 4-5. It shows results from the eleven ground motions with markers indicated

in the legend. The mean value of the results from the eleven ground motions is shown with a white marker face and black marker edge. Table 4-1 shows the statistics of maximum and minimum strain response at the wall base.

The absolute maximum strain in the wall base is reduced with the use of force-limiting connections of any type (i.e., the FD connections, the FD+RB connections, and the Modified FD connections) compared to that with the RE connection. The absolute mean value of the maximum and minimum strain in the wall base is reduced by approximately 55% and 56%, respectively, with the use of force-limiting connections, compared to that with the RE connection. The reduction in the magnitude of the strain demands indicates a potential reduction in the expected structural damage in the core wall piers.

Also, the variability of the absolute strain in the wall base from eleven ground motions is reduced with the use of force-limiting connections of any type (i.e., the FD connections, the FD+RB connections, and the Modified FD connections) compared to that with the RE connection. The absolute STD of the maximum and minimum strain is reduced approximately by 69% and 68%, respectively, with the force-limiting connections, compared to that with the RE connection.

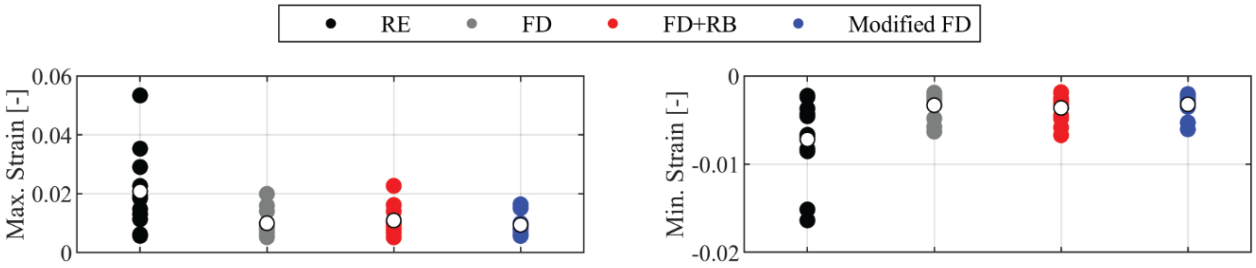

Figure 4-5: Maximum and minimum strain response at the wall base

Table 4-1: Statistics of maximum and minimum strain response at the wall base

	Connection types	Mean [-]	Standard deviation [-]	c.o.v [%]
Maximum strain	RE	0.0208	0.0141	67.53
	FD	0.0100	0.0047	46.81
	FD+RB	0.0109	0.0050	45.75
	Modified FD	0.0094	0.0035	37.13
Minimum strain	RE	-0.0072	0.0047	66.04
	FD	-0.0033	0.0016	47.08
	FD+RB	-0.0036	0.0016	44.69
	Modified FD	-0.0032	0.0013	40.30

4.3 Effect of low-damage coupling beams

4.3.1 Analysis cases to assess the effects of the low-damage coupling beams

The RE analysis case, the Modified FD analysis case, and the Modified FD + LDCB analysis case are compared to assess the effect of using the low-damage coupling beams instead of the reinforced concrete coupling beams on the eighteen-story core wall building. The RE analysis case is included as a reference analysis case of a conventional reinforced concrete core wall building with reinforced concrete coupling beams.

First, the Modified FD + LDCB analysis case will be compared to the Modified FD analysis case. This comparison is made to observe the effect of using the low-damage coupling beams instead of the reinforced concrete coupling beams in the core wall building model with the Modified FD connections. The low-damage coupling beams can potentially be used instead of the reinforced concrete coupling beams if the results from the two analysis cases are similar.

Second, three Modified FD + LDCB analysis cases with different values of design limiting moment (M_L) will be compared. Three design limiting moment (M_L) calculated in

section 2.12 are 7,210 *kip*in* (815 *kN*m*), 10,836 *kip*in* (1,224 *kN*m*), and 15,536 *kip*in* (1,755 *kN*m*), each corresponding to the degree of coupling (DoC) of 0.3, 0.4, and 0.5, respectively.

4.3.2 Difference between the low-damage coupling beam and the reinforced concrete coupling beam in the modeling approach

The main difference between the Modified FD + LDCB analysis case and the Modified FD analysis case is the way the low-damage coupling beams and the reinforced concrete coupling beam are modeled in Opensees, as illustrated in Figure 4-6. The **first** difference is the location and the element used for the source of nonlinearity. The nonlinearity in the reinforced concrete coupling beam is modeled with a shear spring in the global Z-direction located at the center of the coupling beam, whereas the nonlinearity in the low-damage coupling beam is modeled with the rotational spring located at the ends of the coupling beam simulating the rotational friction connections. The direction of the rotational spring is parallel to the width of the coupling beam. The **second** difference is the state of stiffness. The material property of the shear spring model in the reinforced concrete coupling beam has the degradation of stiffness as the moment demand increases. On the other hand, the material property of the rotational spring in the low-damage coupling beam has the same stiffness at all levels of moment demand.

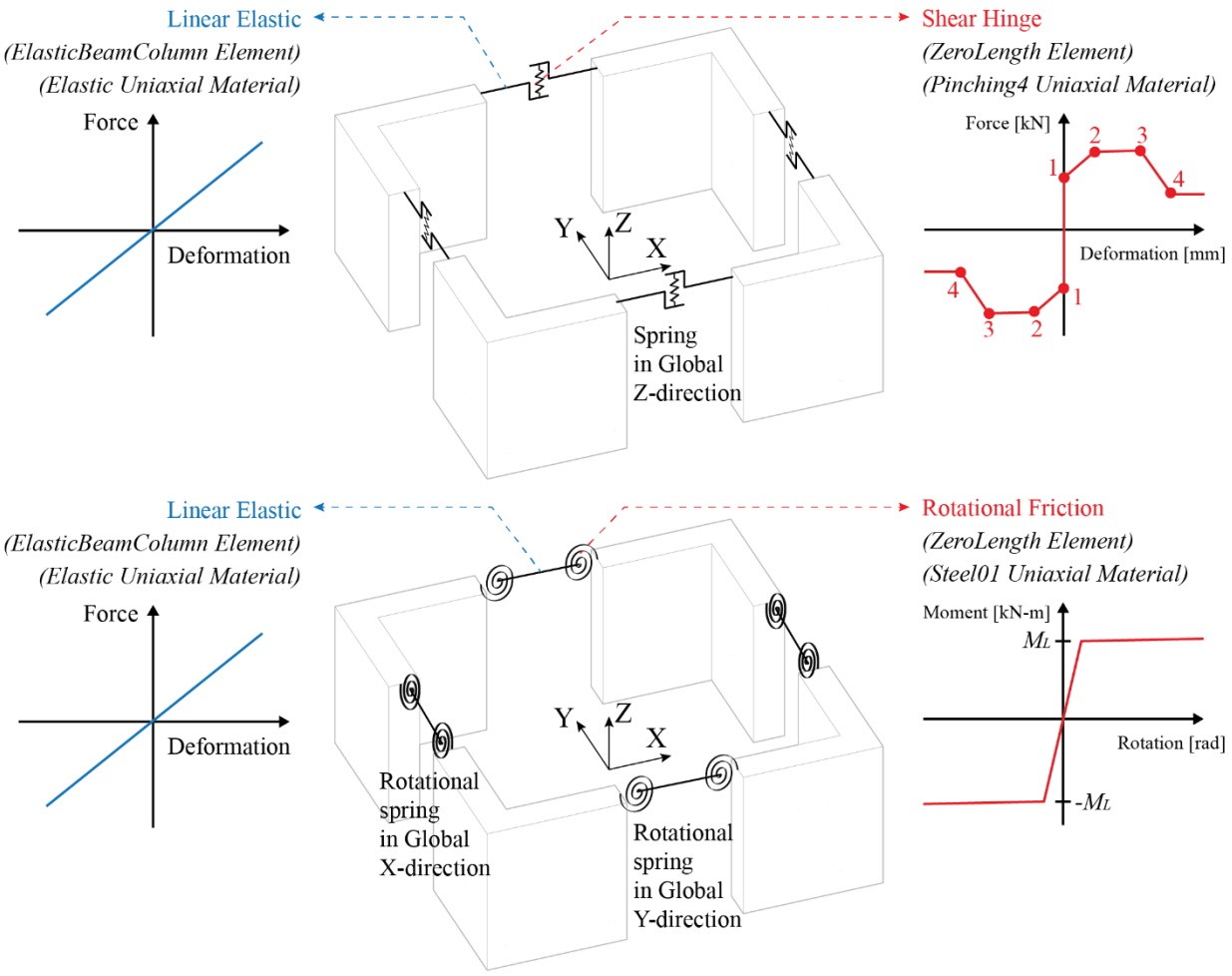

Figure 4-6: Difference between the reinforced concrete coupling beam and the low-damage coupling beam

The **third** difference is the shear and moment capacity along the height of the structure, as shown in Table 4-2. The shear capacity of the reinforced concrete coupling beam is the FU value used in the Pinching4 material, where the $FY = 2A_{vd}f_y \sin\alpha$ and $MY = FY * l_n/2$, as mentioned in section 2.6. The capacity of the reinforced concrete coupling beam is lower as the story level increases, having the highest at the base and lowest at the roof. However, the capacity of the low-damage coupling beam is the same for all story levels, and the value is equal to the

limiting moment (M_L) calculated in section 2.12.1. In future work, the capacity of the low-damage coupling beam can be adjusted to have different capacities at different story levels.

Table 4-2: Capacity of reinforced concrete coupling beam and low-damage coupling beam

Floor Number	Reinforced concrete coupling beam				Low-damage coupling beam					
	Shear Capacity (FU = 1.4 FY)		Moment capacity (1.4 MY)		Moment capacity (M_L), DoC = 0.3		Moment capacity (M_L), DoC = 0.4		Moment capacity (M_L), DoC = 0.5	
[-]	[kips]	[kN]	[kip-in]	[kN-m]	[kip-in]	[kN-m]	[kip-in]	[kN-m]	[kip-in]	[kN-m]
18	138	615	7,641	863	**7,210**	**815**	**10,816**	**1,222**	**15,536**	**1,755**
17	138	615	7,641	863	**7,210**	**815**	**10,816**	**1,222**	**15,536**	**1,755**
16	173	768	9,545	1,078	**7,210**	**815**	**10,816**	**1,222**	**15,536**	**1,755**
15	173	768	9,545	1,078	**7,210**	**815**	**10,816**	**1,222**	**15,536**	**1,755**
14	216	961	11,943	1,349	**7,210**	**815**	**10,816**	**1,222**	**15,536**	**1,755**
13	216	961	11,943	1,349	**7,210**	**815**	**10,816**	**1,222**	**15,536**	**1,755**
12	216	961	11,943	1,349	**7,210**	**815**	**10,816**	**1,222**	**15,536**	**1,755**
11	216	961	11,943	1,349	**7,210**	**815**	**10,816**	**1,222**	**15,536**	**1,755**
10	216	961	11,943	1,349	**7,210**	**815**	**10,816**	**1,222**	**15,536**	**1,755**
9	216	961	11,943	1,349	**7,210**	**815**	**10,816**	**1,222**	**15,536**	**1,755**
8	262	1,163	14,452	1,633	**7,210**	**815**	**10,816**	**1,222**	**15,536**	**1,755**
7	262	1,163	14,452	1,633	**7,210**	**815**	**10,816**	**1,222**	**15,536**	**1,755**
6	262	1,163	14,452	1,633	**7,210**	**815**	**10,816**	**1,222**	**15,536**	**1,755**
5	288	1,282	15,924	1,799	**7,210**	**815**	**10,816**	**1,222**	**15,536**	**1,755**
4	288	1,282	15,924	1,799	**7,210**	**815**	**10,816**	**1,222**	**15,536**	**1,755**
3	288	1,282	15,924	1,799	**7,210**	**815**	**10,816**	**1,222**	**15,536**	**1,755**
2	288	1,282	15,924	1,799	**7,210**	**815**	**10,816**	**1,222**	**15,536**	**1,755**
1	288	1,282	15,924	1,799	**7,210**	**815**	**10,816**	**1,222**	**15,536**	**1,755**

The **fourth** difference is the level of degree of coupling (DoC). The DoC of the three different 'Modified FD + LDCB' analysis cases are 0.3, 0.4, and 0.5. And the DoC of the core wall with the reinforced concrete coupling beam, used by the RE analysis case and the Modified FD analysis case, is calculated as 0.53 using Equation 1-4 which is shown again below. In the equation, the $M_{u,L}$ and the $M_{u,T}$ are calculated using the displacement-controlled pushover analysis as in section 2.12.1, with $P_{u,L}$ and $P_{u,T}$ applied to each wall section, respectively. The value used for $l_{w,L} + l_{CB}$ is equal to 5,029 mm (i.e., 198 inches).

$$DoC = \frac{P_{u,L}\left(l_{w,L} + l_{CB}\right) - P_{u,T}\left(l_{w,T} + l_{CB}\right)}{P_{u,L}\left(l_{w,L} + l_{CB}\right) - P_{u,T}\left(l_{w,T} + l_{CB}\right) + 2\left(M_{u,L} + M_{u,T}\right)}$$

$$P_{u,L} = \sum_{x=1}^{n} W_x + \sum_{x=1}^{n} V_{CB,x} \quad , \; P_{u,T} = \sum_{x=1}^{n} W_x - \sum_{x=1}^{n} V_{CB,x}$$

Table 4-3: Comparison of *DoC* with different types of coupling beams

	Units	Reinforced concrete coupling beam	Low-damage coupling beam		
			DoC = 0.3	DoC = 0.4	DoC = 0.5
$\sum_{x=1}^{n} V_{CB,x}$	[kN]	18,433	12,829	19,245	27,643
	[kips]	4,144	2,884	4,326	6,214
$P_{u,L}$ (wall in compression)	[kN]	23,807	18,211	24,612	33,019
	[kips]	5,352	4,094	5,533	7,423
$P_{u,T}$ (wall in tension)	[kN]	-13,056	-7,460	-13,861	-22,268
	[kips]	-2,935	-1,677	-3,116	-5,006
$M_{u,L}$	[kN-m]	46,288	43,728	46,632	26,995
	[kip-in]	409,689	387,031	412,726	446,437
$M_{u,T}$	[kN-m]	34,973	40,124	34,231	50,440
	[kip-in]	309,540	355,131	302,969	238,929
$\boldsymbol{DoC}$	**[-]**	**0.53**	**0.3**	**0.4**	**0.5**

4.3.3 Structural level responses

The seismic responses at a structural level of the five analysis cases of the eighteen-story building model are shown in Figure 4-7. The figure shows the total floor acceleration, the GLRS story drift ratio, the SFRS story drift ratio, and the SFRS story shear. The horizontal axis shows either the floor number or the story number, and each marker on the figure represents the peak (i.e., absolute maximum) value from the time history response. The color of the marker indicates different analysis cases. On each floor level or story level, for each analysis case (i.e., each marker color), there are eleven markers indicating eleven ground motions considered in the analysis. The mean value of the results from the eleven ground motions is shown with a white marker face and black marker edge.

The statistics of the floor total acceleration, the GLRS drift ratio, the SFRS story drift ratio, and the SFRS story shear are listed in Table 7-19 to Table 7-36. The tables show the mean, standard deviation (STD), and coefficient of variation (c.o.v) of the peak responses from the eleven ground motions.

Floor total acceleration. Replacing the reinforced concrete coupling beams with the low-damage coupling beams did not have a significant effect on the floor total acceleration response in magnitude and variability. Table 7-19, Table 7-20, and Table 7-21 list the mean, STD, and c.o.v of the peak floor total acceleration, respectively. The mean and the STD of the peak floor total acceleration responses from the three Modified FD + LDCB analysis cases are similar to that from the Modified FD analysis case. Within the three Modified FD + LDCB analysis cases, the change in the design limiting moment (M_L) did not have a significant effect on the magnitude and the variability in the ground motions of peak floor acceleration response.

GLRS story drift ratio and SFRS story drift ratio. Replacing the reinforced concrete coupling beams with the low-damage coupling beams reduced the GLRS story drift ratio and the SFRS story drift ratio near the roof in magnitude. Table 7-22, Table 7-23, and Table 7-24 list the mean, STD, and c.o.v of the peak GLRS story drift ratio, respectively. Table 7-25**,** Table 7-26, and Table 7-27 list the mean, STD, and c.o.v of the peak SFRS story drift ratio, respectively. The mean of the peak GLRS story drift ratio and the mean of the peak SFRS story drift ratio near the roof from the Modified FD + LDCB analysis cases are less compared to that from the RE analysis case and the Modified FD analysis case. One explanation of this result is that the low-damage coupling beam assumed a constant limiting moment (M_L) over the height of the structure, whereas the moment capacity of the reinforced concrete coupling beams in the RE analysis case and the Modified FD analysis case decreases as the floor level increases. Replacing the reinforced concrete coupling beams with the low-damage coupling beams did not have a significant effect on the variability of the GLRS story drift ratio and the SFRS story drift ratio. Within the three Modified FD + LDCB analysis cases, the change in the design limiting moment (M_L) did not have a significant effect on the magnitude and the variability in the ground motions of the GLRS story drift ratio and the SFRS story drift ratio.

SFRS story shear. Replacing the reinforced concrete coupling beams with the low-damage coupling beams did not have a significant effect on the SFRS story shear response in magnitude and variability. Table 7-28, Table 7-29, and Table 7-30 list the mean, STD, and c.o.v of the peak SFRS story shear, respectively. The mean and the STD of the peak SFRS story shear of the Modified FD + LDCB analysis case are similar to the mean and the STD of the peak SFRS story shear of the Modified FD analysis case. Within the three Modified FD + LDCB analysis cases, a larger design limiting moment (M_L) results in a larger mean peak SFRS story shear in all

floor levels. And the change in the design limiting moment (M_L) did not have a significant effect on the variability in the ground motions of the peak SFRS story shear.

SFRS story torsional moment. Replacing the reinforced concrete coupling beams with the low-damage coupling beams did not have a significant effect on the SFRS story torsional moment response in magnitude and variability. Table 7-31, Table 7-32, and Table 7-33 list the mean, STD, and c.o.v of the peak SFRS story torsional moment, respectively. The mean and the STD of the peak SFRS story torsional moment from the Modified FD + LDCB analysis cases are similar to that from the Modified FD analysis case. Within the three Modified FD + LDCB analysis cases, a larger design limiting moment (M_L) results in a larger mean peak SFRS story torsional moment from the 1st floor to the 16th floor. And the change in the design limiting moment (M_L) did not have a significant effect on the variability in the ground motions of the peak SFRS story torsional moment.

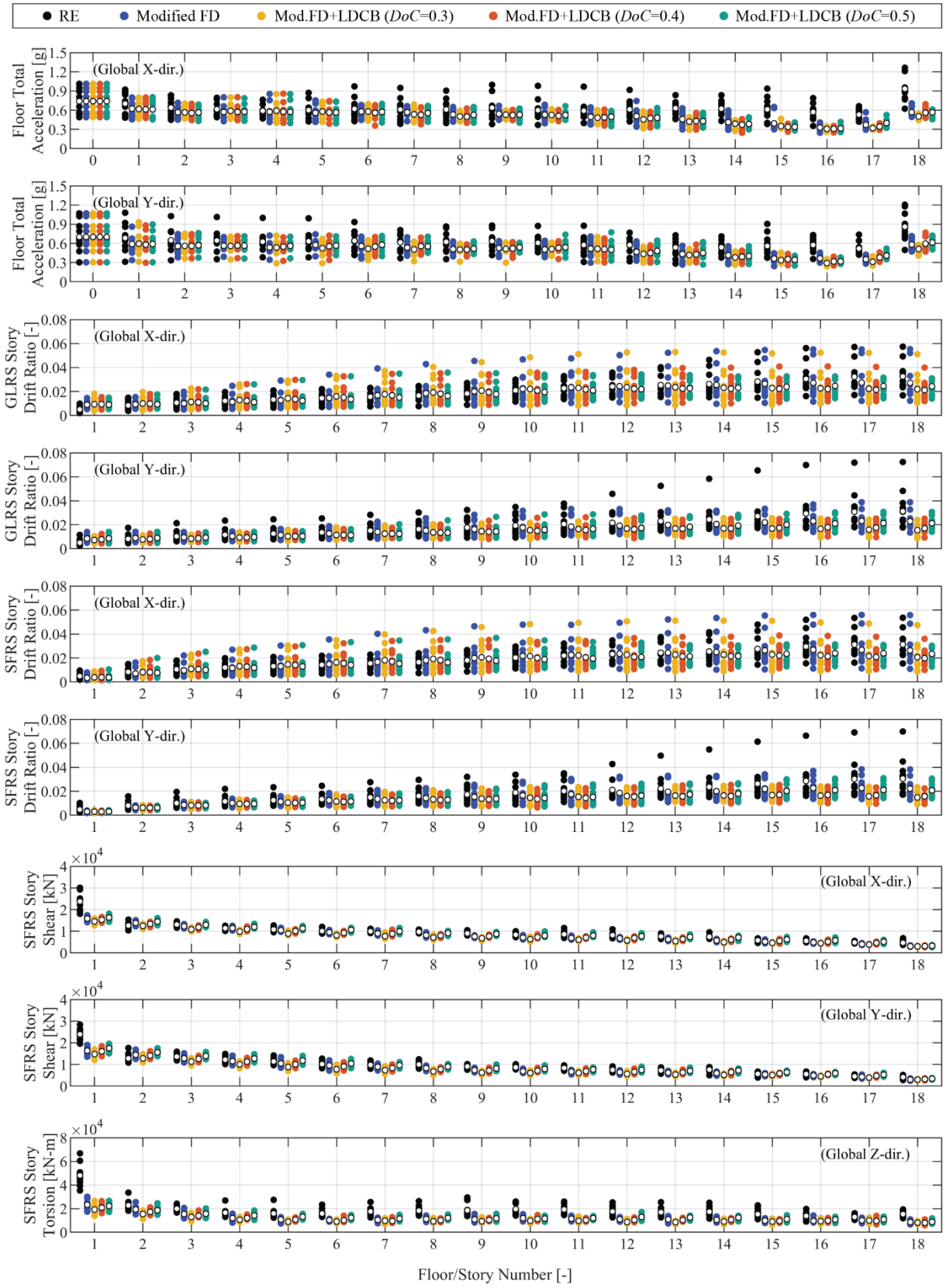

Figure 4-7: Maximum responses of the building models

4.3.4 Force-limiting connection deformation

The peak connection deformation of the force-limiting connection at each floor level in the global *X*-direction and the global *Y*-direction is shown in Figure 4-8. In each direction, there are two force-limiting connections on each floor level. The maximum connection deformation in each direction is calculated as the larger value of the maximum deformation of the two force-limiting connections. The figure shows results from the eleven ground motions with markers indicated in the legend. The mean value of the results from the eleven ground motions is shown with a white marker face and black marker edge.

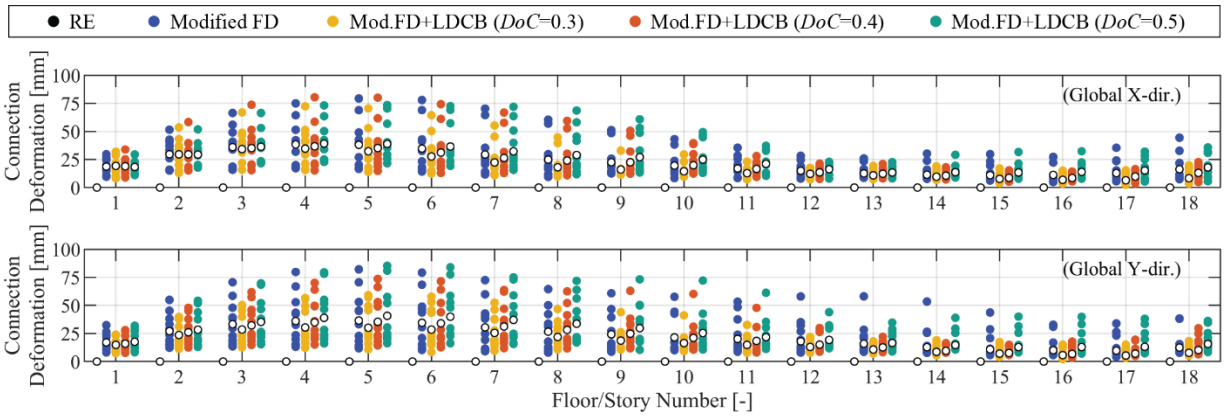

Figure 4-8: Peak response of connection deformation

Replacing the reinforced concrete coupling beams with the low-damage coupling beams does not have a significant effect on the connection deformation in magnitude and variability. The mean of the peak connection deformation of the RE analysis case is zero at all floor levels because the RE connection is intended to simulate the monolithic connection. Table 7-34, Table 7-35, and Table 7-36 list the mean, STD, and c.o.v of the peak connection deformation of the force-limiting connections. The mean and the STD of the peak connection deformation from the Modified FD + LDCB analysis cases are similar to that from the Modified FD analysis case.

Within the three Modified FD + LDCB analysis cases, a larger design limiting moment (M_L) results in a larger magnitude of the connection deformation from the 2nd floor to the 18th floor. A larger design limiting moment (M_L) also results in a larger variability of the connection deformation from the 6th floor to the 14th floor and from the 17th floor to the 18th floor.

4.3.5 Strain at the wall base

Figure 4-9 shows the distribution of the strain demand at the base section of the core wall piers at the time when the moment reaction is equal to the absolute maximum value of the moment reactions from the four core wall piers. It shows a result from the time history analysis of EQ15 out of eleven ground motions.

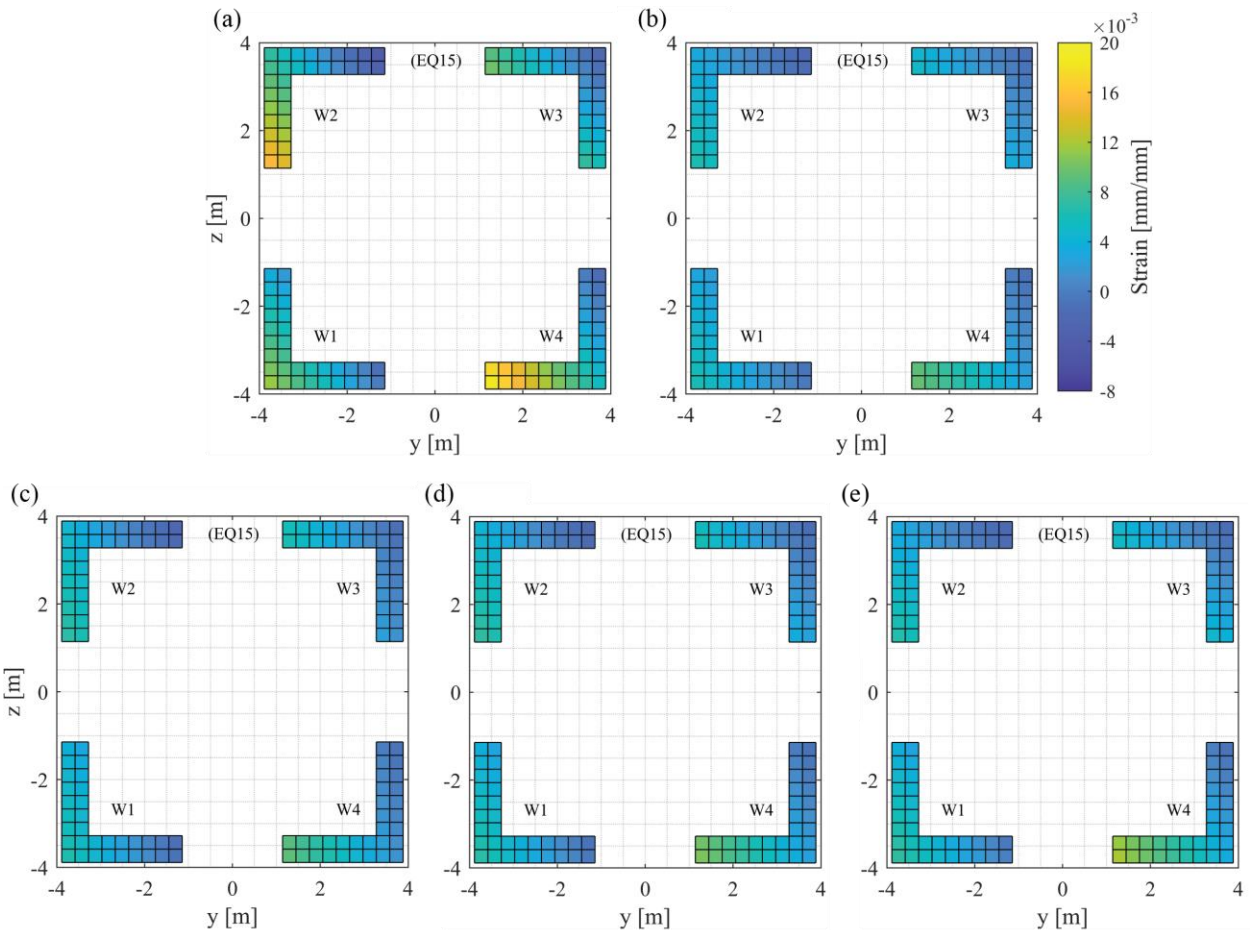

Figure 4-9: Fiber section strain distribution at the wall base with EQ15 from (a) the RE analysis case, (b) the Modified FD analysis case, and the Modified FD + LDCB analysis case with (c) *DoC*=0.3, (d) *DoC*=0.4, and (e) *DoC*=0.5

The maximum and minimum strain response at the wall base from the five analysis cases are shown in Figure 4-10. It shows results from the eleven ground motions with markers indicated in the legend. The mean value of the results from the eleven ground motions is shown with a white marker face and black marker edge. Table 4-4 shows the statistics of maximum and minimum strain response at the wall base.

Replacing the reinforced concrete coupling beams with the low-damage coupling beams did not have a significant effect on the absolute maximum strain in the wall base in magnitude

and variability. The mean and STD of the absolute maximum strain in the wall base from Modified FD + LDCB analysis cases are similar to that from the Modified FD analysis case.

Within the three Modified FD + LDCB analysis cases, the change in the design limiting moment (M_L) did not have a significant effect on the absolute maximum strain in the wall base in magnitude and variability.

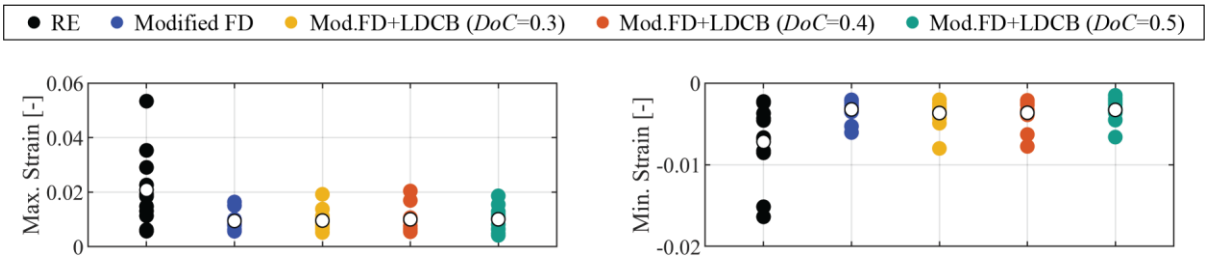

Figure 4-10: Maximum and minimum strain response at the wall base

Table 4-4: Statistics of maximum and minimum strain response at the wall base

	Connection types	Mean [-]	Standard deviation [-]	c.o.v [%]
Maximum strain	RE	0.0208	0.0141	67.53
	Modified FD	0.0094	0.0035	37.13
	Modified FD + LDCB (DoC = 0.3)	0.0090	0.0044	48.77
	Modified FD + LDCB (DoC = 0.4)	0.0101	0.0047	47.12
	Modified FD + LDCB (DoC = 0.5)	0.0101	0.0046	45.70
Minimum strain	RE	-0.0072	0.0047	66.04
	Modified FD	-0.0032	0.0013	40.30
	Modified FD + LDCB (DoC = 0.3)	-0.0035	0.0018	50.40
	Modified FD + LDCB (DoC = 0.4)	-0.0036	0.0018	49.23
	Modified FD + LDCB (DoC = 0.5)	-0.0033	0.0015	45.68

5 Conclusions

5.1 Effect of using the Modified FD force-limiting connections

This thesis examines the seismic responses of a three-dimensional eighteen-story core wall building model with modified force-limiting connections with discrete variable limiting force (i.e., the Modified FD connections). And those seismic responses are compared to the seismic response of the building model with monolithic connections between the GLRS and the SFRS (i.e., the RE connections), the seismic response of the building model with force-limiting connections with constant limiting force (i.e., the FD connections), and the seismic response of the building model with force-limiting connections with linearly varying limiting force (i.e., the FD+RB connections).

The use of the Modified FD connections in the eighteen-story core wall building reduces the magnitude and the variability of the seismic-induced shear force, torsional moment, and acceleration responses of the building compared to the seismic-induced shear force, torsional moment, and acceleration responses of the conventional core wall building with the RE connections.

The use of modified force-limiting connections also reduces the magnitude and variability of the maximum and minimum strain demand in the core wall base, which indicates a potential reduction in the expected structural damage in the core wall piers.

The use of the Modified FD connections in the eighteen-story core wall building has no significant effect on the story drift ratio of the GLRS and the SFRS compared to the conventional core wall building with the RE connections. The GLRS and the SFRS story drift ratios are important indications of structural and nonstructural damages.

The discrete variable limiting force of the Modified FD connections limits the relative displacement between the GLRS and the SFRS to a reasonable range, whereas the constant limiting force (i.e., zero post-elastic stiffness) of the FD connections results in excessive connection deformation.

5.2 Effect of using the low-damage coupling beams

This thesis examines the seismic responses of a three-dimensional eighteen-story core wall building model with the Modified FD connections and the low-damage coupling beams. And those seismic responses are compared to the seismic response of the building model with the Modified FD connections. Also, this thesis examines the seismic responses of a three-dimensional eighteen-story core wall building model with change in the magnitude of design limiting moment (M_L) of the low-damage coupling beams.

The use of the low-damage coupling beams instead of the reinforced concrete coupling beams does not have a significant effect on the magnitude and variability of the seismic-induced shear force, torsional moment, and acceleration responses (i.e., floor total acceleration, GLRS story drift ratio, SFRS story drift ratio, SFRS story shear, SFRS story torsional moment, connection deformation, and the absolute maximum strain in the wall base) of the building model with the Modified FD connections. Therefore, the use of low-damage coupling beams could potentially eliminate the damage expected in the reinforced concrete coupling beams to accelerate the post-earthquake functional recovery of the building.

Having a larger limiting moment (M_L) in the low-damage coupling beams does not have a significant effect on the magnitude and variability of the floor total acceleration, SFRS story shear, and the absolute maximum strain in the wall base. But, a larger limiting moment (M_L) in

the low-damage coupling beams results in a larger magnitude of the SFRS story shear force and the SFRS story torsional moment and a larger magnitude and variability of the connection deformation.

6 [Appendix] Seismic response plots

In section 6.2, section 6.3, section 6.4, and section 6.5, the FD+RB1 connection, the FD+RB2 connection, and the FD+RB3 connection case represents FD+RB connections with $K_{RB} = 22.5\ kip/in = 3{,}940\ kN/m$, $K_{RB} = 45.0\ kip/in = 7{,}880\ kN/m$, and $K_{RB} = 67.5\ kip/in = 11{,}820\ kN/m$, respectively.

6.1 Force-limiting connections with R_{DC} = 1.5 and $K_{RB} = 22.5 kip/in$

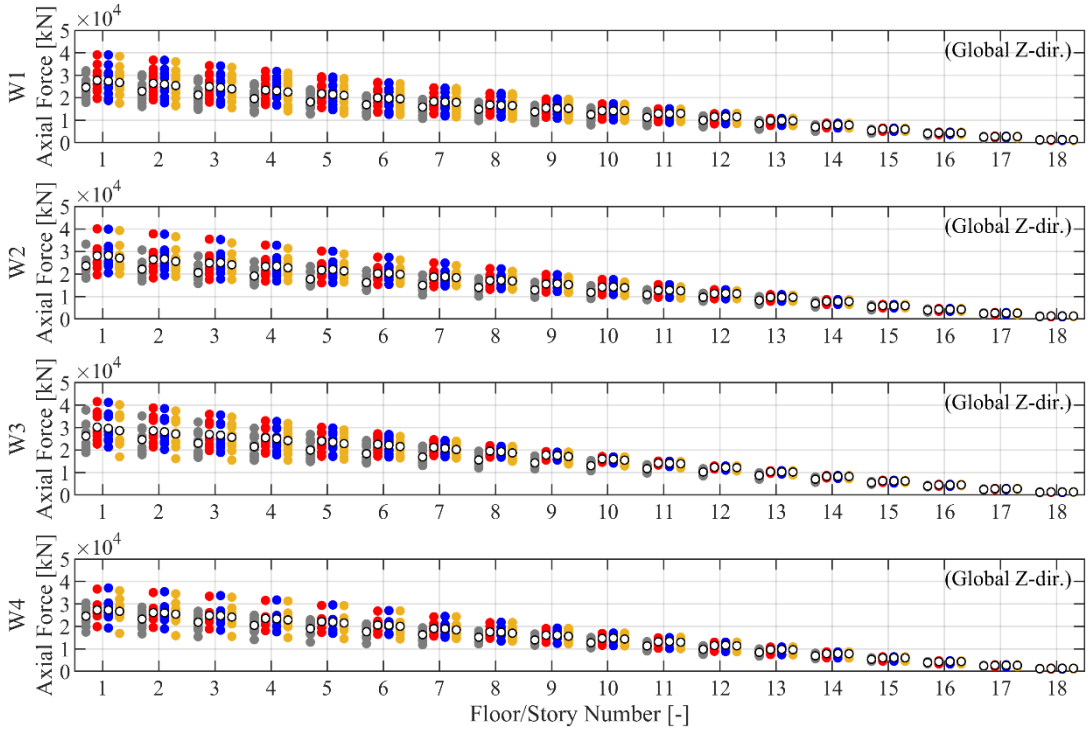

Figure 6-1: Peak axial force of the four wall piers

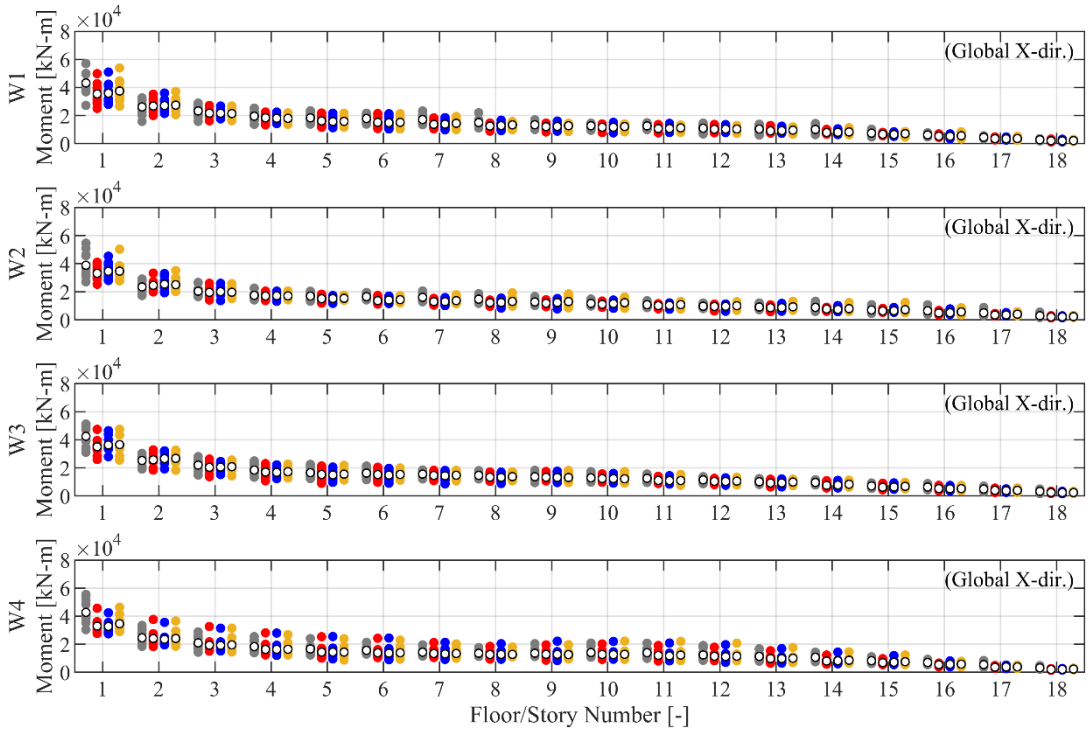

Figure 6-2: Peak moment of the four wall piers about Global X-dir.

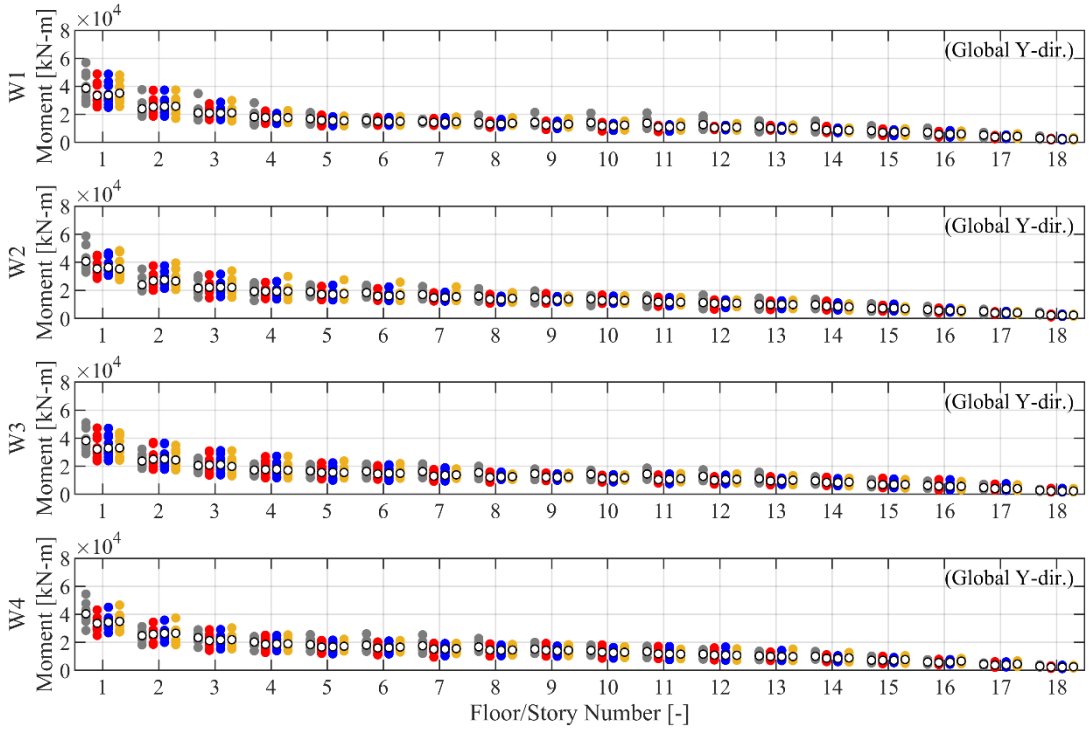

Figure 6-3: Peak moment of the four wall piers about Global Y-dir.

6.2 Force-limiting connections with R_{DC} = 1.0

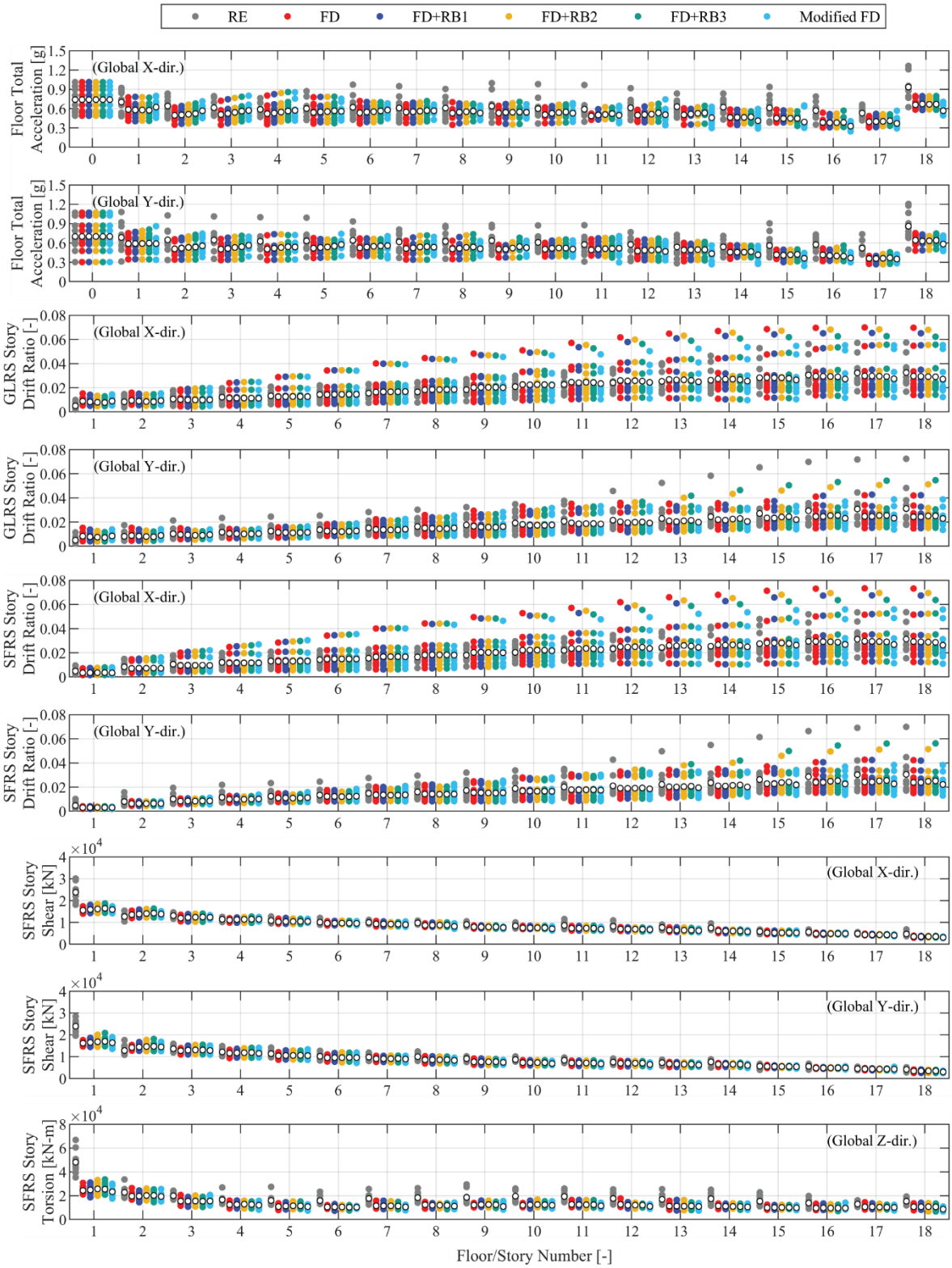

Figure 6-4: Maximum responses of the building models

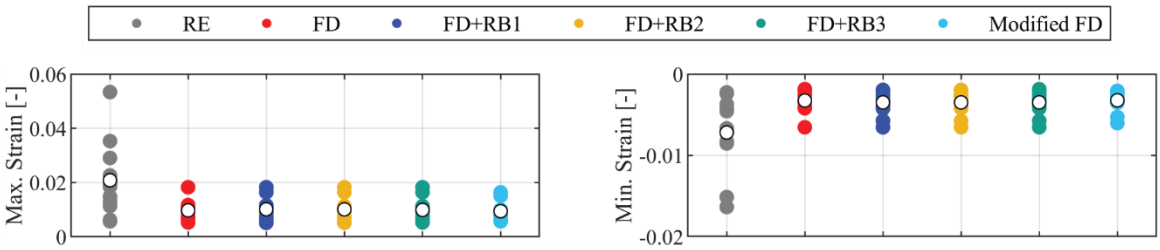

Figure 6-5: Maximum and minimum strain response at the wall base

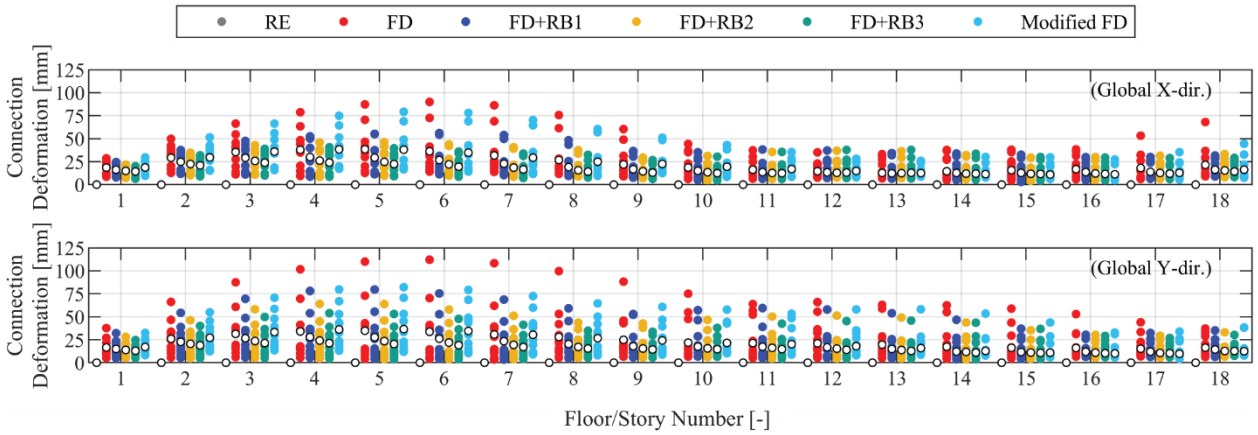

Figure 6-6: Peak connection deformation of the force-limiting connections

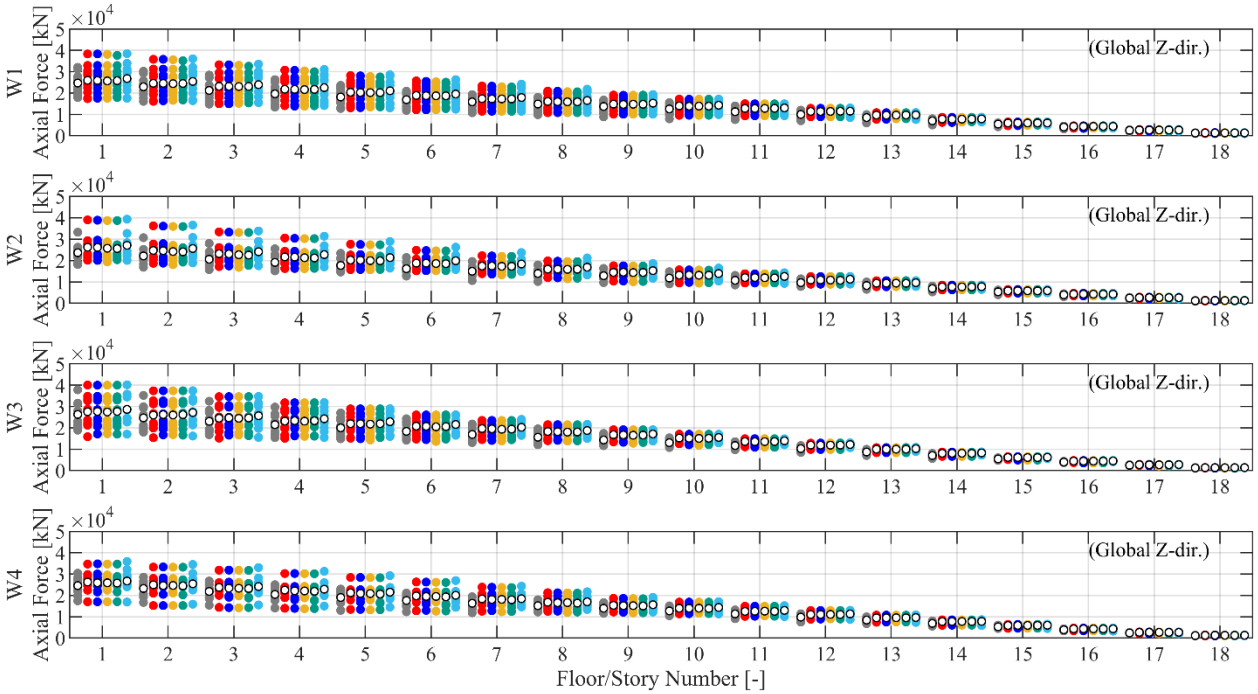

Figure 6-7: Peak axial force of the four wall piers

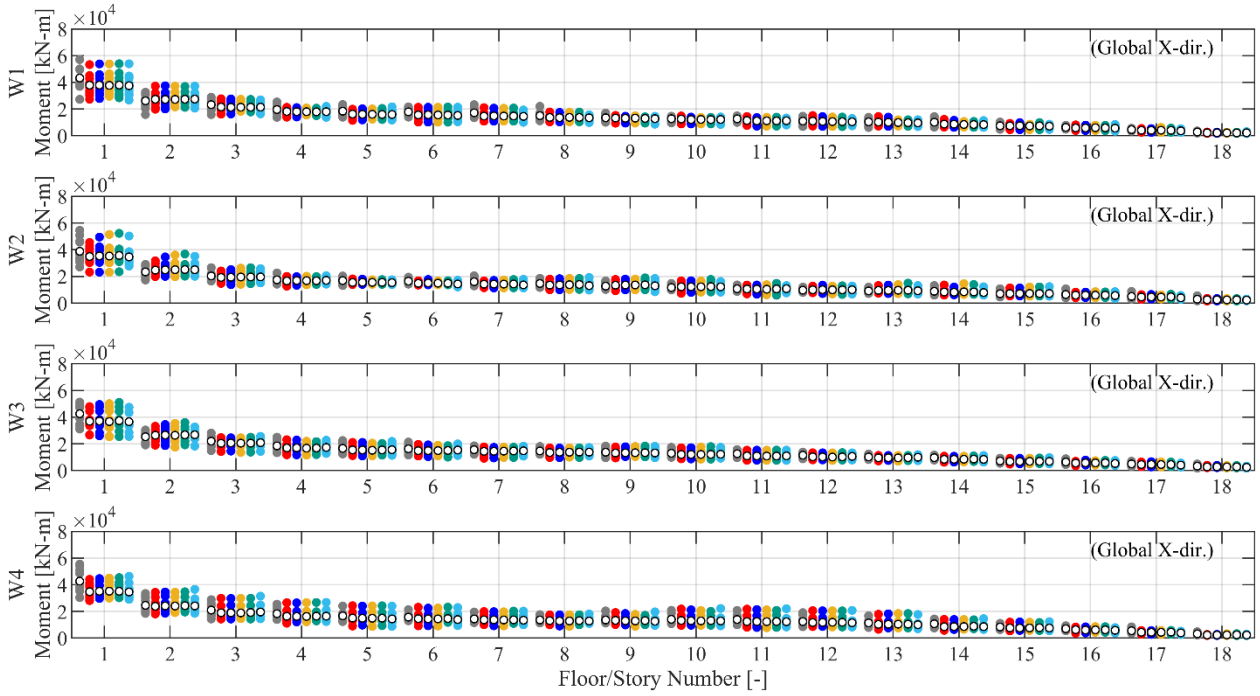

Figure 6-8: Peak moment of the four wall piers about Global X-dir.

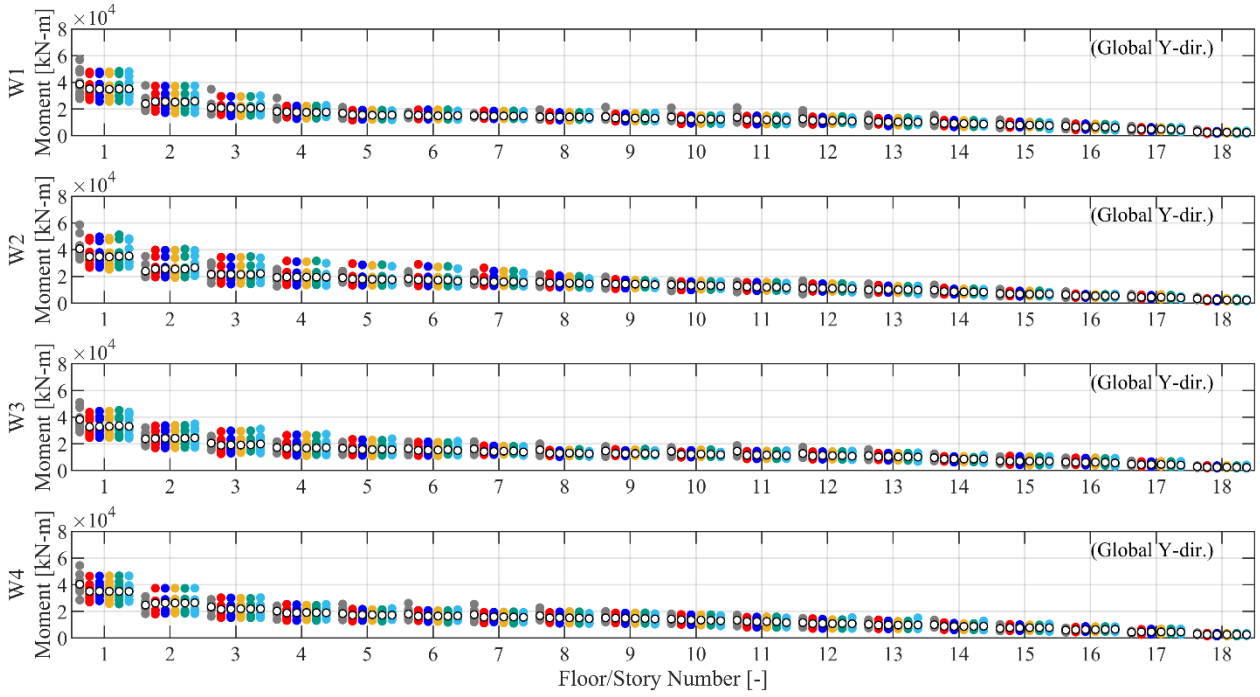

Figure 6-9: Peak moment of the four wall piers about Global Y-dir.

6.3 Force-limiting connections with R_{DC} = 1.5

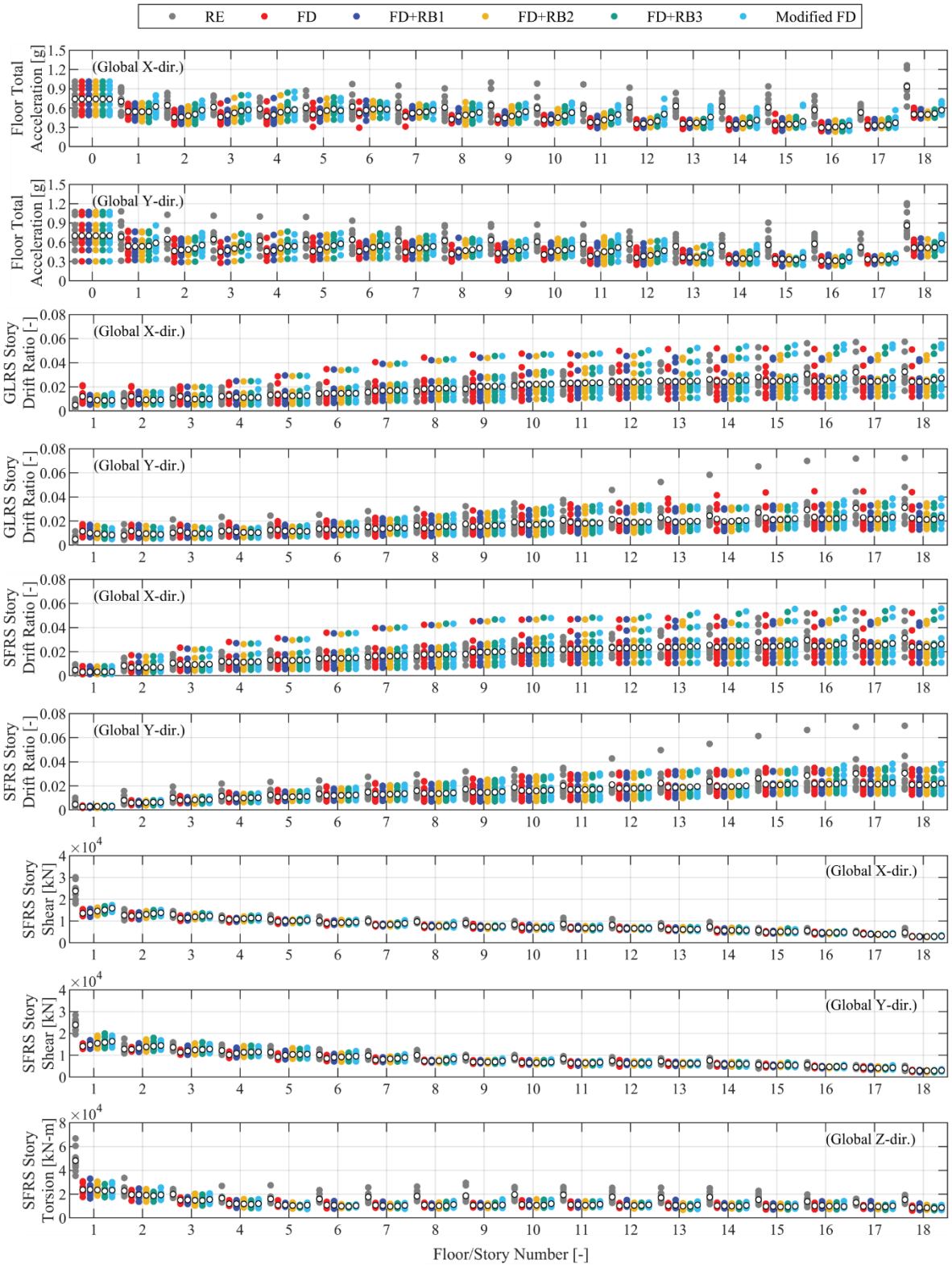

Figure 6-10: Maximum responses of the building models

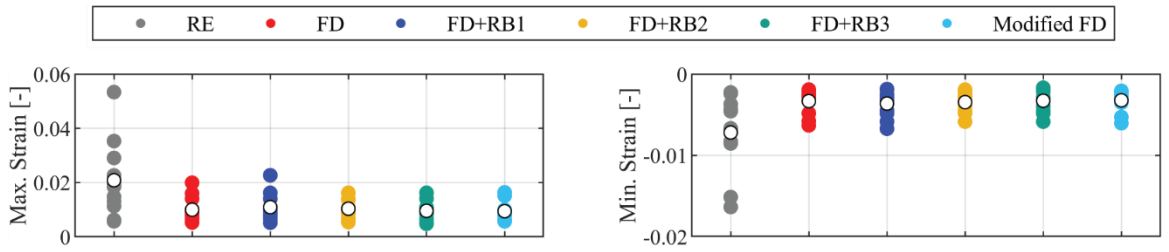

Figure 6-11: Maximum and minimum strain response at the wall base

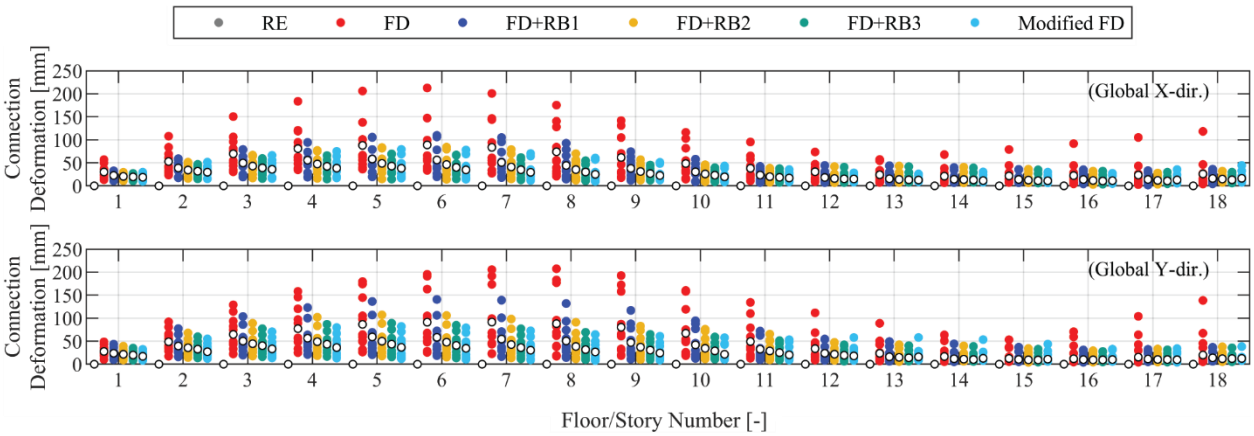

Figure 6-12: Peak connection deformation of the force-limiting connections

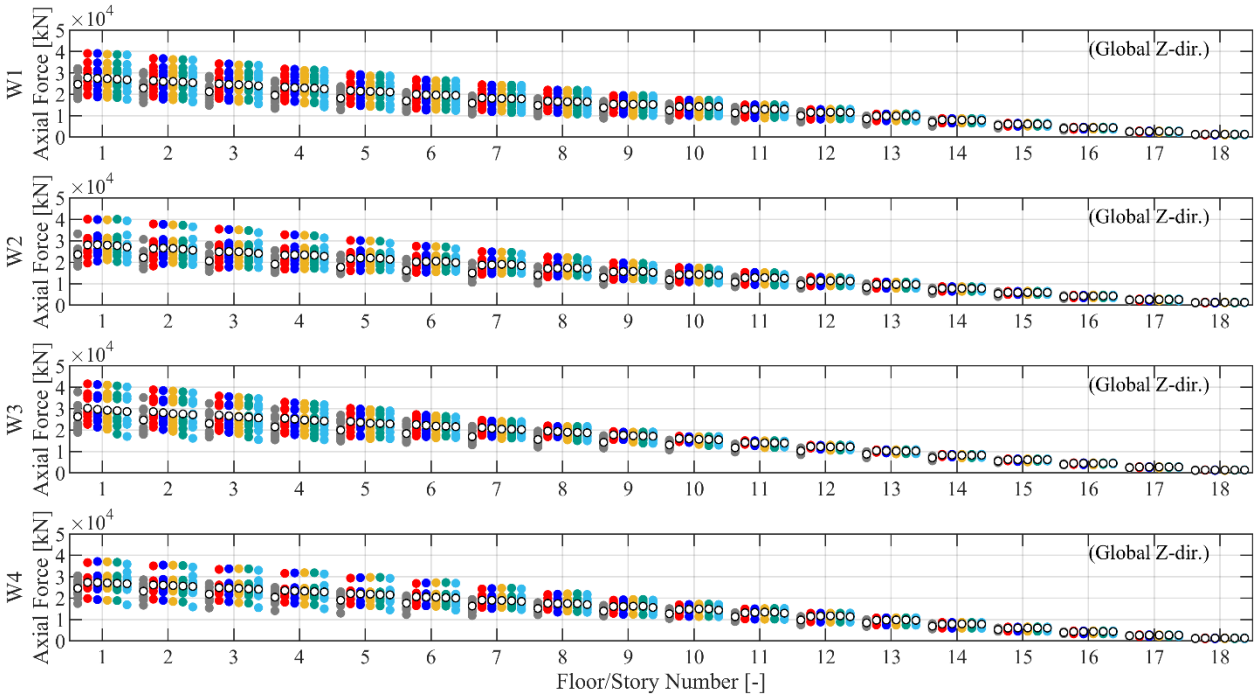

Figure 6-13: Peak axial force of the four wall piers

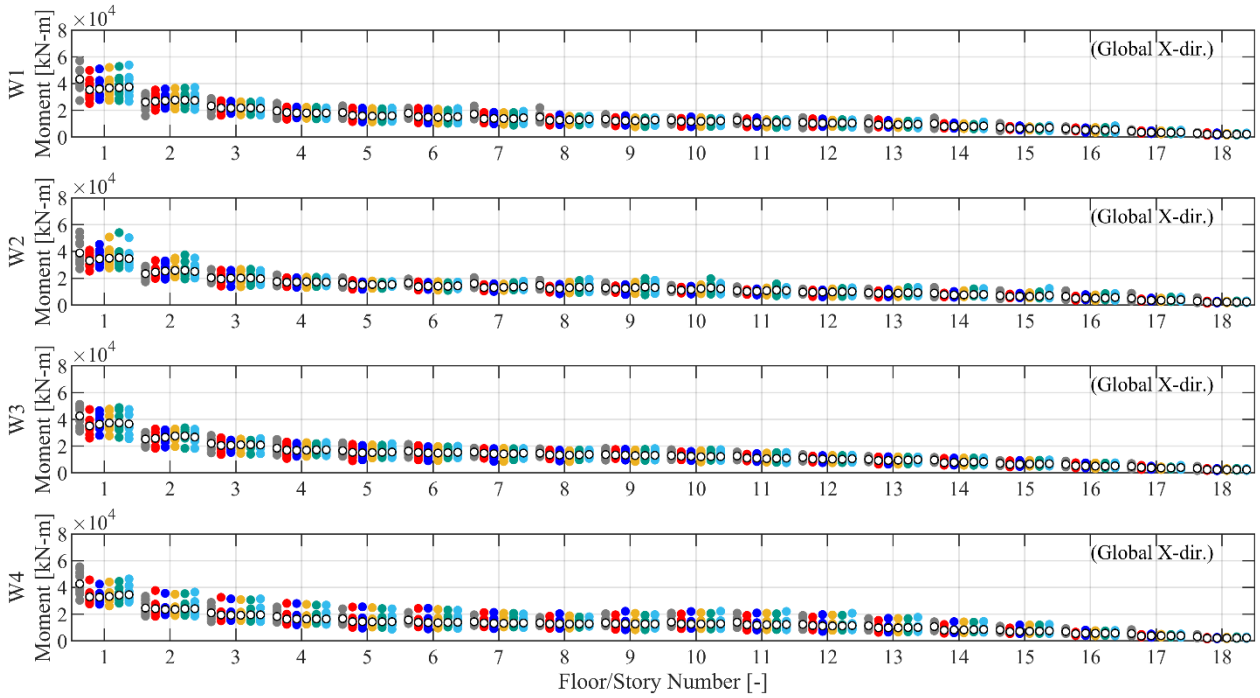

Figure 6-14: Peak moment of the four wall piers about Global X-dir.

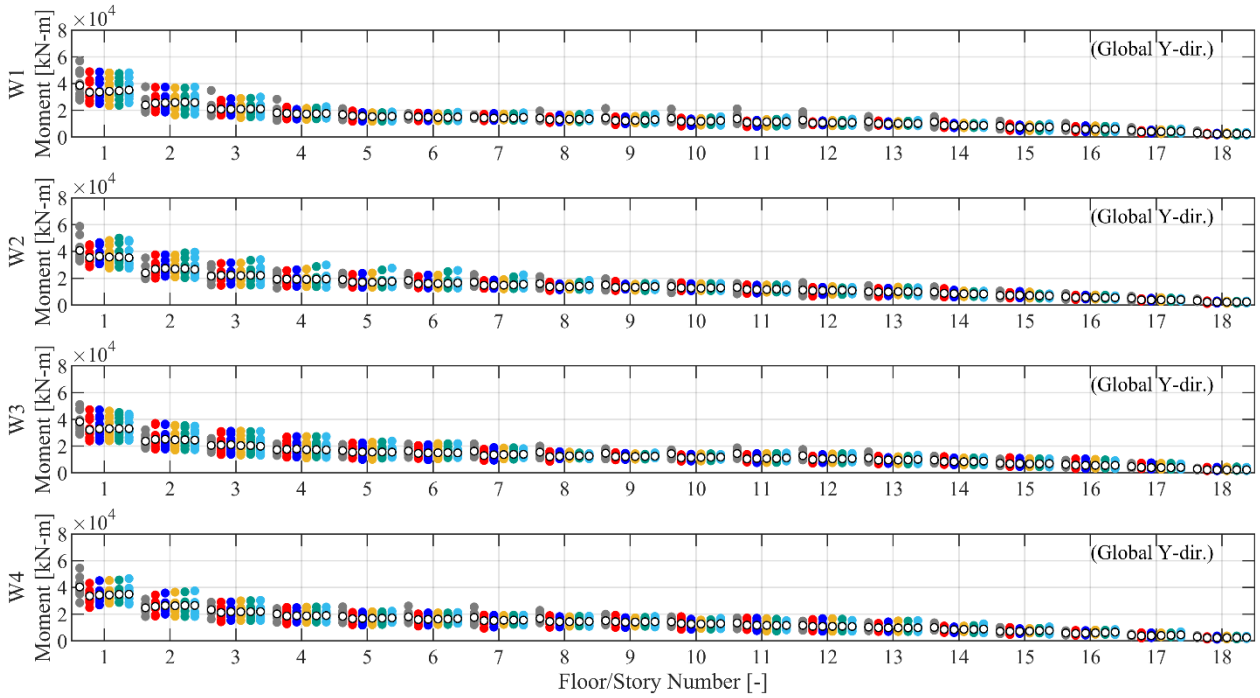

Figure 6-15: Peak moment of the four wall piers about Global Y-dir.

6.4 Force-limiting connections with R_{DC} = 2.0

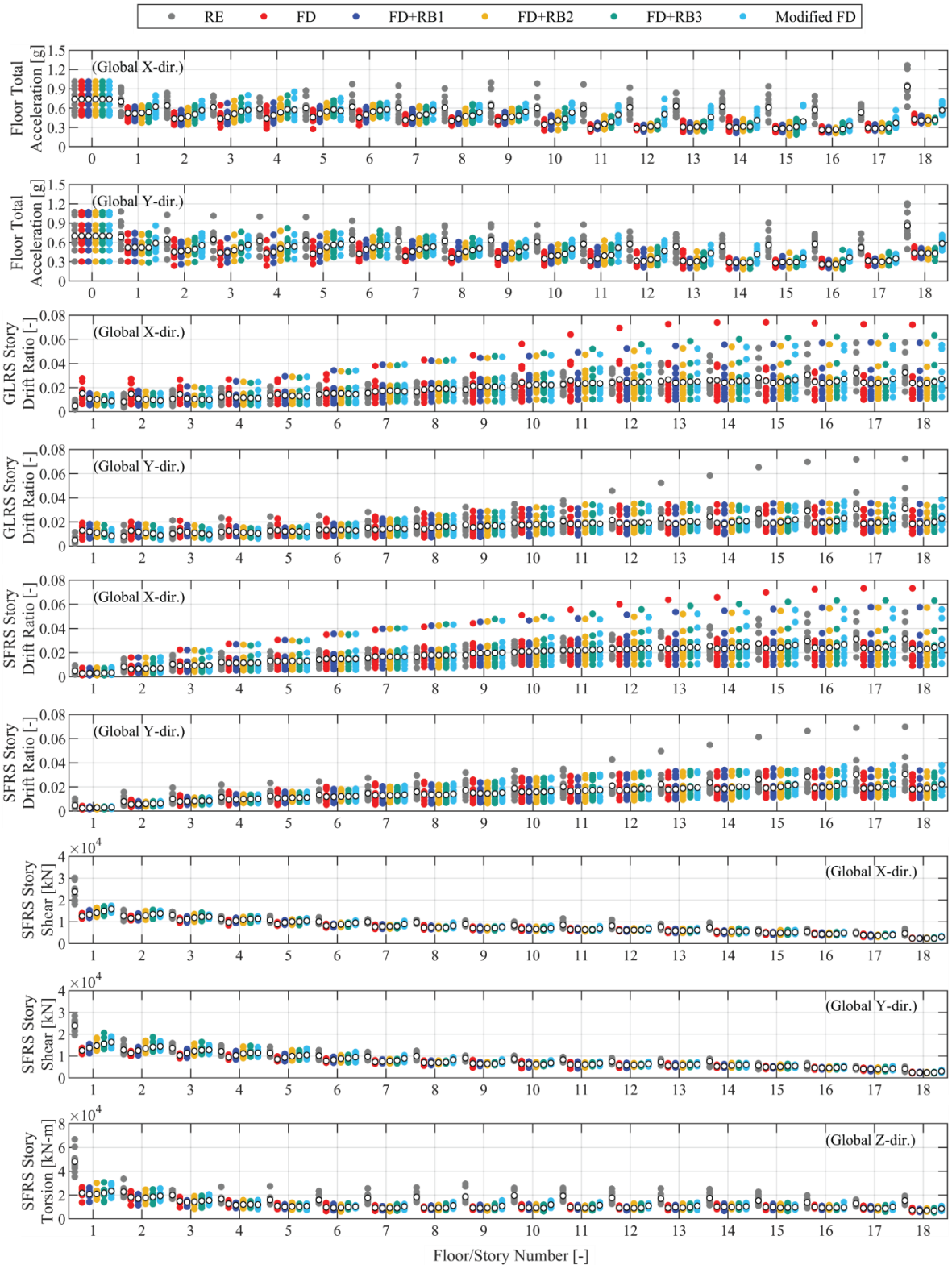

Figure 6-16: Maximum responses of the building models

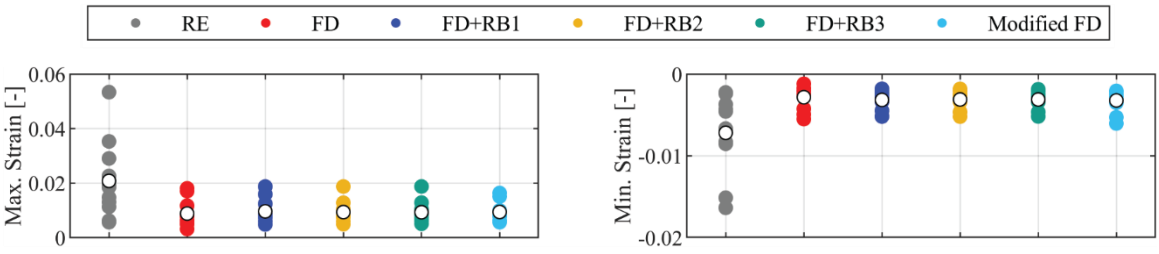

Figure 6-17: Maximum and minimum strain response at the wall base

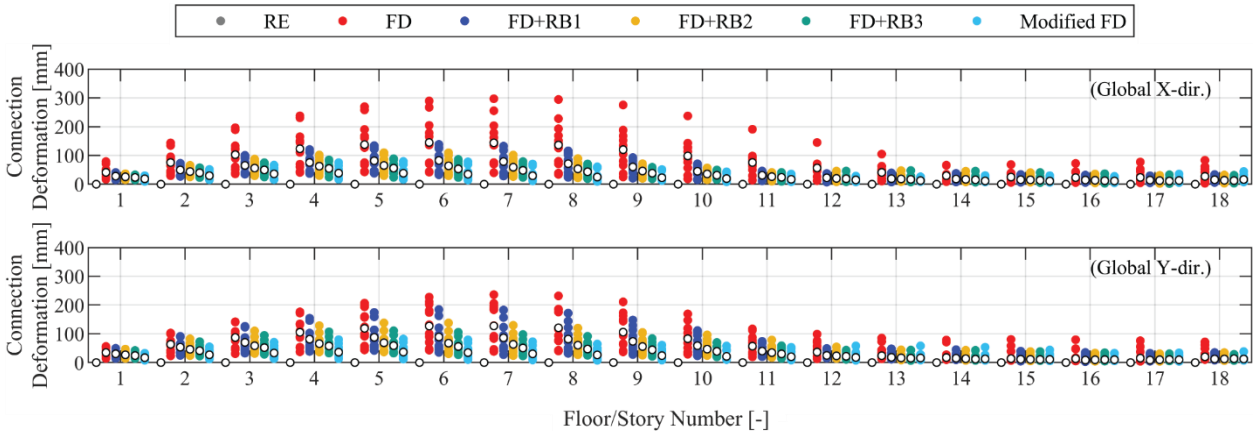

Figure 6-18: Peak connection deformation of the force-limiting connections

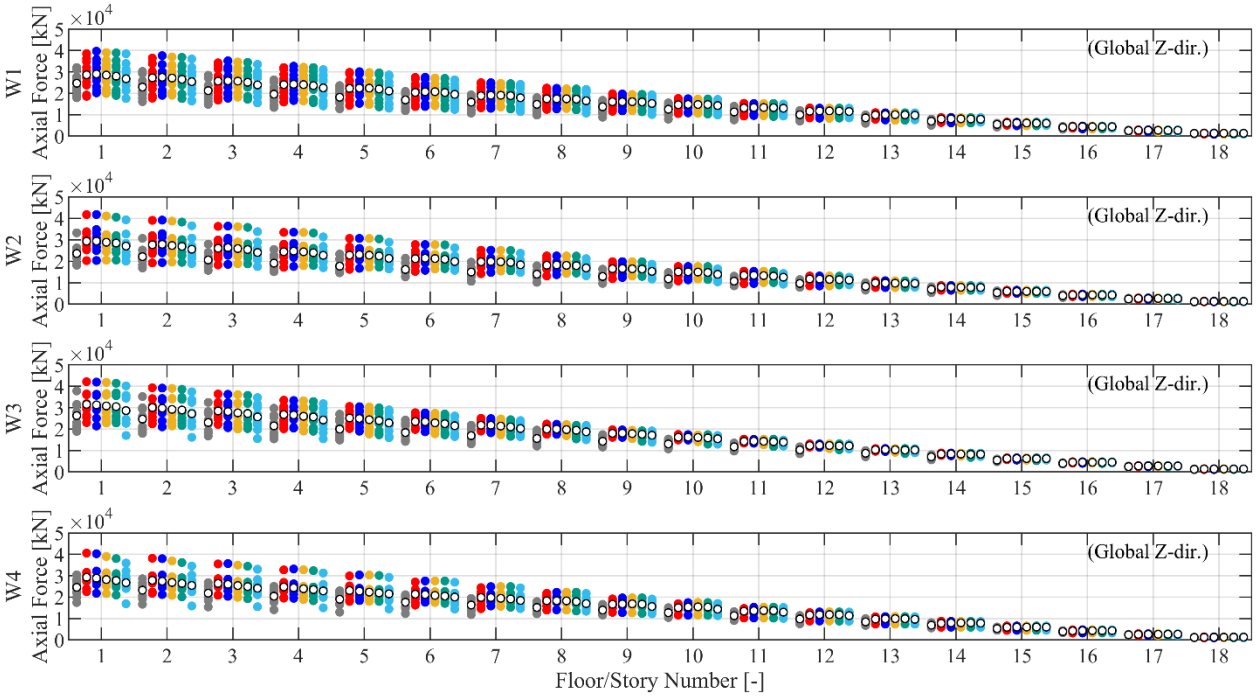

Figure 6-19: Peak axial force of the four wall piers

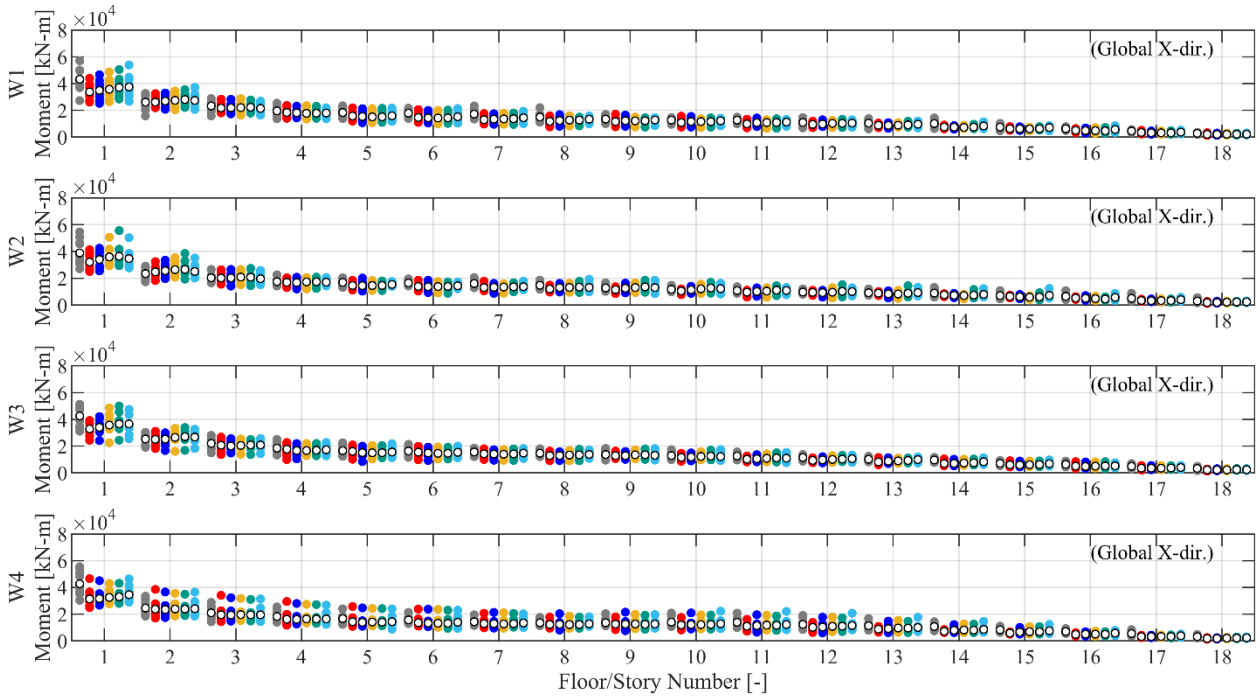

Figure 6-20: Peak moment of the four wall piers about Global X-dir.

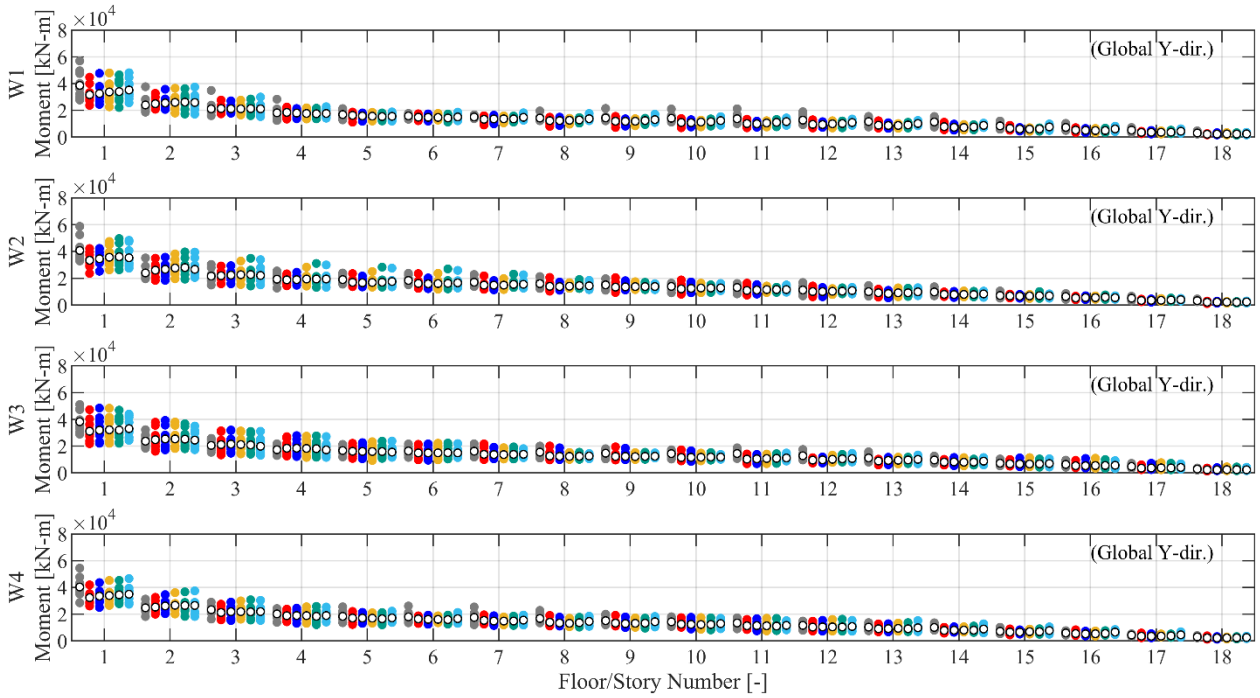

Figure 6-21: Peak moment of the four wall piers about Global Y-dir.

6.5 Force-limiting connections with R_{DC} = 2.5

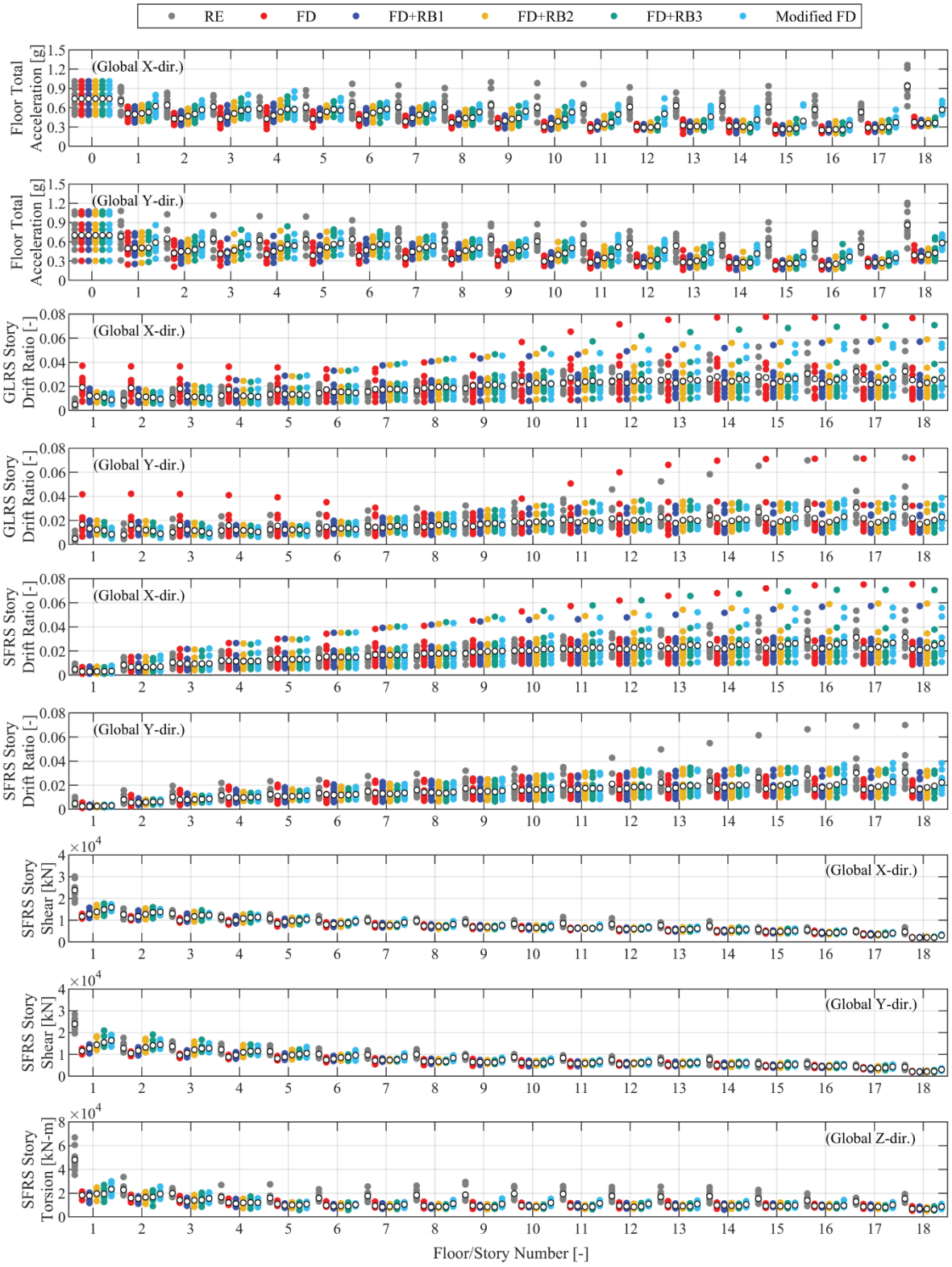

Figure 6-22: Maximum responses of the building models

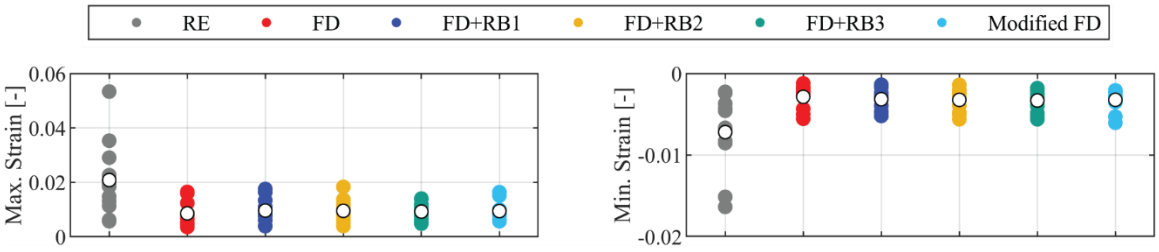

Figure 6-23: Maximum and minimum strain response at the wall base

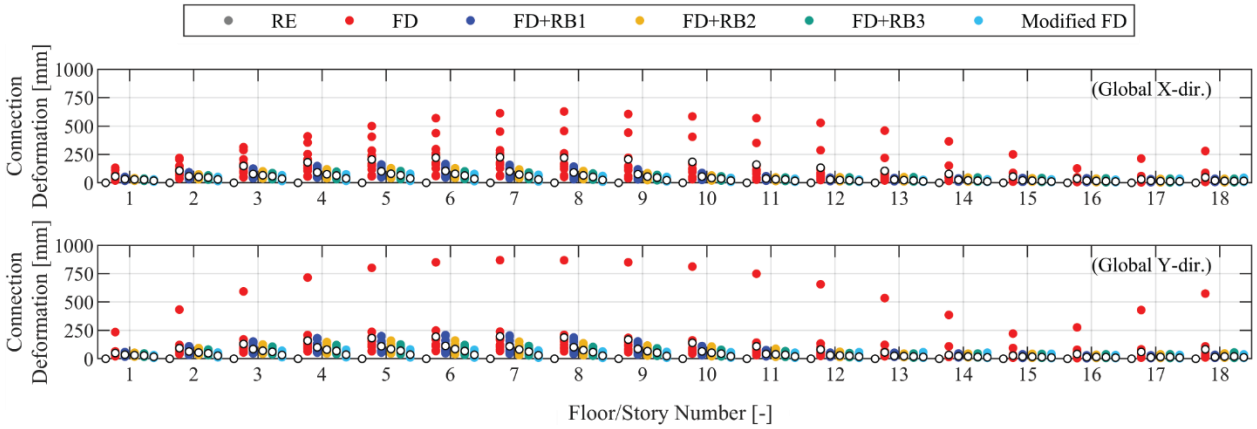

Figure 6-24: Maximum responses of the building models

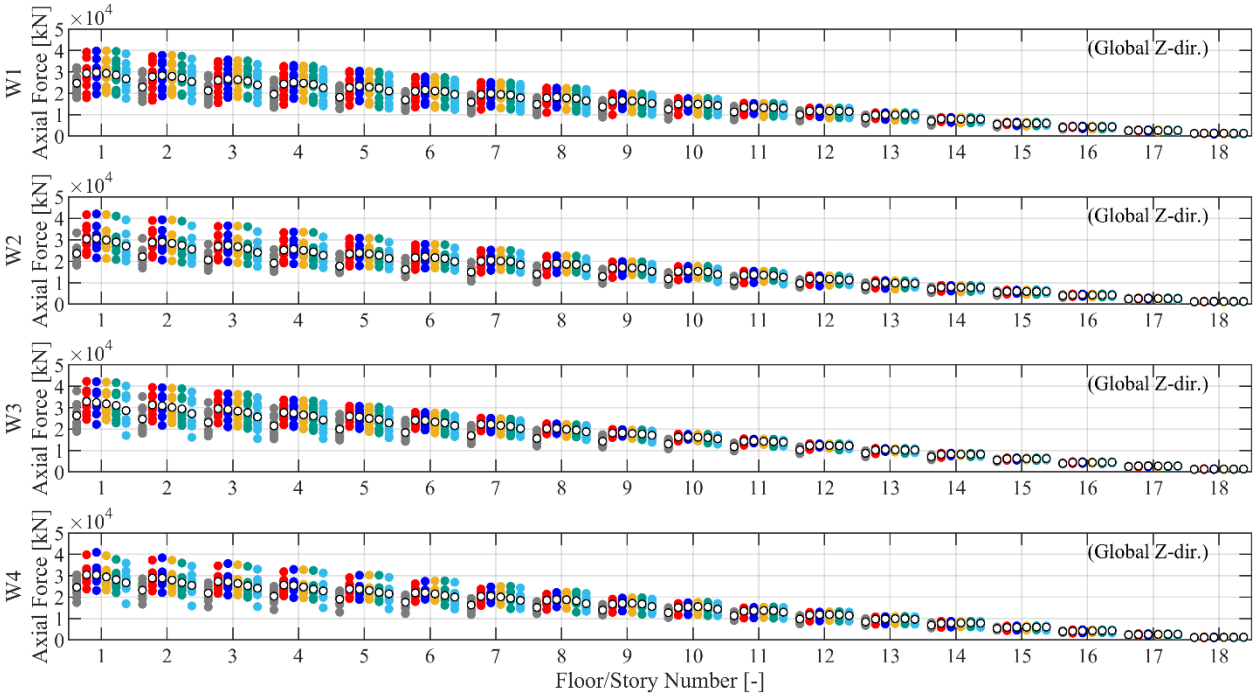

Figure 6-25: Peak axial force of the four wall piers

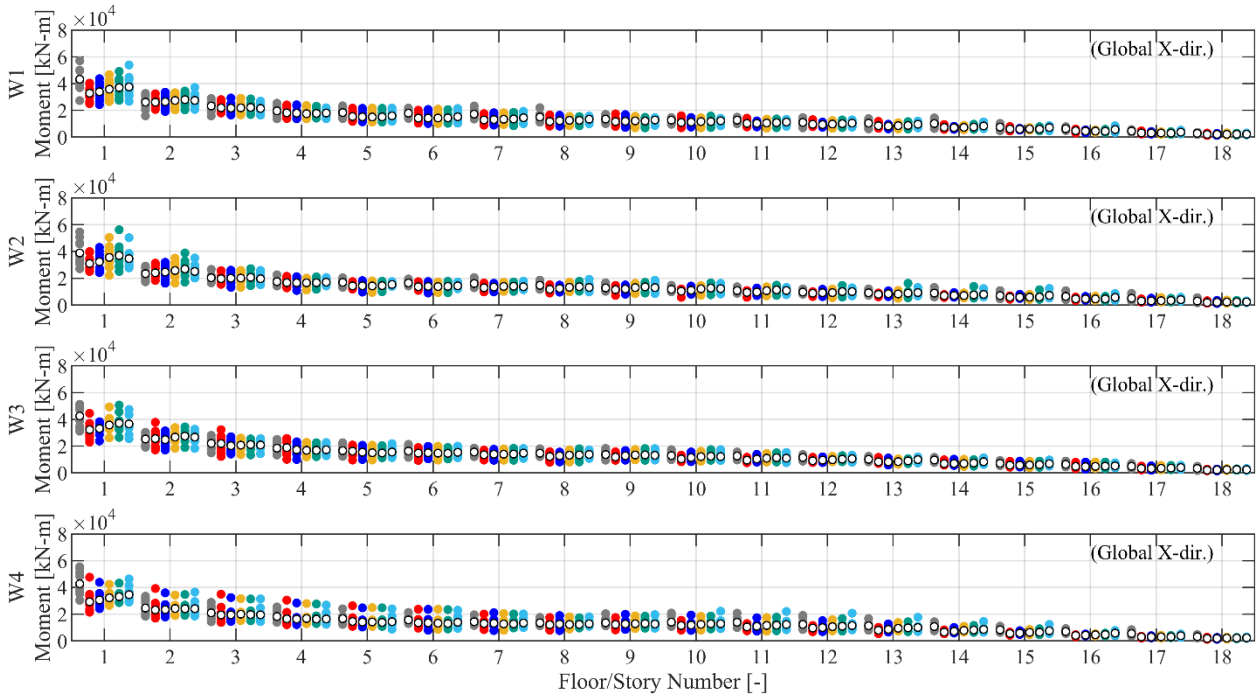

Figure 6-26: Peak moment of the four wall piers about Global X-dir.

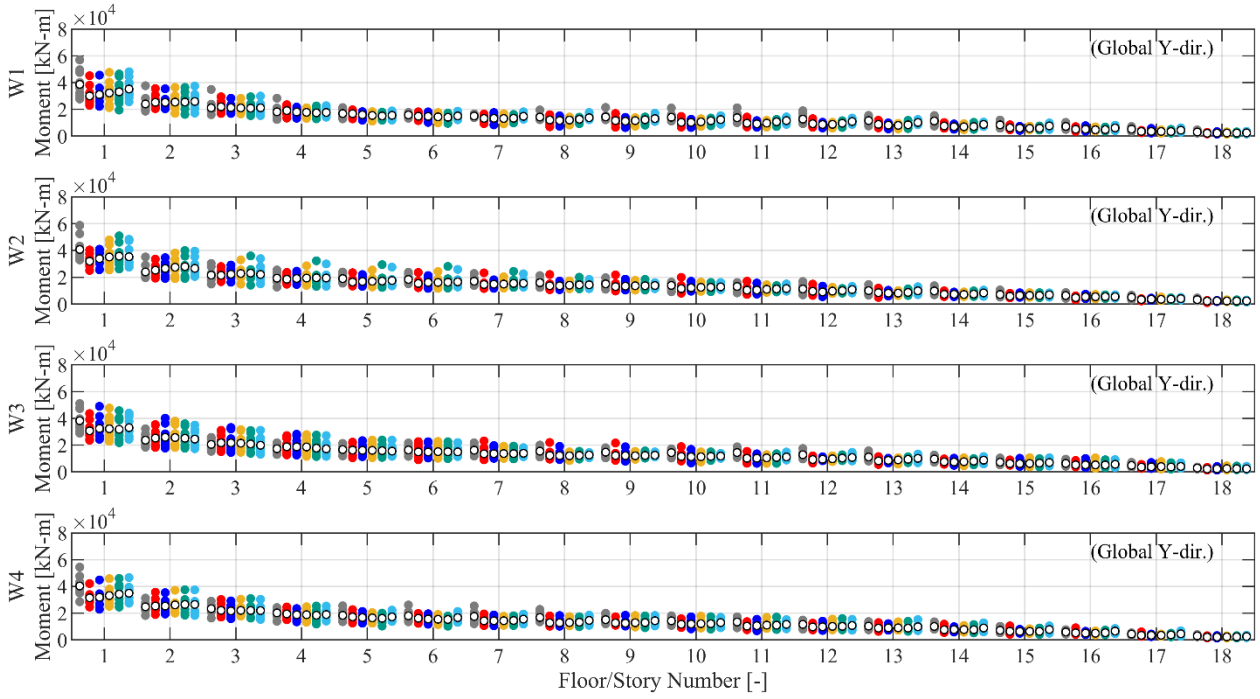

Figure 6-27: Peak moment of the four wall piers about Global Y-dir.

6.6 Low-damage coupling beam

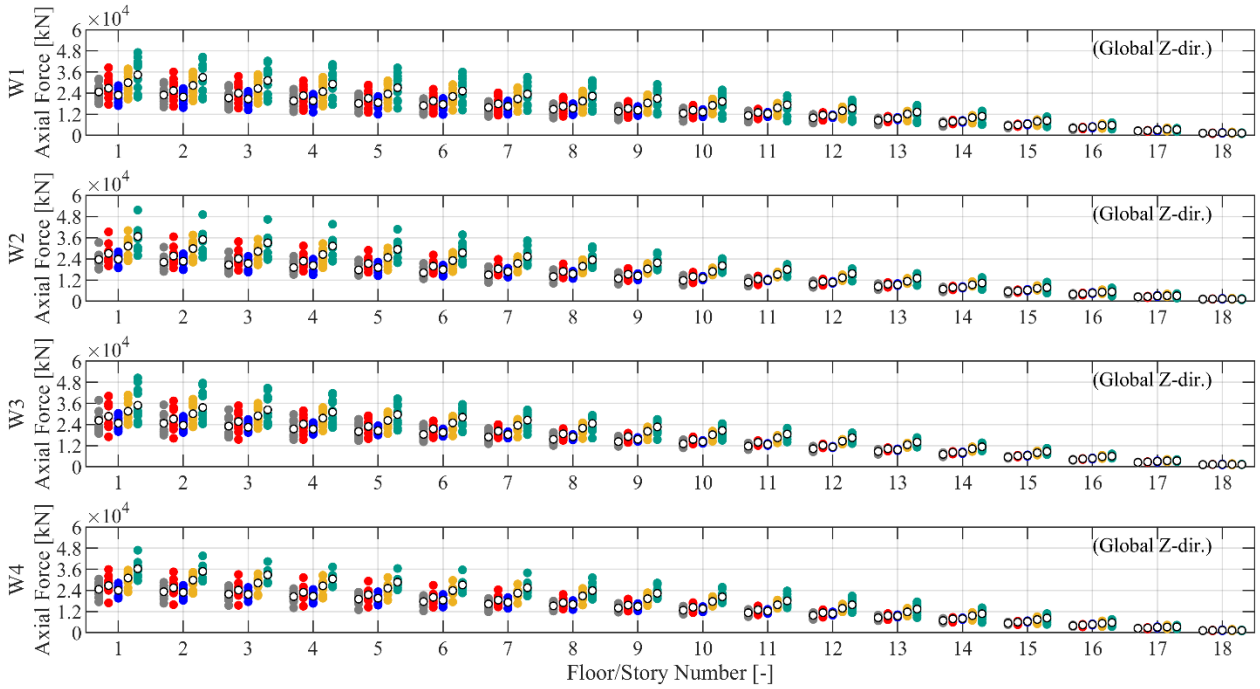

Figure 6-28: Peak axial force of the four wall piers

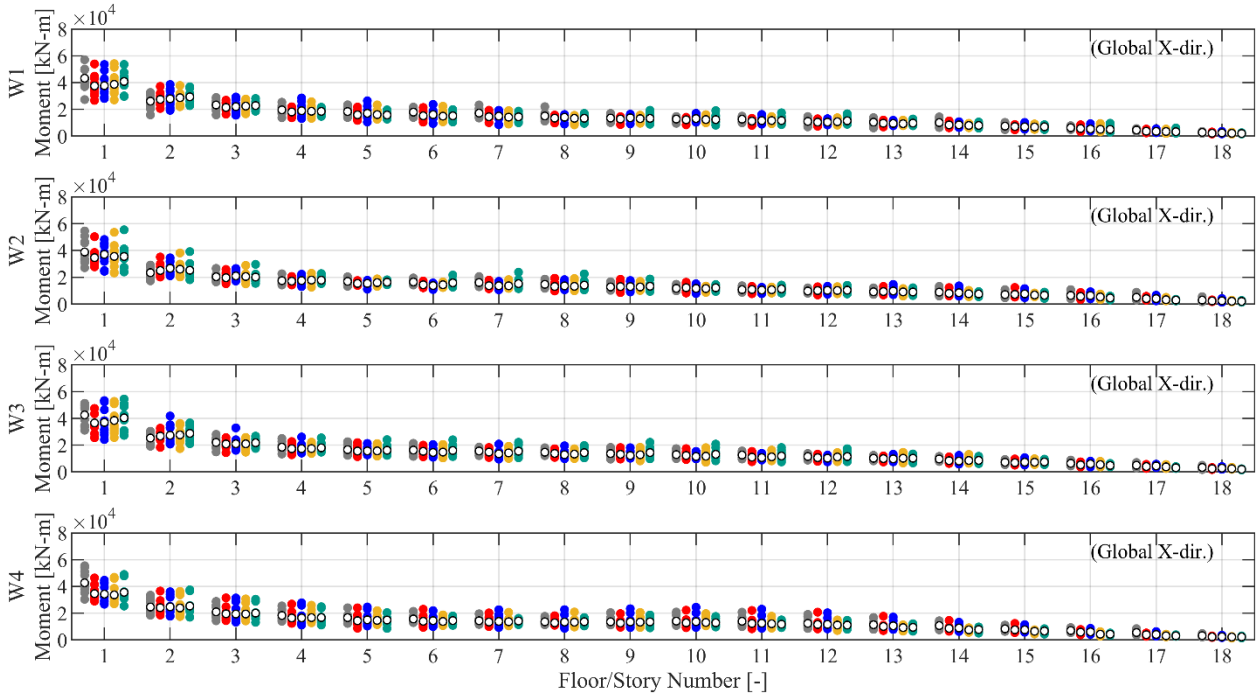

Figure 6-29: Peak moment of the four wall piers about Global X-dir.

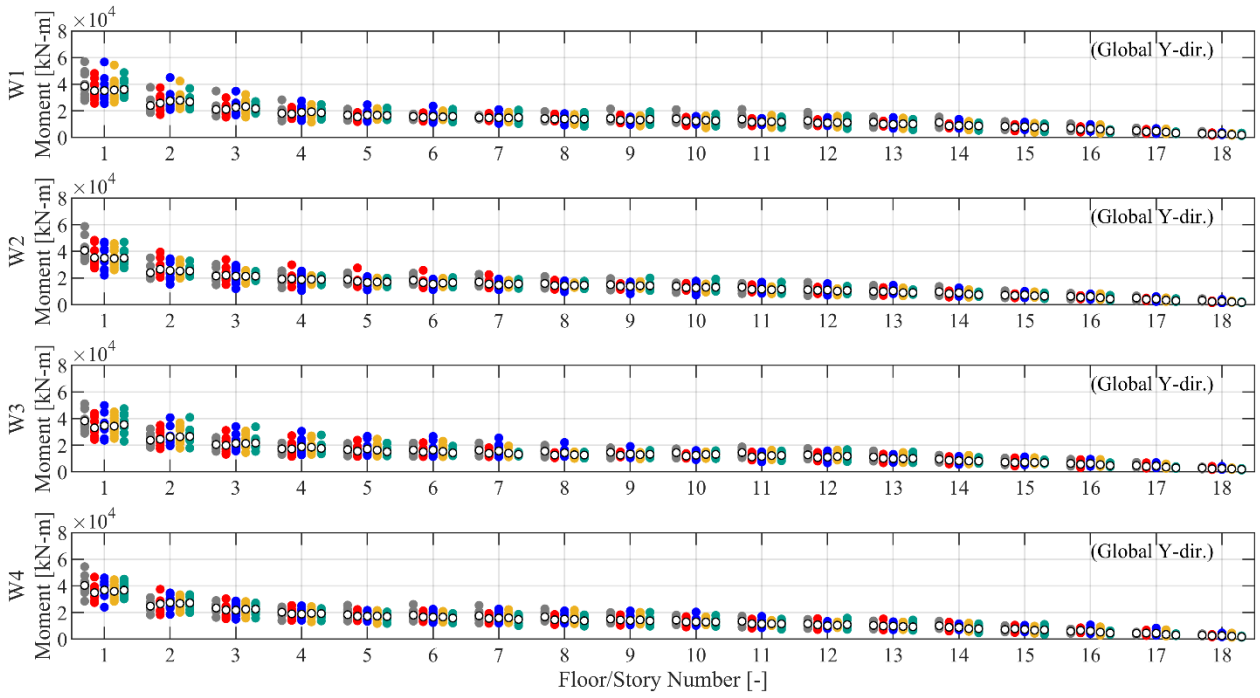

Figure 6-30: Peak moment of the four wall piers about Global Y-dir.

7 [Appendix] Statistics of the earthquake numerical simulation results

7.1 Comparison between the force-limiting connections

7.1.1 Structural level responses

Table 7-1: Peak floor total acceleration, mean [g]

Floor Number	Peak Floor Total Acceleration, Mean [g]							
	(Global *X*-dir.)				(Global *Y*-dir.)			
	RE	FD	FD+RB	Modified FD	RE	FD	FD+RB	Modified FD
Base	0.74	0.74	0.74	0.74	0.70	0.70	0.70	0.70
1	0.70	0.55	0.54	0.62	0.69	0.54	0.54	0.59
2	0.64	0.46	0.46	0.57	0.65	0.46	0.48	0.56
3	0.61	0.46	0.49	0.57	0.65	0.45	0.47	0.56
4	0.59	0.47	0.49	0.57	0.63	0.46	0.47	0.54
5	0.60	0.50	0.53	0.56	0.63	0.46	0.48	0.58
6	0.62	0.52	0.56	0.58	0.64	0.46	0.49	0.56
7	0.61	0.48	0.52	0.57	0.62	0.45	0.48	0.53
8	0.61	0.43	0.47	0.53	0.62	0.42	0.45	0.51
9	0.64	0.42	0.45	0.54	0.64	0.43	0.44	0.53
10	0.60	0.42	0.43	0.53	0.61	0.41	0.45	0.50
11	0.59	0.38	0.38	0.50	0.58	0.38	0.42	0.52
12	0.61	0.35	0.36	0.51	0.58	0.36	0.38	0.47
13	0.63	0.36	0.37	0.46	0.54	0.36	0.36	0.43
14	0.62	0.34	0.35	0.41	0.54	0.34	0.35	0.42
15	0.61	0.33	0.34	0.39	0.56	0.34	0.34	0.36
16	0.57	0.29	0.30	0.33	0.57	0.31	0.31	0.37
17	0.53	0.32	0.33	0.37	0.52	0.33	0.33	0.35
18	**0.94**	**0.50**	**0.50**	**0.57**	0.86	0.51	0.51	0.58
Max.	0.94	0.74	0.74	0.74	0.86	0.70	0.70	0.70
Min.	0.53	0.29	0.30	0.33	0.52	0.31	0.31	0.35

Table 7-2: Peak floor total acceleration, STD [g]

Floor Number	Peak Floor Total Acceleration, STD [%]							
	(Global *X*-dir.)				(Global *Y*-dir.)			
	RE	FD	FD+RB	Modified FD	RE	FD	FD+RB	Modified FD
Base	0.19	0.19	0.19	0.19	0.23	0.23	0.23	0.23
1	0.17	0.10	0.09	0.12	0.21	0.14	0.14	0.16
2	0.14	0.08	0.09	0.09	0.18	0.11	0.11	0.11
3	0.12	0.09	0.10	0.10	0.16	0.08	0.09	0.09
4	0.10	0.10	0.11	0.13	0.15	0.09	0.09	0.10
5	0.13	0.09	0.09	0.10	0.15	0.10	0.10	0.08
6	0.16	0.09	0.08	0.07	0.15	0.08	0.08	0.11
7	0.17	0.06	0.06	0.08	0.14	0.08	0.08	0.08
8	0.15	0.05	0.07	0.08	0.15	0.07	0.08	0.07
9	0.18	0.03	0.06	0.07	0.14	0.08	0.08	0.08
10	0.16	0.05	0.04	0.09	0.12	0.06	0.09	0.08
11	0.14	0.04	0.05	0.09	0.15	0.08	0.13	0.13
12	0.15	0.04	0.04	0.11	0.14	0.09	0.10	0.11
13	0.12	0.04	0.04	0.10	0.15	0.06	0.06	0.09
14	0.13	0.06	0.04	0.10	0.10	0.04	0.05	0.08
15	0.17	0.07	0.05	0.13	0.17	0.04	0.05	0.06
16	0.13	0.04	0.04	0.04	0.11	0.03	0.05	0.06
17	0.10	0.04	0.04	0.08	0.10	0.04	0.04	0.04
18	0.21	0.05	0.04	0.07	0.22	0.07	0.08	0.09
Max.	0.21	0.19	0.19	0.19	0.23	0.23	0.23	0.23
Min.	0.10	0.03	0.04	0.04	0.10	0.03	0.04	0.04

Table 7-3: Peak floor total acceleration, c.o.v [%]

Floor Number	Peak Floor Total Acceleration, c.o.v [%]							
	(Global X-dir.)				(Global Y-dir.)			
	RE	FD	FD+RB	Modified FD	RE	FD	FD+RB	Modified FD
Base	25.9	25.9	25.9	25.9	32.3	32.3	32.3	32.3
1	24.0	17.4	17.3	19.2	30.7	26.8	27.0	27.6
2	21.7	17.7	18.6	16.0	27.1	24.1	22.9	20.5
3	20.0	19.7	20.2	18.1	25.5	18.2	18.3	15.1
4	17.8	21.8	22.8	22.3	24.3	18.8	20.0	17.7
5	21.5	18.9	16.7	18.3	24.1	22.2	20.1	14.7
6	25.9	18.1	14.4	12.0	23.3	16.4	17.2	19.2
7	27.7	12.8	10.7	14.5	22.6	18.0	17.3	15.5
8	24.7	11.3	15.4	15.0	24.8	16.2	18.9	14.1
9	27.5	8.0	12.8	13.0	22.2	17.8	18.3	15.6
10	26.6	12.9	10.0	16.1	19.8	13.7	19.3	15.8
11	24.0	11.5	13.9	18.7	26.1	20.1	29.8	25.1
12	23.9	12.3	10.5	22.5	23.6	25.9	26.7	24.3
13	18.6	12.2	10.8	22.9	27.7	16.1	15.7	20.7
14	20.6	16.6	12.8	23.5	17.8	12.9	14.7	19.7
15	27.3	22.2	15.9	32.0	29.6	12.8	14.6	15.4
16	23.4	14.5	14.8	13.4	19.5	10.7	17.5	17.0
17	17.9	12.4	13.6	22.4	18.4	11.0	10.8	12.0
18	22.4	10.0	9.0	13.1	25.4	14.5	15.4	14.8
Max.	27.7	25.9	25.9	32.0	32.3	32.3	32.3	32.3
Min.	17.8	8.0	9.0	12.0	17.8	10.7	10.8	12.0

Table 7-4: Peak GLRS story drift ratio, mean [%]

Floor Number	Peak GLRS Story Drift Ratio, Mean [%]							
	(Global *X*-dir.)				(Global *Y*-dir.)			
	RE	FD	FD+RB	Modified FD	RE	FD	FD+RB	Modified FD
1	0.50	1.21	0.95	0.89	0.50	1.16	1.01	0.85
2	0.83	1.21	0.98	0.93	0.82	1.18	1.00	0.89
3	1.06	1.22	1.03	1.00	1.03	1.21	1.03	0.95
4	1.22	1.27	1.15	1.13	1.16	1.22	1.10	1.05
5	1.33	1.32	1.29	1.27	1.26	1.28	1.17	1.14
6	1.44	1.47	1.47	1.46	1.36	1.31	1.26	1.27
7	1.55	1.68	1.70	1.68	1.51	1.35	1.37	1.41
8	1.66	1.83	1.87	1.85	1.63	1.41	1.45	1.51
9	1.83	2.02	2.02	2.01	1.76	1.53	1.54	1.62
10	2.09	2.19	2.17	2.21	1.92	1.74	1.68	1.76
11	2.27	2.31	2.29	2.34	2.06	1.91	1.79	1.84
12	2.41	2.41	2.37	2.44	2.15	2.05	1.87	1.92
13	2.53	2.45	2.42	2.49	2.30	2.11	1.91	1.99
14	2.62	2.47	2.44	2.55	2.44	2.17	1.96	2.05
15	2.83	2.48	2.46	2.64	2.71	2.27	2.11	2.20
16	3.05	2.49	2.47	2.72	2.93	2.32	2.17	2.31
17	3.22	2.46	2.44	2.74	3.08	2.29	2.15	2.32
18	3.25	2.44	2.42	2.72	3.12	2.26	2.12	2.29
Max.	3.25	2.49	2.47	2.74	3.12	2.32	2.17	2.32
Min.	0.50	1.21	0.95	0.89	0.50	1.16	1.00	0.85

Table 7-5: Peak GLRS story drift ratio, STD [%]

Floor Number	Peak GLRS Story Drift Ratio, STD [%]							
	(Global *X*-dir.)				(Global *Y*-dir.)			
	RE	FD	FD+RB	Modified FD	RE	FD	FD+RB	Modified FD
1	0.25	0.52	0.29	0.32	0.27	0.37	0.31	0.27
2	0.35	0.50	0.33	0.36	0.38	0.37	0.30	0.25
3	0.42	0.49	0.41	0.45	0.44	0.36	0.26	0.23
4	0.46	0.55	0.51	0.55	0.47	0.37	0.25	0.25
5	0.47	0.67	0.62	0.65	0.49	0.40	0.28	0.31
6	0.48	0.80	0.74	0.77	0.51	0.48	0.37	0.39
7	0.49	0.94	0.85	0.89	0.60	0.56	0.46	0.49
8	0.52	1.05	0.94	0.99	0.65	0.62	0.55	0.57
9	0.59	1.13	1.01	1.08	0.74	0.62	0.62	0.66
10	0.63	1.18	1.05	1.09	0.84	0.67	0.69	0.74
11	0.67	1.16	1.07	1.10	0.90	0.76	0.70	0.78
12	0.72	1.18	1.08	1.16	0.97	0.84	0.69	0.76
13	0.85	1.20	1.07	1.21	1.09	0.91	0.70	0.73
14	1.00	1.22	1.10	1.27	1.23	0.94	0.71	0.69
15	1.14	1.19	1.08	1.34	1.37	0.94	0.70	0.66
16	1.19	1.14	1.02	1.39	1.51	0.94	0.69	0.70
17	1.19	1.13	0.99	1.41	1.61	0.94	0.68	0.73
18	1.21	1.11	0.98	1.42	1.68	0.93	0.68	0.73
Max.	1.21	1.22	1.10	1.42	1.68	0.94	0.71	0.78
Min.	0.25	0.49	0.29	0.32	0.27	0.36	0.25	0.23

Table 7-6: Peak GLRS story drift ratio, c.o.v [%]

Floor Number	Peak GLRS Story Drift Ratio, c.o.v [%]							
	(Global *X*-dir.)				(Global *Y*-dir.)			
	RE	FD	FD+RB	Modified FD	RE	FD	FD+RB	Modified FD
1	50.7	43.1	30.2	35.4	54.2	31.7	31.2	32.1
2	42.4	41.4	33.4	39.0	46.2	31.1	30.1	28.0
3	39.7	40.4	39.7	44.9	42.8	30.3	24.9	23.7
4	37.9	43.5	44.2	48.6	40.5	30.5	22.3	24.1
5	35.7	50.9	48.2	51.1	38.9	31.6	24.3	26.8
6	33.5	54.8	50.5	52.5	37.2	36.2	29.0	30.8
7	31.7	56.1	50.3	52.8	39.5	41.8	33.8	35.0
8	31.4	57.6	50.2	53.7	39.8	44.1	37.8	37.7
9	32.0	55.8	50.2	53.9	41.9	40.6	40.3	40.4
10	29.9	53.7	48.2	49.4	43.8	38.5	40.8	42.0
11	29.4	50.3	46.7	47.0	43.6	39.8	39.1	42.5
12	30.0	49.2	45.5	47.3	45.1	41.0	36.7	39.8
13	33.8	49.0	44.5	48.6	47.5	43.0	36.5	36.7
14	38.3	49.5	44.9	49.9	50.3	43.5	35.9	33.6
15	40.2	48.1	43.7	50.8	50.7	41.6	33.4	30.2
16	39.1	45.9	41.4	51.0	51.4	40.5	31.9	30.5
17	36.9	45.8	40.6	51.3	52.3	40.9	31.5	31.6
18	37.2	45.7	40.4	52.3	54.0	41.0	32.1	31.9
Max.	50.7	57.6	50.5	53.9	54.2	44.1	40.8	42.5
Min.	29.4	40.4	30.2	35.4	37.2	30.3	22.3	23.7

Table 7-7: Peak SFRS story drift ratio, mean [%]

Floor Number	Peak SFRS Story Drift Ratio, Mean [%]							
	(Global *X*-dir.)				(Global *Y*-dir.)			
	RE	FD	FD+RB	Modified FD	RE	FD	FD+RB	Modified FD
1	0.48	0.31	0.32	0.34	0.47	0.27	0.28	0.30
2	0.83	0.68	0.69	0.71	0.80	0.59	0.60	0.64
3	1.05	0.94	0.95	0.96	1.01	0.81	0.82	0.86
4	1.20	1.14	1.15	1.16	1.15	0.97	0.97	1.02
5	1.31	1.28	1.29	1.31	1.25	1.08	1.08	1.13
6	1.43	1.46	1.47	1.48	1.34	1.20	1.19	1.24
7	1.55	1.64	1.64	1.66	1.48	1.31	1.28	1.35
8	1.65	1.78	1.78	1.80	1.60	1.38	1.35	1.42
9	1.80	1.97	1.96	2.00	1.73	1.50	1.46	1.53
10	2.03	2.12	2.11	2.17	1.88	1.62	1.58	1.65
11	2.20	2.21	2.20	2.25	2.02	1.70	1.68	1.74
12	2.33	2.29	2.30	2.36	2.11	1.81	1.78	1.86
13	2.44	2.36	2.37	2.44	2.22	1.90	1.87	1.95
14	2.54	2.38	2.39	2.49	2.36	1.96	1.93	2.01
15	2.75	2.42	2.43	2.63	2.62	2.13	2.09	2.18
16	2.95	2.48	2.45	2.69	2.85	2.18	2.14	2.26
17	3.12	2.46	2.43	2.68	3.02	2.17	2.13	2.27
18	3.13	2.41	2.38	2.63	3.05	2.10	2.08	2.22
Max.	3.13	2.48	2.45	2.69	3.05	2.18	2.14	2.27
Min.	0.48	0.31	0.32	0.34	0.47	0.27	0.28	0.30

Table 7-8: Peak SFRS story drift ratio, STD [%]

Floor Number	Peak SFRS Story Drift Ratio, STD [%]							
	(Global *X*-dir.)				(Global *Y*-dir.)			
	RE	FD	FD+RB	Modified FD	RE	FD	FD+RB	Modified FD
1	0.25	0.19	0.18	0.20	0.24	0.07	0.05	0.07
2	0.36	0.39	0.37	0.39	0.33	0.15	0.11	0.13
3	0.42	0.52	0.50	0.51	0.39	0.22	0.17	0.18
4	0.46	0.63	0.60	0.61	0.43	0.28	0.22	0.23
5	0.47	0.70	0.67	0.69	0.46	0.33	0.26	0.27
6	0.50	0.81	0.79	0.80	0.49	0.43	0.34	0.34
7	0.52	0.90	0.90	0.92	0.58	0.53	0.44	0.43
8	0.54	0.95	0.95	0.99	0.64	0.60	0.52	0.51
9	0.57	1.03	1.02	1.06	0.72	0.69	0.62	0.64
10	0.59	1.08	1.06	1.08	0.81	0.75	0.72	0.76
11	0.63	1.10	1.07	1.08	0.86	0.77	0.75	0.82
12	0.67	1.12	1.09	1.13	0.91	0.80	0.77	0.85
13	0.78	1.15	1.08	1.20	1.03	0.82	0.79	0.84
14	0.90	1.18	1.10	1.25	1.16	0.81	0.78	0.81
15	1.03	1.21	1.11	1.33	1.28	0.78	0.76	0.74
16	1.10	1.20	1.08	1.38	1.42	0.75	0.74	0.76
17	1.11	1.19	1.07	1.39	1.53	0.73	0.73	0.77
18	1.13	1.18	1.05	1.40	1.59	0.71	0.73	0.77
Max.	1.13	1.21	1.11	1.40	1.59	0.82	0.79	0.85
Min.	0.25	0.19	0.18	0.20	0.24	0.07	0.05	0.07

Table 7-9: Peak SFRS story drift ratio, c.o.v [%]

Floor Number	Peak SFRS Story Drift Ratio, c.o.v [%]							
	(Global *X*-dir.)				(Global *Y*-dir.)			
	RE	FD	FD+RB	Modified FD	RE	FD	FD+RB	Modified FD
1	52.6	59.7	57.7	58.2	50.9	25.5	19.4	22.7
2	43.1	57.0	53.9	54.5	41.8	25.1	18.7	20.3
3	39.7	56.1	53.0	53.5	38.7	26.6	20.2	20.7
4	37.9	55.2	52.4	52.9	37.2	29.0	22.6	22.3
5	36.0	54.7	52.0	52.6	36.6	30.9	24.3	23.7
6	34.7	55.6	53.8	54.3	36.3	35.4	28.9	27.3
7	33.3	55.1	54.6	55.2	39.4	40.4	34.5	31.9
8	32.6	53.6	53.4	55.0	40.0	43.5	38.3	36.0
9	31.8	52.2	51.9	53.0	41.9	46.1	42.4	42.1
10	29.2	50.8	50.2	49.9	43.2	46.5	45.3	46.2
11	28.7	49.9	48.5	47.9	42.6	45.5	44.7	47.1
12	28.9	49.1	47.2	47.7	43.4	44.5	43.7	45.7
13	32.1	48.9	45.8	49.2	46.4	43.3	42.1	43.3
14	35.5	49.6	45.9	50.1	49.2	41.5	40.1	40.2
15	37.4	50.0	45.6	50.5	49.0	36.6	36.4	33.9
16	37.2	48.4	43.9	51.2	49.7	34.4	34.4	33.4
17	35.4	48.2	43.9	51.8	50.7	33.6	34.4	33.9
18	36.0	48.9	44.3	53.2	52.1	33.7	34.9	34.8
Max.	52.6	59.7	57.7	58.2	52.1	46.5	45.3	47.1
Min.	28.7	48.2	43.9	47.7	36.3	25.1	18.7	20.3

Table 7-10: Peak SFRS story shear, mean [kN]

Floor Number	Peak SFRS Story Shear, Mean [kN]							
	(Global *X*-dir.)				(Global *Y*-dir.)			
	RE	FD	FD+RB	Modified FD	RE	FD	FD+RB	Modified FD
1	**23,777**	**13,580**	**13,960**	**15,881**	23,973	14,130	14,792	16,404
2	12,659	12,307	12,573	13,823	12,834	12,674	13,315	14,465
3	13,096	11,301	11,495	12,310	13,646	11,362	11,997	12,844
4	11,411	10,582	10,825	11,431	12,203	10,215	10,920	11,539
5	10,828	9,772	10,035	10,460	11,385	9,270	9,983	10,509
6	10,100	8,931	9,165	9,524	10,190	8,549	9,049	9,574
7	9,964	8,139	8,295	8,988	9,806	7,812	8,118	8,939
8	9,747	7,644	7,643	8,187	10,011	7,353	7,358	8,332
9	9,040	7,413	7,385	7,603	9,109	6,918	6,902	7,408
10	8,407	7,000	6,975	7,078	8,698	6,596	6,579	6,871
11	8,618	6,903	6,879	6,882	8,391	6,436	6,461	6,746
12	8,204	6,535	6,607	6,720	7,520	6,326	6,332	6,458
13	7,665	6,145	6,120	6,228	7,300	6,208	6,111	6,227
14	7,444	5,658	5,684	5,743	7,620	5,928	5,873	6,026
15	5,827	4,850	4,965	5,199	5,662	5,209	5,198	5,413
16	5,584	4,557	4,568	4,860	5,585	4,739	4,691	4,946
17	4,857	4,146	4,010	4,058	4,516	4,266	4,237	4,303
18	4,684	2,908	2,904	3,079	4,177	2,940	2,898	3,040
Max.	23,777	13,580	13,960	15,881	23,973	14,130	14,792	16,404
Min.	4,684	2,908	2,904	3,079	4,177	2,940	2,898	3,040

Table 7-11: Peak SFRS story shear, STD [kN]

Floor Number	Peak SFRS Story Shear, STD [kN]							
	(Global *X*-dir.)				(Global *Y*-dir.)			
	RE	FD	FD+RB	Modified FD	RE	FD	FD+RB	Modified FD
1	**3,785**	**1,074**	**1,108**	**1,066**	2,708	795	1,330	1,838
2	1,441	1,019	995	925	2,065	671	1,315	1,480
3	915	807	756	738	1,463	729	1,300	1,327
4	869	604	528	695	1,404	836	1,348	1,336
5	911	618	477	567	1,424	838	1,289	1,579
6	785	542	616	646	1,394	893	1,162	1,633
7	602	432	478	870	1,337	693	747	1,252
8	672	438	399	701	1,297	412	492	920
9	781	660	473	374	927	515	497	715
10	864	626	676	582	826	661	670	595
11	1,429	406	543	609	894	766	637	613
12	1,212	477	407	435	838	871	639	622
13	896	485	465	442	876	564	641	550
14	827	488	587	475	1,105	449	465	585
15	699	351	416	571	857	434	349	425
16	642	372	316	442	880	348	371	460
17	432	302	187	269	431	488	500	563
18	873	146	134	211	721	310	329	311
Max.	3,785	1,074	1,108	1,066	2,708	893	1,348	1,838
Min.	432	146	134	211	431	310	329	311

Table 7-12: Peak SFRS story shear, c.o.v [%]

Floor Number	Peak SFRS Story Shear, c.o.v [%]							
	(Global *X*-dir.)				(Global *Y*-dir.)			
	RE	FD	FD+RB	Modified FD	RE	FD	FD+RB	Modified FD
1	**15.9**	**7.9**	**7.9**	**6.7**	11.3	5.6	9.0	11.2
2	11.4	8.3	7.9	6.7	16.1	5.3	9.9	10.2
3	7.0	7.1	6.6	6.0	10.7	6.4	10.8	10.3
4	7.6	5.7	4.9	6.1	11.5	8.2	12.3	11.6
5	8.4	6.3	4.8	5.4	12.5	9.0	12.9	15.0
6	7.8	6.1	6.7	6.8	13.7	10.4	12.8	17.1
7	6.0	5.3	5.8	9.7	13.6	8.9	9.2	14.0
8	6.9	5.7	5.2	8.6	13.0	5.6	6.7	11.0
9	8.6	8.9	6.4	4.9	10.2	7.4	7.2	9.6
10	10.3	8.9	9.7	8.2	9.5	10.0	10.2	8.7
11	16.6	5.9	7.9	8.8	10.7	11.9	9.9	9.1
12	14.8	7.3	6.2	6.5	11.1	13.8	10.1	9.6
13	11.7	7.9	7.6	7.1	12.0	9.1	10.5	8.8
14	11.1	8.6	10.3	8.3	14.5	7.6	7.9	9.7
15	12.0	7.2	8.4	11.0	15.1	8.3	6.7	7.8
16	11.5	8.2	6.9	9.1	15.8	7.3	7.9	9.3
17	8.9	7.3	4.7	6.6	9.5	11.4	11.8	13.1
18	18.6	5.0	4.6	6.9	17.3	10.5	11.4	10.2
Max.	18.6	8.9	10.3	11.0	17.3	13.8	12.9	17.1
Min.	6.0	5.0	4.6	4.9	9.5	5.3	6.7	7.8

Table 7-13: Peak SFRS story torsional moment, mean [kN-m]

Floor Number	Peak SFRS Story Torsional Moment, Mean [kN-m]			
	(Global *Z*-dir.)			
	RE	FD	FD+RB	Modified FD
1	48,083	23,688	23,826	23,283
2	22,750	19,539	19,460	19,289
3	19,916	14,977	15,112	15,486
4	16,581	11,881	11,890	11,986
5	15,933	10,808	10,869	10,782
6	15,853	10,795	10,646	10,271
7	17,600	10,662	10,301	10,476
8	18,275	10,927	10,322	11,196
9	18,531	10,602	10,467	10,888
10	19,607	11,187	10,802	11,929
11	19,293	10,995	11,098	11,445
12	17,575	10,110	10,958	10,985
13	16,927	10,171	10,582	10,919
14	17,393	10,195	10,126	10,515
15	15,312	9,689	9,684	9,810
16	13,823	10,086	10,501	9,557
17	12,936	9,674	9,981	10,093
18	15,341	8,547	8,633	8,632
max	48,083	23,688	23,826	23,283
min	12,936	8,547	8,633	8,632

Table 7-14: Peak SFRS story torsional moment, STD [kN-m]

Floor Number	Peak SFRS Story Torsional Moment, STD [kN-m] (Global *Z*-dir.)			
	RE	FD	FD+RB	Modified FD
1	9,030	3,793	4,285	3,678
2	4,289	2,468	2,795	2,940
3	2,503	1,879	2,044	2,767
4	3,648	1,517	2,066	2,314
5	4,180	1,472	1,120	1,455
6	3,234	1,687	1,635	886
7	3,599	1,179	1,330	1,220
8	3,603	1,177	1,244	1,749
9	5,140	1,287	1,214	2,257
10	3,936	1,612	1,417	2,043
11	4,264	1,544	1,330	1,697
12	4,102	1,061	1,606	1,383
13	3,660	1,350	1,902	2,045
14	3,988	1,442	1,302	1,801
15	3,863	1,582	1,616	1,280
16	2,873	1,843	1,836	1,682
17	1,706	932	1,727	1,264
18	2,392	1,201	1,412	1,379
max	9,030	3,793	4,285	3,678
min	1,706	932	1,120	886

Table 7-15: Peak SFRS story torsional moment, c.o.v [%]

Floor Number	Peak SFRS Story Torsional Moment, c.o.v [%]			
	(Global *Z*-dir.)			
	RE	FD	FD+RB	Modified FD
1	18.8	16.0	18.0	15.8
2	18.9	12.6	14.4	15.2
3	12.6	12.5	13.5	17.9
4	22.0	12.8	17.4	19.3
5	26.2	13.6	10.3	13.5
6	20.4	15.6	15.4	8.6
7	20.5	11.1	12.9	11.6
8	19.7	10.8	12.1	15.6
9	27.7	12.1	11.6	20.7
10	20.1	14.4	13.1	17.1
11	22.1	14.0	12.0	14.8
12	23.3	10.5	14.7	12.6
13	21.6	13.3	18.0	18.7
14	22.9	14.1	12.9	17.1
15	25.2	16.3	16.7	13.0
16	20.8	18.3	17.5	17.6
17	13.2	9.6	17.3	12.5
18	15.6	14.1	16.4	16.0
max	27.7	18.3	18.0	20.7
min	12.6	9.6	10.3	8.6

7.1.2 Force-limiting connection deformation

Table 7-16: Connection deformation, mean [mm]

Floor Number	Connection Deformation, Mean [mm]							
	(Global *X*-dir.)				(Global *Y*-dir.)			
	RE	FD	FD+RB	Modified FD	RE	FD	FD+RB	Modified FD
1	0.0	27.6	23.6	17.1	0.0	30.1	22.7	18.7
2	0.0	48.7	39.5	27.1	0.0	52.9	38.8	29.6
3	0.0	64.7	50.1	33.3	0.0	69.6	49.6	36.0
4	0.0	77.3	56.5	36.1	0.0	80.8	55.8	38.4
5	0.0	86.5	59.3	36.5	0.0	87.8	58.1	38.1
6	0.0	91.2	58.3	34.6	0.0	88.9	56.3	34.8
7	0.0	91.5	54.6	30.4	0.0	83.5	50.8	29.4
8	0.0	88.1	50.5	26.7	0.0	74.0	44.3	24.9
9	0.0	80.3	47.1	24.3	0.0	61.6	37.9	22.5
10	0.0	67.2	41.9	21.5	0.0	48.5	30.5	19.5
11	0.0	49.2	32.6	20.2	0.0	38.1	23.4	17.0
12	0.0	33.8	23.7	18.0	0.0	30.6	18.3	14.9
13	0.0	23.6	16.0	15.9	0.0	24.0	15.4	12.6
14	0.0	16.7	11.7	12.8	0.0	20.9	14.2	11.4
15	0.0	12.3	10.4	10.9	0.0	21.6	13.9	11.0
16	0.0	11.7	10.0	10.1	0.0	22.3	13.9	11.3
17	0.0	15.3	11.3	9.8	0.0	23.4	13.9	12.9
18	0.0	19.9	13.9	12.5	0.0	25.8	16.0	16.3
Max.	0.0	91.5	59.3	36.5	0.0	88.9	58.1	38.4
Min.	0.0	11.7	10.0	9.8	0.0	20.9	13.9	11.0

Table 7-17: Connection deformation, STD [mm]

Floor Number	Connection Deformation, STD [mm]							
	(Global *X*-dir.)				(Global *Y*-dir.)			
	RE	FD	FD+RB	Modified FD	RE	FD	FD+RB	Modified FD
1	0.0	11.7	9.6	7.7	0.0	14.0	7.5	6.9
2	0.0	23.2	17.7	14.0	0.0	25.3	13.5	12.0
3	0.0	34.6	24.6	18.9	0.0	35.1	18.5	15.4
4	0.0	45.3	30.1	22.4	0.0	43.7	22.7	17.3
5	0.0	54.8	34.2	24.2	0.0	51.5	26.4	18.6
6	0.0	62.1	36.2	24.1	0.0	55.6	28.1	18.9
7	0.0	66.2	36.1	21.7	0.0	55.2	27.4	18.3
8	0.0	67.5	34.5	18.8	0.0	50.1	24.5	16.0
9	0.0	62.8	32.8	17.2	0.0	43.4	19.4	12.7
10	0.0	53.4	30.0	15.7	0.0	34.5	15.0	10.4
11	0.0	41.1	22.8	13.0	0.0	25.6	10.9	8.3
12	0.0	31.4	16.2	10.6	0.0	19.3	10.4	6.3
13	0.0	23.8	10.4	7.6	0.0	17.8	10.4	4.4
14	0.0	17.3	7.9	7.0	0.0	18.4	9.5	4.8
15	0.0	11.5	8.8	7.3	0.0	20.7	8.3	5.5
16	0.0	11.6	9.6	7.5	0.0	25.2	8.8	7.2
17	0.0	16.3	9.8	8.2	0.0	29.5	9.9	9.4
18	0.0	21.5	10.0	9.1	0.0	33.1	10.2	12.5
Max.	0.0	67.5	36.2	24.2	0.0	55.6	28.1	18.9
Min.	0.0	11.5	7.9	7.0	0.0	14.0	7.5	4.4

Table 7-18: Connection deformation, c.o.v [%]

Floor Number	Connection Deformation, c.o.v [%]							
	(Global *X*-dir.)				(Global *Y*-dir.)			
	RE	FD	FD+RB	Modified FD	RE	FD	FD+RB	Modified FD
1	-	42.3	40.5	45.3	-	46.5	33.3	36.9
2	-	47.7	44.9	51.6	-	47.8	34.8	40.4
3	-	53.5	49.2	56.8	-	50.3	37.2	42.7
4	-	58.6	53.3	62.0	-	54.0	40.7	45.1
5	-	63.3	57.7	66.1	-	58.7	45.5	48.7
6	-	68.1	62.1	69.7	-	62.6	49.9	54.4
7	-	72.3	66.2	71.3	-	66.0	54.0	62.3
8	-	76.7	68.4	70.4	-	67.8	55.4	64.2
9	-	78.3	69.6	71.0	-	70.5	51.3	56.6
10	-	79.6	71.6	72.9	-	71.1	49.3	53.1
11	-	83.5	70.0	64.5	-	67.0	46.5	48.6
12	-	93.0	68.3	58.8	-	63.1	56.9	42.0
13	-	101.0	64.8	48.1	-	74.0	67.3	35.2
14	-	103.6	67.0	54.9	-	88.0	66.7	42.0
15	-	93.1	85.4	67.1	-	96.2	59.8	49.8
16	-	99.2	95.9	74.7	-	112.9	63.6	63.9
17	-	106.6	86.8	84.5	-	126.0	71.0	73.0
18	-	108.4	72.0	72.5	-	128.3	63.5	76.7
Max.	-	108.4	95.9	84.5	-	128.3	71.0	76.7
Min.	-	42.3	40.5	45.3	-	46.5	33.3	35.2

7.2 Comparison between the low-damage coupling beams

7.2.1 Structural level responses

Table 7-19: Peak Floor total acceleration, mean [g]

Floor Number	Floor Total Acceleration, Mean [g]									
	(Global X-dir.)					(Global Y-dir.)				
	RE	Modified FD	Mod.FD+ LDCB, DoC=0.3	Mod.FD+ LDCB, DoC=0.4	Mod.FD+ LDCB, DoC=0.5	RE	Modified FD	Mod.FD+ LDCB, DoC=0.3	Mod.FD+ LDCB, DoC=0.4	Mod.FD+ LDCB, DoC=0.5
Base	0.74	0.74	0.74	0.74	0.74	0.7	0.70	0.70	0.70	0.70
1	0.7	0.62	0.62	0.61	0.61	0.69	0.59	0.60	0.58	0.59
2	0.64	0.57	0.56	0.56	0.56	0.65	0.56	0.56	0.56	0.57
3	0.61	0.57	0.59	0.57	0.58	0.65	0.56	0.56	0.57	0.56
4	0.59	0.57	0.59	0.58	0.57	0.63	0.54	0.54	0.55	0.56
5	0.6	0.56	0.58	0.56	0.57	0.63	0.58	0.53	0.56	0.57
6	0.62	0.58	0.58	0.56	0.57	0.64	0.56	0.52	0.55	0.58
7	0.61	0.57	0.53	0.53	0.55	0.62	0.53	0.51	0.56	0.55
8	0.61	0.53	0.50	0.50	0.52	0.62	0.51	0.50	0.50	0.52
9	0.64	0.54	0.53	0.52	0.53	0.64	0.53	0.51	0.52	0.54
10	0.6	0.53	0.52	0.51	0.52	0.61	0.50	0.51	0.53	0.54
11	0.59	0.50	0.48	0.49	0.50	0.58	0.52	0.52	0.51	0.50
12	0.61	0.51	0.46	0.47	0.48	0.58	0.47	0.43	0.45	0.48
13	0.63	0.46	0.42	0.43	0.43	0.54	0.43	0.41	0.43	0.45
14	0.62	0.41	0.39	0.37	0.38	0.54	0.42	0.38	0.39	0.40
15	0.61	0.39	0.35	0.34	0.34	0.56	0.36	0.34	0.35	0.34
16	0.57	0.33	0.31	0.31	0.32	0.57	0.37	0.29	0.32	0.32
17	0.53	0.37	0.32	0.34	0.40	0.52	0.35	0.31	0.38	0.41
18	0.94	0.57	0.50	0.56	0.57	0.86	0.58	0.52	0.60	0.62
Max.	0.94	0.74	0.74	0.74	0.74	0.86	0.70	0.70	0.70	0.70
Min.	0.53	0.33	0.31	0.31	0.32	0.52	0.35	0.29	0.32	0.32

Table 7-20: Peak Floor total acceleration, STD [g]

Floor Number	Floor Total Acceleration, STD [g]									
	(Global X-dir.)					(Global Y-dir.)				
	RE	Modified FD	Mod.FD+ LDCB, DoC=0.3	Mod.FD+ LDCB, DoC=0.4	Mod.FD+ LDCB, DoC=0.5	RE	Modified FD	Mod.FD+ LDCB, DoC=0.3	Mod.FD+ LDCB, DoC=0.4	Mod.FD+ LDCB, DoC=0.5
Base	0.19	0.19	0.19	0.19	0.19	0.23	0.23	0.23	0.23	0.23
1	0.17	0.12	0.11	0.11	0.12	0.21	0.16	0.18	0.16	0.16
2	0.14	0.09	0.08	0.08	0.09	0.18	0.11	0.12	0.11	0.12
3	0.12	0.10	0.10	0.10	0.10	0.16	0.09	0.10	0.09	0.10
4	0.10	0.13	0.13	0.13	0.13	0.15	0.10	0.11	0.09	0.08
5	0.13	0.10	0.09	0.11	0.10	0.15	0.08	0.11	0.10	0.08
6	0.16	0.07	0.09	0.09	0.09	0.15	0.11	0.10	0.10	0.11
7	0.17	0.08	0.09	0.09	0.08	0.14	0.08	0.08	0.08	0.08
8	0.15	0.08	0.06	0.06	0.09	0.15	0.07	0.07	0.06	0.06
9	0.18	0.07	0.05	0.05	0.07	0.14	0.08	0.09	0.08	0.05
10	0.16	0.09	0.06	0.06	0.06	0.12	0.08	0.07	0.08	0.10
11	0.14	0.09	0.08	0.08	0.08	0.15	0.13	0.10	0.12	0.13
12	0.15	0.11	0.09	0.09	0.10	0.14	0.11	0.09	0.09	0.10
13	0.12	0.10	0.06	0.09	0.07	0.15	0.09	0.07	0.08	0.10
14	0.13	0.10	0.06	0.07	0.05	0.10	0.08	0.07	0.07	0.08
15	0.17	0.13	0.04	0.04	0.05	0.17	0.06	0.05	0.05	0.04
16	0.13	0.04	0.03	0.03	0.04	0.11	0.06	0.04	0.04	0.03
17	0.10	0.08	0.02	0.03	0.06	0.10	0.04	0.05	0.05	0.05
18	0.21	0.07	0.04	0.08	0.05	0.22	0.09	0.06	0.10	0.08
Max.	0.21	0.19	0.19	0.19	0.19	0.23	0.23	0.23	0.23	0.23
Min.	0.10	0.04	0.02	0.03	0.04	0.10	0.04	0.04	0.04	0.03

Table 7-21: Peak Floor total acceleration, c.o.v [%]

Floor Number	Floor Total Acceleration, c.o.v [%]									
	(Global X-dir.)					(Global Y-dir.)				
	RE	Modified FD	Mod.FD+ LDCB, DoC=0.3	Mod.FD+ LDCB, DoC=0.4	Mod.FD+ LDCB, DoC=0.5	RE	Modified FD	Mod.FD+ LDCB, DoC=0.3	Mod.FD+ LDCB, DoC=0.4	Mod.FD+ LDCB, DoC=0.5
Base	25.9	25.9	25.9	25.9	25.9	32.3	32.3	32.3	32.3	32.3
1	24.0	19.2	18.4	18.4	19.9	30.7	27.6	30.5	27.9	27.6
2	21.7	16.0	13.9	15.0	15.3	27.1	20.5	21.5	19.4	20.5
3	20.0	18.1	17.3	16.9	17.1	25.5	15.1	16.9	15.8	17.2
4	17.8	22.3	22.0	22.5	23.2	24.3	17.7	20.1	17.1	14.6
5	21.5	18.3	16.3	19.0	18.6	24.1	14.7	20.6	18.8	14.0
6	25.9	12.0	15.2	16.5	14.9	23.3	19.2	19.0	17.6	18.7
7	27.7	14.5	16.1	16.8	14.9	22.6	15.5	16.1	14.4	14.2
8	24.7	15.0	11.5	12.2	17.2	24.8	14.1	14.4	12.0	12.2
9	27.5	13.0	10.2	9.7	13.9	22.2	15.6	18.0	14.5	8.9
10	26.6	16.1	11.1	12.6	12.1	19.8	15.8	14.3	14.4	17.9
11	24.0	18.7	16.7	17.3	16.4	26.1	25.1	20.3	23.9	25.2
12	23.9	22.5	19.2	18.4	20.7	23.6	24.3	19.6	20.1	20.4
13	18.6	22.9	14.6	21.6	17.5	27.7	20.7	17.4	19.5	22.3
14	20.6	23.5	14.3	18.9	14.2	17.8	19.7	17.6	16.9	20.4
15	27.3	32.0	11.6	11.8	13.6	29.6	15.4	14.7	14.6	12.6
16	23.4	13.4	9.1	11.2	13.9	19.5	17.0	12.7	14.0	10.2
17	17.9	22.4	5.2	9.3	14.7	18.4	12.0	15.5	12.1	13.1
18	22.4	13.1	7.0	13.6	8.5	25.4	14.8	11.4	16.3	12.5
Max.	27.7	32.0	25.9	25.9	25.9	32.3	32.3	32.3	32.3	32.3
Min.	17.8	12.0	5.2	9.3	8.5	17.8	12.0	11.4	12.0	8.9

Table 7-22: Peak GLRS story drift ratio, mean [%]

Floor Number	Peak GLRS Story Drift Ratio, Mean [%]									
	(Global X-dir.)					(Global Y-dir.)				
	RE	Modified FD	Mod.FD+ LDCB, DoC=0.3	Mod.FD+ LDCB, DoC=0.4	Mod.FD+ LDCB, DoC=0.5	RE	Modified FD	Mod.FD+ LDCB, DoC=0.3	Mod.FD+ LDCB, DoC=0.4	Mod.FD+ LDCB, DoC=0.5
1	0.50	0.89	0.94	0.94	0.90	0.50	0.85	0.72	0.78	0.86
2	0.83	0.93	1.00	0.98	0.93	0.82	0.89	0.76	0.81	0.89
3	1.06	1.00	1.11	1.09	1.01	1.03	0.95	0.83	0.87	0.93
4	1.22	1.13	1.26	1.22	1.11	1.16	1.05	0.91	0.94	0.97
5	1.33	1.27	1.40	1.35	1.22	1.26	1.14	1.00	1.04	1.04
6	1.44	1.46	1.55	1.50	1.35	1.36	1.27	1.10	1.14	1.13
7	1.55	1.68	1.73	1.66	1.49	1.51	1.41	1.21	1.25	1.24
8	1.66	1.85	1.87	1.79	1.62	1.63	1.51	1.31	1.33	1.33
9	1.83	2.01	2.02	1.92	1.77	1.76	1.62	1.41	1.41	1.43
10	2.09	2.21	2.15	2.07	1.95	1.92	1.76	1.52	1.48	1.57
11	2.27	2.34	2.24	2.15	2.09	2.06	1.84	1.61	1.55	1.66
12	2.41	2.44	2.30	2.21	2.19	2.15	1.92	1.65	1.62	1.73
13	2.53	2.49	2.30	2.23	2.27	2.30	1.99	1.67	1.67	1.83
14	2.62	2.55	2.26	2.22	2.31	2.44	2.05	1.67	1.69	1.93
15	2.83	2.64	2.23	2.22	2.40	2.71	2.20	1.67	1.73	2.01
16	3.05	2.72	2.22	2.19	2.47	2.93	2.31	1.65	1.78	2.11
17	3.22	2.74	2.19	2.14	2.46	3.08	2.32	1.58	1.75	2.13
18	**3.25**	**2.72**	**2.15**	**2.12**	**2.43**	**3.12**	**2.29**	**1.53**	**1.70**	**2.13**
Max.	3.25	2.74	2.30	2.23	2.47	3.12	2.32	1.67	1.78	2.13
Min.	0.50	0.89	0.94	0.94	0.90	0.50	0.85	0.72	0.78	0.86

Table 7-23: Peak GLRS story drift ratio, STD [%]

Floor Number	Peak GLRS Story Drift Ratio, STD [%]									
	(Global X-dir.)					(Global Y-dir.)				
	RE	Modified FD	Mod.FD+ LDCB, DoC=0.3	Mod.FD+ LDCB, DoC=0.4	Mod.FD+ LDCB, DoC=0.5	RE	Modified FD	Mod.FD+ LDCB, DoC=0.3	Mod.FD+ LDCB, DoC=0.4	Mod.FD+ LDCB, DoC=0.5
1	0.25	0.32	0.45	0.39	0.31	0.27	0.27	0.21	0.25	0.33
2	0.35	0.36	0.48	0.43	0.36	0.38	0.25	0.20	0.24	0.31
3	0.42	0.45	0.54	0.49	0.45	0.44	0.23	0.21	0.22	0.27
4	0.46	0.55	0.63	0.58	0.55	0.47	0.25	0.24	0.23	0.25
5	0.47	0.65	0.73	0.67	0.63	0.49	0.31	0.25	0.23	0.25
6	0.48	0.77	0.85	0.76	0.71	0.51	0.39	0.27	0.25	0.27
7	0.49	0.89	0.96	0.82	0.77	0.60	0.49	0.31	0.30	0.35
8	0.52	0.99	1.04	0.85	0.80	0.65	0.57	0.34	0.36	0.41
9	0.59	1.08	1.13	0.87	0.80	0.74	0.66	0.39	0.44	0.48
10	0.63	1.09	1.22	0.87	0.78	0.84	0.74	0.42	0.48	0.52
11	0.67	1.10	1.26	0.88	0.74	0.90	0.78	0.40	0.47	0.55
12	0.72	1.16	1.26	0.90	0.73	0.97	0.76	0.39	0.48	0.58
13	0.85	1.21	1.26	0.91	0.73	1.09	0.73	0.42	0.48	0.57
14	1.00	1.27	1.27	0.91	0.75	1.23	0.69	0.46	0.46	0.54
15	1.14	1.34	1.25	0.89	0.74	1.37	0.66	0.48	0.43	0.54
16	1.19	1.39	1.25	0.85	0.69	1.51	0.70	0.47	0.42	0.52
17	1.19	1.41	1.22	0.82	0.66	1.61	0.73	0.46	0.43	0.51
18	1.21	1.42	**1.19**	**0.80**	**0.64**	1.68	0.73	**0.44**	**0.43**	**0.50**
Max.	1.21	1.42	1.27	0.91	0.80	1.68	0.78	0.48	0.48	0.58
Min.	0.25	0.32	0.45	0.39	0.31	0.27	0.23	0.20	0.22	0.25

Table 7-24: Peak GLRS story drift ratio, c.o.v [%]

Floor Number	Peak GLRS Story Drift Ratio, c.o.v [%]									
	(Global X-dir.)					(Global Y-dir.)				
	RE	Modified FD	Mod.FD+ LDCB, DoC=0.3	Mod.FD+ LDCB, DoC=0.4	Mod.FD+ LDCB, DoC=0.5	RE	Modified FD	Mod.FD+ LDCB, DoC=0.3	Mod.FD+ LDCB, DoC=0.4	Mod.FD+ LDCB, DoC=0.5
1	50.7	35.4	48.2	42.2	34.5	54.2	32.1	28.6	32.7	38.7
2	42.4	39.0	47.9	44.1	39.1	46.2	28.0	26.4	29.7	34.6
3	39.7	44.9	48.6	44.7	44.5	42.8	23.7	25.3	24.8	28.8
4	37.9	48.6	50.2	47.8	49.5	40.5	24.1	26.4	24.3	25.8
5	35.7	51.1	52.3	49.7	51.7	38.9	26.8	25.4	21.8	23.6
6	33.5	52.5	54.5	50.6	52.4	37.2	30.8	24.5	21.7	24.3
7	31.7	52.8	55.5	49.3	51.8	39.5	35.0	25.4	24.2	27.9
8	31.4	53.7	55.8	47.2	49.1	39.8	37.7	26.0	27.2	31.2
9	32.0	53.9	56.2	45.2	45.2	41.9	40.4	27.4	30.9	33.5
10	29.9	49.4	56.7	42.2	39.9	43.8	42.0	28.0	32.3	33.3
11	29.4	47.0	56.2	40.9	35.5	43.6	42.5	24.9	30.1	33.3
12	30.0	47.3	54.8	40.9	33.2	45.1	39.8	23.7	29.9	33.5
13	33.8	48.6	54.8	40.8	32.2	47.5	36.7	25.2	28.5	30.9
14	38.3	49.9	56.4	40.9	32.5	50.3	33.6	27.5	27.2	28.2
15	40.2	50.8	56.0	40.0	30.7	50.7	30.2	28.8	24.9	26.8
16	39.1	51.0	56.2	38.6	28.1	51.4	30.5	28.7	23.7	24.8
17	36.9	51.3	55.9	38.4	26.7	52.3	31.6	28.9	24.5	23.7
18	37.2	52.3	**55.2**	**38.0**	**26.3**	54.0	31.9	**29.0**	**25.0**	**23.4**
Max.	50.7	53.9	56.7	50.6	52.4	54.2	42.5	29.0	32.7	38.7
Min.	29.4	35.4	47.9	38.0	26.3	37.2	23.7	23.7	21.7	23.4

Table 7-25: Peak SFRS story drift ratio, mean [%]

Floor Number	Peak SFRS Story Drift Ratio, Mean [%]									
	(Global X-dir.)					(Global Y-dir.)				
	RE	Modified FD	Mod.FD+ LDCB, DoC=0.3	Mod.FD+ LDCB, DoC=0.4	Mod.FD+ LDCB, DoC=0.5	RE	Modified FD	Mod.FD+ LDCB, DoC=0.3	Mod.FD+ LDCB, DoC=0.4	Mod.FD+ LDCB, DoC=0.5
1	0.48	0.34	0.39	0.39	0.37	0.47	0.30	0.29	0.29	0.31
2	0.83	0.71	0.81	0.80	0.76	0.80	0.64	0.61	0.61	0.62
3	1.05	0.96	1.08	1.07	1.00	1.01	0.86	0.80	0.81	0.82
4	1.20	1.16	1.29	1.27	1.18	1.15	1.02	0.93	0.94	0.95
5	1.31	1.31	1.44	1.41	1.29	1.25	1.13	1.02	1.03	1.04
6	1.43	1.48	1.61	1.55	1.41	1.34	1.24	1.11	1.12	1.15
7	1.55	1.66	1.77	1.69	1.53	1.48	1.35	1.20	1.21	1.23
8	1.65	1.80	1.89	1.80	1.62	1.60	1.42	1.27	1.26	1.28
9	1.80	2.00	2.02	1.92	1.77	1.73	1.53	1.33	1.31	1.37
10	2.03	2.17	2.11	1.99	1.88	1.88	1.65	1.43	1.35	1.43
11	2.20	2.25	2.17	2.03	1.95	2.02	1.74	1.50	1.43	1.51
12	2.33	2.36	2.22	2.08	2.08	2.11	1.86	1.56	1.53	1.63
13	2.44	2.44	2.23	2.12	2.14	2.22	1.95	1.61	1.56	1.74
14	2.54	2.49	2.23	2.14	2.16	2.36	2.01	1.63	1.59	1.80
15	2.75	2.63	2.24	2.19	2.36	2.62	2.18	1.66	1.70	2.03
16	2.95	2.69	2.18	2.14	2.40	2.85	2.26	1.62	1.69	2.10
17	3.12	2.68	2.12	2.08	2.39	3.02	2.27	1.56	1.66	2.12
18	**3.13**	**2.63**	**2.02**	**1.99**	**2.35**	3.05	2.22	1.46	1.57	2.08
Max.	3.13	2.69	2.24	2.19	2.40	3.05	2.27	1.66	1.70	2.12
Min.	0.48	0.34	0.39	0.39	0.37	0.47	0.30	0.29	0.29	0.31

Table 7-26: Peak SFRS story drift ratio, STD [%]

Floor Number	Peak SFRS Story Drift Ratio, STD [%]									
	(Global X-dir.)					(Global Y-dir.)				
	RE	Modified FD	Mod.FD+ LDCB, DoC=0.3	Mod.FD+ LDCB, DoC=0.4	Mod.FD+ LDCB, DoC=0.5	RE	Modified FD	Mod.FD+ LDCB, DoC=0.3	Mod.FD+ LDCB, DoC=0.4	Mod.FD+ LDCB, DoC=0.5
1	0.25	0.20	0.22	0.23	0.25	0.24	0.07	0.07	0.07	0.07
2	0.36	0.39	0.42	0.44	0.45	0.33	0.13	0.14	0.13	0.13
3	0.42	0.51	0.56	0.55	0.56	0.39	0.18	0.19	0.17	0.17
4	0.46	0.61	0.67	0.63	0.63	0.43	0.23	0.23	0.20	0.19
5	0.47	0.69	0.76	0.68	0.66	0.46	0.27	0.25	0.22	0.21
6	0.50	0.80	0.88	0.76	0.72	0.49	0.34	0.29	0.25	0.25
7	0.52	0.92	1.00	0.81	0.76	0.58	0.43	0.33	0.32	0.32
8	0.54	0.99	1.08	0.82	0.77	0.64	0.51	0.38	0.38	0.37
9	0.57	1.06	1.13	0.83	0.80	0.72	0.64	0.45	0.47	0.48
10	0.59	1.08	1.17	0.83	0.74	0.81	0.76	0.49	0.53	0.58
11	0.63	1.08	1.18	0.82	0.70	0.86	0.82	0.48	0.53	0.57
12	0.67	1.13	1.20	0.83	0.70	0.91	0.85	0.46	0.54	0.58
13	0.78	1.20	1.22	0.85	0.67	1.03	0.84	0.45	0.53	0.60
14	0.90	1.25	1.21	0.85	0.68	1.16	0.81	0.46	0.50	0.59
15	1.03	1.33	1.19	0.84	0.71	1.28	0.74	0.45	0.45	0.58
16	1.10	1.38	1.18	0.81	0.69	1.42	0.76	0.43	0.41	0.55
17	1.11	1.39	1.15	0.78	0.67	1.53	0.77	0.43	0.40	0.56
18	1.13	1.40	1.12	0.74	0.66	1.59	0.77	0.42	0.40	0.56
Max.	1.13	1.40	1.22	0.85	0.80	1.59	0.85	0.49	0.54	0.60
Min.	0.25	0.20	0.22	0.23	0.25	0.24	0.07	0.07	0.07	0.07

Table 7-27: Peak SFRS story drift ratio, c.o.v [%]

Floor Number	Peak SFRS Story Drift Ratio, c.o.v [%]									
	(Global X-dir.)					(Global Y-dir.)				
	RE	Modified FD	Mod.FD+ LDCB, DoC=0.3	Mod.FD+ LDCB, DoC=0.4	Mod.FD+ LDCB, DoC=0.5	RE	Modified FD	Mod.FD+ LDCB, DoC=0.3	Mod.FD+ LDCB, DoC=0.4	Mod.FD+ LDCB, DoC=0.5
1	52.6	58.2	57.9	60.3	66.3	50.9	22.7	25.9	22.8	23.4
2	43.1	54.5	52.5	54.8	59.9	41.8	20.3	22.8	21.1	21.5
3	39.7	53.5	51.4	52.0	56.0	38.7	20.7	23.5	21.3	20.7
4	37.9	52.9	52.0	49.9	53.2	37.2	22.3	24.6	21.3	20.0
5	36.0	52.6	52.7	48.6	51.5	36.6	23.7	24.8	21.1	19.9
6	34.7	54.3	54.9	48.8	51.2	36.3	27.3	26.0	22.7	22.0
7	33.3	55.2	56.4	47.6	49.5	39.4	31.9	27.8	26.4	26.1
8	32.6	55.0	57.0	45.7	47.9	40.0	36.0	29.6	29.8	29.3
9	31.8	53.0	55.9	43.3	45.3	41.9	42.1	33.7	35.5	35.2
10	29.2	49.9	55.2	41.6	39.2	43.2	46.2	34.7	39.0	40.2
11	28.7	47.9	54.5	40.5	36.1	42.6	47.1	32.3	37.0	37.9
12	28.9	47.7	54.3	40.1	33.5	43.4	45.7	29.4	35.1	35.5
13	32.1	49.2	54.7	40.2	31.6	46.4	43.3	27.8	33.6	34.5
14	35.5	50.1	54.6	39.6	31.2	49.2	40.2	28.0	31.7	33.1
15	37.4	50.5	53.2	38.5	30.2	49.0	33.9	26.8	26.3	28.4
16	37.2	51.2	53.8	37.8	28.7	49.7	33.4	26.8	24.3	26.5
17	35.4	51.8	54.6	37.3	27.9	50.7	33.9	27.5	24.2	26.3
18	36.0	53.2	55.2	37.1	28.0	52.1	34.8	28.8	25.2	27.0
Max.	52.6	58.2	57.9	60.3	66.3	52.1	47.1	34.7	39.0	40.2
Min.	28.7	47.7	51.4	37.1	27.9	36.3	20.3	22.8	21.1	19.9

Table 7-28: Peak SFRS story shear, mean [kN]

Floor Number	Peak SFRS Story Shear, Mean [kN]									
	(Global X-dir.)					(Global Y-dir.)				
	RE	Modified FD	Mod.FD+ LDCB, DoC=0.3	Mod.FD+ LDCB, DoC=0.4	Mod.FD+ LDCB, DoC=0.5	RE	Modified FD	Mod.FD+ LDCB, DoC=0.3	Mod.FD+ LDCB, DoC=0.4	Mod.FD+ LDCB, DoC=0.5
1	23,777	15,881	14,577	15,379	16,360	23,973	16,404	14,826	16,088	17,546
2	12,659	13,823	12,523	13,439	14,503	12,834	14,465	12,868	14,159	15,601
3	13,096	12,310	10,892	11,887	12,975	13,646	12,844	11,357	12,653	13,953
4	11,411	11,431	9,902	11,016	12,000	12,203	11,539	10,103	11,364	12,795
5	10,828	10,460	8,920	10,150	11,338	11,385	10,509	8,877	10,142	11,823
6	10,100	9,524	8,158	9,302	10,690	10,190	9,574	7,849	9,115	10,481
7	9,964	8,988	7,786	8,857	9,986	9,806	8,939	7,403	8,396	9,711
8	9,747	8,187	7,164	8,049	9,177	10,011	8,332	6,833	7,874	9,061
9	9,040	7,603	6,808	7,770	8,768	9,109	7,408	6,280	7,269	8,218
10	8,407	7,078	6,390	7,301	8,012	8,698	6,871	6,125	7,180	7,972
11	8,618	6,882	6,134	7,105	8,017	8,391	6,746	6,169	6,937	7,725
12	8,204	6,720	5,823	6,910	7,754	7,520	6,458	5,686	6,633	7,528
13	7,665	6,228	5,493	6,442	7,372	7,300	6,227	5,406	6,332	7,090
14	7,444	5,743	5,008	6,127	7,166	7,620	6,026	5,240	6,463	7,282
15	5,827	5,199	4,702	5,557	6,242	5,662	5,413	5,137	5,862	6,458
16	5,584	4,860	4,512	5,224	5,785	5,585	4,946	4,587	5,496	5,967
17	4,857	4,058	3,928	4,638	5,179	4,516	4,303	3,957	4,811	5,326
18	4,684	3,079	**3,004**	**3,130**	**3,307**	4,177	3,040	3,027	3,216	3,497
Max.	23,777	15,881	14,577	15,379	16,360	23,973	16,404	14,826	16,088	17,546
Min.	4,684	3,079	3,004	3,130	3,307	4,177	3,040	3,027	3,216	3,497

Table 7-29: Peak SFRS story shear, STD [kN]

Floor Number	Peak SFRS Story Shear, STD [kN]									
	(Global X-dir.)					(Global Y-dir.)				
	RE	Modified FD	Mod.FD+ LDCB, DoC=0.3	Mod.FD+ LDCB, DoC=0.4	Mod.FD+ LDCB, DoC=0.5	RE	Modified FD	Mod.FD+ LDCB, DoC=0.3	Mod.FD+ LDCB, DoC=0.4	Mod.FD+ LDCB, DoC=0.5
1	3,785	1,066	1,155	941	1,276	2,708	1,838	1,571	1,566	1,276
2	1,441	925	894	839	1,094	2,065	1,480	1,184	1,251	1,094
3	915	738	686	770	848	1,463	1,327	1,065	1,085	848
4	869	695	652	751	826	1,404	1,336	1,141	1,200	826
5	911	567	674	612	676	1,424	1,579	1,284	1,312	676
6	785	646	583	611	677	1,394	1,633	1,440	1,470	677
7	602	870	851	897	955	1,337	1,252	1,181	1,216	955
8	672	701	673	563	713	1,297	920	832	696	713
9	781	374	468	501	583	927	715	561	724	583
10	864	582	674	537	744	826	595	700	667	744
11	1,429	609	482	401	668	894	613	563	766	668
12	1,212	435	460	510	647	838	622	711	833	647
13	896	442	556	583	531	876	550	541	728	531
14	827	475	355	563	806	1,105	585	495	705	806
15	699	571	309	635	766	857	425	361	375	766
16	642	442	187	584	793	880	460	281	280	793
17	432	269	229	457	648	431	563	180	408	648
18	873	211	186	269	331	721	311	227	274	331
Max.	3,785	1,066	1,155	941	1,276	2,708	1,838	1,571	1,566	1,276
Min.	432	211	186	269	331	431	311	180	274	331

Table 7-30: Peak SFRS story shear, c.o.v [%]

Floor Number	Peak SFRS Story Shear, c.o.v [%]									
	(Global X-dir.)					(Global Y-dir.)				
	RE	Modified FD	Mod.FD+ LDCB, DoC=0.3	Mod.FD+ LDCB, DoC=0.4	Mod.FD+ LDCB, DoC=0.5	RE	Modified FD	Mod.FD+ LDCB, DoC=0.3	Mod.FD+ LDCB, DoC=0.4	Mod.FD+ LDCB, DoC=0.5
1	15.9	6.7	7.9	6.1	7.8	11.3	11.2	10.6	9.7	9.3
2	11.4	6.7	7.1	6.2	7.5	16.1	10.2	9.2	8.8	9.2
3	7.0	6.0	6.3	6.5	6.5	10.7	10.3	9.4	8.6	8.9
4	7.6	6.1	6.6	6.8	6.9	11.5	11.6	11.3	10.6	10.3
5	8.4	5.4	7.6	6.0	6.0	12.5	15.0	14.5	12.9	11.5
6	7.8	6.8	7.1	6.6	6.3	13.7	17.1	18.3	16.1	14.5
7	6.0	9.7	10.9	10.1	9.6	13.6	14.0	15.9	14.5	12.2
8	6.9	8.6	9.4	7.0	7.8	13.0	11.0	12.2	8.8	10.0
9	8.6	4.9	6.9	6.5	6.7	10.2	9.6	8.9	10.0	11.9
10	10.3	8.2	10.5	7.4	9.3	9.5	8.7	11.4	9.3	9.8
11	16.6	8.8	7.8	5.6	8.3	10.7	9.1	9.1	11.0	8.5
12	14.8	6.5	7.9	7.4	8.3	11.1	9.6	12.5	12.6	10.2
13	11.7	7.1	10.1	9.1	7.2	12.0	8.8	10.0	11.5	11.6
14	11.1	8.3	7.1	9.2	11.3	14.5	9.7	9.5	10.9	9.5
15	12.0	11.0	6.6	11.4	12.3	15.1	7.8	7.0	6.4	7.9
16	11.5	9.1	4.1	11.2	13.7	15.8	9.3	6.1	5.1	7.1
17	8.9	6.6	5.8	9.9	12.5	9.5	13.1	4.5	8.5	11.5
18	18.6	6.9	6.2	8.6	10.0	17.3	10.2	7.5	8.5	7.6
Max.	18.6	11.0	10.9	11.4	13.7	17.3	17.1	18.3	16.1	14.5
Min.	6.0	4.9	4.1	5.6	6.0	9.5	7.8	4.5	5.1	7.1

Table 7-31: Peak SFRS story torsional moment, mean [kN-m]

Floor Number	Peak SFRS Story Torsional Moment, Mean [kN-m]				
	(Global Z-dir.)				
	RE	Modified FD	Mod.FD+LDCB, DoC=0.3	Mod.FD+LDCB, DoC=0.4	Mod.FD+LDCB, DoC=0.5
1	48,083	23,283	19,179	20,791	22,193
2	22,750	19,289	15,720	17,160	18,602
3	19,916	15,486	12,957	13,933	15,678
4	16,581	11,986	10,593	12,085	14,184
5	15,933	10,782	8,962	10,769	13,090
6	15,853	10,271	8,952	10,135	12,248
7	17,600	10,476	9,679	9,569	11,532
8	18,275	11,196	9,246	10,221	12,071
9	18,531	10,888	9,364	10,351	11,794
10	19,607	11,929	9,712	11,232	11,613
11	19,293	11,445	9,620	10,257	11,981
12	17,575	10,985	8,736	10,409	12,952
13	16,927	10,919	8,659	10,334	12,481
14	17,393	10,515	9,131	10,679	12,427
15	15,312	9,810	8,976	9,550	11,132
16	13,823	9,557	9,367	9,934	10,804
17	12,936	10,093	10,127	9,619	10,857
18	15,341	8,632	8,069	7,981	8,783
max	48,083	23,283	19,179	20,791	22,193
min	12,936	8,632	8,069	7,981	8,783

Table 7-32: Peak SFRS story torsional moment, STD [kN-m]

Floor Number	Peak SFRS Story Torsional Moment, STD [kN-m] (Global Z-dir.)				
	RE	Modified FD	Mod.FD+LDCB, DoC=0.3	Mod.FD+LDCB, DoC=0.4	Mod.FD+LDCB, DoC=0.5
1	9,030	3,678	3,556	3,310	2,866
2	4,289	2,940	2,217	2,106	3,141
3	2,503	2,767	2,015	1,623	2,984
4	3,648	2,314	1,380	1,220	2,261
5	4,180	1,455	984	1,093	1,542
6	3,234	886	1,000	1,504	1,389
7	3,599	1,220	1,486	1,323	1,716
8	3,603	1,749	1,446	1,087	1,443
9	5,140	2,257	1,697	941	2,221
10	3,936	2,043	1,198	1,642	1,494
11	4,264	1,697	1,507	1,033	1,234
12	4,102	1,383	954	1,163	1,934
13	3,660	2,045	1,037	1,200	1,374
14	3,988	1,801	1,501	1,262	1,510
15	3,863	1,280	1,670	1,248	1,986
16	2,873	1,682	1,535	1,460	1,554
17	1,706	1,264	1,750	1,938	1,470
18	2,392	1,379	779	1,385	1,276
max	9,030	3,678	3,556	3,310	3,141
min	1,706	886	779	941	1,234

Table 7-33: Peak SFRS story torsional moment, c.o.v [%]

Floor Number	Peak SFRS Story Torsional Moment, c.o.v [%]				
	(Global Z-dir.)				
	RE	Modified FD	Mod.FD+LDCB, DoC=0.3	Mod.FD+LDCB, DoC=0.4	Mod.FD+LDCB, DoC=0.5
1	18.8	15.8	18.5	15.9	12.9
2	18.9	15.2	14.1	12.3	16.9
3	12.6	17.9	15.6	11.6	19.0
4	22.0	19.3	13.0	10.1	15.9
5	26.2	13.5	11.0	10.2	11.8
6	20.4	8.6	11.2	14.8	11.3
7	20.5	11.6	15.4	13.8	14.9
8	19.7	15.6	15.6	10.6	12.0
9	27.7	20.7	18.1	9.1	18.8
10	20.1	17.1	12.3	14.6	12.9
11	22.1	14.8	15.7	10.1	10.3
12	23.3	12.6	10.9	11.2	14.9
13	21.6	18.7	12.0	11.6	11.0
14	22.9	17.1	16.4	11.8	12.1
15	25.2	13.0	18.6	13.1	17.8
16	20.8	17.6	16.4	14.7	14.4
17	13.2	12.5	17.3	20.1	13.5
18	15.6	16.0	9.7	17.4	14.5
max	27.7	20.7	18.6	20.1	19.0
min	12.6	8.6	9.7	9.1	10.3

7.2.2 Force-limiting connection deformation

Table 7-34: Connection deformation, mean [mm]

Floor Number	Connection Deformation, Mean [mm]									
	(Global X-dir.)					(Global Y-dir.)				
	RE	Modified FD	Mod.FD+ LDCB, DoC=0.3	Mod.FD+ LDCB, DoC=0.4	Mod.FD+ LDCB, DoC=0.5	RE	Modified FD	Mod.FD+ LDCB, DoC=0.3	Mod.FD+ LDCB, DoC=0.4	Mod.FD+ LDCB, DoC=0.5
1	0.0	17.1	14.9	16.0	17.6	0.0	18.7	19.3	19.0	18.3
2	0.0	27.1	23.9	26.2	28.4	0.0	29.6	29.6	29.5	29.4
3	0.0	33.3	28.8	32.3	35.3	0.0	36.0	34.2	35.1	36.4
4	0.0	36.1	30.6	35.0	39.0	0.0	38.4	34.6	36.8	39.2
5	0.0	36.5	30.3	35.5	40.8	0.0	38.1	32.2	35.2	38.9
6	0.0	34.6	28.6	34.1	40.0	0.0	34.8	27.7	31.1	36.6
7	0.0	30.4	25.5	31.3	37.2	0.0	29.4	22.4	26.4	32.3
8	0.0	26.7	22.1	28.3	33.8	0.0	24.9	18.1	24.1	29.0
9	0.0	24.3	18.9	24.9	29.9	0.0	22.5	16.2	22.6	27.2
10	0.0	21.5	16.6	21.1	25.5	0.0	19.5	14.6	20.0	25.0
11	0.0	20.2	15.0	18.5	21.9	0.0	17.0	12.8	16.7	21.2
12	0.0	18.0	13.2	15.1	19.4	0.0	14.9	12.1	13.6	16.4
13	0.0	15.9	10.7	12.7	16.6	0.0	12.6	10.8	12.3	13.4
14	0.0	12.8	8.5	9.6	14.7	0.0	11.4	9.6	10.6	13.7
15	0.0	10.9	7.0	7.7	12.9	0.0	11.0	7.7	8.7	13.4
16	0.0	10.1	5.7	6.8	12.9	0.0	11.3	6.7	8.6	14.0
17	0.0	9.8	5.3	7.0	13.2	0.0	12.9	6.4	9.9	15.2
18	0.0	12.5	7.6	10.2	15.8	0.0	16.3	7.9	13.1	17.9
Max.	0.0	36.5	30.6	35.5	40.8	0.0	38.4	34.6	36.8	39.2
Min.	0.0	9.8	5.3	6.8	12.9	0.0	11.0	6.4	8.6	13.4

Table 7-35: Connection deformation, STD [mm]

Floor Number	Connection Deformation, STD [mm]									
	(Global X-dir.)					(Global Y-dir.)				
	RE	Modified FD	Mod.FD+ LDCB, DoC=0.3	Mod.FD+ LDCB, DoC=0.4	Mod.FD+ LDCB, DoC=0.5	RE	Modified FD	Mod.FD+ LDCB, DoC=0.3	Mod.FD+ LDCB, DoC=0.4	Mod.FD+ LDCB, DoC=0.5
1	0.0	7.7	6.1	7.1	8.6	0.0	6.9	7.5	7.0	5.7
2	0.0	14.0	10.8	12.6	15.2	0.0	12.0	11.7	12.1	9.7
3	0.0	18.9	14.5	16.7	19.9	0.0	15.4	14.7	15.4	12.5
4	0.0	22.4	17.3	19.7	23.2	0.0	17.3	16.2	17.0	14.7
5	0.0	24.2	18.8	21.3	25.1	0.0	18.6	16.5	17.5	16.6
6	0.0	24.1	18.4	20.7	24.6	0.0	18.9	15.4	17.3	17.7
7	0.0	21.7	16.2	19.3	23.1	0.0	18.3	13.2	16.5	18.9
8	0.0	18.8	13.1	17.5	21.4	0.0	16.0	10.6	14.7	19.1
9	0.0	17.2	10.8	16.0	20.4	0.0	12.7	7.2	12.5	16.9
10	0.0	15.7	9.4	14.6	18.8	0.0	10.4	5.8	10.0	13.2
11	0.0	13.0	7.9	12.6	15.2	0.0	8.3	4.7	6.5	8.4
12	0.0	10.6	5.0	8.3	11.0	0.0	6.3	3.3	4.3	5.3
13	0.0	7.6	3.0	3.7	7.0	0.0	4.4	3.3	4.0	4.9
14	0.0	7.0	3.0	3.4	7.3	0.0	4.8	3.2	3.6	5.7
15	0.0	7.3	3.4	3.2	8.3	0.0	5.5	3.0	2.7	6.7
16	0.0	7.5	3.4	2.8	8.7	0.0	7.2	2.8	2.7	7.8
17	0.0	8.2	2.3	2.4	9.1	0.0	9.4	3.0	3.8	8.9
18	0.0	9.1	2.1	4.2	9.0	0.0	12.5	3.7	5.0	10.0
Max.	0.0	24.2	18.8	21.3	25.1	0.0	18.9	16.5	17.5	19.1
Min.	0.0	7.0	2.1	2.4	7.0	0.0	4.4	2.8	2.7	4.9

Table 7-36: Connection deformation, c.o.v [mm]

Floor Number	Connection Deformation, c.o.v [%]									
	(Global X-dir.)					(Global Y-dir.)				
	RE	Modified FD	Mod.FD+ LDCB, DoC=0.3	Mod.FD+ LDCB, DoC=0.4	Mod.FD+ LDCB, DoC=0.5	RE	Modified FD	Mod.FD+ LDCB, DoC=0.3	Mod.FD+ LDCB, DoC=0.4	Mod.FD+ LDCB, DoC=0.5
1	-	45.3	41.0	44.5	49.0	-	36.9	38.8	36.9	30.9
2	-	51.6	45.3	48.0	53.6	-	40.4	39.8	41.0	33.2
3	-	56.8	50.3	51.7	56.5	-	42.7	43.1	44.0	34.4
4	-	62.0	56.7	56.2	59.5	-	45.1	46.8	46.3	37.4
5	-	66.1	61.9	60.0	61.5	-	48.7	51.3	49.8	42.8
6	-	69.7	64.4	60.7	61.5	-	54.4	55.8	55.6	48.3
7	-	71.3	63.5	61.8	62.2	-	62.3	59.1	62.5	58.6
8	-	70.4	59.1	61.8	63.4	-	64.2	58.4	60.9	65.9
9	-	71.0	57.4	64.3	68.4	-	56.6	44.8	55.2	62.2
10	-	72.9	57.0	69.2	73.4	-	53.1	40.1	50.3	52.7
11	-	64.5	52.4	68.1	69.3	-	48.6	37.0	38.7	39.8
12	-	58.8	38.1	55.1	56.7	-	42.0	26.9	31.8	32.4
13	-	48.1	27.9	29.6	42.2	-	35.2	30.7	32.8	36.8
14	-	54.9	35.5	35.4	49.7	-	42.0	33.3	34.0	42.0
15	-	67.1	48.3	41.9	64.3	-	49.8	38.8	30.6	50.1
16	-	74.7	59.3	40.3	67.5	-	63.9	41.6	31.3	56.1
17	-	84.5	44.0	33.5	68.8	-	73.0	47.4	38.8	58.8
18	-	72.5	27.4	41.5	57.3	-	76.7	46.9	38.6	55.9
Max.	-	84.5	64.4	69.2	73.4	-	76.7	59.1	62.5	65.9
Min.	-	45.3	27.4	29.6	42.2	-	35.2	26.9	30.6	30.9

REFERENCES

1. Paulay T, Priestley MJN (1992) Seismic design of reinforced concrete and masonry buildings. Wiley, New York

2. Paulay T (1971) Coupling Beams of Reinforced Concrete Shear Walls. Journal of the Structural Division 97:. https://doi.org/10.1061/JSDEAG.0002848

3. ACI Committee 318 (2019) Building Code Requirements for Structural Concrete (ACI 318-19) and Commentary. American Concrete Institute

4. Moehle JP, Ghodsi T, Hooper JD, Fields DC, Gedhada R (2011) NEHRP Seismic Design Technical Brief No. 6 - Seismic Design of Cast-in-Place Concrete Special Structural Walls and Coupling Beams: A Guide for Practicing Engineers. National Institute of Standards and Technology

5. Li G-Q, Pang M, Sun F, Jiang J, Hu D (2018) Seismic behavior of coupled shear wall structures with various concrete and steel coupling beams. The Structural Design of Tall and Special Buildings 27:. https://doi.org/10.1002/tal.1405

6. Restrepo JI (2021) SE 211 Advanced Structural Concrete [lecture PowerPoint slides]

7. Priestley MJN, Calvi GM, Kowalsky MJ (2008) Displacement-based seismic design of structures. IUSS Press

8. Lu X, Chen C, Chen Y, Shan J (2016) Application of replaceable coupling beams to RC structures. The Structural Design of Tall and Special Buildings 25:. https://doi.org/10.1002/tal.1292

9. Ji X, Hutt CM (2020) Seismic design and application of hybrid coupled walls with replaceable steel coupling beams in high-rise buildings. The Structural Design of Tall and Special Buildings 29:. https://doi.org/10.1002/tal.1727

10. Li S, Jiang H, He L (2019) Study of a new type of replaceable coupling beam in reinforced concrete shear wall structures. The Structural Design of Tall and Special Buildings 28:. https://doi.org/10.1002/tal.1620

11. Kam WY, Pampanin S, Elwood K (2011) Seismic performance of reinforced concrete buildings in the 22 February Christchurch (Lyttelton) earthquake. BNZSEE 44:. https://doi.org/10.5459/bnzsee.44.4.239-278

12. Naish D, Fry A, Klemencic R, Wallace J (2013) Reinforced Concrete Coupling Beams—Part I: Testing. ACI Structural Journal

13. Canbolat BA, Parra-Montesinos GJ, Wight JK (2005) Experimental Study on Seismic Behavior of High-Performance Fiber-Reinforced Cement Composite Coupling Beams. SJ 102:. https://doi.org/10.14359/13541

14. Harries KA, Mitchell D, Redwood RG, Cook WD (1997) Seismic design of coupled walls - a case for mixed construction. 24:

15. Fortney PJ, Shahrooz BM, Rassati GA (2007) Large-Scale Testing of a Replaceable "Fuse" Steel Coupling Beam. J Struct Eng 133:1801–1807. https://doi.org/10.1061/(ASCE)0733-9445(2007)133:12(1801)

16. Ji X, Wang Y, Ma Q, Okazaki T (2017) Cyclic Behavior of Replaceable Steel Coupling Beams. J Struct Eng 143:04016169. https://doi.org/10.1061/(ASCE)ST.1943-541X.0001661

17. Ji X, Wang Y, Zhang J, Okazaki T (2017) Seismic behavior and fragility curves of replaceable steel coupling beams with slabs. Engineering Structures 150:. https://doi.org/10.1016/j.engstruct.2017.07.045

18. Farsi A, Keshavarzi F, Pouladi P, Mirghaderi R (2016) Experimental study of a replaceable steel coupling beam with an end-plate connection. Journal of Constructional Steel Research 122:. https://doi.org/10.1016/j.jcsr.2016.03.018

19. Christopoulos C, Montgomery M (2013) Viscoelastic coupling dampers (VCDs) for enhanced wind and seismic performance of high-rise buildings. Earthquake Engineering & Structural Dynamics 42:. https://doi.org/10.1002/eqe.2321

20. Chung H-S, Moon B-W, Lee S-K, Park J-H, Min K-W (2009) Seismic performance of friction dampers using flexure of rc shear wall system. The Structural Design of Tall and Special Buildings 18:. https://doi.org/10.1002/tal.524

21. Qu Z, Ji X, Shi X, Wang Y, Liu H (2020) Cyclic loading test of steel coupling beams with mid-span friction dampers and RC slabs. Engineering Structures 203:. https://doi.org/10.1016/j.engstruct.2019.109876

22. Cui Y, Tang Q, Wu T, Okazaki T, Wang T (2022) Mechanism and Experimental Validation of Frictional Steel Truss Coupling Beams. Journal of Structural Engineering 148:. https://doi.org/10.1061/(ASCE)ST.1943-541X.0003420

23. Cui Y, Tang Q, Wu T, Wang T (2022) Seismic performance of bending-type frictional steel truss coupling beams. Earthquake Engineering & Structural Dynamics 51:. https://doi.org/10.1002/eqe.3585

24. Mualla IH, Belev B (2002) Performance of steel frames with a new friction damper device under earthquake excitation. Engineering Structures 24:. https://doi.org/10.1016/S0141-0296(01)00102-X

25. Kim J, Choi H, Min K-W (2011) Use of rotational friction dampers to enhance seismic and progressive collapse resisting capacity of structures. The Structural Design of Tall and Special Buildings 20:515–537. https://doi.org/10.1002/tal.563

26. Mirzabagheri S, Sanati M, Aghakouchak AA, Khadem SE (2015) Experimental and numerical investigation of rotational friction dampers with multi units in steel frames subjected to lateral excitation. Archives of Civil and Mechanical Engineering 15:. https://doi.org/10.1016/j.acme.2014.05.009

27. Jarrahi H, Asadi A, Khatibinia M, Etedali S (2020) Optimal design of rotational friction dampers for improving seismic performance of inelastic structures. Journal of Building Engineering 27:. https://doi.org/10.1016/j.jobe.2019.100960

28. Naeem A, Kim J (2020) Seismic retrofit of structures using rotational friction dampers with restoring force. Advances in Structural Engineering 23:3525–3540. https://doi.org/10.1177/1369433220939213

29. Veismoradi S, Yousef-beik SMM, Zarnani P, Quenneville P (2021) Development and parametric study of a new self-centering rotational friction damper. Engineering Structures 235:. https://doi.org/10.1016/j.engstruct.2021.112097

30. Yang C, Li A, Xie L (2022) Development of design method for precast concrete frame with dry-connected rotational friction dissipative beam-to-column joints. Journal of Building Engineering 45:. https://doi.org/10.1016/j.jobe.2021.103563

31. Lee S-J, Choi K-K, Lee J-E, Hieu Dinh N, Park W-I (2022) Hysteresis response of rotary friction dampers developed for seismic operational performance of non-structural components vulnerable to overturning. Structures 43:. https://doi.org/10.1016/j.istruc.2022.07.046

32. Choi K-S, Kim H-J (2014) Strength Demand of Hysteretic Energy Dissipating Devices Alternative to Coupling Beams in High-Rise Buildings

33. Li D (2022) A force-resisting rotary friction damper (RFD): Verification and comparison with traditional RFD. Engineering Structures

34. Calugaru V, Panagiotou M (2012) Response of tall cantilever wall buildings to strong pulse type seismic excitation. Earthquake Engineering & Structural Dynamics 41:. https://doi.org/10.1002/eqe.1185

35. Christopoulos C, Zhong C (2022) Towards understanding, estimating and mitigating higher-mode effects for more resilient tall buildings. Resilient Cities and Structures 1:. https://doi.org/10.1016/j.rcns.2022.03.005

36. Fatemi H, Paultre P, Lamarche C-P (2020) Experimental Evaluation of Inelastic Higher-Mode Effects on the Seismic Behavior of RC Structural Walls. J Struct Eng 146:. https://doi.org/10.1061/(ASCE)ST.1943-541X.0002509

37. Moehle J (2010) February 27, 2010 Chile earthquake reconnaissance team investigation. Reinforced concrete buildings

38. Skinner RI, Kelly JM, Heine AJ (1974) Hysteretic dampers for earthquake-resistant structures. Earthquake Engineering & Structural Dynamics 3:

39. Key DE (1984) The seismic performance of energy absorbing dampers in building structures. Bulletin of the New Zealand Society for Earthquake Engineering 17:. https://doi.org/10.5459/bnzsee.17.1.38-46

40. Luco JE, De Barros FCP (1998) Control of the seismic response of a composite tall building modelled by two interconnected shear beams. Earthquake Engineering & Structural Dynamics 27:. https://doi.org/10.1002/(SICI)1096-9845(199803)27:3<205::AID-EQE712>3.0.CO;2-X

41. Mar D, Tipping S, Mar T (2000) Smart Frame Story Isolation System: A New High-Performance Seismic Technology

42. Johnston H, Watson C, Pampanin S, Palermo A (2014) Shake table testing of an integrated low damage building system. Second European Conference on Earthquake Engineering and Seismology

43. Crane ST (2004) Influence of energy dissipation connections between floors and the lateral force resisting system. MS thesis, Dept of Structural Engineering, Univ of California, San Diego

44. Zhang D, Fleischman R, Restrepo J, Sause R, Maffei J, Mar D, Monti G (2014) Development of a Floor Inertial Force Limiting Anchorage System Building Seismic Response

45. Fleischman R, Restrepo J, Nema A, Zhang D, Shakya U, Zhang Z, Sause R, Tsampras G, Monti G (2015) Inertial Force-Limiting Anchorage System for Seismic Resistant Building Structures. https://doi.org/10.1061/9780784479117.111

46. Tsampras G, Sause R, Zhang D, Fleischman RB, Restrepo JI, Mar D, Maffei J (2016) Development of deformable connection for earthquake-resistant buildings to reduce floor accelerations and force responses: Deformable Connection for Reduced Structural Response. Earthquake Engng Struct Dyn 45:. https://doi.org/10.1002/eqe.2718

47. Tsampras G, Sause R, Fleischman R, Restrepo J, Zhang D, Zhang Z, Nema A, Shakya U (2014) Full-scale, components test of inertial force-limiting floor anchorage systems for seismic resistant building structures using a buckling restrained brace and steel reinforced low damping rubber bearings

48. Tsampras G, Sause R, Fleischman RB, Restrepo JI (2017) Experimental study of deformable connection consisting of buckling-restrained brace and rubber bearings to connect floor system to lateral force resisting system. Earthquake Engineering and Structural Dynamics 46:. https://doi.org/10.1002/eqe.2856

49. Tsampras G, Sause R, Fleischman RB, Restrepo JI (2018) Experimental study of deformable connection consisting of friction device and rubber bearings to connect floor

system to lateral force resisting system. Earthquake Engng Struct Dyn 47:. https://doi.org/10.1002/eqe.3004

50. Deierlein G, Reinhorn A, Willford M (2010) NEHRP Seismic Design Technical Brief No. 4 - Nonlinear Structural Analysis for Seismic Design: A Guide for Practicing Engineers

51. Zhang Z, Fleischman RB, Restrepo JI, Guerrini G, Nema A, Zhang D, Shakya U, Tsampras G, Sause R (2018) Shake-table test performance of an inertial force-limiting floor anchorage system. Earthquake Engineering and Structural Dynamics 47:. https://doi.org/10.1002/eqe.3047

52. Van Den Einde L, Conte JP, Restrepo JI, Bustamante R, Halvorson M, Hutchinson TC, Lai C-T, Lotfizadeh K, Luco JE, Morrison ML, Mosqueda G, Nemeth M, Ozcelik O, Restrepo S, Rodriguez A, Shing PB, Thoen B, Tsampras G (2021) NHERI@UC San Diego 6-DOF Large High-Performance Outdoor Shake Table Facility. Frontiers in Built Environment 6:

53. Tsampras G, Sause R (2022) Force-Based Design Method for Force-Limiting Deformable Connections in Earthquake-Resistant Buildings. J Struct Eng 148:. https://doi.org/10.1061/(ASCE)ST.1943-541X.0003456

54. Chen K, Tsampras G, Lee K, Mayorga CF (2022) Reusable Force-limiting Connection with Variable Friction Force for High-Performance Buildings. 8th Asia Conference on Earthquake Engineering (8ACEE), Taipei, Taiwan

55. Tauberg NA, Kolozvari K, Wallace JW (2019) Ductile Reinforced Concrete Coupled Walls: FEMA P695 Study. University of California, Los Angeles, USA

56. Applied Technology Council, Pacific Earthquake Engineering Research Center (2010) PEER/ATC 72-1: Modeling and Acceptance Criteria for Seismic Design and Analysis of Tall Buildings

57. Pacific Earthquake Engineering Center (2017) Tall Buildings Initiative (TBI): Guidelines for Performance-Based Seismic Design of Tall Buildings, Version 2.03

58. Moehle JP (2014) Seismic design of reinforced concrete buildings. McGraw-Hill Professional

59. Kent DC, Park R (1971) Flexural Members with Confined Concrete. J Struct Div 97:1969–1990. https://doi.org/10.1061/JSDEAG.0002957

60. Coleman J, Spacone E (2001) Localization Issues in Force-Based Frame Elements. J Struct Eng 127:. https://doi.org/10.1061/(ASCE)0733-9445(2001)127:11(1257)

61. Mander JB, Priestley MJN, Park R (1988) Theoretical Stress-Strain Model for Confined Concrete. Journal of Structural Engineering 114:. https://doi.org/10.1061/(ASCE)0733-9445(1988)114:8(1804)

62. Richart FE, Brandtzæg A, Brown RL (1928) A study of the failure of concrete under combined compressive stresses. University of Illinois at Urbana Champaign, College of Engineering Engineering Experiment Station

63. Richart FE, Brandtzæg A, Brown RL (1929) Failure of plain and spirally reinforced concrete in compression. University of Illinois at Urbana Champaign, College of Engineering Engineering Experiment Station

64. Richart FE, Brown RL (1934) An Investigation of reinforced concrete columns ; a report of an investigation conducted by the Engineering Experiment Station, University of Illinois in coöperation with the American Concrete Institute. University of Illinois at Urbana Champaign, College of Engineering Engineering Experiment Station

65. Birrell M, Astroza R, Carreño R, Restrepo JI, Araya-Letelier G (2021) Bayesian parameter and joint probability distribution estimation for a hysteretic constitutive model of reinforcing steel. Structural Safety. https://doi.org/10.1016/j.strusafe.2020.102062

66. Beyer K, Dazio A, Priestley MJN (2008) Quasi-Static Cyclic Tests of Two U-Shaped Reinforced Concrete Walls. Journal of Earthquake Engineering 12:. https://doi.org/10.1080/13632460802003272

67. Mayorga CF, Lee K, Tsampras G (2016) Effect of the Structural Wall Modeling in the Seismic Response of Buildings with Force-limiting Connections between Diaphragm-to-wall Joints. Engineering Mechanics Institute (EMI) Conference, Baltimore, Maryland

68. Los Angeles Tall Buildings Structural Design (2017) An Alternative Procedure For Seismic Analysis And Design Of Tall Buildings Located In The Los Angeles Region. LATBSDC

69. FEMA (2009) Quantification of Building Seismic Performance Factors, FEMA P-695. Federal Emergency Management Agency

70. Los Angeles Tall Buildings Structural Design (2020) An Alternative Procedure For Seismic Analysis And Design Of Tall Buildings Located In The Los Angeles Region. LATBSDC

71. American Institute of Steel Construction (2017) Steel Construction Manual, 15th Edition. AISC

72. Boore DM (2010) Orientation-Independent, Nongeometric-Mean Measures of Seismic Intensity from Two Horizontal Components of Motion. Bulletin of the Seismological Society of America 100:. https://doi.org/10.1785/0120090400

73. American Society of Civil Engineers (2017) ASCE7-16, Minimum Design Loads and Associated Criteria for Buildings and Other Structures, 7th ed. American Society of Civil Engineers, Reston, VA